

# A Preliminary Design Tool For Radial Compressors

**Johannes Schiff**

Thesis for the Degree of Master of Science

---

Division of Thermal Power Engineering  
Department of Energy Sciences  
Faculty of Engineering, LTH  
Lund University  
P.O. Box 118  
SE-221 00 Lund  
Sweden





# A Preliminary Design Tool For Radial Compressors

Thesis for the Degree of Master of Science,  
conducted at the Division of Thermal Power Engineering,  
Department of Energy Sciences,  
Faculty of Engineering, Lund University

June 2013

Johannes Schiff

Supervisor: Magnus Genrup

## Abstract

The aim of this thesis has been to implement a computer program capable of modelling radial compressors. The work was conducted at the Division of Thermal Power Engineering, Department of Energy Sciences at the Faculty of Engineering, Lund University.

With such a large field as radial compressors, some decomposition of the subject was necessary. This thesis focuses on modelling the impeller and diffuser of the compressor, where the components are individually studied. By doing this division between different parts of the compressor, the individual components can be designed in isolation. If, for instance, only a vaned diffuser is to be designed, no impeller design must first be found.

The resulting computer program called LURC (**L**und **U**niversity **R**adial **C**ompressor) have two different design tools for the impeller, one in-depth impeller flow analysis, one vaneless diffuser design tool and one vaned diffuser design tool. The compressor designer can easily perform different analyses with LURC, all design tools being easily accessible at all times. Also, several of the different analysis tools are interconnected, allowing easy data exchange.

The so-called preliminary impeller design tool requires minimum input data from the user, quickly yielding a promising impeller design. It is a one-dimensional analysis method, where most parameters are specified on the mean streamline. The complete impeller geometry is directly generated, making it a perfect tool for the non-experienced compressor designer. Further, the result can be used as input data in any of the two diffuser analyses.

In the detailed impeller design tool more input data must be specified. Also, the geometry and blade shapes are under full control of the designer. This analysis is also one-dimensional but has the capability of creating three-dimensional impeller geometries. Such a tool is well suited to the more experienced designer, knowing what he or she want to achieve. The result can be used in both diffuser analyses, but also in the in-depth impeller flow analysis.

The in-depth impeller flow analysis is based on a quasi three-dimensional calculation method. In this case a streamline curvature method is coupled with a stream function flow analysis, allowing the three-dimensional problem to be composed of two two-dimensional ones. From this analysis tool the velocity distributions along the blades may be found, giving the experienced designer a vital piece of information.

Vaneless diffusers are very common in radial compressors, making it important to incorporate these in LURC. Input data may be entered manually or imported from a previous impeller analysis. The analysis is based on one-dimensional theory, including effects of wall friction. The complete geometry is generated and the key results, such as discharge pressure and velocity, are calculated.

The vaned diffuser design tool are focused on channel diffusers of the wedge type. Also included in the analysis are the vaneless space right after the impeller discharge. As was the case for the vaneless diffuser design tool, inlet data can be entered either manually or fetched from an impeller analysis conducted earlier. The whole diffuser geometry is generated, that is, both the vaneless space and the channel diffuser part. One-dimensional compressible channel flow is the basis for this analysis.

LURC fulfils its main objective; being a fast design tool for establishing promising compressor stage designs. Although mainly based on one-dimensional analyses, it is a very efficient and powerful tool for determining important design parameters in a timely fashion.

## Sammanfattning

Målet med detta examensarbete var att implementera ett datorprogram som modellerar radialkompressorer. Arbetet har utförts på Avdelningen för Kraftverksteknik, Institutionen för Energivetenskaper vid Lunds Tekniska Högskola, Lunds Universitet.

Med ett så brett område som radialkompressorer, behövde ämnet brytas ned i mindre delar. Detta examensarbete är inriktat mot modellering av impeller och diffusor i en kompressor, där varje komponent är analyserad var för sig. Genom att göra denna uppdelning av de olika delarna av kompressorn kan varje komponent designas individuellt. Om, till exempel, endast en beskovlad diffusor ska utformas, krävs det inte att någon impeller designas först.

Det resulterande datorprogrammet benämnt LURC (**L**und **U**niversity **R**adial **C**ompressor) har två olika designverktyg för impellrar, en djupgående flödesanalys av impellrar, ett designverktyg för beskovlingslösa diffusorer samt ett designverktyg för beskovlade diffusorer. Kompressor-designern kan enkelt göra olika analyser med hjälp av LURC, då alla designverktyg hela tiden är enkelt åtkomliga. Dessutom är många av de olika analysverktygen kopplade till varandra, vilket möjliggör smidiga datautbyten.

Det så kallade preliminära designvertyget för impellrar kräver minimalt med indata från användaren, där en lovande impellerdesign snabbt fås fram. Det är en endimensionell analys, där de flesta paramterarna specificeras på medelströmlinjen. Hela impellergeometrin genereras direkt, vilket gör det till ett utmärkt verktyg för den oerfarne kompressor-designern. Vidare kan resultaten användas som indata i någon av de två diffusoranalyserna.

I verktyget för detaljerade impelleranalyser måste mer indata specificeras. Dessutom är även geometri och bladutformning under designerns fulla kontroll. Denna analys är också endimensionell, men har möjligheten att generera tredimensionella impellergeometrier. Ett verktyg av denna karaktär kommer väl till pass för den erfarne designern som vet vad han eller hon vill uppnå. Resultaten kan användas i båda diffusoranalyser, men också i den mer djupgående flödesanalysen av impellrar.

Den djupgående flödesanalysen för impellrar är baserad på en kvasi-tredimensionell beräkningsmetod. Här är en strömlinjekurvaturmetod kopplad med en strömfunktionsanalys, vilket tillåter att det tredimensionella problemet delas upp i två stycken tvådimensionella problem. Med hjälp av detta analysverktyg kan hastighetsfördelningarna längs bladen bestämmas, resultat som den erfarne designern kan finna stor användning för.

Beskovlingslösa diffusorer är mycket vanliga bland radialkompressorer, vilket gör det väldigt viktigt att inkludera dessa i LURC. Indata kan skrivas in för hand, eller importeras från en tidigare impelleranalys. Analysen är baserad på endimensionell teori, vilken inkluderar väggfriktionseffekter. Hela geometrin genereras och resultaten av störst vikt beräknas såsom utloppstryck och utloppshastighet.

Verktyget för beskovlade diffusorer är inriktat mot kanaldiffusorer av kiltyp. Utrymmet utan blad precis efter impellern är också inkluderat i analysen. Precis som för designvertyget till de beskovlingslösa diffusorerna kan indata antingen matas in för hand eller hämtas från en tidigare utförd impelleranalys. Hela diffusorgeometrin genereras, det vill säga både utrymmet utan blad och kanaldiffusordelen. Endimensionell kompressibel kanalströmning står som basis för denna analys.

LURC uppfyller det huvudsakliga målet; att vara ett designverktyg för att snabbt komma fram till lovande kompressor-designer. Trots att det till stor del är baserat på endimensionella analyser, är det ett väldigt effektivt och kraftfullt verktyg för att bestämma viktiga designparamter på kort tid.

# Contents

<b>Preface</b>	<b>vi</b>
<b>Nomenclature</b>	<b>xiii</b>
<b>1 Introduction</b>	<b>1</b>
1.1 Overview . . . . .	1
1.1.1 Radial compressor configurations . . . . .	1
1.1.2 Radial compressor characteristics . . . . .	4
1.2 Analysis techniques . . . . .	7
1.3 The aim of the study . . . . .	9
1.3.1 Report structure . . . . .	9
<b>2 Common modelling and methods</b>	<b>11</b>
<b>3 Preliminary impeller design</b>	<b>19</b>
3.1 Basic relations . . . . .	19
3.2 Geometrical construction . . . . .	25
3.3 Calculation procedure . . . . .	28
3.3.1 Input parameters . . . . .	28
3.3.2 Calculation model . . . . .	30
<b>4 Detailed impeller design</b>	<b>37</b>
4.1 Basic relations . . . . .	37
4.2 Geometrical construction . . . . .	41
4.3 Calculation procedure . . . . .	46
4.3.1 Input parameters . . . . .	46
4.3.2 Calculation model . . . . .	49
<b>5 Impeller internal flow analysis</b>	<b>53</b>
5.1 Basic relations . . . . .	53
5.1.1 Hub-to-shroud flow analysis . . . . .	56
5.1.2 Blade-to-blade flow analysis . . . . .	58
5.2 Calculation procedure . . . . .	64
5.2.1 Input parameters . . . . .	64
5.2.2 Calculation model . . . . .	64

<b>6</b>	<b>Vaneless diffuser design</b>	<b>77</b>
6.1	Basic relations . . . . .	77
6.2	Geometrical construction . . . . .	83
6.3	Calculation procedure . . . . .	85
6.3.1	Input parameters . . . . .	86
6.3.2	Calculation model . . . . .	87
<b>7</b>	<b>Vaned diffuser design</b>	<b>89</b>
7.1	Basic relations . . . . .	90
7.2	Geometrical construction . . . . .	92
7.3	Calculation procedure . . . . .	93
7.3.1	Input parameters . . . . .	94
7.3.2	Calculation model . . . . .	96
<b>8</b>	<b>Computer implementation</b>	<b>101</b>
8.1	Basic program structure . . . . .	101
8.2	Common features and components of the analysis tools . . . . .	102
8.3	Results of the individual analyses . . . . .	104
8.3.1	Start-up of LURC . . . . .	104
8.3.2	Preliminary impeller design . . . . .	106
8.3.3	Detailed impeller analysis . . . . .	108
8.3.4	Impeller internal flow analysis . . . . .	113
8.3.5	Vaneless diffuser analysis . . . . .	117
8.3.6	Wedge diffuser analysis . . . . .	119
8.3.7	About . . . . .	121
<b>9</b>	<b>Conclusions</b>	<b>123</b>
9.1	Questions answered . . . . .	123
9.2	Future work - possible improvements . . . . .	124
<b>10</b>	<b>Bibliography</b>	<b>127</b>
<b>A</b>	<b>Rotated coordinate systems</b>	<b>129</b>
<b>B</b>	<b>Distribution of equally spaced points along a line</b>	<b>131</b>
<b>C</b>	<b>Calculation of passage area and mean streamline</b>	<b>135</b>
<b>D</b>	<b>Crossing of blade and stream surfaces</b>	<b>141</b>
<b>E</b>	<b>Determination of meridional and tangential equilibrium in vaneless space</b>	<b>145</b>
<b>F</b>	<b>Runge-Kutta numerical integration of ordinary differential equations</b>	<b>149</b>
<b>G</b>	<b>One-dimensional channel flow</b>	<b>151</b>

# Preface

To bring five years of study in Mechanical Engineering at the Faculty of Engineering, Lund University, to a sudden end this master's thesis has been carried out at the Division of Thermal Power Engineering, Department of Energy Sciences. The effort of this theses represents one semester's work, or equivalently 30 ECTS.

Looking five years back, I would never have anticipated to what an extent a couple of years at an university can change the way one think and reason. It has with no doubt been some of the best years of my life, yet some of the most hard and challenging. I have had the fortune of making a series of good decisions, leading to the point where I am right now. Not only have I found subjects I didn't know existed before, but also subjects I have fallen for.

Instead looking only half a year back, when I got the opportunity to conduct this thesis, I thought creating a computer program for compressors seemed like a perfect project. The perfect project did quite quickly turn into a project taking a lot of attention and tinkering time. Many nights and weekends were spent on reading, programming and writing. With the final result at hand it feels well worth the effort.

I have learned new things throughout the whole thesis, coming across parts of the turbomachinery field where I had little or practically no knowledge at all. There are especially two persons who made it all possible. First of all, my supervisor Magnus Genrup at the Division of Thermal Power Engineering was the person giving me the opportunity to conduct this thesis. He has also given me valuable input and new ideas throughout the whole project. Magnus is one of the persons opening the door to my interest for turbomachinery. Second of all, and although somewhat of a cliché, I would not have had the strength, energy or sense to at all complete this work if it was not for my girlfriend, Emelie Jönsson. Living apart from each other has not made these months any easier, but it will make coming back so much better.

June 2013  
Baden, Switzerland



# Nomenclature

## Variables

$\alpha$	absolute flow angle, measured from meridional direction or constant in Runge-Kutta integration
$\alpha'$	relative flow angle, measured from meridional direction
$\alpha_C$	streamline/stream surface slope
$\alpha_{QN}$	quasi normal angle as measured from axial direction
$\bar{\beta}$	blade angle at mid impeller passage
$\beta$	blade angle, measured from meridional direction or constant in Runge-Kutta integration
$\chi$	x value in a rotated coordinate system
$\Delta W$	average blade velocity difference
$\Delta z_I$	impeller axial length
$\Delta$	difference in property or property relating to a stream sheet
$\delta$	angle defining a wedge diffuser geometry
$\dot{m}$	mass flow
$\epsilon$	deviation (angle) of quasi normal from an actual normal
$\eta$	efficiency or y value in a rotated coordinate system
$\gamma$	ratio of specific heats at constant pressure and volume or angle between similar points in a vaned diffuser
$\kappa$	velocity distortion or streamline/stream surface curvature
$\lambda$	tip distortion factor, impeller tip absolute tangential to meridional velocity ratio or coordinate along impeller flow passage
$\mu$	head coefficient or dynamic viscosity
$\nu$	specific volume
$\omega$	angular velocity

$\omega_{diff}$	diffuser stagnation pressure loss
$\Phi$	half divergence angle of vaned diffuser wedge
$\phi$	flow coefficient
$\phi_{coord}$	angle of rotated coordinate system
$\Psi$	stream function
$\rho$	density
$\sigma$	slip factor, rake angle or direction along quasi normal
$\tau$	shear stress
$\theta$	tangential (polar) coordinate or vaned diffuser (half) divergence angle
$\varsigma$	coordinate between blade surfaces in a flow passage
$\vec{B}$	vector along blade element
$\vec{e}_\theta$	unit vector in tangential direction
$\vec{e}_n$	unit vector in normal direction
$\vec{S}$	vector tangent to mean camberline
$\vec{T}$	vector normal to blade surface
$\xi$	dimensionless distance along blade element or angle defining a wedge diffuser geometry
$\zeta$	dimensionless meridional distance inside impeller
$A$	passage area, a constant defining the blade angle distribution, parameter in blade-to-blade flow analysis or parameter determining vaneless diffuser geometry
$a$	sonic velocity, a point defining a geometry, incremental area, parameter defining a linearised stream function or function used in Runge-Kutta integration
$AR$	diffuser area ratio
$B$	a constant defining the blade angle distribution, blockage factor, parameter in blade-to-blade flow analysis or parameter determining vaneless diffuser geometry
$b$	hub to shroud passage width, stream sheet thickness, a point defining a geometry or function used in Runge-Kutta integration
$B_D$	non-dimensional passage width in vaneless diffuser
$B_{ss}$	empirical constant
$BL$	blade loading
$C$	absolute velocity, constant defining the blade angle distribution, parameter in blade-to-blade flow analysis or parameter determining vaneless diffuser geometry

$c$	point defining a geometry
$C_f$	friction coefficient
$c_p$	specific heat at constant pressure
$C_s$	fluid constant in Sutherland's formula
$c_v$	specific heat at constant volume
$C_{p,D}$	static pressure recovery coefficient
$C_{slip}$	absolute slip velocity
$CFD$	computational fluid dynamics
$D$	diameter or parameter determining vaneless diffuser geometry
$d$	a parameter defining wedge diffuser geometry
$d_H$	hydraulic diameter
$DR$	diffusion ratio
$E$	variable in blade-to-blade flow analysis or parameter determining vaneless diffuser geometry
$e$	a parameter defining wedge diffuser geometry
$F$	function of, variable in blade-to-blade flow analysis or parameter determining vaneless diffuser geometry
$f$	function of, variable in blade-to-blade flow analysis or a parameter defining wedge diffuser geometry
$G$	variable in blade-to-blade flow analysis
$g$	variable in blade-to-blade flow analysis or a parameter defining wedge diffuser geometry
$GUI$	graphical user interface
$H$	variable in blade-to-blade flow analysis
$h$	specific enthalpy, a parameter defining wedge diffuser geometry or Runge-Kutta integration step
$I$	work input coefficient
$i$	incidence angle or a parameter defining wedge diffuser geometry
$I_B$	blade work input coefficient
$I_{par}$	parasitic loss coefficient
$K$	parameter adjusting the blade angle distribution

$k$	specific Bezier reference point or constant determining the friction factor
$K_\lambda$	parameter needed to determine the tip distortion factor $\lambda$
$K_{ss}$	total number of stream surfaces
$L$	linear extension of circular arc or three-point cubic spline, total length of line, blade segment length or channel diffuser length
$l$	line segment length or spacing between points
$L_B$	blade mean camberline length
$L_S$	mean streamline length
$l_S$	mean streamline line segment length
$M$	Mach number or parameter defining a three-point cubic spline
$m$	coordinate in meridional direction
$m_b$	stream sheet mass flow per stream sheet thickness
$M_{U2}$	machine Mach number
$N$	rotation speed (revolutions per minute) or an index denoting the total amount of specific points or increments
$n$	coordinate in normal direction or number of Bezier reference points
$N_e$	amount of evenly distributed points
$o$	point defining a geometry
$P$	power
$p$	pressure
$P_D$	non-dimensional pressure in vaneless diffuser
$PR$	pressure ratio
$Q$	arbitrary function
$R$	specific gas constant
$r$	radius or radial coordinate
$R_0$	rothalpy
$R_C$	radius of circular arc
$R_D$	non-dimensional radius in vaneless diffuser
$Re$	Reynolds number
$S$	blade passage width

$s$	specific entropy
$T$	temperature
$t_B$	blade thickness, as measured normal to mean camberline
$U$	impeller speed or dimensionless distance along a Bezier curve
$u$	arbitrary direction
$W$	relative velocity
$w$	wedge diffuser width
$X$	x value characterizing a circular arc or three-point cubic spline
$x$	coordinate in the x direction
$Y$	y value characterizing a circular arc or three-point cubic spline
$y$	coordinate in the y direction
$z$	coordinate in the z (axial) direction
$Z_D$	number of vaned diffuser blades
$Z_I$	number of impeller blades

### Subscripts

0	stagnation property or property at compressor inlet
1	property at impeller inlet
2	property at impeller exit
3	property at diffuser blend radius
4	property at vaned diffuser throat
5	property at diffuser exit
$\chi$	parameter in the $\chi$ direction
$\eta$	parameter in the $\eta$ direction
$\infty$	property relating to an infinite number of infinitesimally thin blades
$\lambda$	parameter in the $\lambda$ direction
$\theta$	parameter in the tangential direction
$\varsigma$	parameter in the $\varsigma$ direction
$A$	area enclosed by closed path
<i>annular</i>	variable referring to an annular parameter

<i>avail</i>	property available for the local flow
<i>blades</i>	parameter relating to the impeller blades
<i>bs</i>	blade surface coordinate
<i>C</i>	parameter on streamline/stream surface or closed path
<i>eq</i>	property corresponding to an equal amount
<i>h</i>	parameter on the hub
<i>I</i>	compressor stage inlet property or impeller parameter
<i>i</i>	index indicating a specific point
<i>II</i>	compressor stage discharge property
<i>incr</i>	an increment of the parameter
<i>j</i>	index indicating intermediate (mean) points
<i>k</i>	interval of points defining a three-point cubic spline
<i>l</i>	laminar
<i>LE</i>	leading edge
<i>m</i>	parameter in the meridional direction
<i>max</i>	a maximum value of the parameter
<i>min</i>	a minimum value of the parameter
<i>n</i>	parameter in the normal direction
<i>p</i>	polytropic property or property on pressure side
<i>passage</i>	variable referring to a passage parameter
<i>r</i>	parameter in the radial direction
<i>ref</i>	reference condition
<i>s</i>	parameter on the shroud, parameter on suction side or isentropic change of state
<i>stage</i>	parameter relating to the compressor stage
<i>t</i>	turbulent
<i>taper</i>	property referring to a tapered region
<i>TE</i>	trailing edge
<i>tot – stat</i>	total-to-static property
<i>tot – tot</i>	total-to-total property

$U$	specific Bezier point
$VD$	parameter for vaned diffusers
$VLD$	parameter for vaneless diffusers
$w$	property at wall
$x$	component in the x direction
$y$	component in the y direction
$z$	component in the z direction

### **Superscripts**

$-$	mean property, property at mean location or a vectorial length
$//$	second order derivative
$/$	relative property, first order derivative or already covered line segment
$\sim$	mass averaged property
$\rightarrow$	vectorial quantity





# Chapter 1

## Introduction

This part serves as an introduction to the subject of radial compressors, as well as describing what is to be achieved with the analysis conducted. The reader is assumed to have some basic knowledge of terms typically used in turbomachinery, even though a simple description of the components of a radial compressor follow below.

### 1.1 Overview

One general subdivision of compressors is to separate between turbomachinery and displacement compressors. The distinction between the two types lies in what way mechanical power is transferred to the fluid being compressed. In displacement compressors the compressed fluid is delivered non-continuously, typically involving pistons. Turbomachinery compressors instead continuously supplies energy to the fluid, by the dynamic action of moving parts such as a blade row or an impeller, see Dixon (1998) [1]. Turbomachinery compressors is further subdivided, usually based on the direction of the main flow. Two types of machines is thereby easily distinguished; axial and radial compressors<sup>1</sup>. Axial compressors have the main flow along the axis of the rotation, and usually rather small amounts of fluid transport in the radial direction. The opposite of this would become a radial compressor, where instead a large portion of the fluid transportation is in the radial direction and, compared to the axial compressor, a very short axial path is followed. A third type of compressor could be a combination of the other two types, a so called mixed flow compressor, but these are rarely employed in practice. Following the main subject of this analysis treating radial compressors, the other two configurations are not pursued any further.

#### 1.1.1 Radial compressor configurations

Before any further discussions and analyses a simple description of the typical radial compressor layout is in order. A schematic sketch of a compressor stage together with notations for the various locations along the flow path used throughout this report is seen in figure 1.1. To separate the two main surfaces of the flow path, the surface being concave in the impeller is called the hub, while the convex surface is termed shroud. In subsequent analyses the subscript  $h$  will denote variables associated with the hub while subscript  $s$  denotes corresponding variables on the shroud. The fluid being compressed, typically air, flows into the compressor intake at

---

<sup>1</sup>Radial compressors are quite commonly also termed *centrifugal* compressors

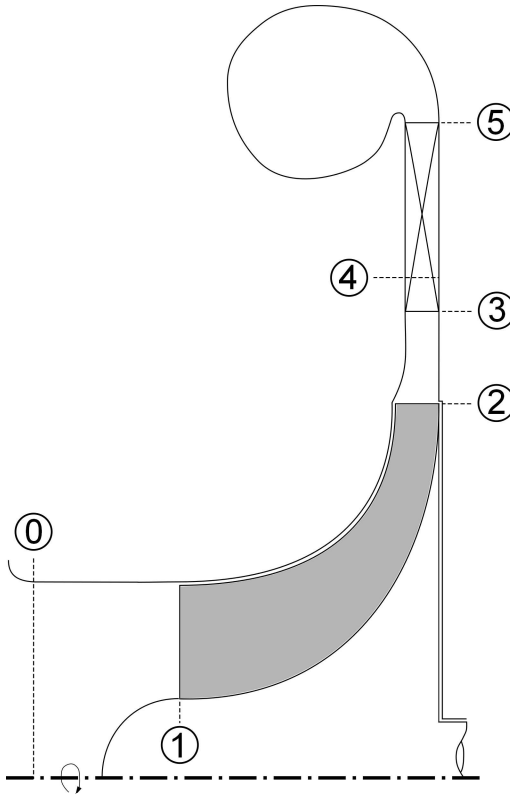


Figure 1.1: Schematic radial compressor stage layout with the different station numbering used in subsequent analyses

location 0, and encounters the impeller inlet<sup>2</sup> at station 1. The impeller is the component transferring energy to the fluid. Within the impeller diffusion takes place, increasing the pressure. In figure 1.1 an axial inlet of the impeller is shown, a so called inducer. When designing an impeller one may also use inducers not being axial, or actually not employ an inducer at all. Examples of three different types of inducers is depicted in figure 1.2. Which inducer type most suited to a specific compressor depends on several factors. As described by Aungier (2000) [2], the general shape of the impeller, especially the inducer, is a strong function of the dimensionless mass flow into the compressor, the so called flow coefficient. Referring to figure 1.2, the flow coefficient would be smallest for the impeller to the right with no inducer, while being largest for the left one with the full inducer. Impellers which falls in between these two will naturally also have a flow coefficient somewhere in between. By choosing an impeller with no inducer, the impeller blading usually employed is of a rather simple nature making them comparatively cheap and easy to manufacture. The main drawback is that impellers with these two-dimensional blade<sup>3</sup> shapes usually suffer from lower efficiencies due to friction effects stemming from long blade passages. Instead, by selecting an impeller with a full inducer one must resort to the more expensive and complicated three dimensional blade shapes. However, the efficiency is usually higher for these kind of impellers but can become somewhat limited because of the strong curvature needed to turn the inlet axial flow into radial. Once again, the

<sup>2</sup>The inlet part extending radially from the impeller hub to the shroud is sometimes referred to an impeller *eye*. In figure 1.1 this coincides with the impeller inlet.

<sup>3</sup>Sometimes impeller blades are instead referred to as *vanes*

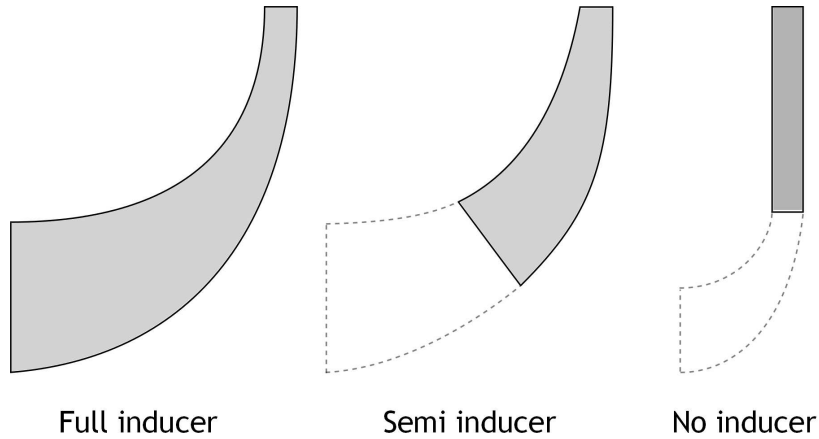


Figure 1.2: Different kind of impeller inducers. Blades are shaded gray, for the semi inducer and no inducer impeller the compressor inlet is shown dotted

semi inducer impeller would be expected to have efficiency levels somewhere in between the two other types. This analysis focuses on full inducer impellers.

Another rather important distinction between impellers can be made, based on the impeller tip construction. In many applications, typically in vehicle turbochargers, the impeller is *uncovered* at the tip, meaning that the shroud just outside the impeller is stationary. In the opposite case, the impeller can also be *covered* and thus having the shroud attached to the tip of the impeller blades. Which design to choose depend on mainly two things; strength and clearance considerations. Attaching a shroud to the impeller can sometimes be advantageous, see for instance Japikse (1996) [3]. One of the main reasons is to avoid leakage between different blade passages. However, by adding extra mass at the end of the blade tips, the mechanical stresses in a shrouded impeller will become much higher, thus limiting the impeller rotation speed to values below that of uncovered impellers. Sometimes the clearance between impeller and the compressor casing is a matter of concern, especially when designing multistage industrial compressors. In these cases the rotating shaft tends to be relatively long, and it thus becomes hard to keep clearances small enough to maintain high efficiencies for unshrouded impellers. Here a shrouded impeller could be employed, being rather insensitive to clearance differences as noted by Aungier (2000).

When the flow leaves the impeller at station 2 it enters the so called *vaneless* space. As the name implies, this is a region where no blades is present, and the fluid is allowed to move radially outwards. The vaneless space can be chosen to be followed by a *vaned diffuser*, or alternatively to be continued as a *vaneless diffuser*. The diffuser's task is to increase the static pressure by lowering the flow velocity. Which diffuser type to choose for a given duty is a rather complicated issue, and each design case will have to be individually studied. Some basic differences can nonetheless be outlined. Starting with the vaneless diffuser, the most striking feature is its mechanical simplicity. No blades have to be designed or manufactured, resulting in a solution associated with low cost. An additional advantage is the quite wide operating range allowed by a vaneless diffuser, since the vaneless space usually is less prone to choke as compared to a vaned ditto, see Japikse (1996). If instead a vaned diffuser is employed, the vaneless space ends at station 3 and a semi vaneless space appears until the throat section of the diffuser is reached, station 4. With the aid of a vaned diffuser the radial extent of the diffuser can be minimized, thus leading to a significantly smaller compressor

stage for a given application. Further, the design point efficiency can usually be higher than for a vaneless diffuser, though generally with deteriorated performance at off-design conditions. The actual vanes can be constructed in various ways, one design solution is to employ airfoil vanes. Another solution is to construct channel diffusers from wedges or drilled conical holes. Common to all diffusers is the, by most authors termed, "extremely complicated flow field" entering the component, making it very hard to model them accurately.

Finally, the flow leaves the diffuser part at station 5 and enters either, as shown in 1.1, a volute or a return channel. A volute is typically applied to the last stage of a compressor unit, where the kinetic energy will not be utilized in downstream parts. The flow is collected and usually led to a single exit pipe. It is important to note that the volute has a major influence of all upstream components in a radial compressor, and may even cause changes in the flow at the impeller inducer, see Breambussche (2013) [4]. If, instead, the compressor stage is not the last one, the flow is lead into a return channel. The purpose of a return channel is to direct the flow from a position of large radius to a position of a smaller radius. To gain an as high efficiency as possible of the downstream stage, it is necessary to remove the swirling flow. This can be achieved with the aid of blades in the return channel passage.

### 1.1.2 Radial compressor characteristics

In order to determine the behaviour of a radial compressor, different designs are usually compared on a non-dimensionalized basis. Following the procedure outlined by Dixon (1998), non-dimensionalized groups can be found based on various thermodynamic properties. These are the stagnation pressure ratio,  $p_{0II}/p_{0I} = PR_{stage,tot-tot}$ , the change in stagnation temperature over inlet stagnation temperature,  $\Delta T_0/T_{0I}$  and the efficiency,  $\eta$ , of a turbomachine. Throughout this analysis subscript  $0$  denotes thermodynamic stagnation conditions, while subscript  $I$  and  $II$  denotes compressor stage inlet and outlet, respectively. The dimensionless parameters can be written as

$$\frac{p_{0II}}{p_{0I}}, \frac{\Delta T_0}{T_{0I}}, \eta = f \left\{ \frac{\dot{m}\sqrt{RT_{0I}}}{D^2 p_{0I}}, \frac{ND}{\sqrt{RT_{0I}}}, Re, \gamma \right\} \quad (1.1)$$

where  $\dot{m}$  denotes the mass flow,  $R$  the specific gas constant,  $D$  a characteristic diameter,  $N$  the rotating speed,  $Re$  the Reynolds number and  $\gamma$  the ratio of specific heats. For a specific turbomachine handling a single fluid, the parameters  $D$ ,  $R$  and  $\gamma$  can be regarded as constant. Further, if the turbomachine is operated at high speed (fully developed flow) the Reynolds number  $Re$  can also be dropped. The final result is

$$\frac{p_{0II}}{p_{0I}}, \frac{\Delta T_0}{T_{0I}}, \eta = f \left\{ \frac{\dot{m}\sqrt{T_{0I}}}{p_{0I}}, \frac{N}{\sqrt{T_{0I}}} \right\} \quad (1.2)$$

Of course, by disregarding these parameters the groups are no longer non-dimensional, nonetheless equation 1.2 is widely used in practice. An example of a schematic compressor curves showing the relationship between the dimensionless groups and the "dimensionless" parameters is seen in figure 1.3. In this figure a number of features can be identified. What is shown is a plot of various constant speed lines, each line spanning from low flow levels near the surge line to higher flow rates where the flow is near or at choke. The surge line indicates the minimum value of the mass flow representing stable flow at the current pressure ratio and rotating speed. Any lowering of the mass flow (or decrease of rotational speed) would cause an inception of the

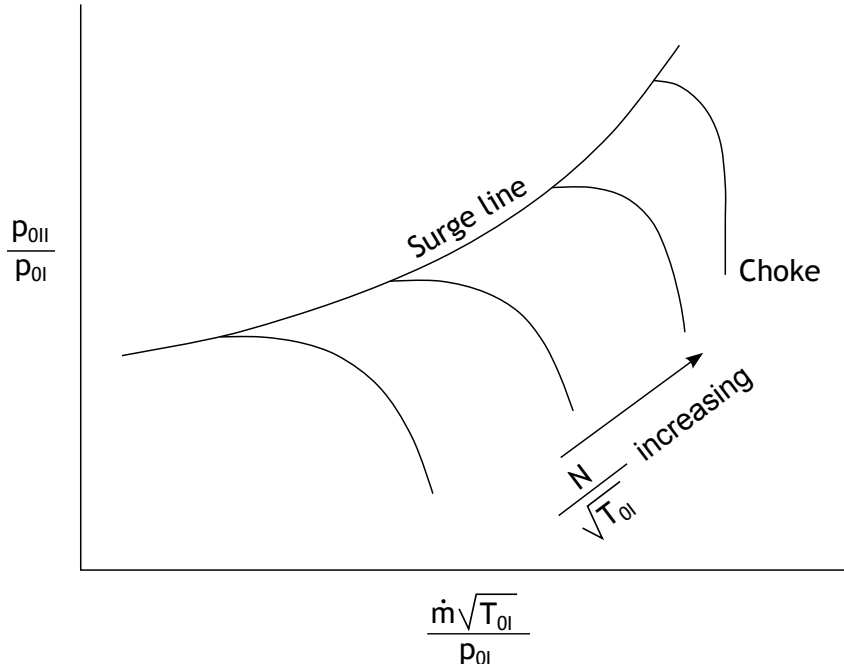


Figure 1.3: Schematic compressor map of stage pressure ratio versus "dimensionless" mass flow. Included are the surge line, constant speed lines and contours of constant efficiency

unstable flow phenomena called surge<sup>4</sup>, hence the name surge line. If, instead the mass flow is increased (or equally, the rotating speed increased) the flow would eventually not be able to be increased any more, and the compressor is said to be choked. This has occurred for the constant speed line representing the highest rotational speed, as can be seen by the vertical line in figure 1.3. Also shown in the figure is constant lines of the compressor efficiency, reaching a maximum somewhere on the performance map. The relation for temperature is not presented, but is related to the total pressure ratio by the polytropic relationship including the compressor efficiency. As an additional example, a map from the investigation of Rodgers (1964) [5] is depicted in figure 1.4. In this figure, the (squared) characteristic diameter has not been dropped and is retained as the impeller inlet area. In this case this is a suitable form, since different impeller types were tested and compared. Another feature of this diagram is that the efficiency is plotted separately, which sometimes can make readings from the graph somewhat easier. As can be seen, the overall trend is similar to the one schematically shown in figure 1.3. These groups of parameters are usually applied when determining the overall performance and behaviour of a compressor. However, different groups are usually employed specifically for radial compressors as described by Aungier (2000), and are used throughout this analysis. The flow coefficient has already been mentioned above and is defined by

$$\phi = \frac{\dot{m}}{\rho_{00}\pi r_2^2 U_2} = \frac{\dot{m}}{\rho_{00} \frac{\pi D_2^2}{4} U_2} \quad (1.3)$$

<sup>4</sup>Surge can be attributed to the fluid's compressibility. Energy is stored in the compressed fluid, and if surge occurs it discharges rapidly with impeller back flow as a consequence. One way to look at it is by recognizing surge as a condition where the impeller pressure rise is too high compared to the mass flow it passes

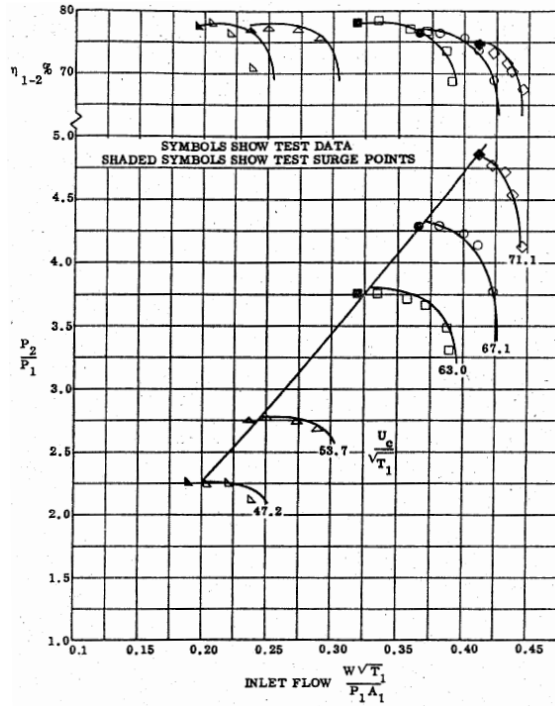


Figure 1.4: Compressor maps showing compressor pressure ratio and efficiency as a function of "dimensionless" mass flow and rotational speed. From Rodgers (1964)

where  $\rho_{00}$  represents the density at the compressor inlet based on stagnation properties,  $r_2$  is the impeller tip radius and  $U_2$  denotes the impeller (tangential) tip speed. When different compressor analyses are being compared, caution must be exercised, because sometimes the term  $\pi/4$  is dropped and sometimes it is retained. In this study the complete expression including  $\pi/4$  is employed, since the physical meaning behind the expression is clearer. Another dimensionless parameter is the head coefficient<sup>5</sup>  $\mu$ , representing how heavily loaded the stage is. This is written as

$$\mu = \frac{\Delta h_{0s}}{U_2^2} \quad (1.4)$$

here,  $\Delta h_{0s}$  represents the isentropic change in specific stagnation enthalpy needed to obtain the compressor stage's total pressure rise. An isentropic (adiabatic process, with no change in entropy) is regarded as the ideal compression process as outlined by many basic textbooks on the subject, see for instance Dixon (1998) or Çengel and Boles (2007) [6]. Having a high difference in enthalpy over the stage while operating at low rotating speed will yield a large head coefficient and thus a large stage loading. The opposite case with a low head coefficient would of course instead yield a lightly loaded stage. An example of a schematic head - flow coefficient characteristic is seen in figure 1.5, giving an idea of the typical behaviour of a stage. From the head coefficient curve in this figure, one can conclude that the flow is stable at most operating points. This can be seen from the fact that where the curve has a negative slope ( $d\mu/d\phi < 0$ ) a sudden drop in mass flow would increase the work input, thus striving to restore

<sup>5</sup>The name *head* coefficient has its origin from pump practice, where the term head refers to the geometrical height of a water column. In axial compressors it is instead denoted stage loading and is usually assigned the Greek letter  $\psi$

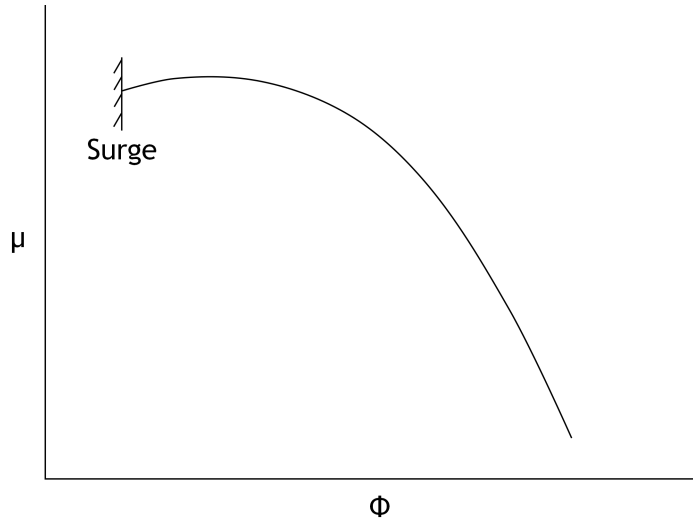


Figure 1.5: Typical head - flow characteristic of a radial compressor. A schematic point of the unstable flow phenomena surge is also displayed

the mass flow to its original value. Also depicted in figure 1.5 is the onset of surge at low flow coefficients. This phenomena has already been briefly discussed above, and here it suffices to say that the initiation of surge is to a large extent the result of operating in a region where the work input reduces with a dropped mass flow, see for instance Cumpsty (2004) [7] for an in-depth analysis. Finally, a third parameter called the rotational Mach number, or the machine Mach number is defined by

$$M_{U2} = \frac{U_2}{a_{00}} \quad (1.5)$$

where  $a_{00}$  is the sonic velocity based on inlet stagnation thermodynamic conditions. The machine Mach number is a measure of the general Mach numbers in the compressor and is restricted by the largest tolerable rotating speed. This parameter will thus, to a large extent, be limited by the material of choice for the impeller.

The main working principle of a radial compressor stage has now been outlined, together with typical parameters determining the performance and efficiency. The various components will be studied in greater detail when they are modelled in the subsequent chapters.

## 1.2 Analysis techniques

Throughout the industry a number of different approaches for determining the actual design of a radial compressor is being employed. They span from being non-dimensional to three-dimensional. One division between different methods is outlined by Japiske (1996), where three different levels of design and development are defined. The level one design employs similitude meaning that new compressor designs would, to the highest degree possible, be scaled. A scaling design methodology implies already having a finished, and preferably successful, compressor and is therefore not applicable when having no previous experience in the field. When a similitude approach can be utilized, it often is. One reason is the obvious cost-advantage of the reduced development work needed. Further, a known and trusted design will usually perform in a similar way, even when scaled down or up. There are limitations to this method

though. In all cases a similitude design strategy cannot be justified, typically when the duty is of a significantly different nature. One example of this is if the scaled version of the existing compressor would demand extremely high rotational speed to obtain complete similitude. The maximum rotational speed is typically determined by the structural integrity of the impeller, and must therefore be limited to reasonable levels. Another problem with scaling stems from the fact that the Reynolds number rarely can be scaled properly, partly loosing the complete similitude. The level two design also relies on experience to a certain extent, in this case different relationships for important parameters must be known. These typically involves correlations for impeller efficiency, or the whole stage efficiency. The correlations are used to back up one dimensional calculations throughout the whole compressor stage. With this design strategy the compressor is divided into the different main components, for example compressor inlet, impeller, diffuser and volute. These main components must, however, work well together and one component should not be designed without the other components in mind. For instance, a very strong coupling exist between the diffuser and the impeller, and a compressor design without proper matching of the stage as a whole would never perform satisfactory. To quite a large extent the level two modelling does not require the full understanding of the internal flow phenomena. One-dimensional methods are typically employed, neglecting many fundamental features of the flow. However, experience gained from previous compressor developments will many times suffice to recognise good or poor designs. One advantage with the method is the speed with which satisfactory solutions can be found. A one-dimensional calculation is completed in the order of magnitude of seconds, while actually gaining more information about the compressor than a level one design approach allows. The level three design is instead very detailed and take as many gas dynamic effects as possible into account. An analysis of this complexity is justified in many cases, typically involving compressors to be produced in large series, or compressor stages being extremely critical for its application. Again, it is necessary to partially resort to empirical data, and for this method to be as advantageous as possible a large number of previous compressor builds is essential for obtaining input data.

Nowadays, practically no turbomachinery is designed and evaluated without the aid of detailed three-dimensional computer analyses, as outlined by Cumpsty (2004). A computational fluid dynamics, CFD, approach is almost always justified, and computer running times are constantly being reduced. A typical CFD application could for instance be a detailed study of a flow at a certain region of the compressor. Still, the emphasis of CFD should not be over estimated. One reason is the very non steady flow encountered in most components of the stage, combined with the strong coupling between different components. Another reason is the fact that conducting multiple CFD calculations (including the above mentioned effects) is no guarantee for a good and reliable compressor design. Almost in all cases experience and engineering judgement regarding "good" design must be employed. This is partly because of the need to reduce development time, partly to actually obtain a compressor which works efficiently while still being manufacturable, reliable and having an as large operation range as possible.

As already noticed above, empirical data is needed as input almost regardless of which design methodology one chooses to follow. Therefore experiments are very useful and, when performed correctly, can give a lot of applicable results. Since the internal flow is of such complexity, actual test runs are the only way to assess the final performance of turbomachinery, Japikse (1996). The disadvantages lies within the time and cost involved of conducting such experiments. Tests can be performed following company specific test procedures or more generally according to different test codes, for instance the VDI 2045 (1993) [8].



## 1.3 The aim of the study

The objective of this analysis is to construct a computer program capable of quickly coming up with radial compressor component designs. It is preferable if as little input data as possible is needed. However, the accuracy of the calculation may not be compromised, nor the applicability of the program itself. Further, parameters that are critical in the view of performance influence should be under the control of the designer. Depending on the parameter in question, it could either be specified as design input or given as a calculation result. Another important part is the visualisation of the compressor geometry generated, since this tells the designer a great deal of information. Typical characteristics made visible includes the severity of the turning from axial to radial flow in the impeller, or just how (geometrically) large the compressor will be during certain constraints. The program must be able to compute the overall trends in critical parameters such as the impeller discharge total pressure or vaned diffuser inlet flow angle, just to mention a few examples. An additional objective of the program is to let users with almost no experience in the design of radial compressors understand what parameters have a large impact on the compressor itself.

Different compressor components must be possible to analyse individually. As has already been stressed, no compressor component can be viewed in complete isolation if a successful design is to be arrived at. However, if the computer program can be split up in several sub programs where the result data from one analysis can be used as input to another, no connection between components is lost. The advantage would be that individual components still can be designed. If for instance an existing compressor stage is being retrofitted with a vaned diffuser, the impeller outlet parameters are already specified. Then, there is little merit of first having to re-model the impeller and not until after this actually being able to look into the component of interest, the vaned diffuser.

In order to complete these objectives the following questions must be answered:

- How can the impeller of a radial compressor be modelled in an accurate, yet simple and fast way?
- Is there a method to cover a more in-depth analyse of the impeller, based on the simpler model mentioned above?
- How can a model for vaneless diffusers be implemented?
- In what way can the geometry and performance of a vaned diffuser be determined?

Answering these questions will require in-depth analyses of each separate component, with emphasis on different physical models.

### 1.3.1 Report structure

Chapter 2 is a common base for the main part of the analyses. Here, concepts used in several of the subsequent in-depth models are covered in order to ease the understanding and avoid mentioning similar details multiple times.

In chapter 3 to 4 two different ways of modelling the impeller is brought up; the first following the approach described by Aungier (2000) while the other, to a large extent, follows the method of Japikse (1996). The main difference between those methods is the way empirical data is being used. The first method uses a built in "recommended" target efficiency, mainly depending on the flow coefficient and generates an impeller geometry typical of the compressor

design target. Instead, the other method allows the user to completely determine the target efficiency or stage pressure rise, and the impeller geometry itself can be customized. In this study the method covered in chapter 3 is referred to the *preliminary* design, whilst the method in chapter 4 is denoted *detailed* design. It is important to note that the detailed design does not by itself generate more detailed or accurate results, but the design input (and how the calculated results should be interpreted) is of a more detailed character.

To get a more in-depth analysis of the impeller design generated, chapter 5 presents a method to determine the three-dimensional flow within the impeller itself. The method is based on dividing the complicated three-dimensional problem into two simpler two-dimensional ones. The main theory behind this method is adopted from Aungier (2000).

In the following two chapters different diffuser designs is instead modelled; vaneless diffusers in chapter 6 and channel diffusers of the so called wedge type in chapter 7. The channel diffuser calculation also takes the vaneless space between the impeller and vaned diffuser into account. Both methods generate the geometry based on user input, and calculate main parameters of interest. For vaneless space calculations the method of Stanitz (1952) [9] is used, taking many different aspects into account. The geometry of the wedge diffuser is adopted from Japikse (1996) and employs traditional compressible channel flow calculations.

Chapter 8 presents the computer implementation of the different component models. No programming details are brought up, the study being of a nature towards the turbomachinery field rather than computer science. What type of results one can obtain from the different tools are explained, together with different features of the program, in order to get as much useful information as possible out of an analysis.

In chapter 9 conclusions are being drawn. The chapter has its main focus on the four questions brought up earlier in this section and gives some reflections on the resulting computer program. Also, potential improvements of the compressor modelling techniques are briefly outlined.

Finally a set appendices are included, dealing with some of the more detailed calculations and concepts. These are included to show important methods and theories applied within the chapters. They have been regarded too bulky and extensive to be presented within the chapters considering the different analyses. The appendices may be skipped without great loss of understanding, but are recommended for the curious reader.

## Chapter 2

# Common modelling and methods

This chapter serves as a basis for the following five chapters explaining the physics and implementation of the various compressor components. Here, fundamental concepts common in two or more of the implementation chapters are described making the reading somewhat easier. It also allows the reader to quickly understand what typical methods have been employed in all analyses and which overall approximations have been made.

In order to quickly come up with promising radial compressor designs with minimum input data one-dimensional approaches are adopted for all but one analyses, corresponding to the level two design approach outlined above. This ensures speedy calculations which generally are accurate enough to base early design decisions on. An additional advantage is of course that the amount of input data is reduced, and enables novice designers to get a feel for various design parameters.

Common to the modelling of all components is the handling of gas properties. Throughout the study the gaseous fluid being compressed is assumed ideal, with constant specific heats<sup>1</sup>. No compressibility factors are employed, hence, the equation of state becomes the ideal gas law

$$p = \rho RT \quad (2.1)$$

and

$$h = c_p T \quad (2.2)$$

With the specific heats being constant, the ratio of the same is also constant according to

$$\gamma = \frac{c_p}{c_v} \quad (2.3)$$

where  $c_p$  and  $c_v$  is the specific heat at constant pressure and volume, respectively. Compressible flow analysis regarding perfect gases almost always involves calculations between temperature and pressure ratios, and the basic relationships are given below, from Greitzer, Tan and Graf (2006) [10]. The relation between specific stagnation enthalpy, specific static enthalpy and velocity  $C$  is given by

$$h_0 = h + \frac{C^2}{2} \quad (2.4)$$

and since specific heats are considered constant, a combination of equation 2.2 and 2.4 yields

$$T_0 = T + \frac{C^2}{2c_p} \quad (2.5)$$

---

<sup>1</sup>An ideal gas, having constant specific heats is sometimes termed a *perfect* gas

To relate pressure  $p$  to temperature the relation

$$\frac{p_0}{p} = \left( \frac{T_0}{T} \right)^{\frac{\gamma}{\gamma-1}} \quad (2.6)$$

is valid for isentropic processes, or properties in one single point. Sometimes it is instead useful to have temperature and pressure ratios related to the Mach number  $M$  defined by

$$M = \frac{C}{\sqrt{\gamma RT}} \quad (2.7)$$

Using the Mach number, the relation for temperature ratios is given by

$$\frac{T_0}{T} = 1 + \frac{\gamma-1}{2} M^2 \quad (2.8)$$

By combining equation 2.6 and 2.8 the pressure ratio can be written

$$\frac{p_0}{p} = \left( 1 + \frac{\gamma-1}{2} M^2 \right)^{\frac{\gamma}{\gamma-1}} \quad (2.9)$$

Equation 2.6 can also be modified to include the polytropic efficiency  $\eta_p$ , enabling the expression to be used between any two working points if the efficiency is known. This is well illustrated by Dixon (1998) and Rogers, Cohen, Saravanamuttoo and Straznicky (2009) [11]; the stagnation pressure ratio is given by

$$\frac{p_{0II}}{p_{0I}} = \left( \frac{T_{0II}}{T_{0I}} \right)^{\frac{\gamma \eta_p}{\gamma-1}} \quad (2.10)$$

In some cases the viscosity of the fluid being compressed is needed. For most gases it is found that the viscosity mainly varies with temperature, and not pressure. A somewhat "classic" relation determining the dynamic viscosity  $\mu$  at any temperature is Sutherland's formula, see for instance Anderson (2011) [12], and is given by

$$\mu = \mu_{ref} \frac{T_{ref} + C_s}{T + C_s} \left( \frac{T}{T_{ref}} \right)^{\frac{3}{2}} \quad (2.11)$$

Here,  $\mu_{ref}$  and  $T_{ref}$  is a viscosity and temperature, respectively, at some reference condition. The constant  $C_s$  depends on the fluid, and must also be specified.

The specific entropy  $s$  may also need to be determined, and a suitable relation can be found with Gibbs' second law as a basis (see for instance Çengel and Boles (2007))

$$Tds = dh - \nu dp \quad (2.12)$$

where  $\nu$  is the specific volume. The differential specific enthalpy change may be written

$$dh = d(c_p T) = c_p dT \quad (2.13)$$

which holds for constant specific heats.  $\nu$  may be found from the ideal gas law, equation 2.1, noting that it is the reciprocal of the density. Inserting these relations into equation 2.12 yields

$$Tds = c_p dT - \frac{RT}{p} dp \quad (2.14)$$

or equivalently

$$ds = c_p \frac{dT}{T} - R \frac{dp}{p} \quad (2.15)$$

Upon integration from state 1 to state 2, one find the following useful relationship

$$s_2 - s_1 = c_p \ln \frac{T_2}{T_1} - R \ln \frac{p_2}{p_1} \quad (2.16)$$

Hence, the absolute value of the specific entropy at any point can be determined from an arbitrary chosen reference condition. Which temperature, pressure and specific entropy used for the reference condition does not matter; as long as the same reference condition is used for all calculations, the entropy *differences* are consistent with each other.

A very useful relation, when looking at the impeller, is the Euler turbomachinery equation. This equation relates the change in tangential velocity over the impeller to the power input into the machine. It is derived in most basic turbomachinery textbooks, for instance Dixon (1998) or Rogers, Cohen, Saravanamuttoo and Straznicky (2009) and may be expressed according to

$$\Delta h_{0,blades} = \omega(r_2 C_{\theta 2} - r_1 C_{\theta 1}) = U_2 C_{\theta 2} - U_1 C_{\theta 1} \quad (2.17)$$

where  $\Delta h_{0,blades}$  denotes the actual work supplied from the blades to the fluid,  $\omega$  the angular velocity of the impeller and subscript  $\theta$  a component in the tangential direction. In equation 2.17 the relation

$$U = \omega r \quad (2.18)$$

was used to relate the angular velocity and radius to the tangentially directed machine velocity  $U$ . From equation 2.17 one notice that if preswirl<sup>2</sup> ( $C_{\theta 1} \neq 0$ ) is present at impeller inlet, the work input will be reduced. Hence, in order to maintain a prescribed pressure rise, the outlet tangential velocity must increase. This in turn leads to higher (absolute) exit Mach numbers, with the risk of complex shock structures at impeller exit and diffuser inlet. As described by Braembussche (2013) these shocks can actually be beneficial for the efficiency. This can be understood from the fact that the static pressure rise over a shock can be rather efficient as compared to the corresponding pressure rise due to channel diffusion.

The power  $P$  required to drive the compressor can be found from

$$P = \dot{m} \Delta h_0 \approx \dot{m} \Delta h_{0,blades} \quad (2.19)$$

where  $\Delta h_0$  represents the specific stagnation enthalpy difference over the impeller. This is not in general equal to the work supplied by the blades to the fluid, since parasitic losses such as disc friction must also be taken into account, see Dixon (1998).

An additional feature of all component calculations is the assumption of an adiabatic compressor. This highly simplifies the calculation procedure, and is usually regarded as a good approximation. The effect of this assumption is, for instance, no stagnation temperature changes in stationary components.

Another useful feature employed in many calculations is the cylindrical coordinate system, sometimes a natural choice since the machine itself is circular. The coordinates utilized in most studies is seen in figure 2.1. Many times the cylindrical coordinate system  $z - r - \theta$  is used directly, but of great importance is the two-dimensional  $z - r$  representation. This so-called meridional  $z - r$  plane is typically employed when looking at stream surfaces in different components. In addition, a curvilinear coordinate system is very useful when conducting an

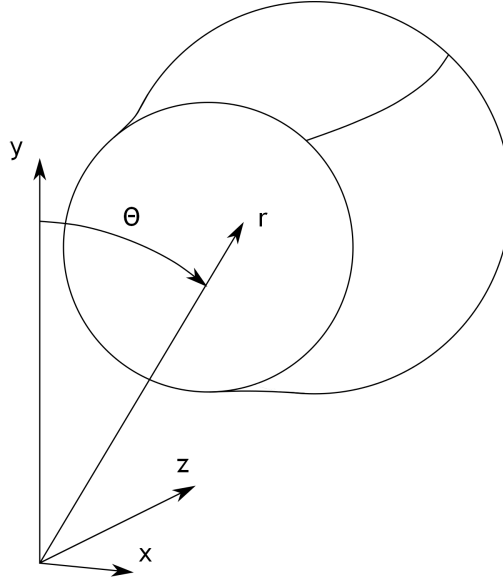


Figure 2.1: The coordinate systems used in subsequent analyses. As is seen, both a Cartesian and a cylindrical coordinate system is typically employed

analysis along a flow path such as that depicted in figure 2.2. The curvilinear coordinate system has the meridional component  $m$  parallel to the stream surface at the current point, and the normal component  $n$  normal to it. In figure 2.2 both the  $z - r$  and the  $m - n$  coordinate system is depicted for one and the same polar angle  $\theta$ . Also included in the figure is the slope of the stream surface at the current point, here denoted  $\alpha_C$ . Throughout this study all flow and blade angles are defined from the meridional direction, with the obvious exception of the local stream surface angle defined in figure 2.2.

When performing calculations in any general gas path, for instance the impeller flow passages or in a vaneless diffuser, the concept of *quasi-normals* can be advantageous to utilize. A quasi-normal, as the name implies, is a line segment almost normal to the flow. Ideally these lines would be perfect normals, but it is impossible to achieve this when having passages with generally shaped walls. The quasi-normals are connected from the component's hub contour to it's shroud contour, between points of the same non-dimensional passage distance. Figure 2.3 gives a typical example of this concept. Here it is clearly shown that the quasi normal only approximates a normal to both the hub and shroud wall. The angle  $\epsilon$  denotes the difference between an actual normal and the quasi normal, defined at both hub and shroud. Any calculation should compensate for the "non-normalness" inevitably created by quasi normals, typically by utilizing  $\epsilon$ . A typical task well suited for the use of quasi-normals is, for instance, when calculating passage areas in a general flow path. Also, blade angles can be set to vary linearly from a value at the hub to another value at the shroud along these line segments, which will be demonstrated later.

When analysing turbomachinery one almost always encounters different velocity triangles. This is simply velocity vectors in specific planes, typically a developed stream surface, normal to the meridional plane. Velocity diagrams are very useful for relating velocities and their

---

<sup>2</sup>Preswirl is sometimes employed in order to reduce the relative inlet Mach number and/or to increase the operating range. This can be introduced with the aid of *IGVs*, inlet guide vanes

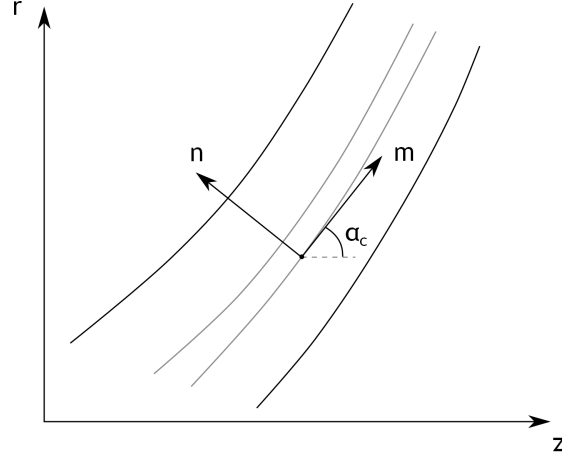


Figure 2.2: A  $z$ - $r$  coordinate system displaying a particular point with a curvilinear coordinate system  $m - n$  included. Both coordinate systems are depicted for the same polar angle  $\theta$ . The slope of the stream surface at the point of interest is  $\alpha_c$

different directions and is a fundamental part of this study. The velocity diagram for an impeller inlet is shown in figure 2.4. Note that this velocity diagram is not representative of typical designs, but is very useful when setting up algebraical relations, since all angles are shown in the positive direction. If all mathematical expressions are set up with correct angle definitions, no problems will occur if velocity vectors suddenly acquire negative angles. The angles shown are the absolute flow angle  $\alpha$ , the relative flow angle  $\alpha'$ , the blade angle  $\beta$  and the incidence angle  $i$ . Incidence is the difference between the blade angle and the relative flow angle according to

$$i = \beta - \alpha' \quad (2.20)$$

If the incidence is equal to zero, the relative flow follows the blade mean camberline exactly. Also shown in figure 2.4 is the different velocity vectors. Both the absolute velocity  $C$  and relative velocity  $W$  have velocity components in the meridional and tangential direction. Of course, the blade speed is entirely in the tangential direction. Also note that all velocity components with a vertical alignment is termed meridional velocity (subscript  $m$ ), while any horizontally aligned velocity components is called tangential (subscript  $\theta$ ).

Performing calculations within a rotating part of any turbomachinery a very useful quantity  $R_0$ , the rothalpy, may be derived from the Euler turbomachinery equation and the above presented velocity triangle. Insertion of equation 2.4 in equation 2.17 yields

$$h_2 + \frac{C_2^2}{2} - U_2 C_{\theta 2} = h_1 + \frac{C_1^2}{2} - U_1 C_{\theta 1} \quad (2.21)$$

From the velocity triangle it is easily seen that the squared absolute velocity can be expressed as

$$\begin{aligned} C^2 &= C_m^2 + C_\theta^2 = C_m^2 + (W_\theta + U)^2 \\ &= W_m^2 + W_\theta^2 + 2UW_\theta + U^2 \\ &= W^2 + 2UW_\theta + U^2 \end{aligned} \quad (2.22)$$

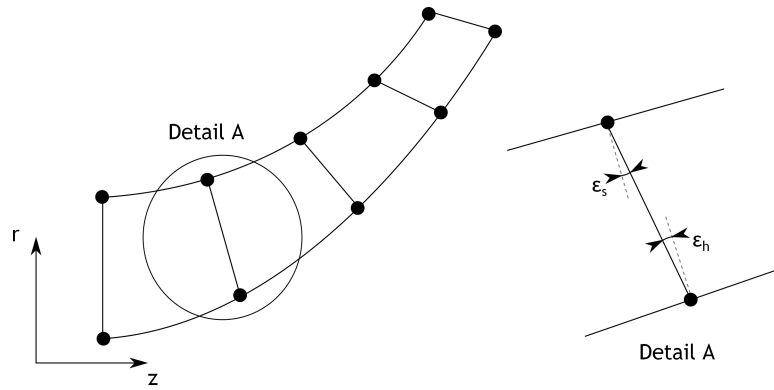


Figure 2.3: Schematic sketch showing the use of quasi-normals. Here, five quasi-normals are shown connected between points on the hub and shroud, each pair of points with the same dimensionless passage length along it's respective contour. Detail A shows one quasi-normal with higher resolution, where it is seen that the line segment is not exactly normal to either the hub or shroud

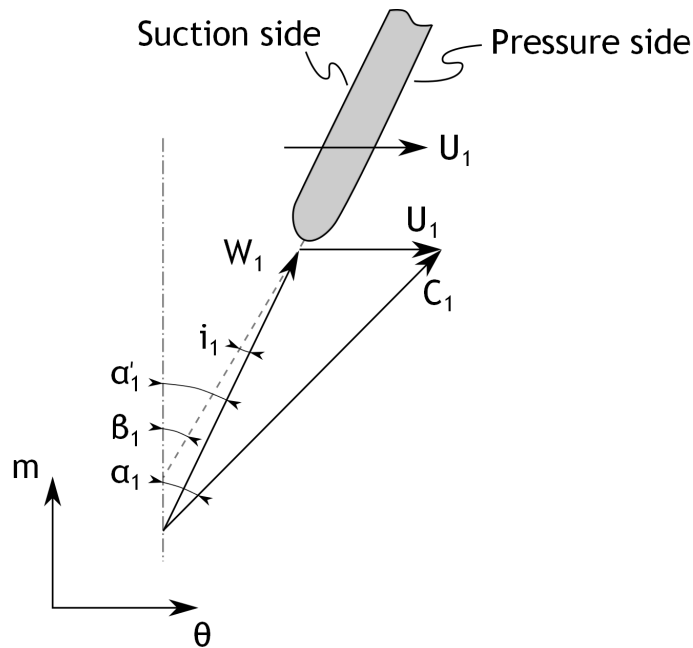


Figure 2.4: Sketch of an impeller inlet velocity triangle in a developed stream surface, coinciding with a developed tangential plane. Here, all velocities are drawn with positive angles, on the right hand side of the meridional direction. Also, the pressure and suction side of the blade are indicated



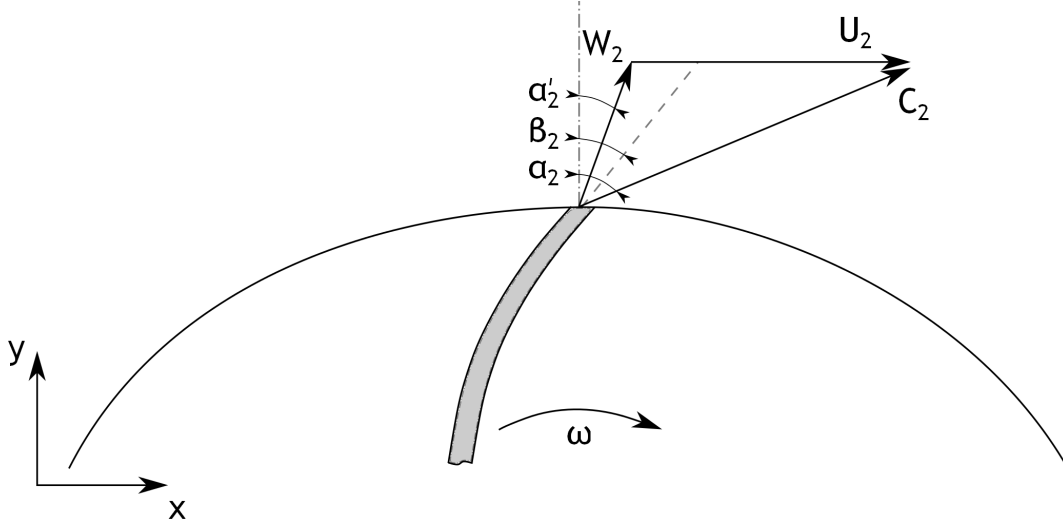


Figure 2.5: Sketch of an impeller exit velocity triangle in a developed stream surface. The stream surface on which the velocities are shown is in this case parallel to the  $x - y$  plane. Here, all velocities are drawn with positive angles, on the right hand side of the meridional direction. Note that this impeller has forward swept blades, which would normally not be used in practice

and the following relation must hold

$$\begin{aligned} \frac{C^2}{2} - UC_\theta &= \frac{W^2}{2} + 2UW_\theta + U^2 - UC_\theta = \frac{W^2}{2} + U \left( \frac{U}{2} - (C_\theta - W_\theta) \right) \\ &= \frac{W^2}{2} + U \left( \frac{U}{2} - U \right) = \frac{W^2}{2} - \frac{U^2}{2} \end{aligned} \quad (2.23)$$

Inserting this result into equation 2.21 one obtain

$$h_2 + \frac{W_2^2}{2} - \frac{U_2^2}{2} = h_1 + \frac{W_1^2}{2} - \frac{U_1^2}{2} \quad (2.24)$$

Obviously the quantities on either side of the equality is conserved over the component of interest. Consequently the rothalpy  $R_0$  is defined as

$$R_0 = h + \frac{W^2}{2} - \frac{U^2}{2} \quad (2.25)$$

It is easily seen that the conservation of rothalpy reduces to the conservation of stagnation enthalpy for a stationary component ( $U \rightarrow 0$  and  $W \rightarrow C$ ). Sometimes it is more useful to directly work with the Euler turbomachine equation, and the rothalpy can instead be expressed according to

$$R_0 = h_0 - UC_\theta \quad (2.26)$$

Also, a relative specific stagnation enthalpy  $h'_0$  may be written as

$$h'_0 = h + \frac{W^2}{2} \quad (2.27)$$

This quantity can be directly related to the definition of rothalpy, equation 2.25. Hence

$$h'_0 = R_0 + \frac{U^2}{2} \quad (2.28)$$

must hold along any streamline. Note that rothalpy is conserved in both the stationary and rotating frame of reference. However, the rothalpy cannot be conserved *between* a stationary and rotating component since there is a discontinuity in  $U$  (from zero to a finite value).

Another detail found in figure 2.4 is the different names of the blade's sides. The side on which the velocity will be the highest, and hence the pressure the lowest, is called the suction side. The opposite is true of the other side and is therefore called the pressure side. One can also imagine the pressure side as the side that will "push", or press, fluid in the direction of rotation, while at the suction side fluid will follow the blades' rotation. However, as noted by Braembussche (2013), in the radial part of the compressor, it is not always clear which blade side is the pressure or suction side. This stems from the fact that the normal velocity gradient has two contributors with opposite sign; one from the blade curvature and one from the Coriolis acceleration. Hence, in the rear part of a radial compressor, where the Coriolis acceleration is substantial, the convex side may turn out to be the pressure side.

Similarly as for the inlet, a velocity triangle is constructed at the impeller exit as seen in figure 2.5. Once again, all angles are drawn positive yielding a configuration not reflecting actual designs. As was the case for the inlet velocity triangle, a sketch of this type simplifies the algebraical procedures by defining a common positive direction for the angles. In fact, this figure shows an unrealistic impeller configuration in that the impeller has forward swept blades ( $\beta_2 > 0$ ). Employing forward swept blades will yield an unstable compressor, causing severe operating difficulties as noted in most of the literature covering radial compressor design, see for instance Cumpsty (2004).

## Chapter 3

# Preliminary impeller design

The purpose of the preliminary impeller design is to very easily and quickly generate a candidate design from which further analyses can be conducted. The strength of having such a method is to yield reasonable designs, capable of reaching the performance target. If used properly large time savings in a design process can be realized since quickly arriving at a good design certainly will minimize the quantity of in-depth calculations.

First, the main relations are presented together with the physical reasoning, after which the geometrical construction is presented. The last section explains the calculation procedure of the preliminary impeller design.

### 3.1 Basic relations

The basic calculation procedure is outlined by Aungier (2000), based on a previous paper from the same author; Aungier (1995) [13]. The current study is restricted to flow coefficients in the range typically encountered when using impellers with full inducers,  $0.025 < \phi < 0.2$ . Further, it is assumed that the inlet velocity distribution is uniform, without any velocity differences in the radial direction. Some parts of the analysis require property differences between impeller outlet and inlet. Since the relative properties change in the radial direction (the tangential speed increases when moving radially outwards), properties on the mean stream surface are utilized. The mean stream surface contain some arbitrariness in how it is defined. Here it is taken to be the surface which separates equal amount of fluid mass flow below and above it. Also, the surface itself is assumed to be uniform in the tangential direction. The inlet flow coefficient can be calculated from the inlet stagnation conditions, the desired inlet mass flow and the impeller tip radius according to formula 1.3, repeated below for clarity

$$\phi = \frac{\dot{m}}{\rho_{00}\pi r_2^2 U_2} \quad (3.1)$$

By knowing the impeller rotational speed, the impeller tip speed  $U_2$  is easily determined by using equation 2.18, repeated below for clarity

$$U_2 = \omega r_2 \quad (3.2)$$

Aungier (2000) introduce an additional parameter  $I$  in analogy to the head coefficient, but instead of using the isentropic stagnation enthalpy difference, the actual stagnation enthalpy difference is used, representing the work actually being supplied to the flow. The so-called

work input coefficient can thus be written as

$$I = \frac{\Delta h_0}{U_2^2} \quad (3.3)$$

where  $\Delta h_0$  is the actual specific stagnation enthalpy difference over the impeller. The author gives relations between the impeller work input coefficient and the flow coefficient, enabling calculation of the enthalpy rise over the impeller from known parameters. Also, different correlations are given depending on whether the impeller is shrouded or not. For shrouded impellers the work input coefficient is given by

$$I = 0.62 - \left(\frac{\phi}{0.4}\right)^3 + \frac{0.0014}{\phi} \quad (3.4)$$

while for unshrouded impellers  $I$  is written as

$$I = 0.68 - \left(\frac{\phi}{0.37}\right)^3 + \frac{0.002}{\phi} \quad (3.5)$$

An estimation of the amount of the externally supplied work actually being transferred to the blades is given by the blade work input factor  $I_B$ , again in analogy with the work input coefficient. The difference between the work input coefficient  $I$  and the blade work input factor represents the parasitic loss<sup>1</sup> coefficient  $I_{par}$ . Aungier (2000) gives a correlation for  $I_{par}$ , simply dependent on the inlet flow coefficient according to

$$I_{par} = \frac{0.0014}{\phi} \quad (3.6)$$

This equation is valid for shrouded impellers. When instead using an unshrouded impeller the parasitic losses becomes somewhat higher and is instead given by

$$I_{par} = \frac{0.002}{\phi} \quad (3.7)$$

Hence, the work input to the blades (and thereby the fluid) can be determined by

$$I_B = I - I_{par} \quad (3.8)$$

The blade work input factor itself corresponds to the work supplied determined by the Euler turbomachinery equation 2.17 and  $I_B$  thus becomes

$$I_B = \frac{\Delta h_{0,blades}}{U_2^2} = \frac{C_{\theta 2}}{U_2} - \frac{U_1 C_{\theta 1}}{U_2^2} \quad (3.9)$$

In the same manner as for the impeller work input coefficient, Aungier (2000) supplies relations for the polytropic head coefficient and the polytropic efficiency of the compressor stage. Again, different relations are given for shrouded and unshrouded impellers, with the added dependence of which kind of diffuser found downstream of the impeller (vaneless, subscript  $VLD$ , or vaned, subscript  $VD$ , diffusers). For unshrouded impellers the head coefficient is determined by

$$\mu_{p,VD} = 0.51 + \phi - 7.6\phi^2 - \frac{0.00025}{\phi} \quad (3.10)$$

---

<sup>1</sup>Parasitic losses typically involves "disc friction losses" meaning friction work are being done by the impeller on the stationary compressor shroud. This means extra work input, without doing any useful work on the fluid

and the polytropic efficiency  $\eta_p$  takes the form of

$$\eta_{p,VLD} = \eta_{p,VD} - \frac{0.017}{0.04 + 5\phi + \eta_{p,VD}^3} \quad (3.11)$$

continuing, the corresponding parameters for unshrouded impellers is given by

$$\mu_{p,VD} = 0.59 + 0.7\phi - 7.5\phi^2 - \frac{0.00025}{\phi} \quad (3.12)$$

and

$$\eta_{p,VLD} = \eta_{p,VD} - \frac{0.017}{0.04 + 5\phi + \eta_{p,VD}^3} \quad (3.13)$$

Polytropic parameters have the advantage over isentropic ditto of being independent of the pressure ratio. The drawback of the isentropic parameters stems from a thermodynamic effect, having its root in the divergence of constant pressure line in a h-s diagram, as explained by Dixon (1998), for instance. As is seen in relation 3.10 to 3.13 it is necessary to determine efficiencies out of the polytropic head. This presents no problem since the polytropic head coefficient  $\mu_p$  can be written as

$$\mu_p = \frac{\Delta h_{0p}}{U_2^2} \quad (3.14)$$

here,  $\Delta h_{0p}$  denotes the specific stagnation enthalpy change under an ideal polytropic compression. In a similar manner the polytropic efficiency becomes

$$\eta_p = \frac{\Delta h_{0p}}{\Delta h_0} \quad (3.15)$$

By combining the last two equations one end up with

$$\eta_p = \mu_p \frac{U_2^2}{\Delta h_0} \quad (3.16)$$

enabling easy conversions from polytropic head coefficients to efficiencies, and vice versa. The polytropic enthalpy change can also be directly related to the pressure rise by combining equation 2.2 and 2.6 by writing

$$\begin{aligned} \Delta h_{0p} &= h_{02p} - h_{01} = c_p (T_{02p} - T_{01}) \\ &= c_p T_{01} \left( \frac{T_{02p}}{T_{01}} - 1 \right) = c_p T_{01} \left( \left( \frac{p_{02}}{p_{01}} \right)^{\frac{\gamma}{\gamma-1}} - 1 \right) \end{aligned} \quad (3.17)$$

A measure of the internal efficiency of the impeller itself would not take the parasitic losses into account, and only consider flow phenomena and losses within the fluid passage. It is defined as the ratio of the polytropic head coefficient to the impeller blade work input factor, and is estimated by

$$\eta_I = \frac{\mu_p}{I_B} = 0.95 - \frac{0.0005}{\phi} \quad (3.18)$$

The impeller tip is a region of an extremely complicated flow field, and still today all flow phenomena are not fully understood. Empirical data can be used to support a one dimensional analysis and to improve a new design, looking at designs from successful development programs in the past. On the contrary, Japikse (1996) notes that, for instance, employing a blockage factor when using calculations based on homogeneously mixed flow is conceptually wrong.

Nevertheless Aungier (2000) recommends the use of a so-called tip distortion factor  $\lambda$ , depending on multiple factors. It is defined according to

$$\lambda = \frac{1}{1 - B_2} \quad (3.19)$$

where  $B_2$  is a blockage factor at the impeller tip. The main dependence has, again, been found to be on the inlet flow coefficient but another factor,  $K_\lambda$ , is also included according to

$$\lambda = K_\lambda + \left(\frac{0.00175}{\phi}\right)^2 + \frac{0.0015}{\phi} - 0.22 \ln \phi \quad (3.20)$$

The tip distortion factor should also recognize what kind of impeller being used, and when employing an unshrouded impeller  $\lambda$ , as given by equation 3.20, should be increased by a factor 1.02. The factor  $K_\lambda$  is dependent on several parameters. These include not only the blade angle  $\beta$  and passage area  $A$  at both inlet and outlet, but also the passage width  $b$  at outlet and the blade mean camberline length  $L_B$ . The last variable,  $L_B$  makes the calculation procedure somewhat difficult, since the blade camberline length is not known until the impeller geometry is determined. On the other hand, the geometry depends on the value of the tip distortion factor, hence an iterative approach is needed.  $K_\lambda$  is expressed as

$$K_\lambda = 1 + \left(0.3 + \left(\frac{b_2}{L_B}\right)^2\right) \frac{b_2 A_2^2 \cos^2 \beta_2}{L_B A_1^2 \cos^2 \beta_1} \quad (3.21)$$

Depending on what type of diffuser used in the compressor stage different absolute exit flow angles  $\alpha_2$  from the impeller should be aimed at. Once again correlations was found based on the flow coefficient since this parameter, to a large extent, determines which type of loss dominates the flow. For low flow coefficients rather narrow flow passages appear, and to minimize wall friction losses, as wide passages as possible should be strived for. This can be accomplished by choosing an as large outlet angle as possible (this would minimize the meridional velocity component, forcing the passage width to be larger from continuity considerations). On the opposite, a high flow coefficient stage yields comparatively wide passages, giving rise to losses associated with less guidance, typically diffusion losses. Here, the flow angle is preferably as small as possible giving rise to higher meridional velocities. The impeller exit flow angle when using vaneless diffusers is given by

$$\tan \alpha_2 = \frac{1}{0.26 + 3\phi} \quad (3.22)$$

For vaned diffusers good design point performance cannot be considered alone, since the aspect of the off-design behaviour often determine the stage's practical usefulness. Often a trade-off has to be made between high design point efficiency and a wide operating range. Thus, it is important to choose outlet angles making the diffuser as insensitive as possible to changes in the outlet flow from the impeller. This criteria yields rather large impeller exit absolute flow angles, which can be determined from

$$\alpha_2 = 72^\circ - 0.5 \ln \phi - 585\phi^2 \quad (3.23)$$

An important concept regarding the impeller tip region is the so-called slip factor. The slip factor represents the relation between the actual tangential velocity and an ideal ditto<sup>2</sup>. An

---

<sup>2</sup>It should be noted that the slip factor is in total analogy with the deviation usually encountered in axial blading

ideal tangential velocity could be the velocity obtained with an infinite number of infinitesimally thin blades. With radial blading ( $\beta_2 = 0$ ) this would make the fluid have the impeller tip speed as the tangential velocity component. However, the "american" slip factor is used in this analysis, where not only this "ideal" tangential velocity is taken into account, but also the impeller tip speed  $U_2$ . A thorough description of the slip factor  $\sigma$  is outlined by Cumpsty (2004), and is here defined as

$$\sigma = 1 - \frac{C_{\theta 2, \infty} - C_{\theta 2}}{U_2} = 1 - \frac{C_{slip}}{U_2} \quad (3.24)$$

where  $C_{\theta 2, \infty}$  represents the tangential velocity under the idealized case of an infinity amount of blades and  $C_{slip}$  is the difference between this velocity and the actual tangential velocity. In practice it exists many different empirically derived expressions to determine the slip factor. The one adopted here is the Wiesner slip factor at zero flow, written according to

$$\sigma = 1 - \frac{\sqrt{\cos \beta_2} \sin \alpha_{C2}}{Z_I^{0.7}} \quad (3.25)$$

here,  $Z_I$  denotes the number of impeller blades. Further, equation 3.24 at zero flow ( $C_{\theta 2, \infty} = C_{2, \infty} = U_2$ ) reduces to

$$\sigma = \frac{C_{\theta 2}}{C_{\theta 2, \infty}} \quad (3.26)$$

The slip factor can be directly related to the impeller work input, equation 3.9 and the one-dimensional continuity equation at the tip including tip blockage through equation 3.19. Incorporating the above mentioned tip blockage, the available flow area  $A_{2,avail}$  is the passage area less the value predicted by the blockage factor

$$A_{2,avail} = A_2 (1 - B_2) = \frac{A_2}{\lambda} \quad (3.27)$$

The one dimensional continuity equation at the impeller tip demands

$$\dot{m} = \rho_2 C_{m2} A_{2,avail} = \frac{\rho_2 C_{m2} A_2}{\lambda} \quad (3.28)$$

The ratio of the ideal tangential velocity (with an infinite number of blades) to the impeller tip velocity can be written

$$\frac{C_{\theta 2, \infty}}{U_2} = \frac{U_2 - (U_2 - C_{\theta 2, \infty})}{U_2} = 1 - \frac{C_{m2} \tan \beta_2}{U_2} \quad (3.29)$$

with the aid of figure 3.1 showing the impeller tip velocity triangle. As seen in this figure the ideal flow direction equals the blade angle  $\beta_2$ . The relative flow velocity is denoted  $W$ . Combining equation 3.28 and 3.29 yields

$$\frac{C_{\theta 2, \infty}}{U_2} = 1 - \frac{\lambda \dot{m} \tan \beta_2}{\rho_2 A_2 U_2} \quad (3.30)$$

Finally, using equation 3.9, 3.26, and 3.30 one end up with

$$I_B = \sigma \left( 1 - \frac{\lambda \dot{m} \tan \beta_2}{\rho_2 A_2 U_2} \right) - \frac{U_1 C_{\theta 1}}{U_2^2} \quad (3.31)$$

Another important parameter is the blade loading. Keeping the blade loading within certain limits is one way to control the severity of the impeller flow field. If previous designs

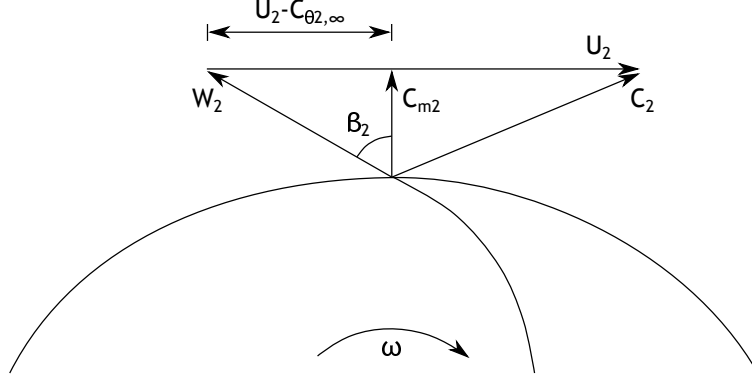


Figure 3.1: The impeller tip velocity triangle for an idealized flow with the relative flow velocity  $W$  following the blade with no deviation. Only one blade is shown for reasons of clarity

have worked well with a certain amount of blade loading, a good starting point for a new design would be similar values. One common method of determining the amount of loading is by relating the inlet and outlet relative velocities to the velocity difference at the blade's suction and pressure side. Aungier (2000) defines the blade loading  $BL$  as

$$BL = \frac{2\Delta W}{W_1 + W_2} \quad (3.32)$$

where  $\Delta W$  is the average blade velocity difference between the suction and pressure side of a blade. This difference can in turn be estimated from a simple irrotational flow approach by

$$\Delta W = \frac{4\pi r_2 U_2 I_B}{Z_I L_B} \quad (3.33)$$

The value of the blade loading is suggested to be kept below 0.9.

In order to yield a good impeller design suggestion, the mean camberline blade angle distribution must be specified. From Aungier (1995) blade angles along the shroud contour are given by

$$\beta_s = \beta_{1s} + (\beta_2 - \beta_{1s}) (3\zeta^2 - 2\zeta^3) \quad (3.34)$$

where  $\zeta$  denotes the dimensionless meridional distance along the impeller fluid passage. In a similar manner, the blade angle distribution along the hub is expressed as

$$\beta_h = \beta_{1h} + A\zeta + B\zeta^2 + C\zeta^3 \quad (3.35)$$

here,  $A$ ,  $B$  and  $C$  are constants, given by

$$A = -4 (\beta_2 - \bar{\beta}_h + \beta_{1h}) \quad (3.36)$$

$$B = 11\beta_2 - 16\bar{\beta}_h + 5\beta_{1h} \quad (3.37)$$

$$C = -6\beta_2 + 8\bar{\beta}_h - 2\beta_{1h} \quad (3.38)$$

and  $\bar{\beta}_h$  is the blade angle along the hub contour at mid passage, determined by

$$\bar{\beta}_h = 90K + \frac{(1-K)(\beta_2 + \beta_{1h})}{2} \quad (3.39)$$



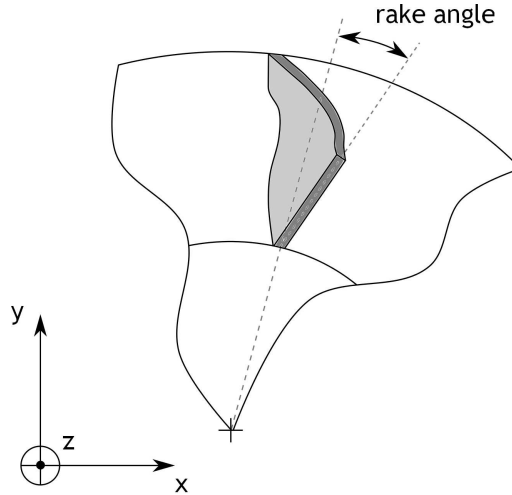


Figure 3.2: Schematic sketch showing the rake angle, here at the impeller inlet. View in the axial direction, looking downstream. Only one blade is shown for reasons of clarity

The parameter  $K$  is used to adjust  $\bar{\beta}_h$  in order to keep the rake angles<sup>3</sup> reasonable. Rake angles are angles between the blade hub-to-shroud surface and a meridional surface passing through the impeller rotating axis as illustrated in figure 3.2. One reason for making use of rake angles is the effect they have on creating backsweep with radially shaped blades. This lowers the mechanical stress levels in the blades since no bending stress appears in radial blading, see Cumpsty (2004). Breambussche (2013) further notes that altering rake angles can be an efficient way to redistribute the impeller tip velocity, and thereby improve the downstream diffuser performance.

The blade angles at locations other than hub or shroud is set to vary linearly along the passage width. The blade themselves have a finite thickness which must be taken into account when calculating flow passage areas. Because of the blade's thickness  $t_B$ , the available flow area is reduced with an amount depending on both the number of blades and the blade thickness. For the preliminary design the blade thickness are assumed to be equally thick in the hub to shroud direction, but have a thinner leading edge than trailing edge. The leading edge thickness is set to increase linearly until 10% of the meridional passage length, from which point the thickness are held constant. Any extra blockage effect from rake angles being non-zero is neglected, a reasonable assumption for relatively small angles.

## 3.2 Geometrical construction

Aungier (2000) also found a correlation between impeller axial length, inlet flow coefficient and the radius ratio  $r_{1h}/r_2$ , giving a very important parameter needed to construct the impeller geometry. The impeller axial length  $\Delta z_I$  can be determined from

$$\frac{\Delta z_I}{2r_1} = 0.014 + 0.023 \frac{r_2}{r_{1h}} + 1.58\phi \quad (3.40)$$

<sup>3</sup>Rake angles are sometimes also called lean angles

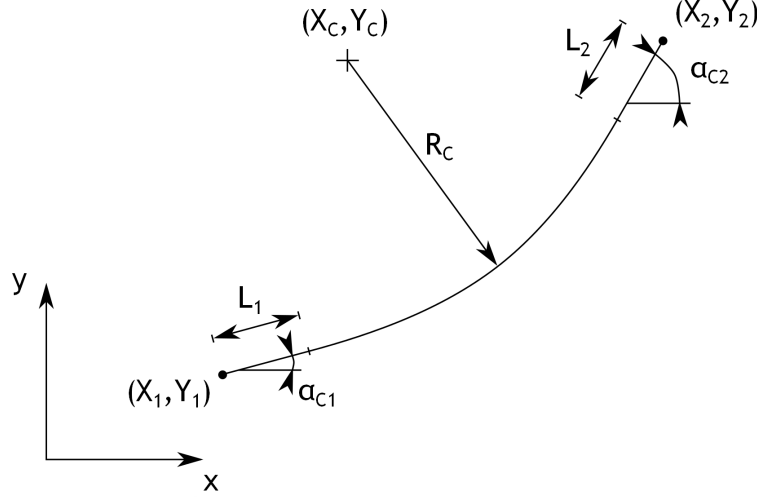


Figure 3.3: The basic layout of a circular arc with angles  $\alpha_{C1}$  and  $\alpha_{C2}$  at the beginning and end, respectively. Also, linear segments are added at the two end points. The arc's radius is denoted  $R_C$

How the hub and shroud contour are chosen is a non-trivial matter. In the work of Aungier (2000) it is recommended to use a circular arc of an as large radius as possible for the hub contour. Depending on the slope of the hub at inlet and exit it may be necessary to add linear line segments in the beginning and/or at the end of the arc. Figure 3.3 shows the features of such a circular arc. From this figure it is seen that the differences in x- and y-values is given by

$$X_2 - X_1 = R_C (\sin \alpha_{C2} - \sin \alpha_{C1}) + L_2 \cos \alpha_{C2} + L_1 \cos \alpha_{C1} \quad (3.41)$$

$$Y_2 - Y_1 = R_C (\cos \alpha_{C1} - \cos \alpha_{C2}) + L_2 \sin \alpha_{C2} + L_1 \sin \alpha_{C1} \quad (3.42)$$

Equation 3.41 and 3.42 can be combined to yield

$$L_2 - L_1 = \frac{(Y_2 - Y_1) (\sin \alpha_{C2} - \sin \alpha_{C1}) - (X_2 - X_1) (\cos \alpha_{C1} - \cos \alpha_{C2})}{1 - \sin \alpha_{C1} \sin \alpha_{C2} - \cos \alpha_{C1} \cos \alpha_{C2}} \quad (3.43)$$

hence, the linear line segments  $L_1$  and  $L_2$  cannot be chosen independently of the curve slopes at the beginning and end of the line. When actually constructing a circular arc it is useful to make use of the arc centre determined according to

$$X_C = X_1 + L_1 \cos \alpha_{C1} - R_C \sin \alpha_{C1} \quad (3.44)$$

$$Y_C = Y_1 + L_1 \sin \alpha_{C1} + R_C \cos \alpha_{C1} \quad (3.45)$$

For the shroud contour generation a three-point cubic spline curve is used. It is well suitable to this task, since it can be made to fit at both impeller inlet and exit, while controlling an additional point along the gas path. This extra point is here chosen at midpassage in order to give passage area distributions in line with good design practice. Aungier (2000) suggests a linear annular area distribution from the impeller inlet to discharge. The cubic spline curve used in this preliminary analysis is shown in figure 3.4. In order to ease calculations the slope of the initial and final line segment can be written as

$$Y_1' = \tan \alpha_{C1} \quad (3.46)$$

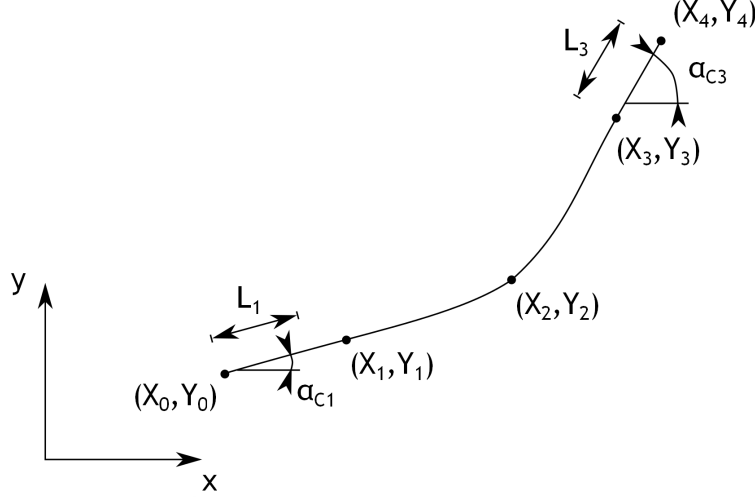


Figure 3.4: The basic layout of a three-point cubic spline arc with angles  $\alpha_{C1}$  and  $\alpha_{C3}$  at the beginning and end, respectively. Also, linear segments  $L_1$  and  $L_3$  are added at the two end points. Note the third point in the middle of the line

$$Y_3' = \tan \alpha_{C3} \quad (3.47)$$

To construct the line, three different coefficients are used, defined by

$$M_2 = \frac{6(Y_3 - Y_2)}{(X_3 - X_2)(X_3 - X_1)} - \frac{6(Y_2 - Y_1)}{(X_2 - X_1)(X_3 - X_1)} + \frac{2(Y_1' - Y_3')}{X_3 - X_2} \quad (3.48)$$

$$M_1 = \frac{3(Y_2 - Y_1)}{(X_2 - X_1)^2} - \frac{3Y_1'}{X_2 - X_1} - \frac{M_2}{2} \quad (3.49)$$

$$M_3 = \frac{3Y_3'}{X_3 - X_2} - \frac{3(Y_3 - Y_2)}{(X_3 - X_2)^2} - \frac{M_2}{2} \quad (3.50)$$

which is used to define the cubic polynomial according to

$$\begin{aligned} y &= \frac{M_{k-1}(X_k - x)^3}{6(X_k - X_{k-1})} + \frac{M_k(x - X_{k-1})^3}{6(X_k - X_{k-1})} \\ &+ \left( \frac{Y_k}{X_k - X_{k-1}} - \frac{M_k(X_k - X_{k-1})}{6} \right) (x - X_{k-1}) \\ &+ \left( \frac{Y_{k-1}}{X_k - X_{k-1}} - \frac{M_{k-1}(X_k - X_{k-1})}{6} \right) (X_k - x); \end{aligned} \quad (3.51)$$

where  $X_{k-1} \leq x \leq X_k$

hence, the calculation of the polynomial is divided into two parts, one where  $x$  varies between  $X_1$  and  $X_2$ , the other where  $x$  varies between  $X_2$  and  $X_3$ . With these curve types, both contours of the impeller can geometrically be constructed. One potential danger when using  $\tan \alpha_C$  for the curve slope is the occurrence of  $90^\circ$  angles. This leads to an infinite slope, and would certainly lead to numerical problems. A rather simple way of avoiding this situation is to employ a rotated coordinate system, as outlined in appendix A.

Various strategies for the blade geometrical construction can be employed. The blade angles are given by equations 3.34 and 3.35 and the blades themselves consists of straight line elements connected from the same dimensionless passage position along the hub and shroud. In order to determine the blade shape at impeller inlet Aungier (2000) suggests setting the relative flow angle to  $60^\circ$  and letting the hub incidence become one fourth of the incidence at shroud.

### 3.3 Calculation procedure

As has already been stressed above, the calculation procedure takes an iterative form since many variables depend on each other. The essential reason for this is that no geometry is known from the beginning, the geometry being something many other parameters heavily depends on. An overview of the calculation order and iteration loops is given in figure 3.5. As is seen, several calculation steps are necessary and many of them contain different iterations. One main iteration loop can be identified; this loop is continued until the number of blades has converged. Within this loop several iteration loops exist, for instance when determining the impeller inlet design and the shroud contour of the impeller.

#### 3.3.1 Input parameters

One purpose of the preliminary design is to generate an impeller with as little data input as possible. However, some data must be supported in order to yield designs following the main performance targets.

Rather obvious is the specification of the fluid parameters. No calculation can be undertaken until it is known what properties the fluid being compressed possess. Following the ideal gas assumption the specific gas constant  $R$  must be given. Additionally, any polytropic compression process end up with the ratio of specific heats,  $\gamma$ , with also must be supplied. Following the assumption of a perfect gas, that is constant specific heats, the specific heat at constant pressure is needed in order to relate temperature to enthalpy. One may notice that these three gas properties are interrelated; the third one can be found from the other two. However, some merit of specifying all three exist. For example, if some corrective measure for the temperature rise over the compressor is desired, the value of  $c_p$  can be adjusted, while letting the other two parameters be non-changed.

In order to determine the absolute impeller exit conditions it also necessary to specify the inlet stagnation properties. Most analyses specify the inlet stagnation temperature and pressure, a practice also adopted here. It can also be noted that the preliminary impeller design assumes zero loss in the intake, implying that both the impeller inlet stagnation temperature and pressure are known (and equal to the intake properties).

As has been described above, some correlations taking the following diffuser into consideration are necessary. Thus, the diffuser type is something that has to be specified by the designer. Having to specify the overall stage configuration already at this stage also reminds the inexperienced designer of the tight relationship between various compressor components. In the same manner the impeller shroud design must also be provided, that is, if a shrouded or unshrouded design is employed.

Another set of parameters characterizing the impeller is the rotational speed and the inlet mass flow. Both of these are usually known in advance, especially the mass flow. The rotational speed  $N$  determines, together with the impeller tip radius  $r_2$  (also specified), the maximum stress levels in the impeller. These parameters are therefore limited to certain levels, but the

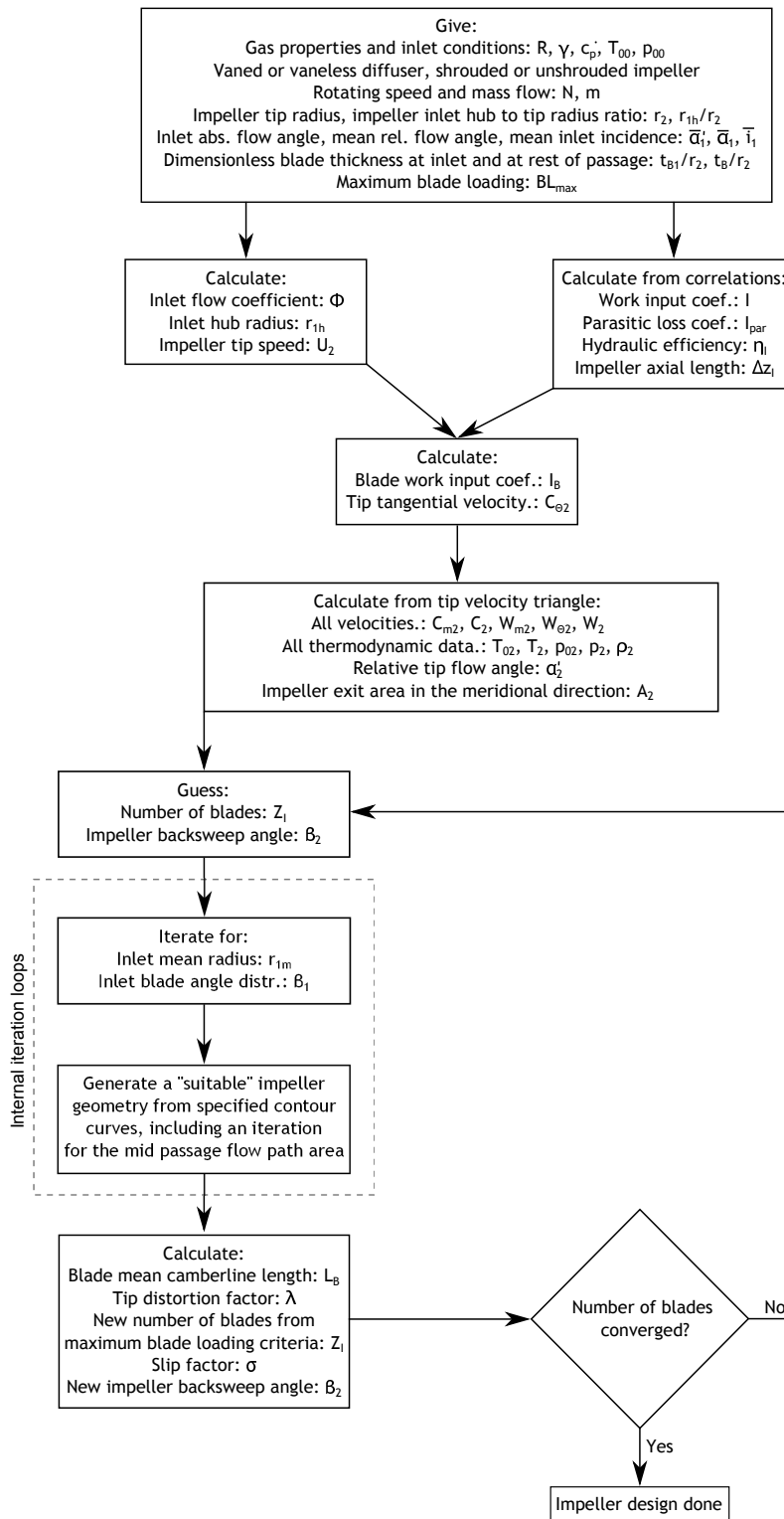


Figure 3.5: The calculation procedure for the preliminary design, showing the main features of the iterative process. Note that certain parts of the main iteration loop contain iterations of their own

relation between them can be adjusted. The mass flow  $\dot{m}$  have a large impact of the design, in how "wide" the impeller needs to be for compressing the desired amount of fluid. This is typically a parameter known, since a given duty often requires a specified amount of mass flow. Further, in order to determine the inducer size, some inlet radius is required as input data. Here, the parameter chosen is the inlet hub radius non-dimensionalized with the impeller tip radius. One reason for choosing such a parameter is that the radius ratio, instead of an absolute radius, can be obtained from previous (successful) designs of sizes different from the impeller currently being designed.

The inlet region also requires a set of angles to be specified. In the preliminary design, values at the "mean" radius are sometimes specified, where "mean" can be interpreted as at the mean stream surface. Two of these parameters include the relative mean inlet flow angle  $\bar{\alpha}'_1$  and the inlet mean incidence  $\bar{i}_1$ . Additionally, the inlet flow can be chosen not being completely axial, and thus have a homogeneous inlet angle  $\alpha_1$  relative to the meridional direction. This input can be useful if, for instance, inlet guide vanes have been placed in front of the impeller and a performance analysis is requested.

Some characteristics must also be said about the blades. The blade thickness must be chosen to give sufficient mechanical strength, still thin enough to give an as small negative impact as possible on the aerodynamic performance. The blade thickness distribution is further complicated by various resonance phenomena, and many times blade shaping is dominated by mechanical considerations. Cumpsty (2004) gives a great overview of this. Here, the blade thickness at inlet  $t_{B1}$  must be specified, non-dimensionalized with the impeller tip radius. Also, the thickness  $t_B$  at other locations than the inlet region is non-dimensionalized and specified. Another parameter connected with the blades, especially the number of blades, is the blade loading. Here, a maximum blade loading  $BL_{max}$  is specified in order to ensure results with reasonable loadings.

### 3.3.2 Calculation model

A number of calculations can be conducted without any iterations, starting with the determination of the flow coefficient  $\phi$ . This in turn requires the inlet density and impeller tip velocity to be found. Therefore, the inlet stagnation temperature and pressure is used in equation 2.1 to yield the inlet stagnation density  $\rho_{00}$ . The impeller tip velocity is determined by equation 3.2 by using the given rotational speed (converted from revolutions per minute to radians per second). Also, the parameters given in non-dimensional form can be recalculated to give the absolute values. This includes the inlet hub radius and blade thickness.

Since the flow coefficient now is known all empirical relations using  $\phi$  as a parameter can be calculated. The compressor configuration is also specified. Hence the impeller exit absolute flow angle, work input coefficient, parasitic loss coefficient, hydraulic efficiency and axial length can be determined. With the aid of equation 3.8 the blade work input coefficient  $I_B$  can be calculated. Assuming the inlet impeller velocity  $U_1$  is much smaller than it's tip velocity  $U_2$ , and a small inlet absolute flow angle  $\alpha_1$ , equation 3.9 reduces to

$$I_B = \frac{C_{\theta 2}}{U_2} \quad (3.52)$$

This relation enables the tip tangential velocity  $C_{\theta 2}$  to be determined. Since the absolute flow angle is also known, the impeller tip velocity triangle is fully determined. The thermodynamic condition at the impeller tip can also be established. Using the definition of the work input coefficient, equation 3.3, the stagnation enthalpy can be calculated at impeller discharge and

thereby the stagnation temperature. Having both the velocity and stagnation temperature, determining the static temperature is straight forward. Further, the stagnation pressure can also be established by combining equation 3.14, 3.17 and 3.18. Knowing both the stagnation temperature, static temperature and the stagnation pressure enables a simple calculation of the static pressure by using equation 2.6. Since all data is known at the impeller tip, the necessary passage area can also be determined from a simple one-dimensional continuity equation. As is understood by studying the impeller tip velocity triangle, figure 2.5, it is the meridional velocity components determining the mass flow. Hence

$$A_2 = \frac{\dot{m}}{\rho_2 C_{m2}} \quad (3.53)$$

So far no iterations have been necessary. However, the rest of the impeller design will be of an iterative nature. As was shown in figure 3.5, one main iteration loop determining the number of blades must be employed. This iteration loop consists of several other iterations, see figure 3.6. After giving reasonable start values to the number of blades and the backsweep angle, the next step is to determine the inlet annular area. This requires an iterative solution since the inlet shroud and mean radius is unknown. After giving initial values to these parameters the absolute inlet velocity  $C_1$  can be determined from the inlet flow angle, the specified mean radius relative flow angle and the rotating speed. This can be understood by looking at the inlet velocity triangle, figure 2.4. The exact same logic is used to determine the relative flow angles at hub and shroud, but in reversed order. Here we want the relative flow angle, but now know the absolute velocity (since the velocity is assumed non-distorted). From these relative flow angles the blade angles can be specified by using the specified mean radius incidence and the constraint of a hub incidence 25% of the shroud incidence. Since the impeller considered is of a full inducer type, the whole inlet is completely radial in the  $r - z$  plane. Therefore the blade angle  $\beta$  at radial position  $r$  is given by

$$\beta = \frac{r - r_{1h}}{r_{1s} - r_{1h}} (\beta_{1s} - \beta_{1h}) + \beta_{1h} \quad (3.54)$$

By combining this relation with the definition of incidence, equation 2.20, together with the constraint  $i_{1h} = 0.25i_{1s}$  a simple algebraic exercise yields

$$i_{1h} = \frac{\bar{\alpha}'_1 + \bar{i}_1 - \alpha'_{1h} - \frac{\bar{r}_1 - r_{1h}}{r_{1s} - r_{1h}} (\alpha'_{1s} - \alpha'_{1h})}{1 - \frac{3}{4} \frac{\bar{r}_1 - r_{1h}}{r_{1s} - r_{1h}}} \quad (3.55)$$

Now, the blade angles at hub and shroud can be calculated by again using the incidence definition. The situation is also similar to the one found at the impeller tip; the stagnation temperature is known together with the absolute velocity. Also, the stagnation pressure is known, and all thermodynamic properties can be determined at the inlet as well. Therefore, all parameters needed to calculate the impeller inlet annulus area, and thereby the inlet tip and mean radius, is determined. However, the amount of blade blockage depends on the blade angle which in this case varies from hub to shroud. To overcome this problem it is needed to split up the calculation in discrete steps where the blade angle is considered constant. The smaller the steps, the more accurate the result. Here, the inlet area is divided into equal parts, and each area increment can approximately be calculated by

$$A_{1,incr} = (r_{1,i+1}^2 - r_{1,i}^2) \pi - \frac{Z_I t_{B1}}{\cos \beta_{1,i}} (r_{1,i+1} - r_{1,i}) \quad (3.56)$$

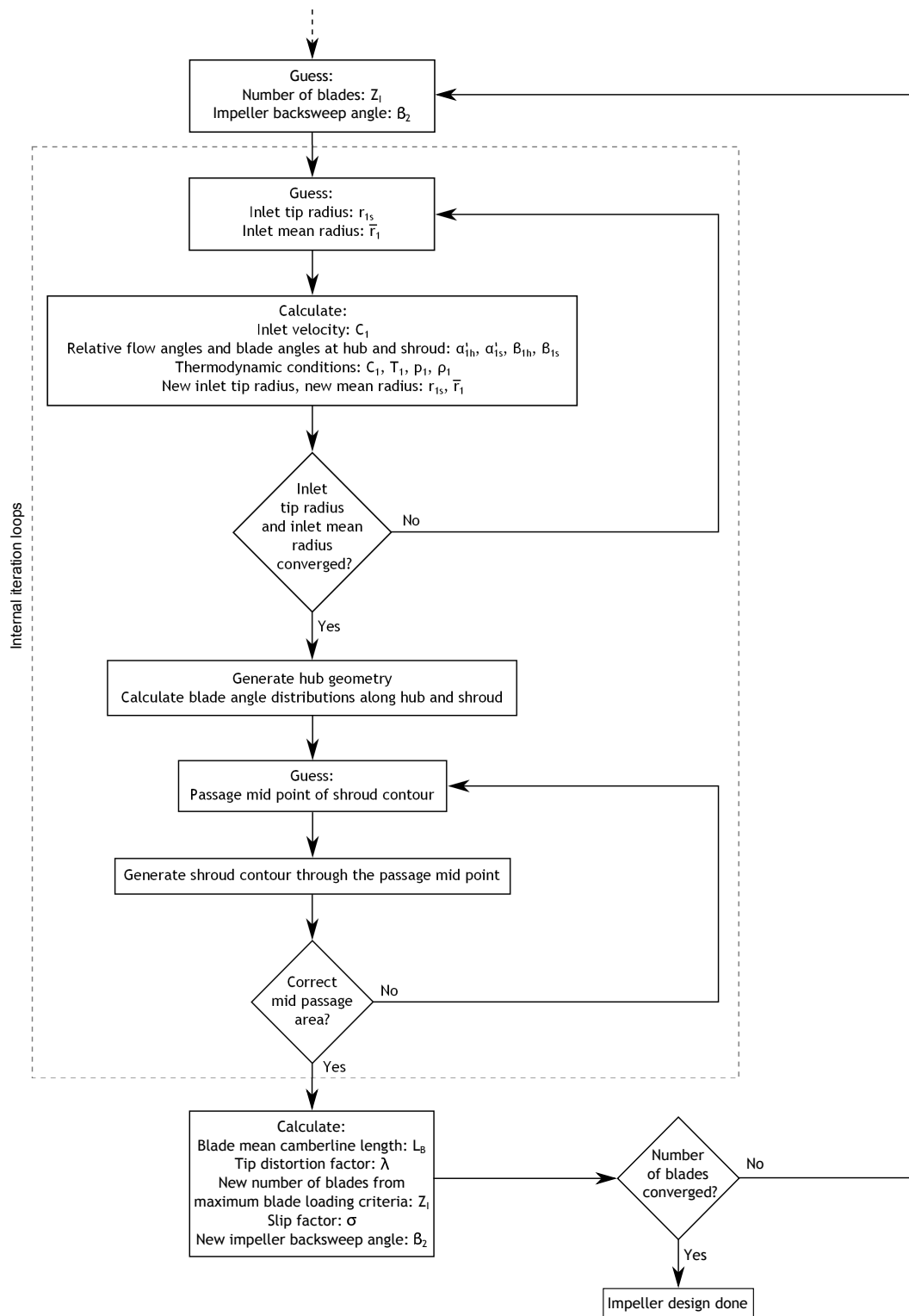


Figure 3.6: The calculation procedure for the preliminary design, showing the internal iteration loops of greatest importance



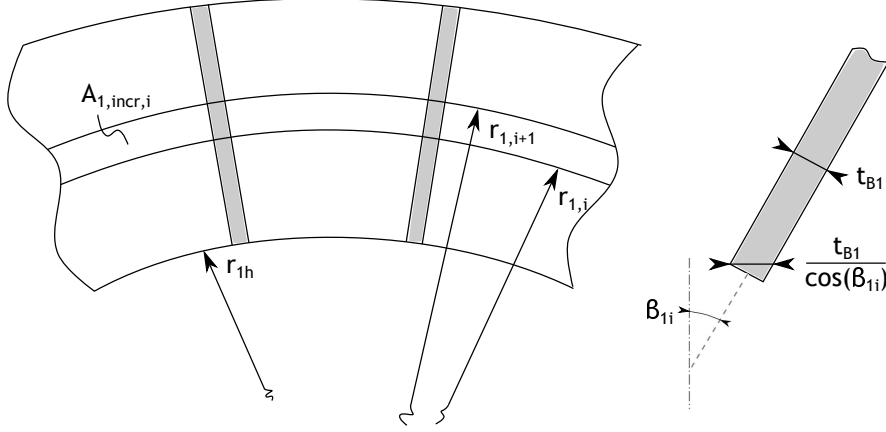


Figure 3.7: Sketch showing the main features of the inlet annulus area calculation. To the left a section of the inlet is shown with the incremental area  $A_{1,incr}$  arbitrarily positioned. To the right is a schematic drawing showing a blade section at radius  $r_i$ , and the resulting blockage that occurs

where  $r_{1,i}$  is the small radius and  $r_{1,i+1}$  is the large radius of the area increment, see figure 3.7. Knowing the incremental area  $A_{1,incr}$ , equation 3.56 can be solved for the "next" radius  $r_{i+1}$  through

$$r_{1,i+1} = \frac{Z_I t_{B1}}{2\pi \cos \beta_{1,i}} + \sqrt{\left(\frac{Z_I t_{B1}}{2\pi \cos \beta_{1,i}}\right)^2 - \frac{Z_I t_{B1} r_{1,i}}{\pi \cos \beta_{1,i}} + \frac{A_{1,incr}}{\pi} + r_{1,i}^2} \quad (3.57)$$

Of course, the area increments themselves can be determined directly from the continuity equation

$$A_{1,incr} = \frac{\dot{m}}{N \rho_1 C_{m1}} \quad (3.58)$$

here,  $N$  denotes the number of area increments. By calculating the "next" radius  $r_{i+1}$  for all area increments, the last radius determined will equal the shroud radius. It is advantageous to choose equal number of area increments in the calculations, since this automatically will yield a mean radius according to

$$\bar{r}_1 = r_{N/2+1} \quad (3.59)$$

The calculations are repeated until the shroud radius has converged. After converging, the blade angles at impeller inlet and exit are known, enabling the determination of any blade angle along the hub and shroud by using equations 3.34 to 3.39.

After sizing the inlet, the rest of the impeller can be shaped. The first step is to generate the hub contour with a circular arc as outlined above. In this case, no straight line element is used at inlet but may appear at the impeller tip. Further the hub slope at inlet,  $\alpha_{C1h}$ , is set to zero. In order to determine the hub contour at impeller tip, the hub slope at impeller tip,  $\alpha_{C2h}$ , is initially set to  $90^\circ$ . However, this could yield a negative length of the straight line element  $L_2$  when using equation 3.43, which has no physical meaning. If this happens  $\alpha_{C2h}$  is reduced until the line segment is larger than or equal to zero. This situation appears for impellers with large flow coefficients and will thus yield a mixed-flow impeller. The line is represented by a set of discrete points which will generally not be equally spaced along the arc, especially when a linear extension  $L_2$  is employed. Equally spaced points are necessary when

subsequently making use of quasi normals extending from hub to shroud at equal amounts of fractional passage length. Hence, the method described in appendix B is used to obtain a suitable description of the hub contour.

The final geometrical part, and the most intricate to determine, is the shroud contour. The annulus area at both impeller inlet and exit is determined, hence the annulus area at mid passage (annulus area is set to vary linearly along the passage length) becomes the mean value of these. The starting point of the shroud contour is determined by the impeller inlet sizing, while the shroud contour end depends on the chosen tip radius, calculated impeller axial length and the impeller tip width determined from

$$b_2 = \frac{A_2}{2\pi r_2 - \frac{Z_I t_B}{\cos \beta_2}} \quad (3.60)$$

This relation also takes the blockage effect from the blades into account. Note that the calculation at the impeller tip is much simpler than at the inlet, since here the blade angles are constant over the whole width. The iteration begins with guessed values of the mid passage location along the shroud, in order to get a calculation starting point. When having a starting point, mid point and end point a three-point cubic spline can be constructed, see section 3.2 above. Initially, the inlet slope,  $\alpha_{C1s}$ , is set to zero and the exit slope,  $\alpha_{C2s}$ , to  $90^\circ$ . Once again, it is necessary to distribute points with equal spacing along the line (see appendix B), in order to determine the actual mid point of the generated line. It is very important that the shroud contour suits the already set hub contour, and yield an impeller with reasonable passage area distributions. For instance, Aungier (2000) recommends the use of a "similar" straight line segment on the shroud contour to the one employed at the hub contour. Here, the length of the linear tip segment at the shroud is set to the same relative length the straight line  $L_2$  occupies at the hub contour. This is true until too lengthy line segments are encountered, after which the shroud segment is set to a constant value. For similar reasons the inlet and exit slopes are also "tuned" for the specific design. The inlet contour angle of the shroud is set to scale with the relative length of the shroud to the hub contour. Instead, the exit contour angle scales with the flow coefficient where larger  $\phi$ 's is associated with smaller angles. When the parameters are tuned a new cubic spline can be constructed, with the corrected values.

Since both the hub and the shroud contour now are determined one can calculate the actual mid passage annular area and compare it with the correct value. This is performed along a quasi normal connected between the mid passage length at hub and shroud. To accomplish this, a curvilinear coordinate system is employed, with the  $\chi$ -axis located along the quasi normal. At both the hub and shroud the deviation from an actual normal,  $\epsilon$ , is calculated, and the mean value is used to correct for the quasi normal only being approximately a normal. As was the case for the impeller inlet, the blade angles vary linearly along the quasi normal, and to accurately determine the annulus area (including the effect of blade blockage) a method with passage width increments is necessary. With the aid of figure 3.8, an area increment is approximately determined by

$$A_{incr,QN} = (\chi_{i+1} - \chi_i) \left( 2\pi \bar{r}_i - \frac{Z_I t_B}{\cos \bar{\beta}_i} \right) \cos \epsilon \quad (3.61)$$

where the mean blade angle  $\bar{\beta}_i$  is defined by

$$\bar{\beta}_i = \frac{\beta_i + \beta_{i+1}}{2} \quad (3.62)$$

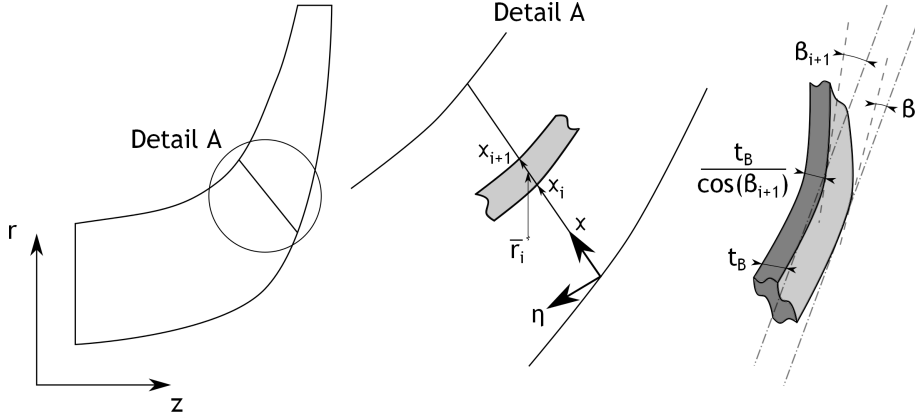


Figure 3.8: Schematic representation of the mid passage area calculation. To the left is the impeller shown as a whole, with both the hub and shroud contour. In the middle the quasi normal of interest is shown in greater detail, including the curvilinear coordinate system  $\chi - \eta$ . To the right is a blade element used for calculations shown, including the different blade angles at various locations along the quasi normal

and the mean radius  $\bar{r}_i$  of the blade segment is written

$$\bar{r}_i = \frac{r_i + r_{i+1}}{2} \quad (3.63)$$

Subscript  $i + 1$  refers to the blade segment's end point closest to shroud, while subscript  $i$  denotes the corresponding end point closest to the hub. Summing all calculated increments yield the current annular area. If this is not equal to the correct area, new mid point coordinates at the shroud are set, and the whole process repeated until convergence. This procedure has many aspects similar to the passage area and mean stream line calculation outlined in appendix C. For more details the curious reader is referred to this appendix.

When the geometry generation is completed the impeller passage area and mean streamline are determined by the method outlined in appendix C. Having calculated the mean stream line length  $L_B$  the "new" number of blades can be calculated to yield a blade loading smaller or equal to the specified maximum blade loading,  $BL_{max}$ . Further, the tip distortion factor can also be determined using equation 3.20 and 3.21 since  $L_B$  is now known. Knowing the tip distortion factor enables the backsweep angle  $\beta_2$  to be calculated and used in the next iteration loop.

All calculations, from the impeller inlet design to the impeller backsweep angle, is repeated until the number of blades have converged.



# Chapter 4

## Detailed impeller design

The detailed design, as has already been stressed in chapter 1, does not employ more advanced or more accurate mathematical models as compared to the preliminary impeller analysis, but does instead require more knowledge of the designer. Used in the right way, this is a very powerful design tool since many aspects of the modelled compressor are in direct control of the designer. However, this is also its largest drawback. Less guidance than in the preliminary impeller design method is given and more input and decisions from the designer are needed.

This chapter follows the same steps as in chapter 3 by first introducing the main physical reasoning, then the geometrical construction and finally how the problem is solved and calculated as a whole.

### 4.1 Basic relations

The main part of the detailed impeller design is based on traditional one dimensional relations, most of them presented by Japikse (1996). Compared to the preliminary impeller design, chapter 3, less empirical correlations are used. Also, the flow is assumed to be mixed out at the impeller exit.

Starting with the inlet inducer, it is now well established that there exist an optimum inlet shroud radius (and therefore also an optimum inlet shroud blade angle) which minimizes the relative velocity  $W_{1s}$  for a given mass flow. This is outlined by Korpela (2011) [14] and Casey and Rusch (2012) [15]. If the inlet tip radius is chosen too large, the relative Mach number will be high because of the large impeller tip velocity ( $U_{1s}$ ). If instead the radius is picked too small, the meridional velocity component must become high in order to pass the desired mass flow. Again, the inlet tip Mach number would increase. There must exist an optimum where both of these effects are suppressed.

Minimizing the relative tip velocity is beneficial since this reduces the overall Mach number levels in the whole impeller. As noted by Japikse (1996), an inlet relative Mach number of 0.7 will yield "high local Mach numbers", indicating that substantial acceleration takes place in the inlet region. Too high a Mach number will eventually lead to substantial losses associated with shocks, a situation preferably avoided. Different relations expressing these kind of losses have been developed, one reported by Braembussche (2013), directly relating the shroud Mach number with the compressor efficiency.

Another reason for decreasing the inlet relative Mach number is the impact it has on the operating range. Generally, a higher tip Mach number will yield an impeller inlet more

sensitive to changes in incidence. Consequently, the operating range is reduced between too large incidence (risk of stall and/or surge) and too low (choke).

Further, a small relative tip speed implies a small impeller tip radius. Therefore, the compressor itself get smaller, something very important in for instance the automotive or aeronautical industry.

The relations between different velocity components can be seen in figure 2.4. In this analysis, as compared to the preliminary impeller design, an inlet velocity distortion is modelled as described by Herbert (1980) [16]. The velocity distortion  $\kappa$  is defined as

$$\kappa = \frac{C_{m1s}}{\bar{C}_{m1}} \quad (4.1)$$

where  $C_{m1s}$  denotes the inlet meridional velocity at the shroud, and  $\bar{C}_{m1}$  is the mean inlet meridional velocity. The velocity  $C_{m1}$  at any inlet radius  $r_1$  is determined by

$$C_{m1} = \bar{C}_{m1} \left( 1 + (\kappa - 1) \frac{r_1 - r_{1,ref}}{r_{1s} - r_{1,ref}} \right) \quad (4.2)$$

Herbert (1980) presents a proof from continuity reasoning, showing that the reference radius  $r_{1,ref}$  can be determined by

$$r_{1,ref} = \frac{2r_{1s}^2 + r_{1s}r_{1h} + r_{1h}^2}{3(r_{1s} + r_{1h})} \quad (4.3)$$

In this case the absolute flow angle  $\alpha_1$  is regarded constant, a reasonable assumption for a well designed inlet.

If using the tip meridional velocity for calculating the impeller inlet area, the proposed formula from Japikse (1996) including blockage effects can be used. It is given by

$$A_{1,avail} = \frac{\dot{m}}{\rho_1 C_{m1s} (1 - B_1)} \quad (4.4)$$

where  $B_1$  denotes an inlet blockage factor. In this case this includes the effect of blade blockage, and the velocity distortion. In an iterative procedure, this blockage factor can be adjusted to give the correct inlet area. The correct inlet area can in turn be determined by the exact same way as in the preliminary impeller design, see section 3.3.2. As was the case previously, the blade angles are set to vary linearly along the passage width.

Another parameter instead relating to the impeller exit flow is the diffusion ratio, defined by

$$DR = \frac{W_{1s}}{W_2} \quad (4.5)$$

As noted in Cumpsty (2004) a large set of different diffusion factors and ratios have been defined. Many of these have their origin in axial compressors but are nevertheless transferred to the design of radial compressors. The diffusion ratio gives an idea of how much pressure is being built up by lowering the fluid (relative) velocity. As is also described by Cumpsty (2004) the major part of the pressure rise in a radial compressor stems from the change of radius and not the slowing down of the fluid. The pressure rise obtained by this effect comes from purely kinematic reasoning and is thus completely loss free. This is the reason why radial compressors can have rather high efficiencies with major parts of the flow separated in the impeller passages. A typical maximum value of the diffusion ratio is about 1.7. If it is increased too much, losses in the impeller passages will be sufficiently large to yield an unusable design.

As a complement for the absolute exit flow angle of the impeller, the parameter  $\lambda_2$  is used to describe the ratio between the impeller tip absolute tangential to meridional velocity according to

$$\lambda_2 = \frac{C_{\theta 2}}{C_{m 2}} = \tan \alpha_2 \quad (4.6)$$

As is described by Japikse (1996), there exist an optimum value of  $\lambda_2$  where the pressure recovery is as at maximum. Each side of the maxima represents either having insufficient pressure recovery or an inefficient pressure recovery. The exact level of this optimum value depends on the impeller and especially on the following diffuser. Also, the velocity ratio determines the impeller tip width, as can be seen from continuity reasons at the tip. A larger value suggests a wider impeller tip, keeping other parameters constant.

Another parameter determining the behaviour of the flow at impeller exit is the slip factor. The same slip factor as was employed in the preliminary analysis (see section 3.1), the Wiesner slip factor, is used here as well. One difference, however, is that no restriction to zero flow is made. In this case the influence of the exit contour slope is neglected (that is, a completely radial flow is assumed), and equation 3.25 reduces to

$$\sigma = 1 - \frac{\sqrt{\cos \beta_2}}{Z_I^{0.7}} \quad (4.7)$$

By introducing the slip velocity  $C_{slip}$  at the tip, defined as the difference between the ideal absolute tangential velocity (that is, with no "slip" of the fluid) and the actual absolute tangential velocity one obtain

$$C_{slip} = C_{\theta 2, \infty} - C_{\theta 2} \quad (4.8)$$

The two different velocity triangles for an ideal and a real flow is shown in figure 4.1. The triangles are drawn for the same impeller tip velocity  $U_2$  and the same mass flow (thus equal meridional velocities, assuming other parameters are held constant). As can be seen in this figure, the ideal relative tangential velocity can be written

$$W_{\theta 2, \infty} = C_{m 2} \tan \beta_2 \quad (4.9)$$

In order to determine the absolute tangential velocity  $C_{\theta 2}$  an additional relation can be found with the aid of figure 4.1, namely

$$C_{\theta 2} = U_2 + W_{\theta 2} = U_2 + (W_{\theta 2, \infty} - C_{slip}) = U_2 + (C_{m 2} \tan \beta_2 - C_{slip}) \quad (4.10)$$

Note that the relative velocity vectors are drawn in the negative direction and hence the relative tangential velocities in equation 4.10 would become negative. As opposed to figure 2.5 serving as a basis for the sign convention employed, figure 4.1 shows the typical appearance of a tip velocity triangle. From the definition of slip factor, equation 3.24, the slip velocity turns out to be

$$C_{slip} = U_2 (1 - \sigma) \quad (4.11)$$

As is obvious from the tip velocity triangle, figure 4.1, are the following two relations

$$U_2 = C_{\theta 2} - W_{\theta 2} \quad (4.12)$$

$$W_2^2 = W_{m 2}^2 + W_{\theta 2}^2 \quad (4.13)$$

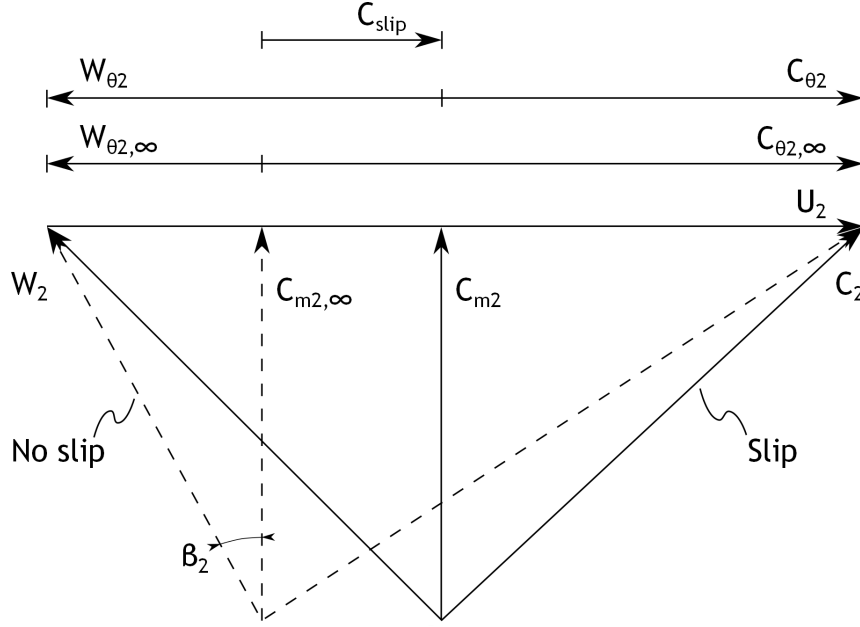


Figure 4.1: Two velocity triangles representing an ideal and a real flow, the ideal velocity vectors being shown dashed. The triangles are drawn for the same impeller tip speed  $U_2$  and the same mass flow. Also shown are the different velocities, including the slip velocity  $C_{slip}$

Combining these equations with equation 4.6, 4.10 and 4.11 yields two useful relationships in determining the impeller tip flow state. These are

$$C_{m2} = \sqrt{\frac{(\sigma W_2)^2}{(\tan \beta_2 + \sigma \lambda_2 - \lambda_2)^2 + \sigma^2}} \quad (4.14)$$

and

$$U_2 = \frac{C_{m2} (\lambda_2 - \tan \beta_2)}{\sigma} \quad (4.15)$$

By knowing the presented parameters and the exit static or stagnation pressure, the impeller tip flow is fully determined. A number of different ways to determine these pressures exist, some of them requiring information of the following diffuser. One of the more simple parameters is the impeller pressure ratio. If the designer know what pressure is needed right after the impeller this is the parameter to give. The stagnation pressure ratio  $PR_I$  is given by

$$PR_I = \frac{p_{02}}{p_{00}} \quad (4.16)$$

A different way of determining the impeller exit is by specifying the impeller polytropic efficiency. The definition of this has already been covered in chapter 3 and by combining equation 2.2, 3.15 and 3.17 the following relation results

$$\eta_I = \frac{PR_I^{\frac{\gamma-1}{\gamma}}}{\frac{T_{02}}{T_{00}}} \quad (4.17)$$

from which the exit stagnation pressure can be determined after specifying the efficiency. A third way to find the exit pressure is by knowing the whole stage static to stagnation pressure



ratio, together with the diffuser static pressure recovery coefficient. One huge advantage with such a method is that it incorporates the diffuser, and therefore describes the tight relationship between these components. With the aid of the stage total-to-static pressure ratio  $PR_{stage,tot-stat}$ , the stage discharge static pressure  $p_5$  can be calculated from

$$PR_{stage,tot-stat} = \frac{p_5}{p_{00}} \quad (4.18)$$

With the use of the diffuser static pressure recovery coefficient,  $C_{p,D}$ , defined by

$$C_{p,D} = \frac{p_5 - p_2}{p_{02} - p_2} \quad (4.19)$$

the impeller exit pressure can be determined. Finally, a fourth method to determine these pressures is by using the stage polytropic efficiency together with a total pressure loss over the diffuser. Here, the efficiency is calculated from stagnation properties alone (a so called total-to-total efficiency), through

$$\eta_{p,stage,tot-tot} = \frac{\left(\frac{p_{05}}{p_{00}}\right)^{\frac{\gamma-1}{\gamma}} - 1}{\frac{T_{02}}{T_{00}} - 1} \quad (4.20)$$

Consequently, the compressor discharge stagnation pressure can be calculated upon specifying the total-to-total efficiency. A stagnation pressure loss  $\omega_{diff}$  of the diffuser is also given, and written

$$\omega_{diff} = \frac{p_{05} - p_{02}}{p_{02} - p_2} \quad (4.21)$$

again, the impeller exit pressure can now be determined.

Once knowing either the impeller exit static or stagnation pressure all other conditions at impeller outlet can be calculated. The tip passage width must take the blade blockage into account, and the very same procedure as for the preliminary impeller design can be used.

## 4.2 Geometrical construction

One main difference from the preliminary impeller design is how the geometry is created. In chapter 3 very little geometry input was needed to be provided by the designer. In this analysis however, only the inlet and exit widths are provided by calculation procedures. The actual hub and shroud contours are to be supplied by the designer.

When leaving such important impeller characteristics to the designer, it is very important to enable easy usage and full control of the actual contours. A now well established way of allowing curves to be interactively modified is the usage of so called Bezier polynomials. One example of Bezier polynomials implemented into a turbomachinery design process is described by Casey, Gersbach and Robinson (2008) [17]. The main features of Bezier curves are outlined by Aungier (2000). These polynomials are described by a set of reference points, which typically are in control of the designer, see figure 4.2.

It is worth mentioning that a Bezier polynomial always remains continuous, a feature easing the design process. Also, the curve passes through the two endpoints and the end point slopes can be controlled by the points adjacent to the end points themselves.

When constructing a Bezier polynomial  $n + 1$  reference points is utilized. These are numbered from 0 to  $n$  with the current point denoted  $k$ . The polynomial is defined as a

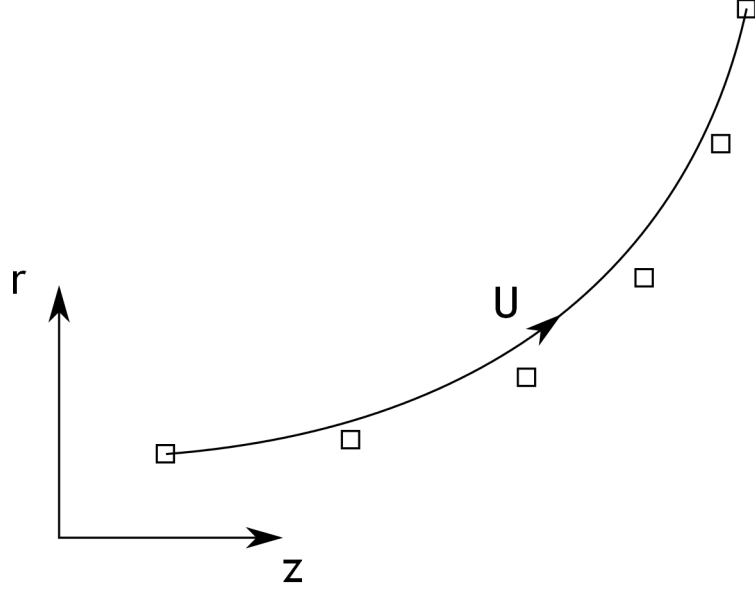


Figure 4.2: A typical example of a Bezier polynomial having six reference points shown by squares. The reference points do generally not lie on the Bezier polynomial but determine the general shape of it

function of  $U$ , following the line itself. It can be interpreted as a non-dimensional curvilinear coordinate varying from 0 to 1 along the line. The corresponding  $z$  and  $r$  coordinates of the polynomial can be determined by

$$[z_U \ r_U] = \sum_{k=0}^n [z_k \ r_k] B_k^n(U) \quad (4.22)$$

where  $B_k^n$  is the Bezier polynomial itself defined according to

$$B_k^n(U) = \binom{n}{k} U^k (1-U)^{n-k} \quad (4.23)$$

and the binomial coefficient  $\binom{n}{k}$  is written

$$\binom{n}{k} = \frac{n(n-1)(n-2)\dots(n-k+1)}{k!} \quad (4.24)$$

In practice, equation 4.22 is most easily divided into two parts, one for each component in the two directions. This yields

$$z_U = \sum_{k=0}^n z_k B_k^n(U) \quad (4.25)$$

$$r_U = \sum_{k=0}^n r_k B_k^n(U) \quad (4.26)$$

Hence,  $U$  is varied from 0 to 1  $n$  times, one time for each reference point. The result of each variation of  $U$  is summed up to yield the coordinates of the polynomial.

The Bezier polynomial is used for constructing both the hub and shroud contour. Also, Bezier curves are used to define the blade angle distribution along the hub and shroud. This approach was also implemented in the analysis conducted by Casey, Gersbach and Robinson (2008) and provide a very powerful mean to quite arbitrarily choose the blade angle distribution. Therefore, the blade angle distribution is also under full control of the designer. As is the case for the impeller contours, this is ideal for the more experienced designer, knowing what kind of shapes and distributions to be aimed at.

An additional geometric feature of any detailed impeller calculation is the three-dimensional representation of the impeller itself. In order to determine the shape of an impeller blade, the mean camberline must be known, and hence not only the blade angle distribution and extension in the  $z - r$  plane. The blades are thought of as being constructed of straight blade elements between the equally spaced points defining the hub and shroud contour, see figure 4.3. Here, two arbitrary points  $i$  and  $i + 1$  are shown on either a developed plane of the hub or

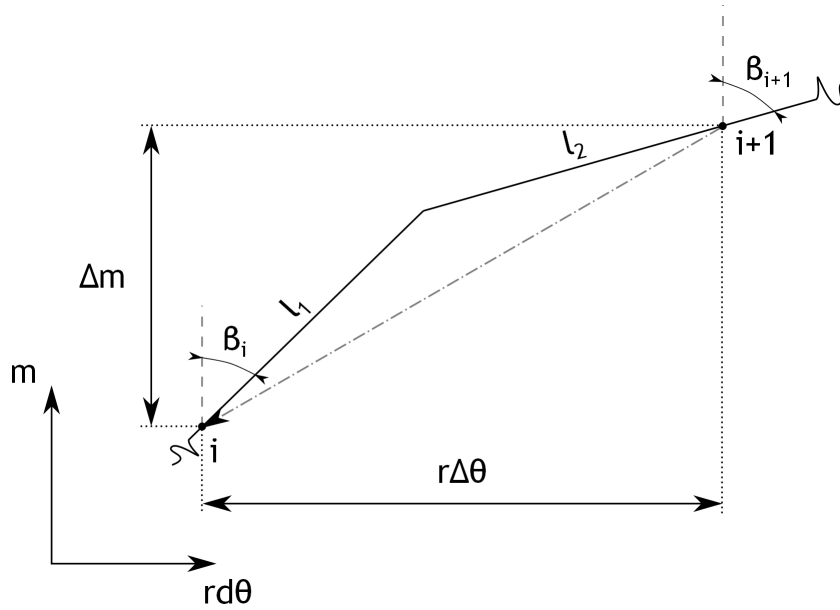


Figure 4.3: A schematic sketch in a developed hub or shroud plane. The solid lines shows two half blade elements having the exact slope defined by  $\beta$ . The dash-dotted line represents the straight line elements resulting from the outlined method

shroud surface. The solid lines shows two imaginary blade segments having the slope of the prescribed blade angles  $\beta_i$  and  $\beta_{i+1}$  in the points of interest. Also shown is a dash-dotted line, representing the blade segment resulting from the method outlined below. The meridional distance between point  $i$  and  $i + 1$ , with points located sufficiently close to each other, can be approximated by

$$\Delta m = \sqrt{(z_{i+1} - z_i)^2 + (r_{i+1} - r_i)^2} \quad (4.27)$$

In order to determine the tangential angle  $\Delta\theta$  between the points, a mean radius  $\bar{r}$  is defined as

$$\bar{r} = \frac{r_{i+1} + r_i}{2} \quad (4.28)$$

One additional constraint is needed to determine  $\Delta\theta$ . By assuming the line segments  $l_1$  and  $l_2$  are equally long, the simple geometry supplemented by figure 4.3 yields

$$\Delta\theta = \frac{\Delta m \sin \beta_i + \sin \beta_{i+1}}{\bar{r} \cos \beta_i + \cos \beta_{i+1}} \quad (4.29)$$

By specifying an inlet rake angle<sup>1</sup>, the tangential positions of all points defining the hub and shroud blade mean camberline may be found. A rake angle, together with the inlet geometry fully determines the tangential offset between the hub and shroud mean camberlines and may be determined from figure 4.4 and the law of cosines. Points  $o$ ,  $a$  and  $c$  is known directly from

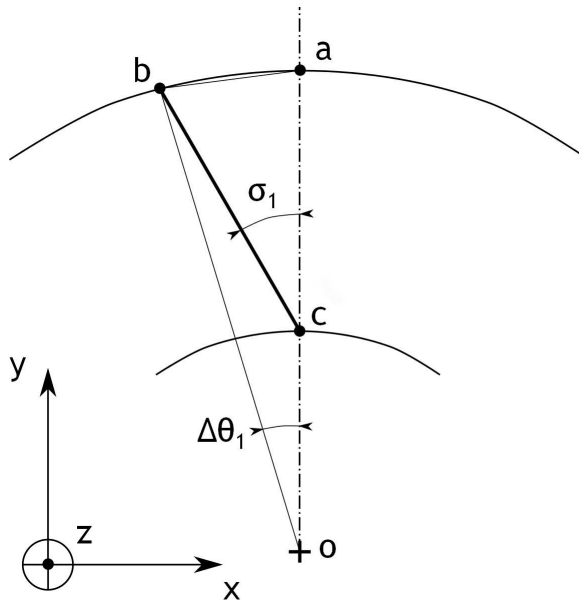


Figure 4.4: The parameters needed to determine the tangential offset of the hub and shroud mean camberline in order to satisfy the desired inlet rake angle  $\sigma_1$

the impeller inlet geometry, while point  $b$  is easily determined from the inlet rake angle  $\sigma_1$  and the other points. Letting subscripts  $x$  and  $y$  denote the respective component of each point, it is seen that

$$b_x = c_x - \bar{cb} \sin \sigma_1 \quad (4.30)$$

$$b_y = c_y + \bar{cb} \cos \sigma_1 \quad (4.31)$$

where  $\bar{cb}$  is the length of the line segment between point  $c$  and  $b$ .  $\bar{cb}$  may be found from the law of cosines rewritten according to

$$\bar{cb} = \bar{oc} \cos(\pi - \sigma_1) + \sqrt{\bar{oc}^2 \cos^2(\pi - \sigma_1) + \bar{ob}^2 - \bar{oc}^2} \quad (4.32)$$

here,  $\bar{ob}$  and  $\bar{oc}$  are the lengths of the line segments between the points of interest. Again, using the law of cosines, the tangential offset angle  $\Delta\theta_1$  may be found from

$$\Delta\theta_1 = \arccos \left( \frac{\bar{oa}^2 + \bar{ob}^2 - \bar{ab}^2}{2 \bar{oa} \bar{ob}} \right) \quad (4.33)$$

<sup>1</sup>Inlet rake angles are sometimes termed *lean* angles, in analogy with axial turbomachinery

where again  $\overline{ab}$  and  $\overline{oa}$  represents the length of the lines between the different points. Thus, starting from the inlet, all tangential locations of the mean camberlines may be determined, by adding  $\Delta\theta_i$  to the tangential angle "accumulated" up to point  $i$ . Knowing the tangential position of any point defining a mean camberline, it is an easy matter to find the corresponding  $x$  and  $y$  value. These coordinates are found from

$$x_i = r_i \cos \theta_i \quad (4.34)$$

and

$$y_i = r_i \sin \theta_i \quad (4.35)$$

Of course, the  $z$  coordinate is unchanged, and thus also known. Thereby, the mean camberlines at hub and shroud are fully determined in all three dimensions.

Aungier (2000) presents a novel method to find the blade surfaces from the blade thickness distribution and mean camberline coordinates. Here, linear line segments between hub and shroud points are employed, a reasonable approximation for the impeller blades. Three unit vectors are defined (see figure 4.5);  $\vec{S}$  tangent to the mean camberline on any stream surface,  $\vec{B}$  along the blade element and  $\vec{T}$  normal to the blade surface. All of these vectors are orthogonal

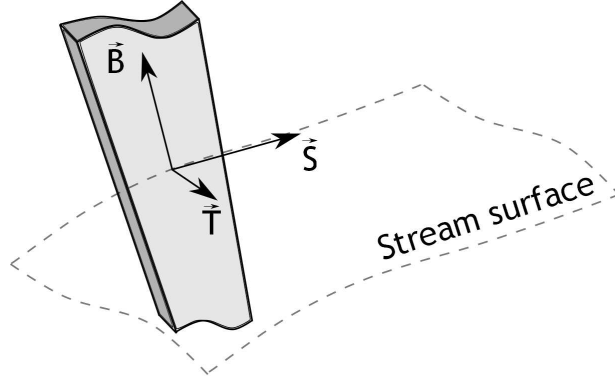


Figure 4.5: The three vectors defining the important directions while determining the blade surface coordinates

to each other, and by knowing  $\vec{S}$  and  $\vec{B}$ , the third vector  $\vec{T}$  may be found from the cross product of the other two

$$\vec{T} = \vec{S} \times \vec{B} \quad (4.36)$$

The different components of  $\vec{S}$  can be determined from

$$S_x = \sin \theta \sin \alpha_C \cos \beta + \cos \theta \sin \beta \quad (4.37)$$

$$S_y = \cos \theta \sin \alpha_C \cos \beta - \sin \theta \sin \beta \quad (4.38)$$

$$S_z = \sin \alpha_C \cos \beta \quad (4.39)$$

where  $\alpha_C$  is the slope of the stream surface at the blade (or equally hub or shroud contour). In a similar manner the components of  $\vec{B}$  is possible to express as

$$B_x = \frac{x_s - x_h}{L} \quad (4.40)$$

$$B_y = \frac{y_s - y_h}{L} \quad (4.41)$$

$$B_z = \frac{z_s - z_h}{L} \quad (4.42)$$

where  $L$  is the length of the blade segment, in turn found from

$$L = \sqrt{(x_s - x_h)^2 + (y_s - y_h)^2 + (z_s - z_h)^2} \quad (4.43)$$

here, parameters with subscript  $h$  and  $s$  represents coordinates at the hub and shroud surface, respectively. Inserting the components of  $\vec{S}$  and  $\vec{B}$  into equation 4.36, the components of  $\vec{T}$  are determined by

$$T_x = S_z B_y - S_y B_z \quad (4.44)$$

$$T_y = S_x B_z - S_z B_x \quad (4.45)$$

$$T_z = S_y B_x - S_x B_y \quad (4.46)$$

Finally, the blade surface coordinates  $x_{bs}$ ,  $y_{bs}$  and  $z_{bs}$  in the three different directions may be expressed as

$$x_{bs} = x \pm \frac{1}{2} t_B T_x \quad (4.47)$$

$$y_{bs} = y \pm \frac{1}{2} t_B T_y \quad (4.48)$$

$$z_{bs} = z \pm \frac{1}{2} t_B T_z \quad (4.49)$$

where  $x$ ,  $y$  and  $z$  represents mean camberline coordinates and  $t_B$  is the blade thickness of the blade element in question. It is understood that the blade surface is defined at the equally spaced points along the hub and shroud. From the surface coordinates at hub and shroud, the blade is constructed by connecting these points by straight lines.

### 4.3 Calculation procedure

The calculation will start with an optimization of the impeller inducer. This requires an iterative approach, in order to come up with the correct inlet area. However, the rest of the calculation is rather straight forward, and no main iteration covering an as large part as in the preliminary impeller design is needed. This can be attributed to the absence of any advanced geometry generation. The different steps in the detailed calculation can be seen in figure 4.6.

#### 4.3.1 Input parameters

As was the case for the preliminary impeller calculation, it is necessary to know what the fluid properties are. Again, it is only necessary to specify the specific gas constant  $R$ , the specific heat at constant pressure  $c_p$  and the specific heat ratio  $\gamma$ . Also, the inlet stagnation properties need to be given in the form of stagnation temperature  $T_{00}$  and stagnation pressure  $p_{00}$ . The intake loss is neglected, hence the impeller inlet stagnation properties are the same as for the intake.

The rotational speed  $N$  need also be specified, being a parameter usually known at early stages in any compressor design process. Also, as was noted in the preliminary design analysis, the rotational speed is in tight relationship with the mechanical stresses in the impeller. Further,

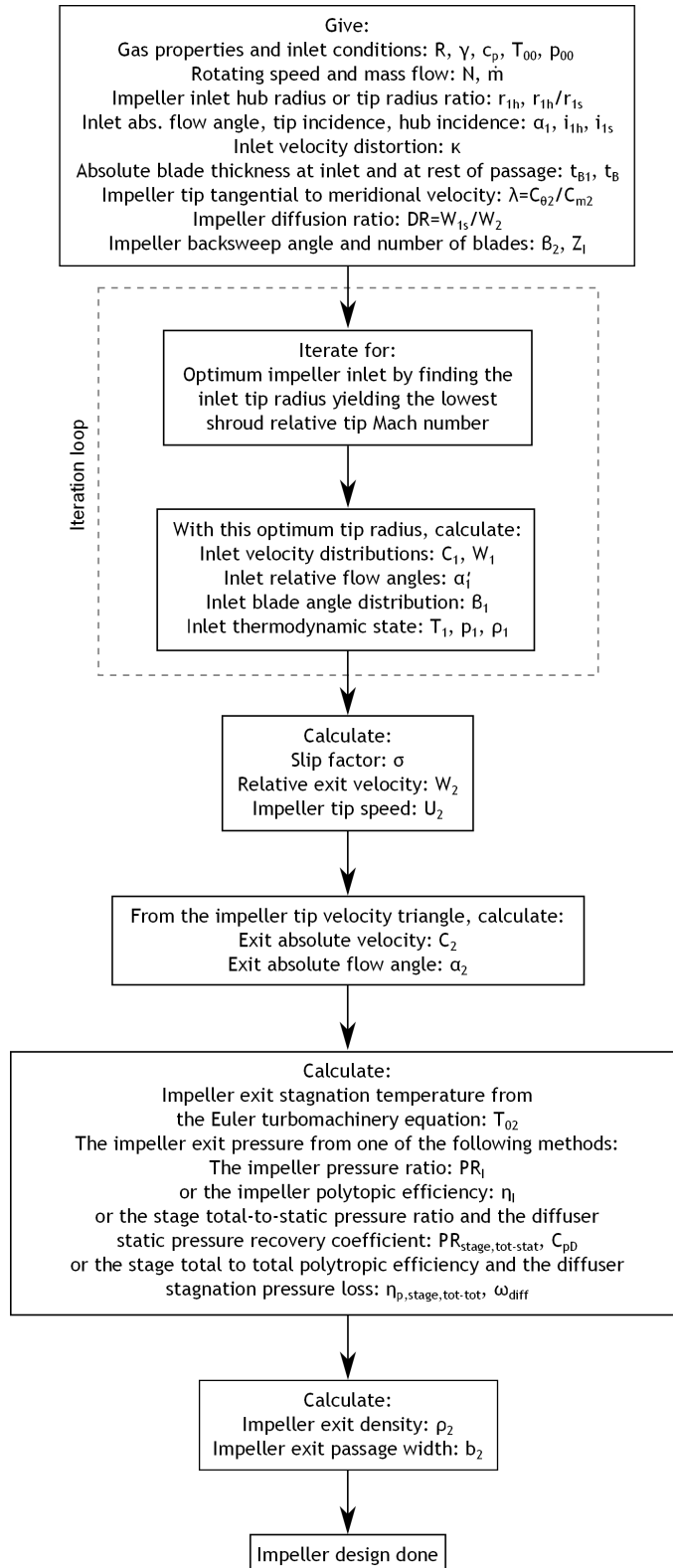


Figure 4.6: The main calculation procedure to determine the impeller inlet and exit states. Note the internal iteration loop necessary to size an optimum inlet

the target mass flow  $\dot{m}$  is generally always known, since a specific compressor is typically designed for a given duty requiring a specific mass flow.

One of the few geometrical parameters needed for the detailed calculation is some information regarding the inlet size. Here, the designer can choose to either specify the absolute inlet hub radius  $r_{1h}$  or the inlet hub to tip radius ratio,  $r_{1h}/r_{1s}$ . Having this choice, a designer can more quickly come up with a solution suited for his or her duty cycle. An absolute radius is useful to specify if, for instance, the inlet hub radius must be larger than a certain value to provide space for a front bearing. Instead, the radius ratio is useful when not having a constraint on the hub radius absolute value. This is typically the situation if one wants to choose a compressor configuration similar to a past design (with a known inlet hub to tip radius ratio).

In order to handle situations with non-axial flow, the inlet absolute flow angle  $\alpha_1$  must be specified. This could for instance be the case if inlet guide vanes are used, or the impeller is one of a series in a multi stage compressor. Also, in order to have full control of the inlet region both the incidence at hub,  $i_{1h}$ , and shroud,  $i_{1s}$ , should be specified. The incidence plays a major part in determining the flow field of the inducer region, see Japikse (1996). A major reason for the importance of a well designed inducer region is the high velocities encountered, followed by a strong diffusion. Hence, ability to choose correct incidences is of prime importance, even in the early steps of a design. Also coupled to the inducer design is the inlet velocity distortion  $\kappa$ . This parameter can be picked to yield velocity profiles representing the effect of viscous effects in the intake. Sometimes the intake must be made rather long, and additionally with rather large curvatures. This will give rise to a distorted flow, having an adverse effect on the impeller flow field. Even though the velocity distortion is a simple model of usually complex intake flows, it has its place in the early stages of a compressor design.

As was the case for the preliminary design calculation, the blade thickness must be chosen at both inlet,  $t_{B1}$ , and over the rest of the impeller passage,  $t_B$ . This is not only for aerodynamic reasons, but also to avoid resonance of the impeller blades. Of course, the choice of blade thickness depends on the passage width, and hence how "slender" the blades become. The passage width does itself depend on the blade thickness, and therefore the designer may be forced to resort to an iterative approach, in finding the correct width-to-thickness ratio.

Now, turning the attention to the impeller exit region, a direct measure of the impeller exit velocities is the diffusion ratio  $DR$ . This parameter gives the designer some control of the diffusion level in the impeller and is one of the governing parameters in the two zone modelling presented by Japikse (1996). Further, Braembussche (2013) notes that the diffusion ratio should take the downstream diffuser into account. If  $DR > 1.4$ , the stage efficiency becomes increasingly more dependent on the diffuser performance.

Naturally, the ratio of the impeller absolute tangential to meridional velocity  $\lambda_2$  is a key parameter in determining the impeller exit flow. As was described above, it is in total analogy with an absolute exit flow angle. It is vital that  $\lambda_2$  is chosen to suit the diffuser following the impeller, and the designer must make wise decisions based on previous experience. Finally, the backsweep angle  $\beta_2$  must be specified. Having full control of this angle is rather beneficial since the stability of the whole compressor is highly dependant on the backsweep. Also, if preswirl is employed at reduced mass flows, the backsweep can keep the work input almost constant and thereby counteract the effect described related to the Euler turbomachinery equation in chapter 2. A thorough description is provided by Braembussche (2013), and the fundamental reason for the effect can be attributed to the alternating absolute tangential velocity at the tip when decreasing the meridional velocity component. This may easily be seen in a tip velocity triangle. A third influence the backsweep angle may have is its effect on blade loading, and



chosen wisely the blade loading at impeller tip can be minimized. Thus, the backsweep angle is a very powerful parameter, and must be chosen carefully at the design stage.

To take the discussion even further, the diffusion ratio and the backsweep angle will, for a given pressure rise, to large extent determine the impeller tip width to tip radius ratio ( $b_2/R_2$ ). This parameter is important, in that the loss source will depend on it's value. For large values, the clearance and friction loss will become relatively small. If instead a small value is obtained, the losses associated with flow separation will be smaller (larger curvature radius of the shroud contour). Consequently, the combination of these two input parameters are of very high importance and must at all design problems be chosen wisely.

Additionally, the number of blades need specification. It is a non-trivial matter to determine the amount of blades, and a balance must be found between diffusion losses, friction losses and blockage considerations. Braemsbussche (2013) states that 14 to 18 blades generally lead to good performance, while a larger stable operating range can be found with 10 to 12 blades. Of course, the blade loading is significant and may be reduced by employing an increased number of blades.

Finally, two parameters the designer must specify, not shown on figure 4.6, are the impeller axial length and inlet rake angle. These are not a part of the impeller inlet and discharge calculation, and are thus left out of this figure. The impeller axial length is of great importance, not only because of the size and weight of the compressor, but also because it largely determines the flow condition inside the impeller. Too short an impeller, the smaller must the curvature radius of the shroud become. Decreasing this radius increases the risk of a massive flow separation on the shroud end wall resulting in large losses. If instead the axial length is chosen too long, large friction losses may occur, and an as good compromise as possible must be found. The value of this parameter is typically based on previous designs and are thus scaled with the impeller tip radius. Instead, turning the attention to the inlet rake angle, it is a degree of freedom necessary to control the impeller exit rake angle. It is typically chosen to keep the hub and shroud mean camberline at a reasonable tangential distance from each other in an as large part of the impeller passage as possible. Sometimes this parameter is not capable to achieve reasonable and realistic blade shapes alone. In those cases the designer may have to resort to altering either the hub and shroud contours or the blade angle distribution.

### 4.3.2 Calculation model

As is outlined in figure 4.6, the calculation is begun by optimizing the impeller inducer. This is based on an iterative procedure, and is presented in figure 4.7. The iteration is initiated by guessing a value of the inlet blockage factor  $B_1$ . This factor compensates both for the blade blockage and the inlet velocity distortion, and enables an inlet area to be calculated from the tip meridional velocity. Casey and Rusch (2012) presents a set of analytical expressions for determining the inlet parameters for an optimized inlet. However, this does not include any of the above mentioned effects. Here, instead, a rather crude approach is used; vary the absolute tip meridional velocity, calculate the tip condition, and find which value of  $C_{m1s}$  minimizes the tip relative velocity  $W_{1s}$ . For each value of  $C_{m1s}$  the first step is to calculate the absolute velocity at the tip, simply from the absolute flow angle, see the inlet velocity triangle presented in figure 2.4. From the stagnation temperature and the absolute velocity, the static temperature follows. Further, with aid of equation 2.6, the tip static pressure can be calculated. Thus, the thermodynamic condition at the impeller tip is fully determined, including the density from the ideal gas law, equation 2.1. With the assumed amount of blockage, the inlet area follows directly from equation 4.4. After determining this area, the impeller inlet tip radius can be

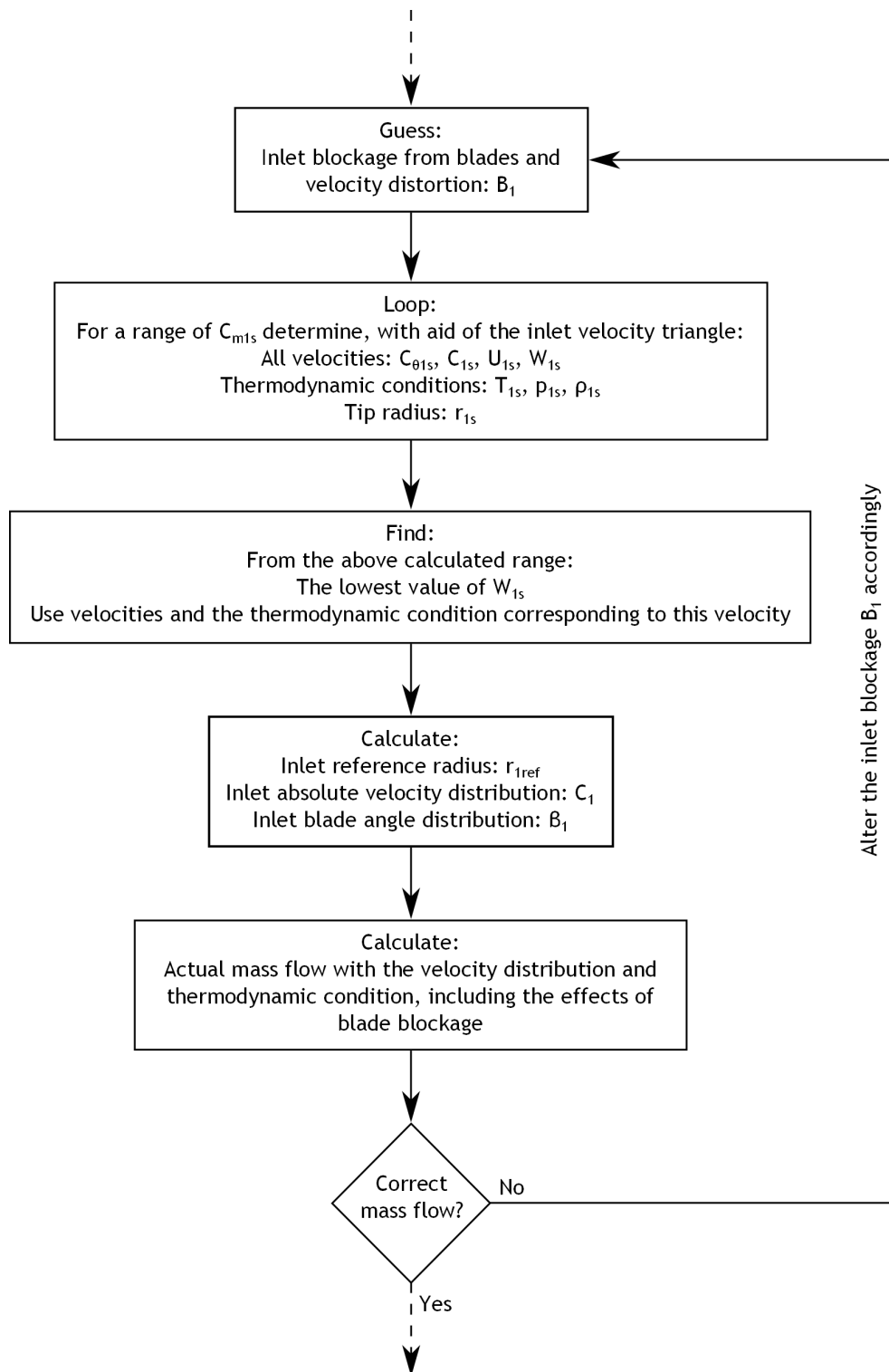


Figure 4.7: The iterative calculation procedure utilized to size the impeller inducer. After finding a solution, the lowest possible inlet relative Mach number is found, based on constraints added by the user

determined. Depending on what parameter given ( $r_{1h}$  or  $r_{1h}/r_{1s}$ ) by the designer, different formulas must be used. If the absolute hub radius is given, the tip radius is given by

$$r_{1s} = \sqrt{\frac{A_{1,avail}}{\pi} + r_{1h}^2} \quad (4.50)$$

while if the radius ratio  $r_{1h}/r_{1s}$  is specified, the tip radius can be calculated from

$$r_{1s} = \sqrt{\frac{A_{1,avail}}{\pi \left(1 - \left(\frac{r_{1h}}{r_{1s}}\right)^2\right)}} \quad (4.51)$$

and the hub radius follows directly from the given radius ratio.

In order to determine whether the guessed blockage factor is correct, the mass flow is calculated with the current tip radius. As was the case in the preliminary analysis, the blade angles vary from hub to tip, and hence the amount of blockage. Therefore, a similar calculation as outlined in section 3.3.2 must be employed. However, in this case the area increments need not be of the exact same size, it suffices to use equal radius increments. Using these radius increments instead of area increments simplifies the calculation procedure in that no iterative solution is needed. To enable such a calculation, it is necessary to determine the blade angle distribution from the relative flow angles. Hence, the impeller velocity at both hub and shroud is needed. These are calculated from the rotational speed and the different radii using equation 2.18. The tip relative flow direction follows directly from the tip optimization, but to calculate the flow condition at any other radius it is necessary include the inlet velocity distortion. With equations 4.1 to 4.3 the absolute meridional velocity (equal to the relative ditto) at any radius can be determined. Thus the relative flow angle at hub can be calculated, again using the inlet velocity diagram.

Knowing the relative flow angles at both hub and shroud, the blade angles at the same locations are easily calculated from the specified incidences, equation 2.20. Since the blade angles are assumed to vary linearly along the passage width, the blade angle  $\beta_1$  at any radius  $r_1$  follows from

$$\beta = \frac{r_1 - r_{1h}}{r_{1s} - r_{1h}} (\beta_{1s} - \beta_{1h}) + \beta_{1h} \quad (4.52)$$

The size of an area increment as shown in figure 4.8 can be determined by

$$A_{1,incr,i} = \left(r_{1,i+1}^2 - r_{1,i}^2\right) \pi - \frac{ZItB_1}{\cos \bar{\beta}_{1,i}} (r_{i+1} - r_i) \quad (4.53)$$

where  $\bar{\beta}_{1,i}$  is the mean blade angle at the mean radius of  $r_{1,i}$  and  $r_{1,i+1}$ , simply calculated from

$$\bar{\beta}_{1,i} = \frac{\beta_{1,i} + \beta_{1,i+1}}{2} \quad (4.54)$$

At each incremental flow area the incremental mass flow is also determined with the velocity obtained from the distorted inlet velocity distribution. As was described above for the inlet tip, the thermodynamic condition can also be fully determined at each radius  $r_{1,i}$ . The incremental mass flow  $\dot{m}_{1,i}$  at area increment  $A_{1,incr,i}$  becomes

$$\dot{m}_{1,i} = \bar{\rho}_{1,i} \bar{C}_{m1,i} A_{1,incr,i} \quad (4.55)$$

where the local density  $\bar{\rho}_{1,i}$  and the local meridional velocity  $\bar{C}_{m1,i}$  are determined at the mean radius of the area increment. Summing all incremental mass flows yields the total mass flow,

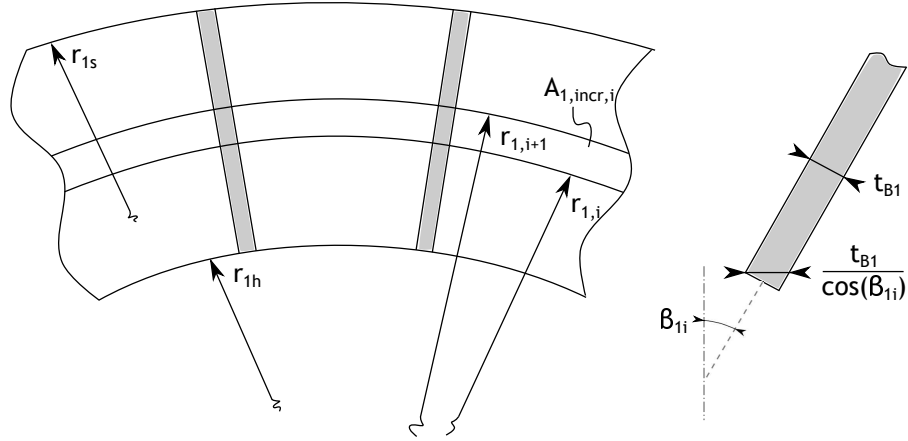


Figure 4.8: The main parameters in determining the inlet flow area, including effects of blade blockage. The figure is similar to the one shown in section 3.3.2, however the inlet shroud radius  $r_{1s}$  is in this case known

which can be compared to the value specified by the designer. In general, these mass flows will not be equal, and the whole inlet sizing and optimization is repeated until convergence. If the calculated mass flow was too large, the blockage factor  $B_1$  should be decreased during the next iteration in order to reduce the impeller inlet shroud radius. Of course, if the calculated mass flow is too small, the blockage should instead be increased.

Having sized the impeller inlet section, the next step is to determine the impeller exit condition. The slip factor follows directly from equation 4.7, inserting values of the number of blades and the impeller backsweep angle. Similarly, having sized the inducer, determining the relative exit velocity from the specified diffusion ratio, equation 4.5, is a straightforward task. Using these parameters together with the given impeller tip absolute velocity ratio  $\lambda_2$  the meridional flow velocity and the impeller speed at the tip can be calculated directly from equations 4.14 and 4.15. Having specified  $\lambda_2$  the absolute impeller exit angle is determined through equation 4.6. From the tip velocity triangle all other velocities can be calculated.

After choosing one of the four different ways to calculate the impeller discharge pressure, the thermodynamic condition is fully determined. Hence, the impeller tip width can be calculated following the exact same reasoning as in Section 3.3.2, including effects of blockage. Therefore, after employing equation 3.60 the impeller inlet and exit is fully sized. Other parameters, for instance the mean stream line coordinates, need the hub and shroud geometry to be established. Thus, after the designer has chosen hub and shroud contours, together with the blade angle distribution, the whole impeller geometry is specified and the analysis finished.

## Chapter 5

# Impeller internal flow analysis

After establishing a promising impeller design in a one-dimensional manner, it is of huge interest for the designer to verify whether the compressor will perform satisfactory. A very common way of doing this is by performing some three-dimensional flow field analysis, within the blade passages. One of the more accurate ways of doing this is by exporting the determined design to a CFD solver. Some disadvantages comes with this technique; it is usually very time consuming and sometimes hard - not to say impossible - to interpret the result. As noted by Cumpsty (2004) one of the greatest limitations of CFD is most designers inability to think in three dimensions.

To overcome these disadvantages and still yield results taking the most important effects into account, a streamline curvature method together with a blade-to-blade flow analysis is most useful. This type of solution procedure was originally devised by Wu (1952) [18], presenting a very thorough analysis and derivation. The main idea is to split up the complicated three-dimensional flow into simpler flows acting in two different planes. Some simplifications from the original model are made, and here the analysis closely follows the quasi three-dimensional analysis proposed by Aungier (2000). Further, only inviscid flow is considered. Speaking in general terms, streamline curvature models are widely accepted throughout the industry and are still in use and under development, see Casey and Robinson (2008) [19].

In this chapter the governing equations are first presented, together with the basic tools to solve them. No derivations are presented, the curious reader are referred to either Wu (1952) or Aungier (2000). No geometric construction is needed, in that the impeller design is given as input to the analysis. Finally, how the different equations are solved and implemented are shown.

### 5.1 Basic relations

As has already been briefly mentioned above, the three-dimensional flow field is split up in two different simpler surface representations. These two different types of surfaces are shown in figure 5.1 and are denoted S1 and S2. Surfaces S1 and S2 are here referred to as blade-to-blade and hub-to-shroud surfaces, respectively. Generally these surfaces will have some extent of twist, being hard to explain in any coordinate system. However, if assuming the amount of twist to be negligible, it simplifies the analysis somewhat. This means that the blade-to-blade surfaces reduces to axisymmetric surfaces while the hub-to-shroud surfaces reduces to planes of constant tangential angle, i.e. a  $r - z$  (meridional) plane using cylindrical coordinates.

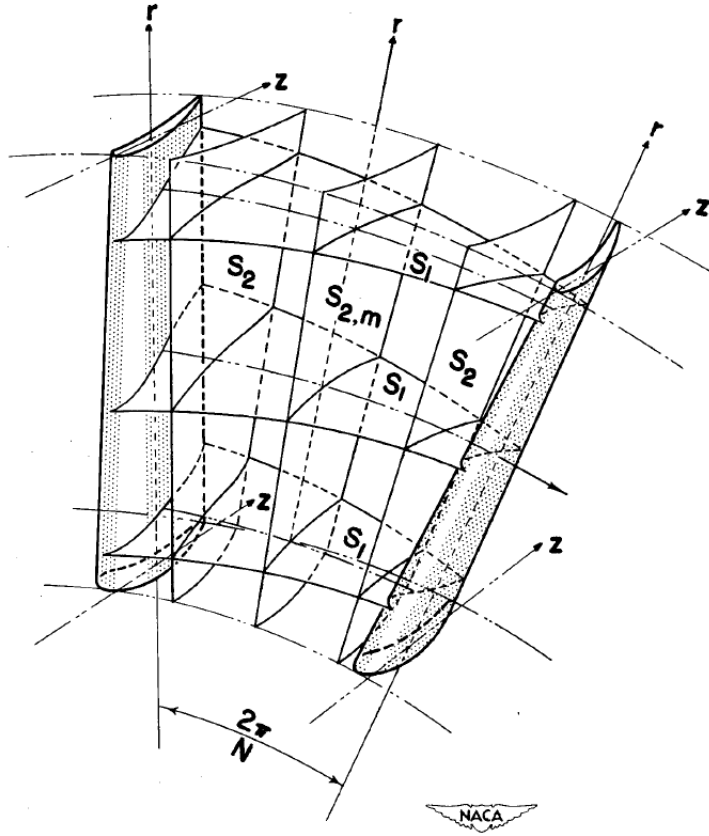


Figure 5.1: The two different surfaces S1 and S2 in a quasi three-dimensional analysis. Note the twisting of the different surfaces. From Wu (1952)

The equations to solve in the hub-to-shroud plane are

$$\frac{\partial r \rho W_m}{\partial m} + \kappa_n r \rho W_m = 0 \quad (5.1)$$

$$\kappa_m W_m^2 + \frac{W_\theta}{r} \frac{\partial (r W_\theta + r U)}{\partial n} + W_m \frac{\partial W_m}{\partial n} = \frac{\partial R_0}{\partial n} - T \frac{\partial s}{\partial n} \quad (5.2)$$

$$\frac{\partial R_0}{\partial m} = 0 \quad (5.3)$$

where  $\kappa$  denotes the stream surface curvature,  $n$  a direction normal to some stream surface and subscript  $n$  parameters in the normal direction to a stream surface. This set of equations can be thought of as describing an averaged flow within a blade passage, while being exact for vaneless passages. Further, it is assumed that both entropy and rothalpy are constant around the complete circumference of a specific stream surface.

Outside any blade passage the tangential momentum must be conserved, which can be written as

$$\frac{\partial (r W_\theta + r U)}{\partial m} = \frac{\partial r C_\theta}{\partial m} = 0 \quad (5.4)$$

This relation enables the flow angles to be calculated from known inlet conditions anywhere in vaneless passages. For blade passages these angles must be determined from a blade-to-blade

analysis. On these blade-to-blade surfaces the equations to solve are

$$\frac{\partial r b \rho W_m}{\partial m} + \frac{\partial b \rho W_\theta}{\partial \theta} = 0 \quad (5.5)$$

$$\frac{\partial W_m}{\partial \theta} - \frac{\partial (r W_\theta + r U)}{\partial m} = 0 \quad (5.6)$$

$$R_0 = \text{const.} \quad (5.7)$$

$$s = \text{const.} \quad (5.8)$$

here,  $b$  denotes the stream sheet thickness (the distance between two stream surfaces creating a stream sheet).

The main idea is therefore to first solve the hub-to-shroud equations with relative flow angles from the last blade-to-blade flow analysis. The hub-to-shroud solution then provide the following blade-to-blade flow analysis with the stream sheet thickness. Thus, the two analyses are strongly coupled to each other. To solve the equations some discretization must be done, since any geometry must be possible to analyse. This discretization is performed with aid of quasi normals, placed along the flow passage. By using these quasi normals, derivatives along the quasi normal rather than the ones with respect to the exact normal direction is desired. These derivatives are related to each other by

$$\frac{\partial}{\partial n} = \frac{1}{\cos \epsilon} \left( \frac{\partial}{\partial \sigma} - \sin \epsilon \frac{\partial}{\partial m} \right) \quad (5.9)$$

where  $\sigma$  denotes the quasi normal direction, see figure 5.2.

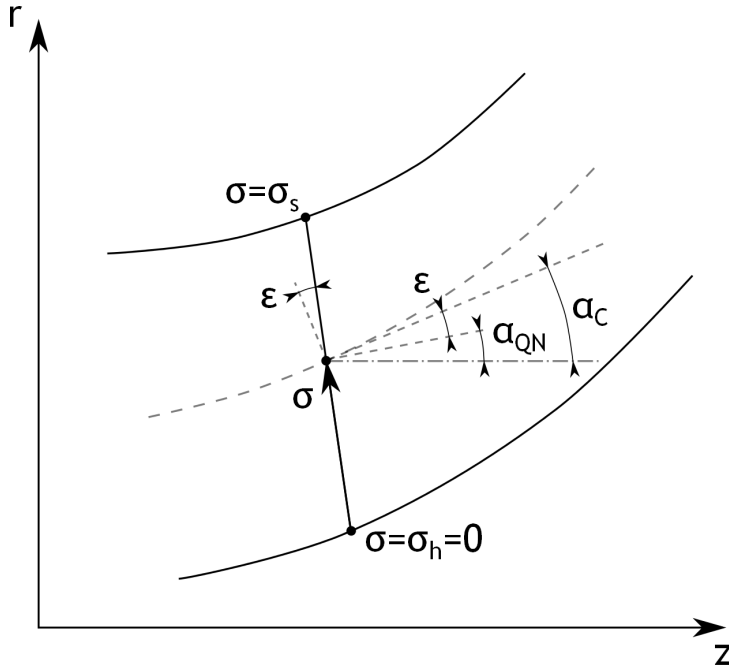


Figure 5.2: A stream surface crossing a quasi normal at position  $\sigma$ . Note that  $\sigma$  equals zero on the hub contour

### 5.1.1 Hub-to-shroud flow analysis

The hub-to-shroud analysis solves the mass conservation and momentum equations in a  $r - z$  plane. The momentum equation is used to find fluid dynamic parameters along a quasi normal. These properties must be consistent with the mass conservation equation, in order to yield the correct mass flow. Mass conservation may be expressed as

$$\dot{m} = 2\pi \int_0^{\sigma_s} K_B r \rho W_m \cos \epsilon \, d\sigma \quad (5.10)$$

where  $K_B$  is a blockage factor, taking the blade blockage into account. The momentum equation is different depending on whether blades exist or not at the quasi normal of interest. When no blades exist (and the flow angle may be determined from equation 5.4) it is given by

$$\frac{\partial W_m}{\partial \sigma} + W_m \left( \kappa_m \cos \epsilon - \frac{\sin \epsilon}{W_m} \frac{\partial W_m}{\partial m} \right) + \frac{W_\theta}{r W_m} \frac{\partial (r C_\theta)}{\partial \sigma} = \frac{1}{W_m} \left( \frac{\partial R_0}{\partial \sigma} - T \frac{\partial s}{\partial \sigma} \right) \quad (5.11)$$

When blades do exist, the flow angle is found from the blade-to-blade flow analysis and is explicitly incorporated in the formula. It is then given by

$$\begin{aligned} \frac{1}{\cos^2 \alpha'} \frac{\partial W_m}{\partial \sigma} + W_m \left( \kappa_m \cos \epsilon - \frac{\sin \epsilon}{W_m \cos^2 \alpha'} \frac{\partial W_m}{\partial m} + \frac{\tan \alpha'}{r} \left( \frac{\partial r \tan \alpha'}{\partial \sigma} - \sin \epsilon \frac{\partial r \tan \alpha'}{\partial m} \right) \right) \\ + 2\omega \tan \alpha' (\cos \alpha_{QN} - \sin \alpha_C \sin \epsilon) = \frac{1}{W_m} \left( \frac{\partial R_0}{\partial \sigma} - T \frac{\partial s}{\partial \sigma} \right) \end{aligned} \quad (5.12)$$

where  $\alpha_{QN}$  is the quasi normal angle measured from the axial direction, as depicted in figure 5.2.

As may be seen from the above formulas, regardless if blades are present or not, the meridional velocity derivative along a quasi normal can be written

$$\frac{\partial W_m}{\partial \sigma} = f_1(\sigma) W_m + f_2(\sigma) + \frac{f_3(\sigma)}{W_m} \quad (5.13)$$

The functions  $f_1(\sigma)$ ,  $f_2(\sigma)$  and  $f_3(\sigma)$  are different depending on whether blades are present at the quasi normal or not. Inside the blade passage, these may be written

$$f_1(\sigma) = \frac{\sin \epsilon}{W_m} \frac{\partial W_m}{\partial m} + \cos^2 \alpha' \left( -\kappa_m \cos \epsilon - \frac{\tan \alpha'}{r} \left( \frac{\partial r \tan \alpha'}{\partial \sigma} - \sin \epsilon \frac{\partial r \tan \alpha'}{\partial m} \right) \right) \quad (5.14)$$

$$f_2(\sigma) = -2\omega \sin \alpha' \cos \alpha' (\cos \alpha_{QN} - \sin \alpha_C \sin \epsilon) \quad (5.15)$$

$$f_3(\sigma) = \cos^2 \alpha' \left( \frac{\partial R_0}{\partial \sigma} - T \frac{\partial s}{\partial \sigma} \right) \quad (5.16)$$

If the quasi normal is positioned in a vaneless passage, the functions are instead given by

$$f_1(\sigma) = -\kappa_m \cos \epsilon + \frac{\sin \epsilon}{W_m} \frac{\partial W_m}{\partial m} \quad (5.17)$$

$$f_2(\sigma) = 0 \quad (5.18)$$

$$f_3(\sigma) = \frac{\partial R_0}{\partial \sigma} - T \frac{\partial s}{\partial \sigma} - \frac{C_\theta}{r} \frac{\partial r C_\theta}{\partial \sigma} \quad (5.19)$$

The last set of equations is easily employed outside the impeller. However, it may be more useful to write equations 5.14, 5.15 and 5.16 in the absolute, non-rotating frame of reference.



The main reason for this is that the absolute flow angles are more likely to be known at the passage inlet, rather than the absolute tangential velocities. This yields the following relations for the three different functions

$$f_1(\sigma) = \cos^2 \alpha \left( -\kappa_m \cos \epsilon - \frac{\tan \alpha}{r} \frac{\partial r \tan \alpha}{\partial \sigma} + \frac{\sin \epsilon}{W_m} \frac{\partial W_m}{\partial m} \right) \quad (5.20)$$

$$f_2(\sigma) = 0 \quad (5.21)$$

$$f_3(\sigma) = \cos^2 \alpha \left( \frac{\partial R_0}{\partial \sigma} - T \frac{\partial s}{\partial \sigma} \right) \quad (5.22)$$

By studying these equations it is noted that the solution of  $W_m$  contain meridional derivatives of itself. To avoid this, the conservation of mass for a stream sheet may be incorporated by writing

$$\Delta \dot{m} = \rho W_m \Delta A \quad (5.23)$$

where  $\Delta \dot{m}$  is the mass flow in the stream sheet and  $\Delta A$  is the cross sectional area of the stream sheet at the quasi normal. Taking the derivative of this equation and noting that  $\Delta \dot{m}$  does not vary in the meridional direction one obtain

$$\frac{1}{W_m} \frac{\partial W_m}{\partial m} = - \frac{1}{\rho \Delta A} \frac{\partial \rho \Delta A}{\partial m} \quad (5.24)$$

Density will still depend on the solution, but to a lesser extent than the meridional velocity. Further, it is seen that equation 5.13 becomes very large for small meridional velocities ( $\partial W_m / \partial \sigma \rightarrow \infty$  when  $W_m \rightarrow 0$ ). Again using equation 5.23, a new function  $f_4(\sigma)$  may be written

$$f_4(\sigma) = f_2(\sigma) + f_3(\sigma) \frac{\rho \Delta A}{\Delta \dot{m}} \quad (5.25)$$

while the momentum equation instead takes the form of

$$\frac{\partial W_m}{\partial \sigma} = f_1(\sigma) W_m + f_4(\sigma) \quad (5.26)$$

With such a differential equation a solution may be found from

$$W_m = W_m(0) F(\sigma) + F(\sigma) \int_0^{\sigma_s} \frac{f_4(\sigma)}{F(\sigma)} d\sigma \quad (5.27)$$

here it is understood that  $W_m(0)$  is the meridional velocity at hub. The function  $F(\sigma)$  is in turn given by

$$F(\sigma) = \exp \left( \int_0^{\sigma} f_1(\sigma) d\sigma \right) \quad (5.28)$$

It is easily seen that  $F$  takes the value of 1 at hub, and equation 5.27 reduces to the hub velocity. These equations are solved by iteratively updating the hub meridional velocity until the conservation of mass is fulfilled. After convergence is reached, the mass flow within each stream sheet will usually not be equal. Hence, the current stream surfaces must be repositioned, and the momentum and conservation of mass equations recalculated to conform to this new geometry. This must be repeated until the stream surface positions no longer change, and overall convergence is reached.

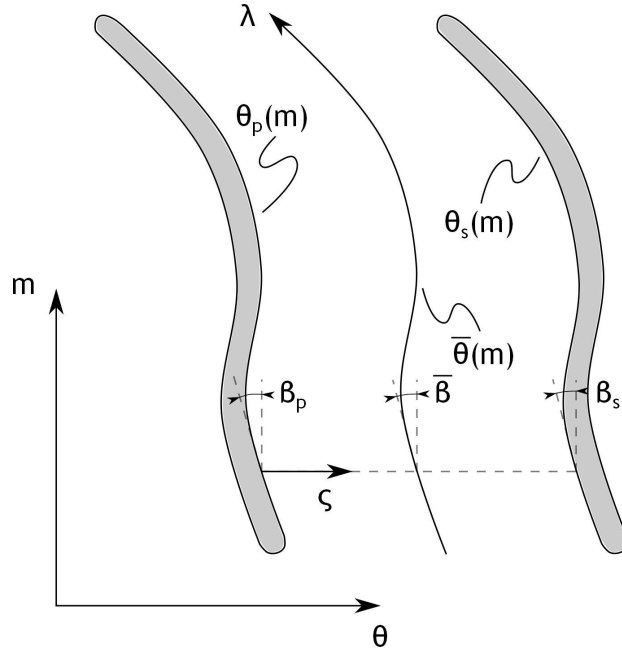


Figure 5.3: A schematic sketch of the two-dimensional blade-to-blade flow problem. Note that the blade passage is characterized by the tangential angle  $\theta$ , the meridional distance  $m$ , the coordinate  $\lambda$  following the passage itself and  $\zeta$  having a constant meridional position. Adapted from Aungier (2000)

### 5.1.2 Blade-to-blade flow analysis

The blade-to-blade flow analysis is based on a stream function flow solution, and can thus only handle subsonic flow velocities. This method assumes the flow within each blade passage equal to other passages, therefore only one passage need attention. The solution of the governing equations takes place at three different main locations; at the blade pressure side, the blade suction side, and at a mean position located in the middle of the other two locations. A schematic sketch of the two-dimensional problem is seen in figure 5.3. As is seen, the blade surfaces are characterized by the tangential angle  $\theta$  and the meridional position  $m$ . Two additional coordinates are;  $\lambda$  following the flow passage, and  $\zeta$  across the passage.  $\zeta$  varies between 0 and 1, having the lower value on the pressure side. Hence

$$\zeta = \frac{\theta - \theta_p}{\theta_s - \theta_p} \quad (5.29)$$

is valid, where  $\theta_p$  is the local tangential angle of the pressure surface while  $\theta_s$  is the corresponding angle at the suction side. Knowing the blade angles on the pressure and suction side, the angle  $\beta$  of any other constant  $\zeta$  line may be found from

$$\tan \beta = \tan \beta_p + \zeta (\tan \beta_s - \tan \beta_p) \quad (5.30)$$

What is also shown in figure 5.3 is the mean station, in the middle between the pressure and suction side. All parameters at this location is denoted with an overbar. It is easily seen that this "mean" position occurs at  $\zeta = 1/2$ .

Another parameter simplifying the expressions to be developed is the (local) blade passage width  $S$ . Having axisymmetric stream surfaces it may be written as

$$S = r(\theta_s - \theta_p) \quad (5.31)$$

Further, two additional velocity vectors  $W_\lambda$  and  $W_n$  is defined according to figure 5.4. These are easily related to the meridional and tangential velocities by

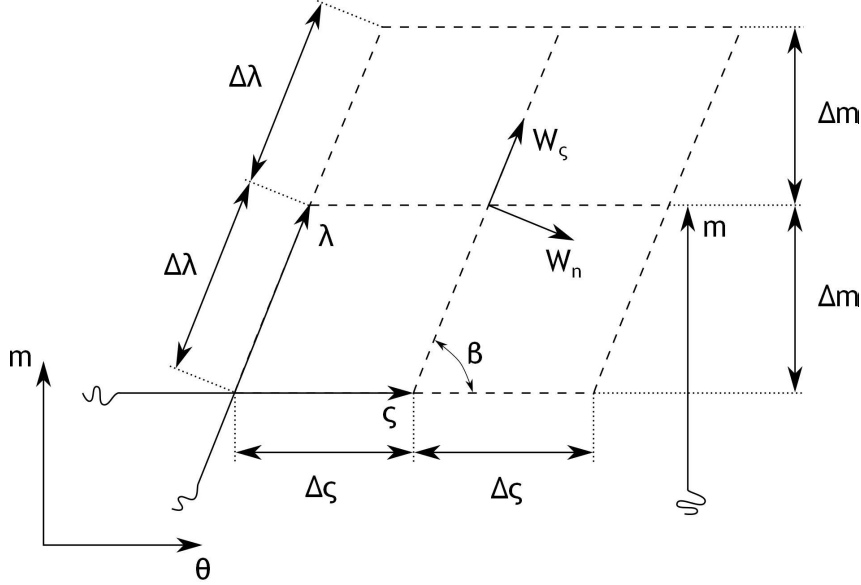


Figure 5.4: A control volume defined in the blade-to-blade plane. Two velocity vectors are defined; one parallel to the  $\lambda$  direction,  $W_\lambda$ , and one normal to the same direction,  $W_n$ . Adapted from Aungier (2000)

$$W_\lambda = W_m \cos \beta + W_\theta \sin \beta \quad (5.32)$$

$$W_n = W_\theta \cos \beta - W_m \sin \beta \quad (5.33)$$

and similarly

$$W_m = W_\lambda \cos \beta - W_n \sin \beta \quad (5.34)$$

$$W_\theta = W_n \cos \beta + W_\lambda \sin \beta \quad (5.35)$$

By taking a simple mass balance of the control volume presented in figure 5.4 one end up with

$$2\Delta m \left( \left( \frac{\rho b W_n}{\cos \beta} \right)_{(\lambda, \zeta - \Delta \zeta)} - \left( \frac{\rho b W_n}{\cos \beta} \right)_{(\lambda, \zeta + \Delta \zeta)} \right) + 2\Delta \zeta \left( (S\rho b W_m)_{(m - \Delta m, \zeta)} - (S\rho b W_m)_{(m + \Delta m, \zeta)} \right) = 0 \quad (5.36)$$

where, again,  $b$  is the stream sheet thickness, perpendicular to the plane shown in figure 5.4. Letting  $\Delta \zeta \rightarrow 0$  and  $\Delta m \rightarrow 0$  a differential equation describing conservation of mass is found. It can be written

$$\frac{\partial}{\partial \zeta} \left( \frac{\rho b W_n}{\cos \beta} \right) + \frac{\partial (S\rho b W_m)}{\partial m} = 0 \quad (5.37)$$

At this point an additional assumption is introduced; the flow remains irrotational throughout the impeller. This may be expressed as

$$\vec{\nabla} \times \vec{C} = \vec{\nabla} \times (\vec{W} + r\omega\vec{e}_\theta) = 0 \quad (5.38)$$

here,  $\vec{e}_\theta$  is a unit vector in the tangential direction. With aid of equation 5.38 Stokes's theorem, see for instance Andersson (2011), may be written

$$\oint_C \vec{W} \cdot d\vec{l} = \int_A (\vec{e}_n \cdot (\vec{\nabla} \times \vec{W})) da = - \int_A (\vec{e}_n \cdot (\vec{\nabla} \times r\omega\vec{e}_\theta)) da \quad (5.39)$$

where subscript  $C$  stands for a closed path, subscript  $A$  the area enclosed by the closed path,  $d\vec{l}$  an incremental length,  $da$  an incremental area and  $\vec{e}_n$  an unit vector in the normal direction. By again using the control volume indicated in figure 5.4, the above equation becomes

$$2\Delta m \left( \left( \frac{W_\lambda}{\cos \beta_{(\lambda, \varsigma + \Delta \varsigma)}} \right) - \left( \frac{W_\lambda}{\cos \beta_{(\lambda, \varsigma - \Delta \varsigma)}} \right) \right) + 2\Delta \varsigma \left( (SW_\theta)_{(m - \Delta m, \varsigma)} - (SW_\theta)_{(m + \Delta m, \varsigma)} \right) = 4\Delta \varsigma \Delta m \frac{S}{r} \frac{\partial r^2 \omega}{\partial r} \quad (5.40)$$

Using the same approach as above, letting  $\Delta m \rightarrow 0$  and  $\Delta \varsigma \rightarrow 0$ , one find

$$\frac{\partial}{\partial \varsigma} \left( \frac{W_\lambda}{\cos \beta} \right) = \frac{\partial SW_\theta}{\partial m} + 2S\omega \sin \alpha_C \quad (5.41)$$

This equation may be integrated, preferably in the  $\varsigma$  direction. By noting that no normal velocity component can exist at the blade surfaces, equation 5.41 becomes upon integration

$$\frac{W_s}{\cos \beta_s} - \frac{W_p}{\cos \beta_p} = \int_p^s \frac{\partial SW_\theta}{\partial m} d\varsigma + 2S\omega \sin \alpha_C \quad (5.42)$$

In order to solve the two-dimensional problem, a stream function  $\Psi$  is defined by

$$\dot{m} \frac{\partial \Psi}{\partial m} = -\rho b (W_\theta - W_m \tan \beta) \quad (5.43)$$

and

$$\dot{m} \frac{\partial \Psi}{\partial \varsigma} = S\rho b W_m \quad (5.44)$$

From these equations, the tangential and meridional velocity components are easily found, and are given by

$$W_m = \frac{\dot{m}}{S\rho b} \frac{\partial \Psi}{\partial \varsigma} \quad (5.45)$$

$$W_\theta = \frac{\dot{m}}{\rho b} \left( \frac{\tan \beta}{S} \frac{\partial \Psi}{\partial \varsigma} - \frac{\partial \Psi}{\partial m} \right) \quad (5.46)$$

In order to find a solution to the stream function Aungier (2000) presents a linearised solution. This method will be adopted here. The stream function is written

$$\Psi = \Psi(m, \varsigma) = a(m) (\varsigma - \varsigma^2) + \varsigma^2 \quad (5.47)$$

here,  $a$  is a parameter only varying in the meridional direction. The derivatives of the stream function in the meridional and  $\varsigma$  direction can thus be written

$$\frac{\partial \Psi}{\partial m} = a' (\varsigma - \varsigma^2) \quad (5.48)$$

$$\frac{\partial \Psi}{\partial \zeta} = a(1 - 2\zeta) + 2\zeta \quad (5.49)$$

where the ' denotes meridional derivatives.

Equation 5.42 requires some additional work. On any blade surface, the velocity can be written

$$W = \frac{W_m}{\cos \beta} = \frac{1}{\cos \beta} \frac{\dot{m}}{S\rho b} \frac{\partial \Psi}{\partial \zeta} \quad (5.50)$$

Inserting the linearised stream function, equation 5.47, into the above expression one obtain

$$\frac{W_p}{\cos \beta_p} = \frac{\dot{m}a}{S\rho b \cos^2 \beta_p} \quad (5.51)$$

$$\frac{W_s}{\cos \beta_s} = \frac{\dot{m}(2-a)}{S\rho b \cos^2 \beta_s} \quad (5.52)$$

at the pressure and suction surface, respectively. The first term on the right hand side of equation 5.42 must also be expressed in a different way by again introducing the stream function. Equations 5.46 and 5.47 can be combined to yield

$$SW_\theta = \frac{\dot{m}}{\rho b} \left( \tan \beta (a - 2a\zeta + 2\zeta) - a'S (\zeta - \zeta^2) \right) \quad (5.53)$$

Two additional variables,  $f$  and  $g$ , are introduced to simplify the soon to be found equations somewhat. They are defined according to

$$f = f(m, \zeta) = \frac{\dot{m} \tan \beta}{\rho b} \quad (5.54)$$

$$g = g(m, \zeta) = \frac{\dot{m}S}{\rho b} \quad (5.55)$$

Therefore, the meridional derivative of equation 5.53 can be expressed as

$$\frac{\partial SW_\theta}{\partial m} = f'(a - 2a\zeta + 2\zeta) + (1 - 2\zeta) f a' - (g a'' + g' a') (\zeta - \zeta^2) \quad (5.56)$$

where '' denotes second order derivatives with respect to the meridional direction. All integrals in the  $\zeta$  direction are approximated with

$$\int_p^s Q(\zeta) d\zeta = \frac{Q_p + 4\bar{Q} + Q_s}{6} \quad (5.57)$$

In this expression  $Q$  represents an arbitrary variable. It is thus emphasized that all parameters need only to be found at three locations; the blade pressure side, the mean location and the blade suction side. This highly simplifies all calculations, since no complicated calculation grid need to be constructed. Using the integral approximation of equation 5.57 in equation 5.56 the following expression arises

$$\int_p^s \frac{\partial SW_\theta}{\partial m} d\zeta = \frac{a f'_p + f_p a' + 4\bar{f}' - \bar{g} a'' - \bar{g}' a' + f'_s (2 - a) - f_s a'}{6} \quad (5.58)$$

A linear differential equation may then be found as a solution to equation 5.42 by using equation 5.51, 5.52 and 5.58. It can be written as

$$a'' + Aa' + Ba = C \quad (5.59)$$

here,  $A$ ,  $B$  and  $C$  are given by

$$A = A(m) = \frac{\bar{g}' - f_p + f_s}{\bar{g}} \quad (5.60)$$

$$B = B(m) = \frac{f'_s - f'_p}{\bar{g}} - \frac{6}{\bar{g}S^2} \left( \frac{g_s}{\cos^2 \beta_s} + \frac{g_p}{\cos^2 \beta_p} \right) \quad (5.61)$$

$$C = C(m) = \frac{12S\omega \sin \alpha_C + 4\bar{f}' + 2f'_s}{\bar{g}} - \frac{12g_s}{\bar{g}S^2 \cos^2 \beta_s} \quad (5.62)$$

This provides a complete solution for the blade-to-blade flow. However, boundary conditions at both leading and trailing edge must be determined. Since inviscid flow is analysed, the tangential momentum in vaneless parts of the flow channel is conserved. This means that the mean tangential momentum is known at the leading edge, therefore also the relative tangential velocity (at a given radius). Letting the average tangential velocity  $\overline{W_{\theta,LE}}$  be approximated by equation 5.57, equation 5.46 yield the following relation

$$6S\overline{W_{\theta,LE}} = f_p a + 4\bar{f}' - \bar{g}a' + f_s(2 - a) \quad (5.63)$$

This equation may be expressed as

$$a' + Ba = C \quad (5.64)$$

$B_1$  and  $C_1$  are easily shown to equal

$$B_1 = \frac{f_s - f_p}{\bar{g}} \quad (5.65)$$

$$C_1 = \frac{4\bar{f}' + 2f'_s - 6S\overline{W_{\theta,LE}}}{\bar{g}} \quad (5.66)$$

Instead turning the attention to the impeller's trailing edge, the Kutta condition (see Anderson (2011)), can be introduced. This condition require the velocities at both suction and pressure side to be equal, hence also the densities. Combining equation 5.51 and 5.52 yields

$$a = \frac{2 \cos \beta_p}{\cos \beta_p + \cos \beta_s} \quad (5.67)$$

Depending on the amount of meridional grid points, multiple equations coupled to each other must be solved simultaneous. Aungier (2000) presents a very novel matrix method to efficiently solve these equations. All meridional derivatives are approximated with three-point-differences, where all meridional points have been evenly distributed within the calculation domain. For interior points (i.e. not on the leading or trailing edge) these can be written

$$Q'_i = \frac{Q_{i+1} - Q_{i-1}}{2\Delta m} \quad (5.68)$$

$$Q''_i = \frac{Q_{i+1} - 2Q_i + Q_{i-1}}{(\Delta m)^2} \quad (5.69)$$

where again  $Q$  represents an arbitrary variable, subscript  $i^1$  a calculation point index and  $\Delta m$  the difference in meridional distance between two adjacent points. For points located at the leading edge (with  $i = 1$ ), the derivatives are instead given by

$$Q'_1 = \frac{4Q_2 - 3Q_1 - Q_3}{2\Delta m} \quad (5.70)$$

---

<sup>1</sup>In this chapter, subscripts  $i$  will in general denote a "current" point. Subscript  $i - 1$  would imply a point before the "current" point, while  $i + 1$  a point ahead of the "current" one, and so forth

$$Q_1'' = \frac{Q_3 - 2Q_2 + Q_1}{(\Delta m)^2} \quad (5.71)$$

Finally, derivatives for points positioned at the trailing edge (with the last point index denoted  $N$ ) are approximated by

$$F_N' = \frac{3F_N - 4F_{N-1} + 2F_{N-2}}{2\Delta m} \quad (5.72)$$

$$F_N'' = \frac{F_N - 2F_{N-1} + F_{N-2}}{(\Delta m)^2} \quad (5.73)$$

Approximating all derivatives with respect to the meridional direction with the above relations, equation 5.59 and it's parameters  $A$ ,  $B$  and  $C$  can be presented in the following matrix form

$$\begin{bmatrix} E_1 & F_1 & H_1 & 0 & 0 & \dots & 0 & 0 & 0 \\ D_2 & E_2 & F_2 & 0 & 0 & \dots & 0 & 0 & 0 \\ 0 & D_3 & E_3 & F_3 & 0 & \dots & 0 & 0 & 0 \\ & & & \vdots & & & & & \\ 0 & 0 & 0 & 0 & \dots & 0 & D_{N-1} & E_{N-1} & F_{N-1} \\ 0 & 0 & 0 & 0 & \dots & 0 & 0 & D_N & E_N \end{bmatrix} \begin{bmatrix} a_1 \\ a_2 \\ a_3 \\ \vdots \\ a_{N-1} \\ a_N \end{bmatrix} = \begin{bmatrix} G_1 \\ G_2 \\ G_3 \\ \vdots \\ G_{N-1} \\ G_N \end{bmatrix} \quad (5.74)$$

At the leading edge the parameters  $E_1$ ,  $F_1$ ,  $H_1$  and  $G_1$  are given by

$$E_1 = 2B_1\Delta m - 3 \quad (5.75)$$

$$F_1 = 4 \quad (5.76)$$

$$H_1 = -1 \quad (5.77)$$

$$G_1 = 2C_1\Delta m \quad (5.78)$$

which follows from the leading edge boundary condition and the approximate numerical derivatives. Similarly, for an interior point  $i$ , the parameters are instead given by

$$D_i = 1 - 0.5A_i\Delta m \quad (5.79)$$

$$E_i = B_i(\Delta m)^2 - 2 \quad (5.80)$$

$$F_i = 1 + 0.5A_i\Delta m \quad (5.81)$$

$$G_i = C_i(\Delta m)^2 \quad (5.82)$$

which again follows from the numerical derivatives, but this time in combination with equation 5.59 and it's parameters.  $A_i$ ,  $B_i$  and  $C_i$  refers to values of equations 5.60, 5.61 and 5.62 at the specific interior point  $i$ . Finally, at the trailing edge  $D_N$ ,  $E_N$  and  $G_N$  are equal to

$$D_N = 0 \quad (5.83)$$

$$E_N = 1 \quad (5.84)$$

$$G_N = \frac{2 \cos \beta_p}{\cos \beta_p + \cos \beta_s} \quad (5.85)$$

This is of course a direct consequence of the trailing edge boundary condition.

To determine the values of all the gridpoint's a:s, a simple matrix inversion may be performed. Since the matrix mainly contain zeros, inversion can be expected to be rather fast.

## 5.2 Calculation procedure

In order to solve the quasi three-dimensional flow the hub-to-shroud flow and blade-to-blade flow equations must be solved together, in a highly iterative manner. The calculations are initiated by assigning reasonable start values to most parameters, not until then a first hub-to-shroud analysis can be conducted. From the found stream surface shapes, blade-to-blade analyses are run at all surfaces, yielding new relative flow angles as input to the next hub-to-shroud analysis. The main iteration procedures for a complete quasi three-dimensional analysis can be seen in figure 5.5.

### 5.2.1 Input parameters

Surprisingly little input are needed to the impeller internal flow analysis, bearing in mind that the geometry has already been determined previously. Of course, all inlet and running conditions have also been specified before, but it usually of huge interest to alter some of the most important parameters. As was the case for the other analyses, the fluid being compressed must be defined. This is again accomplished by specifying a specific gas constant  $R$ , the specific heat at constant pressure  $c_p$  and the ratio of specific heat at constant pressure and volume,  $\gamma$ .

In order to handle non-uniform inlet conditions, the parameters relating to the passage inlet are set at both hub and shroud. Both the inlet stagnation temperature  $T_{00}$  and the stagnation pressure  $p_{00}$  must be set, since these conditions set the overall temperature and pressure level inside the impeller. Further, the inlet angular momentum must be determined at the impeller inlet in order to solve the above presented equations. This is most easily done by specifying the passage inlet absolute flow angle  $\alpha_0$ . The inlet flow angle is typically known when designing an impeller. Also, different operation conditions can be studied including altered inlet angles from, for instance, inlet guide vanes.

Finally, two additional operating conditions must be set; the rotating speed  $N$ , and the target mass flow  $\dot{m}$ . The rotating speed typically has a large impact on the blade loading but are also related to the mass flow passed through the impeller. Again, various operating conditions can be studied by varying  $N$ . The target mass flow is the desired mass flow the impeller is intended to pass. However, the generated geometry may not be able to pass this mass flow, that is, a choked condition has appeared. If a choked flow is encountered, the mass flow may be lowered during the solution, consequently the name *target* mass flow.

### 5.2.2 Calculation model

As is seen in figure 5.5, a complete solution will require quite a lot of calculations. Here, the most important features of these calculations are presented, providing the fundamental aspects of the analyses.

#### Hub-to-shroud flow analysis

In order to begin the first hub-to-shroud calculation initial values need to be assigned, the most important being initial stream surface positions. Aungier (2000) recommends placing the first stream surfaces with equal passage areas at each quasi normal; it is used in this analysis. The placement of these surfaces are possible since the impeller geometry is given, and equally spaced quasi normals (along hub and shroud) are easily set. To obtain more accurate values of the stream surface properties (local surface angles  $\alpha_C$  and curvature  $\kappa$ , for instance) two quasi normals are also placed outside the impeller, both upstream and downstream, see figure



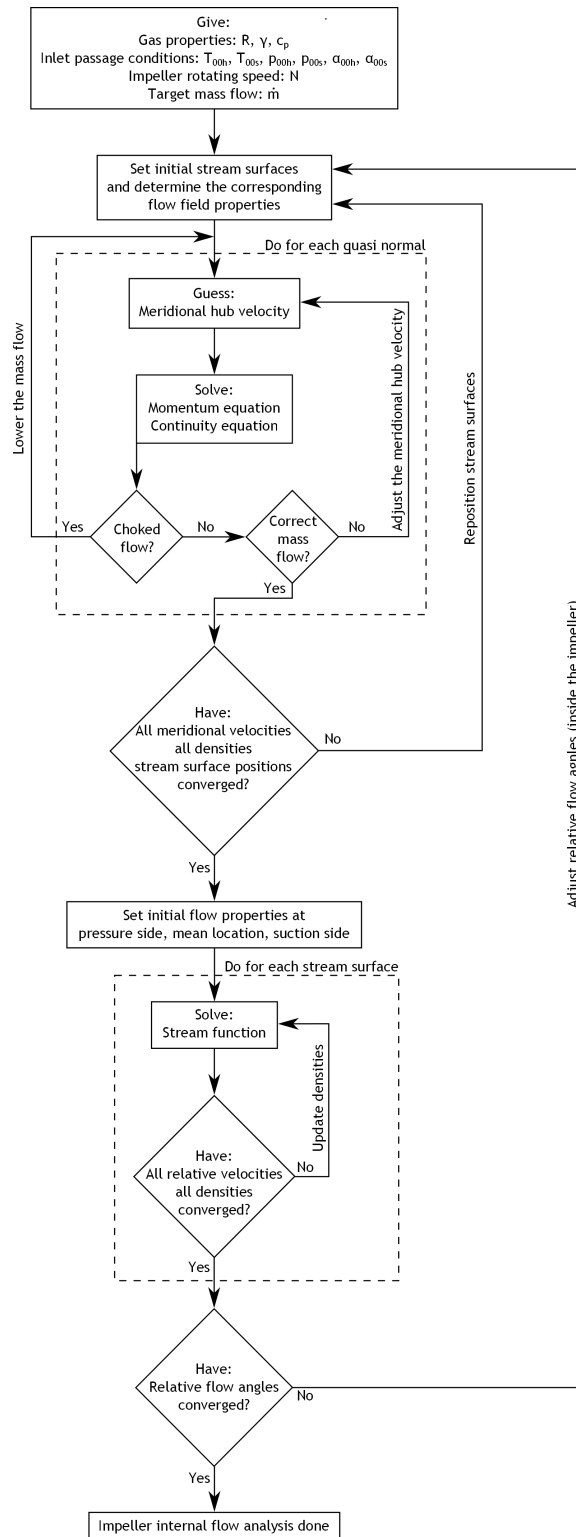


Figure 5.5: The main iteration loops for a complete quasi three-dimensional analysis. Note that several analyses require solution for all quasi normals. These calculations contain themselves iteration loops

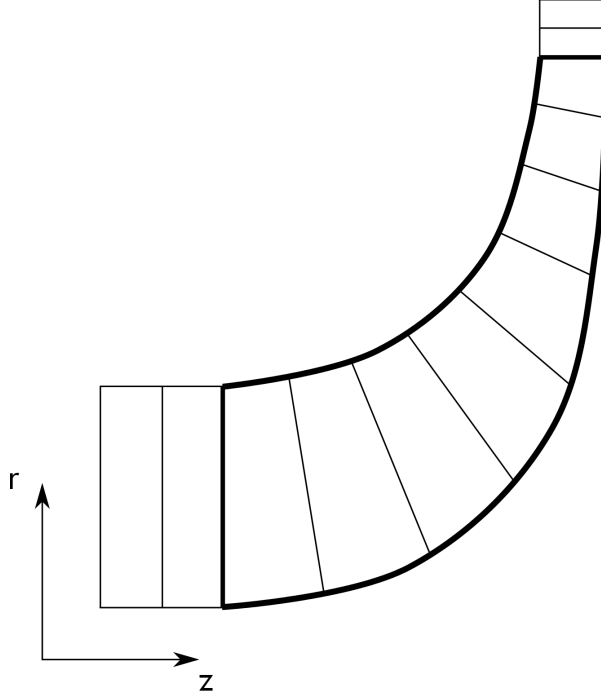


Figure 5.6: Placement of quasi normals in the hub-to-shroud solution. Note that two quasi normals are placed outside the impeller, both upstream and downstream of it. Also, quasi normals are placed at the mean camberline leading and trailing edge

5.6. Another reason for using quasi normals outside the blade passage is that the inlet flow properties are usually not known exactly at the impeller leading edge, but rather at some upstream position of the impeller inlet. As is also seen in this figure, quasi normals are placed at the leading and trailing edge, for the mean camberline of the blades. Having set the quasi normals once, the need not be replaced during any subsequent calculation. Placing the surfaces with equal passage areas may be performed with aid of the procedure outlined in appendix C. By knowing the stream surface locations, not only the axial and radial position at each quasi normal are known, but also the meridional distances. Here, the impeller leading edge quasi normal is defined as the reference point. The meridional distance  $m_i$  for a point  $i$  on a stream surface may be calculated by

$$m_i = m_{i-1} + \sqrt{(z_i - z_{i-1})^2 + (r_i - r_{i-1})^2} \quad (5.86)$$

where index  $i - 1$  represents a point preceding the current one, located on the same stream surface. In a similar manner, the  $\sigma$  coordinate of all surfaces along each quasi normal are easily determined. Since  $\sigma = 0$  at hub, any other  $\sigma$  coordinate (at the same quasi normal) may be found from

$$\sigma = \sqrt{(z_C - z_h)^2 + (r_C - r_h)^2} \quad (5.87)$$

here, index  $C$  denotes stream surface coordinates and  $h$  values at hub.

Having placed the stream surfaces, some properties can be determined instantly. Firstly, the distribution of inlet stagnation properties can be determined. These are given at the passage inlet, i.e. at the first quasi normal. This quasi normal is placed at a specific axial position, and

has thus only a radial extension, see figure 5.6. The inlet properties at an arbitrary stream surface radius  $r_C$  can be determined from

$$T_{00} = T_{00h} + (T_{00s} - T_{00h}) \frac{r_C - r_{0h}}{r_{0s} - r_{0h}} \quad (5.88)$$

$$p_{00} = p_{00h} + (p_{00s} - p_{00h}) \frac{r_C - r_{0h}}{r_{0s} - r_{0h}} \quad (5.89)$$

$$\alpha_{00} = \alpha_{00h} + (\alpha_{00s} - \alpha_{00h}) \frac{r_C - r_{0h}}{r_{0s} - r_{0h}} \quad (5.90)$$

where  $r_{0h}$  and  $r_{0s}$  is the passage inlet hub and shroud radius, respectively. As one note from the above equations, the inlet properties are assumed to vary linearly over the passage width.

Secondly, the stream surface slopes and curvatures can be determined. The slopes are defined by

$$\alpha_C = \frac{\partial r}{\partial m} \quad (5.91)$$

while the curvatures in the meridional direction can be written

$$\kappa_m = -\frac{\partial \alpha_C}{\partial m} \quad (5.92)$$

In order to yield as accurate results as possible, and avoid numerical instabilities, these are defined in a somewhat more rigorous way as compared to the other analyses presented before (see for instance appendix C). Aungier (2003) [20] presents the following numerical approximations to derivatives for interior points (i.e. points not on a calculation grid end point)

$$\left(\frac{\partial Q}{\partial u}\right)_i = \frac{1}{u_{i+1} - u_{i-1}} \left( (Q_i - Q_{i-1}) \frac{u_{i+1} - u_i}{u_i - u_{i-1}} + (Q_{i+1} - Q_i) \frac{u_i - u_{i-1}}{u_{i+1} - u_i} \right) \quad (5.93)$$

where, again,  $Q$  represents an arbitrary variable, and  $u$  is a direction in which  $Q$  varies. Numerical derivatives relating to end points may also be found. For start points (i.e. with  $i = 1$ ) the following relation holds

$$\left(\frac{\partial Q}{\partial u}\right)_1 = \frac{1}{u_3 - u_2} \left( (Q_2 - Q_1) \frac{u_3 - u_1}{u_2 - u_1} - (Q_3 - Q_1) \frac{u_2 - u_1}{u_3 - u_1} \right) \quad (5.94)$$

Similarly, for end points (with  $i = N$ )

$$\left(\frac{\partial Q}{\partial u}\right)_N = \frac{1}{u_{N-1} - u_{N-2}} \left( (Q_N - Q_{N-1}) \frac{u_N - u_{N-2}}{u_N - u_{N-1}} - (Q_N - Q_{N-2}) \frac{u_N - u_{N-1}}{u_N - u_{N-2}} \right) \quad (5.95)$$

These expressions are the more general expressions for three-point numerical derivatives, allowing non-equal differences between points, as compared to the ones employed in section 5.1.2. Aungier (2003) recommends using the more numerically stable two-point difference for end points when determining meridional derivatives. These may be written

$$\left(\frac{\partial Q}{\partial u}\right)_1 = \frac{Q_2 - Q_1}{u_2 - u_1} \quad (5.96)$$

for start points, while

$$\left(\frac{\partial Q}{\partial u}\right)_N = \frac{Q_N - Q_{N-1}}{u_N - u_{N-1}} \quad (5.97)$$

holds for end points.

With these expressions for numerical derivatives, the stream surface slopes and curvatures are easily determined. Further, from the stream surface slopes  $\alpha_C$  and the quasi normal angles  $\alpha_{QN}$ , the local deviation  $\epsilon$  of quasi normals from the normal direction are easily determined by

$$\epsilon = \alpha_C - \alpha_{QN} \quad (5.98)$$

When performing the first calculation of an analysis, the density are of course not known from a prior iteration. Again, the recommendation of Aungier (2000) is used; the static densities are set equal to the local stagnation density. Within the impeller the relative stagnation density are used. In order to determine the relative thermodynamic conditions inside the impeller, the concept of rothalpy comes into use. Since the angular momentum are preserved in the inlet portion, the rothalpy at any leading edge position are easily determined from equation 2.26. From the now known rothalpy (being conserved along each stream surface), the relative stagnation temperature follows from equation 2.28. The relative stagnation pressure is then determined from equation 2.6, where the inlet stagnation properties may be inserted, since the stream surfaces are assumed isentropic. All stagnation properties are not only used to set initial density values, but also to determine the static temperature and pressure when solving the momentum equation.

Another set of parameters not known before a blade-to-blade flow calculation has been conducted are the relative flow angles inside the impeller. Especially in the inlet region, the flow will deviate quite significantly from the local blade angles. In the first 15 % of the impeller passage Aungier (2000) presents the following equation to set as good start values as possible

$$\tan \alpha' = \tan \alpha'_{LE} + (\tan \beta - \tan \alpha'_{LE}) \left( \frac{1}{0.15} \frac{m - m_{LE}}{m_{TE} - m_{LE}} \right)^2 \quad (5.99)$$

where  $\alpha'_{LE}$  are the relative flow angles at leading edge and  $m_{LE}$  and  $m_{TE}$  are the meridional position of the leading and trailing edge, respectively. In the rest of the flow passage, the relative flow angles are set equal to the local blade angles.

In all hub-to-shroud analyses, the parameter  $\rho\Delta A$  need to be determined at all calculation points. However, the parameter  $\Delta A$  cannot be directly related to a stream surface, being infinitesimally thin. To overcome this problem, a rather simple solution may be found. The mean density is calculated *between* two adjacent stream surfaces. The passage area,  $\Delta A$ , of the stream sheet between these surfaces are well defined. Hence, a value of  $\rho\Delta A$  is found at a location in the middle of two stream surfaces. By simple linear interpolation, the value of  $\rho\Delta A$  are found at all stream surfaces.

A general case is shown in figure 5.7. In this figure, an arbitrary quasi normal are shown, with different (known)  $\sigma$  positions of the stream surfaces. The mean positions are denoted  $\bar{\sigma}$  with the subscript  $j$ , where  $\sigma_i > \bar{\sigma}_j$ . A mean radius  $\bar{r}_j$  at  $\bar{\sigma}_j$  may be found from

$$\bar{r}_j = \frac{r_i + r_{i-1}}{2} \quad (5.100)$$

Similarly, the average angle  $\epsilon$  at this middle location are determined by

$$\bar{\epsilon}_j = \frac{\epsilon_i + \epsilon_{i-1}}{2} \quad (5.101)$$

Finally, the blade angle at this location is written

$$\bar{\beta}_j = \frac{\beta_i + \beta_{i-1}}{2} \quad (5.102)$$

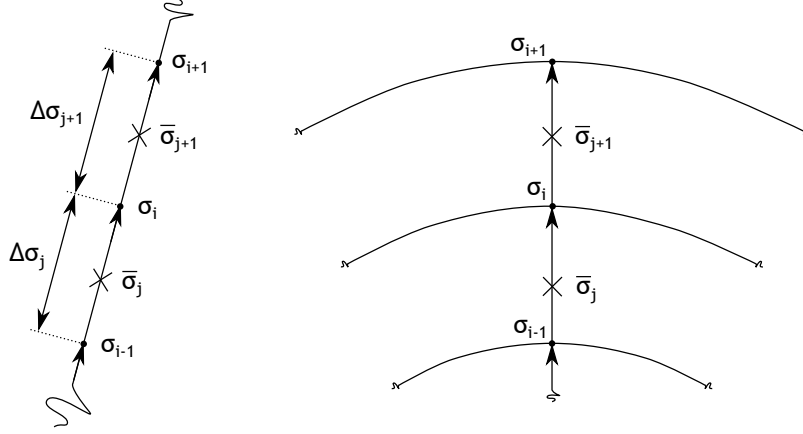


Figure 5.7: A sketch of a set of stream surfaces along a quasi normal, where properties are known at locations in between these surfaces (indicated by crosses). By linear interpolation the properties may be found at the calculation points, here shown as solid dots. Also, a developed quasi normal plane are shown

The approximate local passage area can thus be calculated by

$$\Delta A = \Delta \sigma_j \left( 2\pi \bar{r}_j - \frac{Z_I t_B}{\cos \bar{\beta}_j} \right) \cos \bar{e}_j \quad (5.103)$$

where  $\Delta \sigma_j = \sigma_i - \sigma_{i-1}$ . Following the same procedure as above, the density,  $\bar{\rho}_j$ , at the mean location is determined by

$$\bar{\rho}_j = \frac{\rho_i + \rho_{i-1}}{2} \quad (5.104)$$

Thus, the quantity  $(\bar{\rho} \Delta A)_j$  may be found at all intermediate points. In order to find this parameter at the calculation points, the already mentioned linear interpolation is employed. First, all properties *not* on the hub and shroud must be found. The  $\sigma$  position of the mean points shown in figure 5.7 are easily determined by

$$\bar{\sigma}_j = \frac{\sigma_i + \sigma_{i-1}}{2} \quad (5.105)$$

and

$$\bar{\sigma}_{j+1} = \frac{\sigma_{i+1} + \sigma_i}{2} \quad (5.106)$$

$\rho \Delta A$  at point  $i$  can finally be expressed as

$$\begin{aligned} (\rho \Delta A)_i &= (\bar{\rho} \Delta A)_j + \left( (\bar{\rho} \Delta A)_{j+1} - (\bar{\rho} \Delta A)_j \right) \frac{\sigma_i - \bar{\sigma}_j}{\bar{\sigma}_{j+1} - \bar{\sigma}_j} \\ &= (\bar{\rho} \Delta A)_j + \left( (\bar{\rho} \Delta A)_{j+1} - (\bar{\rho} \Delta A)_j \right) \frac{\sigma_i - \sigma_{i-1}}{\sigma_{i+1} - \sigma_{i-1}} \end{aligned} \quad (5.107)$$

where equations 5.105 and 5.106 have been used to simplify the expression. Note that even though  $\rho \Delta A$  do not have a direct meaning at a single point, it do refer to the meridional velocity as was shown in section 5.1.1. The meridional velocity is easier and more straight forward to understand as a single point property. For the hub and shroud surface the value

of  $\rho\Delta A$  can now be found,  $(\rho\Delta A)_j$  being a mean value of the same parameter of the surface at and closest to the contour.

All derivatives in the momentum equations with respect to the  $\sigma$  direction are determined with equations 5.93, 5.94 and 5.95. As has already been mentioned, meridional derivatives uses equation 5.93 for interior points, but the simpler two-point difference for start and end points, equations 5.96 and 5.97 respectively.

In order to solve the momentum equation, integrals must also be determined numerically. Again Aungier (2003) lists useful expressions to approximate these. To obtain an as high accuracy as possible, the second order derivative for interior must also be incorporated. It can be written

$$\left(\frac{\partial^2 Q}{\partial u^2}\right)_i = \frac{2}{u_{i+1} - u_{i-1}} \left( \frac{Q_{i+1} - Q_i}{u_{i+1} - u_i} - \frac{Q_i - Q_{i-1}}{u_i - u_{i-1}} \right) \quad (5.108)$$

were again  $Q$  represents an arbitrary parameter and  $u$  some direction in which the derivative is to be found. For interior points the integral can be expressed as

$$\int_{u_{i-1}}^{u_i} Q du = (u_i - u_{i-1}) \left( Q(u_i) - \left(\frac{\partial Q}{\partial u}\right)_i \frac{u_i - u_{i-1}}{2} + \left(\frac{\partial^2 Q}{\partial u^2}\right)_i \frac{(u_i - u_{i-1})^2}{6} \right) \quad (5.109)$$

while for last points it is instead given by

$$\int_{u_{N-1}}^{u_N} Q du = (u_N - u_{N-1}) \left( Q(u_{N-1}) - \left(\frac{\partial Q}{\partial u}\right)_{N-1} \frac{u_N - u_{N-1}}{2} + \left(\frac{\partial^2 Q}{\partial u^2}\right)_{N-1} \frac{(u_N - u_{N-1})^2}{6} \right) \quad (5.110)$$

Note that no numerical integral need to be found for the first point, since the integration always starts from hub. Thus, the integral becomes zeros for all hub points.

When solving the momentum and continuity equation, it is possible to encounter choked flow. If not any special measures are taken to cope with such a condition, it is quite likely that the whole solution will fail to converge. Thus, the hub-to-shroud analysis must be able to identify such a condition. Mathematically a choke can be written

$$\frac{\partial \dot{m}}{\partial W_m(0)} \leq 0 \quad (5.111)$$

The interpretation of this expression is that the mass flow does not increase when increasing the meridional velocity at hub. If this situation occurs, the mass flow must be lowered in order to yield a solution. The easiest way of accomplish this is to simply calculate the maximum mass flow the choking quasi normal can pass, and set the new target mass flow to this. Not only are the whole hub-to-shroud solution based on this lowered mass flow, but also the following blade-to-blade flow analyses. However, after rearranging stream surfaces and finding new relative flow angles, the impeller may actually be able to pass the desired mass flow. Hence, if a choke has appeared, the mass flow should be set to the desired one after completing the blade-to-blade flow analysis and entering a "new" hub-to-shroud analysis. Further, it is understood that as soon as a choked flow condition has appeared, all upstream quasi normals must be recomputed, since down stream quasi normal solutions depend on the upstream dittos.

The overall solution procedure for all quasi normals in a hub-to-shroud analysis are shown in figure 5.8. In this figure it is shown that some parameters downstream of one quasi normal can and must be determined as a consequence of it's solution. One example is the last impeller quasi normal. After solving the momentum and continuity equation here, the absolute tangential velocity can be determined. Therefore, the absolute angular momentum is also known. Since

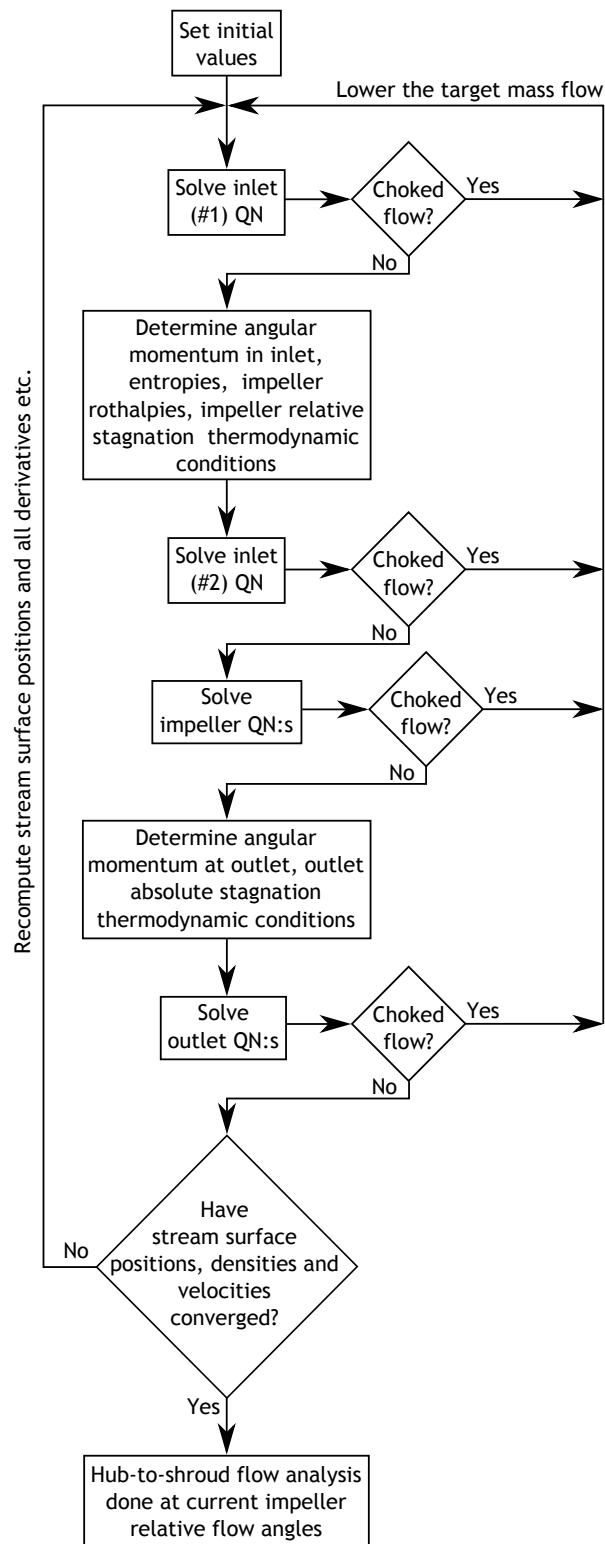


Figure 5.8: The solution procedure of all quasi normals, and the intermediate calculations. Note that if a choke occurs, all upstream quasi normals need recalculation

the angular momentum is conserved along each stream surface in vaneless passages, all absolute (and relative) tangential velocities can be determined in the vaneless outlet passage, downstream of the last impeller quasi normal. The tangential velocity must be known when solving the momentum equation for vaneless passages.

When the momentum and continuity equation have been solved at all quasi normals, new stream surface positions must be determined. This is accomplished at all quasi normals, making use of the  $\sigma$  coordinate. First, the mass flow per stream sheet thickness,  $m_b$ , is determined for each stream sheet by

$$m_{b,j} = \frac{\Delta \dot{m}_j}{\Delta \sigma_j} \quad (5.112)$$

where subscript  $j$  denotes the stream sheet in question,  $\Delta \dot{m}$  the mass flow in the stream sheet and  $\Delta \sigma$  the stream sheet thickness as measured in the quasi normal direction. The stream sheet thickness  $\Delta \sigma_{j,eq}$  needed to pass an equal amount of mass flow in *all* stream sheets can then be determined by

$$\Delta \sigma_{j,eq} = \frac{\dot{m}}{m_{b,j} (K_{ss} - 1)} \quad (5.113)$$

here  $K_{ss}$  represents the total number of stream surfaces employed in the analysis. After determining  $\Delta \sigma_{j,eq}$  for all stream sheets, the new stream surface positions can be determined by

$$\sigma_i = \sigma_{i-1} + \Delta \sigma_{j,eq} \frac{\sigma_s}{\sum_{j=1}^{K_{ss}-1} \Delta \sigma_{j,eq}} \quad (5.114)$$

where subscript  $i$  denotes the "current" stream surface. Of course, stream surfaces at hub and shroud will not alter during iterations. In order to reduce the possibility of too large changes in stream surface positions (especially during early iterations) some numerical damping must be employed. Aungier (2000) describe two different damping factors, depending on whether blades are present or not. For stream surfaces in vaneless parts of the passage, the damping factor  $F_{ss}$  is written

$$F_{ss} = \left( 1 + \frac{(1 - M_m^2) (\sigma_s - \sigma_h)^2}{(\Delta m_{min})^2 B_{ss}} \right)^{-1} \quad (5.115)$$

$\Delta m_{min}$  is the minimum meridional distance of the current quasi normal with one of the two adjacent quasi normals,  $B_{ss}$  is an empirical constant and  $M_m$  is the meridional Mach number defined as

$$M_m = \frac{W_m}{\sqrt{\gamma RT}} \quad (5.116)$$

For passages with blades, the damping factor instead takes the form of

$$F_{ss} = \left( 1 + \frac{(1 - M') (\cos \alpha' (\sigma_s - \sigma_h))^2}{(\Delta m_{min})^2 B_{ss}} \right)^{-1} \quad (5.117)$$

where  $M'$  is the relative Mach number defined as

$$M' = \frac{W}{\sqrt{\gamma RT}} \quad (5.118)$$

Thus, instead of directly moving the stream surfaces to the newly calculated position, they are moved a fraction  $F_{ss}$  of the distance.

The hub-to-shroud analysis has converged when the stream surfaces no longer need repositioning. It is also good practice to make sure that both velocities and densities have converged and thus no longer change between iterations.



## Blade-to-blade flow analysis

Having finished the hub-to-shroud flow analysis, a blade-to-blade flow analysis is to be carried out on the determined stream surfaces. Thus no new geometry need to be determined when carrying out the blade-to-blade analysis. However, interpolations will be necessary to find corresponding values on the calculation points of the stream surfaces, since the two analysis will not use the same calculation spacing. As has already been mentioned above, equal meridional distances of the discrete points is necessary if the method of section 5.1.2 is to be used.

The calculation domain of the blade-to-blade flow analysis is of course within the blade passage. Aungier (2000) notes, however, that placing the end points of the calculation grid at the exact leading and trailing edge can cause numerical problems. In order to avoid such problems, the first  $\zeta$  line (closest to the leading edge) is placed at the largest meridional position of the pressure and suction side, without any leading edge extension. This is illustrated in figure 5.9. Another advantage of this method is that no special leading edge extension must

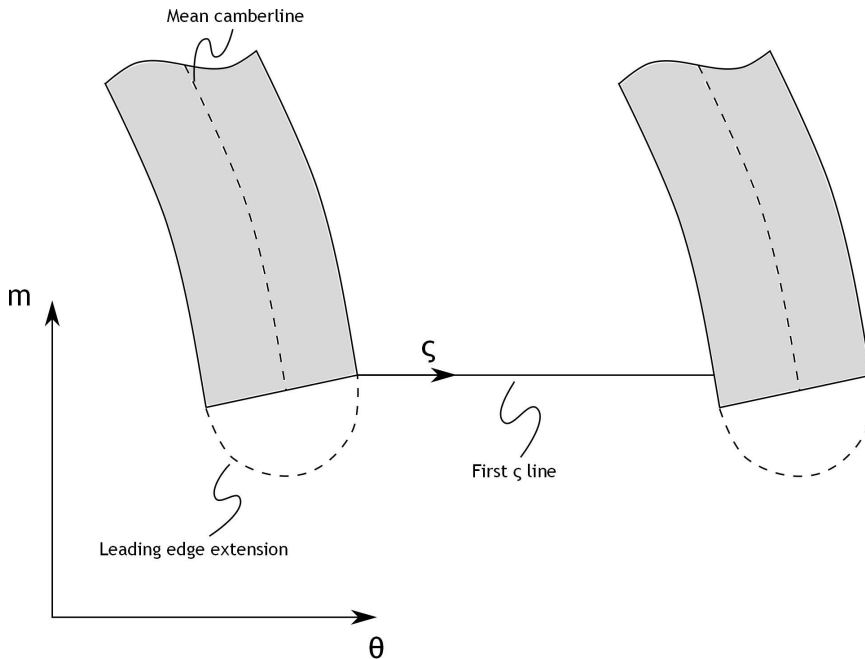


Figure 5.9: The solution domain of the leading edge region. Note that the blade surface of the largest meridional position determines where the first  $\zeta$  line is placed

be created, enabling use of only the actual pressure and suction side surface. The exact same procedure holds for the trailing edge, with the obvious difference of which surface determine the end of the calculation domain; the blade surface with it's endpoint located at the smallest meridional position sets the location of the last  $\zeta$  line.

Knowing the actual domain of the calculation, the geometry from the hub-to-shroud analysis can be transferred to the blade-to-blade analysis. The first thing to do is finding  $x,y$  and  $z$  coordinates where the stream surfaces connects with the blade surfaces. Knowing these coordinates enables determination of all other geometrical properties needed for the analysis. How these coordinates are found is presented in appendix D. Of course, the coordinates must be found for both the pressure and suction side.

Having expressed the stream surfaces in all three coordinates (at the blade surfaces), calculation points of equal meridional distances must be found. Expressed in another way; the coordinates at these locations must be found. A rather simple procedure is employed. The coordinates are linearly interpolated along each stream surface, with equal meridional spacing. Thus, the  $x$ ,  $y$  and  $z$  coordinate are known at each point of interest. Additionally, the blade angles are also found by linear interpolation. However, one extra feature of the blade angles at the surfaces must be kept in mind. If an inlet blade taper is used, the blade surface angle at this location will differ from the blade's mean camberline angle. Such a situation is illustrated in figure 5.10. As one notice, the blade angle of the suction surface is smaller than the mean

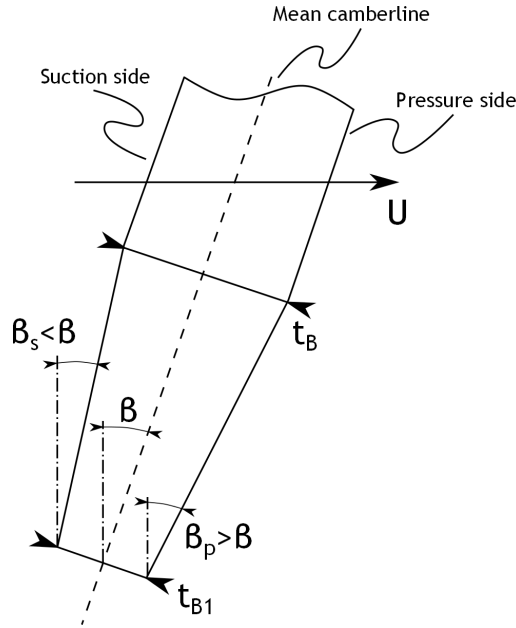


Figure 5.10: The features of a tapered leading edge. The blade surface angles on the suction side will be lower than the mean camberline blade angle. The opposite is true for the pressure side

camberline blade angle. On the pressure side, the angle is instead larger. The blade angles in this inlet taper region can, with aid of figure 5.10 be expressed as

$$\beta_s = \beta - \arctan\left(\frac{t_B - t_{B1}}{2\lambda_{taper}}\right) \quad (5.119)$$

and

$$\beta_p = \beta + \arctan\left(\frac{t_B - t_{B1}}{2\lambda_{taper}}\right) \quad (5.120)$$

where  $\lambda_{taper}$  denotes the mean camberline length of the inlet taper.

Since all Cartesian blade surface coordinates now are known at the calculation points of the blade-to-blade flow analysis, the tangential coordinates of the blade surfaces can be determined from

$$\theta_{bs} = \arcsin\frac{x_{bs}}{r_{bs}} \quad (5.121)$$

from which the local passage width can be calculated by equation 5.31.

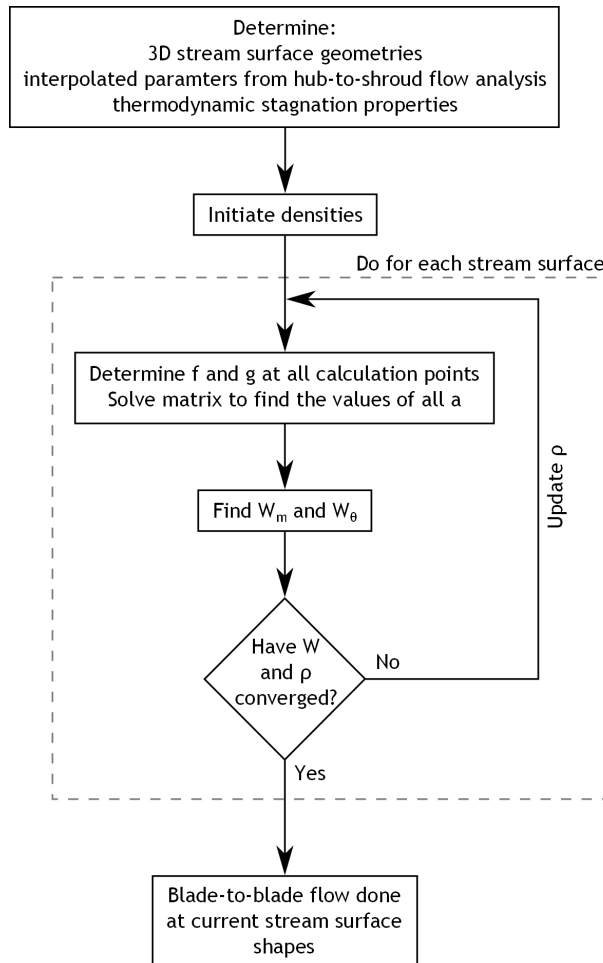


Figure 5.11: The blade-to-blade flow iteration in detail. One can observe that the densities lag the relative velocities by one iteration

In order to solve the blade-to-blade flow governing equations, the property  $\dot{m}/b$  must be determined from the hub-to-shroud analysis. As was the case for the property  $\rho\Delta A$  in the above hub-to-shroud flow section, it cannot be directly connected to stream surfaces being infinitesimally thin. However, the exact same interpolation procedure as for  $\rho\Delta A$  is employed, and need no further explanation. Again, linear interpolation along each stream surface is necessary to find the value of  $\dot{m}/b$  at the points used by the blade-to-blade flow analysis.

One final set of parameters must also be determined; the stagnation properties at each calculation point. Relative stagnation temperatures are easily determined from equation 2.28, using the fact that the rothalpy of the impeller stream surfaces are known. The relative stagnation pressures can in turn be found from equation 2.6, applicable along any stream surface since the entropy remains unchanged along these.

Since all geometric and other, during the blade-to-blade flow analysis, constant parameters now are known, the flow analysis itself can begin. As was seen in figure 5.5, one must resort to an iterative solution in order to find the relative velocities. The different steps of the blade-to-blade flow analysis is shown in greater detail in figure 5.11. A first guess of the static densities is necessary to start the computation. Again, the static density is approximated

with the relative stagnation density yielding quite reasonable start values. The solution of the blade-to-blade flow must be carried out on each stream surface, one at a time. Thus for the current stream surface, values of  $f$  and  $g$  are found from equations 5.54 and 5.55. Further, the derivatives of  $f$  and  $g$  in the meridional direction are calculated with equations 5.68, 5.70 and 5.72. Knowing these parameters, solving the matrix 5.74 is straight forward. Finally, having the values of all  $a$ :s, the relative meridional and tangential velocity follows from equations 5.45 and 5.46. With these velocity components a static temperature can be computed, from which new densities can be found. Consequently, the iterative solution continue until both the relative velocities and static densities no longer change. The blade-to-blade flow analysis is finished when the velocities in all stream surfaces have been found.

In order to use the result from the blade-to-blade flow analysis in the hub-to-shroud flow analysis, new relative flow angles within the impeller must be found, before starting the next hub-to-shroud calculation. These are found from the relative meridional and tangential velocities. Mass averaged velocities are used, with values from the pressure side, passage mean location and the suction side. The mass averaged meridional velocity  $\tilde{W}_m$  can be expressed as

$$\tilde{W}_m = \frac{\int_0^1 \rho b W_m^2 d\zeta}{\int_0^1 \rho b W_m d\zeta} \quad (5.122)$$

while the mass averaged tangential velocity  $\tilde{W}_\theta$  takes the form of

$$\tilde{W}_\theta = \frac{\int_0^1 \rho b W_m W_\theta d\zeta}{\int_0^1 \rho b W_m d\zeta} \quad (5.123)$$

These integrals are approximated with equation 5.57, using values at all three locations. One can note that the stream sheet thickness  $b$  is constant for one and the same stream sheet (at a certain point) and can therefore be dropped in the two above equations. The relative flow angle is finally given by

$$\tan \alpha' = \frac{\tilde{W}_\theta}{\tilde{W}_m} \quad (5.124)$$

Since the blade-to-blade flow analysis use different spacing between the calculation points as compared to the hub-to-shroud analysis, meridional interpolations along each stream surface are necessary when transferring the relative flow angles to the hub-to-shroud analysis. The whole quasi three-dimensional analysis is continued until these relative flow angles have converged at all positions within the impeller.

# Chapter 6

## Vaneless diffuser design

Having sized an impeller for a given duty, the next component of prime importance is the diffuser. This section focuses on the vaneless diffuser, a rather common diffuser in radial compressor stages. One reason for its popularity is, of course, the cost advantage due to its mechanical simplicity.

Because of the absence of blades and rotating parts within the flow path, it is easily believed that the vaneless diffuser is a simple component to model, and all flow phenomena associated with it is well understood. However, this is not the case. The flow field downstream of the impeller is extremely complicated and thus very hard to model accurately. Not only is the flow to a large extent heavily distorted, it is also unsteady. This is a fact many authors have recognized, see for instance Japikse (1996) and Cumpsty (2004).

This chapter is disposed similarly to the impeller modelling chapters. First, the basic flow physics and relations are described, then the geometrical description of the hub and shroud contours follow. Further, how the different equations are solved is showed in the last section.

### 6.1 Basic relations

In the analysis of vaneless diffusers, a one-dimensional approach is followed. The simplest way of modelling a vaneless diffuser is by assuming the tangential momentum is conserved, and hence the tangential velocity would vary inversely with radius according to

$$rC_\theta = \text{const.} \quad (6.1)$$

Such an assumption implies negligible wall friction and is a rather crude assumption. To improve the modelling in this analysis, wall friction effects are included by specifying a wall friction coefficient by

$$C_f = \frac{\tau_w}{\rho \frac{C^2}{2}} \quad (6.2)$$

where  $\tau_w$  is the wall friction shear stress. Most of the following relationships are based on the force balance of a fluid element in an arbitrary annulus flow path, as presented by Stanitz (1952). A section of a vaneless flow passage is shown in figure 6.1. In turn, a fluid element in such a passage is shown in figure 6.2. This figure shows the fluid element in relation to three different planes. To the right is the fluid element depicted as one would see it when looking in the axial direction. In the middle is shown how the fluid element is inclined with the local streamline slope  $\alpha_C$ . Finally, to the left is the element's actual side shown in the mean stream surface plane.

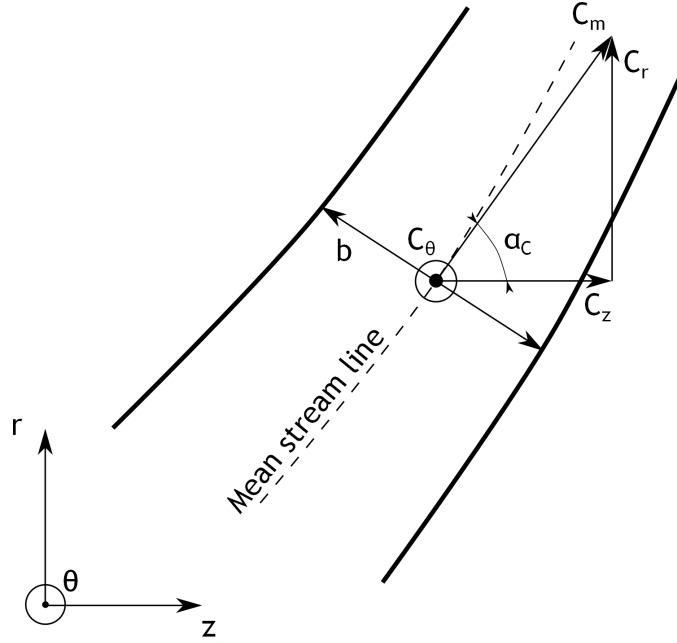


Figure 6.1: An arbitrary section of a vaneless flow passage. All velocity components are shown along with the local passage width  $b$ . Note the mean stream line slope  $\alpha_c$  at the point of interest. Adopted from Stanitz (1952)

When deriving relations for compressible flow inside passages, the Mach number  $M$  is a parameter easing the process. It is defined in equation 2.7, repeated below for convenience.

$$M^2 = \frac{C^2}{\gamma RT} \quad (6.3)$$

By taking the derivative of the Mach number with respect to the radius  $r$ , one obtain

$$\frac{1}{M^2} \frac{dM^2}{dr} = \frac{1}{C^2} \frac{dC^2}{dr} - \frac{1}{T} \frac{dT}{dr} \quad (6.4)$$

by regarding both the ratio of specific heats,  $\gamma$ , and the specific gas constant,  $R$ , constant. As was described in chapter 2, the stagnation temperature is related to the velocity by equation 2.5. With aid of equation 2.8 it can instead be written

$$T_0 = T \left( 1 + \frac{\gamma - 1}{2} M^2 \right) \quad (6.5)$$

and taking the derivative, again with respect to the radius, yields

$$\frac{1}{T_0} \frac{dT_0}{dr} = \frac{1}{T} \frac{dT}{dr} + \left( \frac{\frac{\gamma - 1}{2} M^2}{1 + \frac{\gamma - 1}{2} M^2} \right) \frac{1}{M^2} \frac{dM^2}{dr} \quad (6.6)$$

By combining equation 6.4 and equation 6.6, the resultant relation becomes

$$\frac{1}{C^2} \frac{dC^2}{dr} = \left( \frac{1}{1 + \frac{\gamma - 1}{2} M^2} \right) \frac{1}{M^2} \frac{dM^2}{dr} + \frac{1}{T_0} \frac{dT_0}{dr} \quad (6.7)$$

In plane of mean stream surface

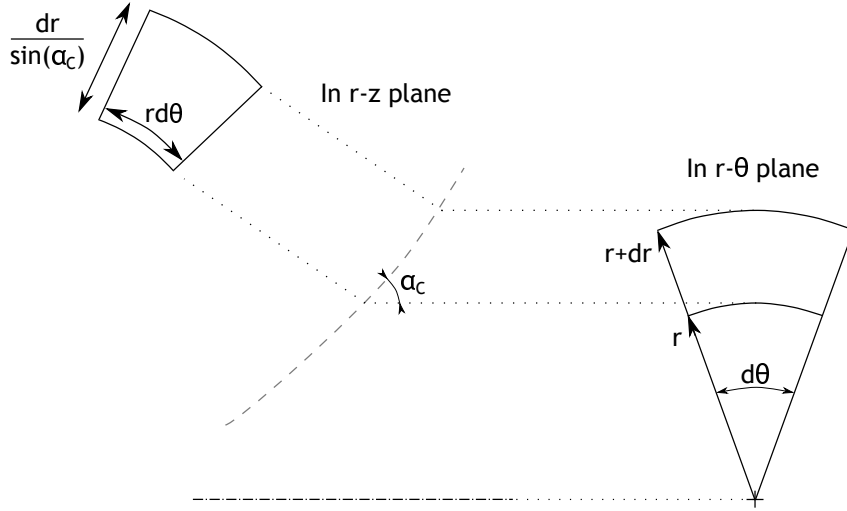


Figure 6.2: An incremental fluid element in a vaneless annular flow passage. Three different views of the element are shown; one simply in the  $r - \theta$  plane, one in the  $r - z$  plane and finally one in the plane of the mean stream surface. Adopted from Stanitz (1952)

This equation couples the change in velocity  $C$  with both the change in Mach number  $M$  and stagnation temperature  $T_0$  along the radius  $r$ . Next, the mass continuity is considered. It can be expressed as

$$\dot{m} = \rho C_m 2\pi r b = \text{const.} \quad (6.8)$$

or equally

$$\rho C_m r b = \text{const.} \quad (6.9)$$

the meridional velocity  $C_m$  being the velocity component responsible for the mass transportation in and out of the diffuser. Differentiating this equation with respect to the radius yields

$$\begin{aligned} \frac{1}{\rho} \frac{d\rho}{dr} + \frac{1}{C_m} \frac{dC_m}{dr} + \frac{1}{b} \frac{db}{dr} + \frac{1}{r} \\ = \frac{1}{\rho} \frac{d\rho}{dr} + \frac{1}{C \cos \alpha} \frac{d(C \cos \alpha)}{dr} + \frac{1}{b} \frac{db}{dr} + \frac{1}{r} = 0 \end{aligned} \quad (6.10)$$

This equation instead relate the change in meridional velocity  $C_m$  to the change in density  $\rho$  and passage width  $b$  along the radius  $r$ . An additional relation is obtained by differentiating the ideal gas law, equation 2.1, and dividing the result with the same equation. This give rise to the following equation relating the change in pressure to differences in density and temperature along the radial direction

$$\frac{1}{p} \frac{dp}{dr} = \frac{1}{\rho} \frac{d\rho}{dr} + \frac{1}{T} \frac{dT}{dr} \quad (6.11)$$

Two additional equations can be found when analysing the force balance of a fluid element, and the derivation of these relations are outlined in appendix E. From equation E.10, the force equilibrium equation in the meridional direction is

$$\frac{1}{\rho} \frac{dp}{dr} + C_f \frac{C^2 \cos \alpha}{b \sin \alpha_C} = \frac{(C \sin \alpha)^2}{r} - C \cos \alpha \frac{d(C \cos \alpha)}{dr} \quad (6.12)$$

while the corresponding equation in the tangential direction, equation E.15, reads

$$-C_f \frac{C^2 \sin \alpha}{b \sin \alpha_C} = C \cos \alpha \frac{dC \sin \alpha}{dr} + C \cos \alpha \frac{C \sin \alpha}{r} \quad (6.13)$$

All governing equations are now known, and they must be combined to yield a set of ordinary differential equations. By combining the meridional and tangential equilibrium equations, one obtain

$$\begin{aligned} \frac{1}{\rho} \frac{dp}{dr} &= -C_f \frac{C^2 \cos \alpha}{b \sin \alpha_C} - C_f \frac{C^2 \sin^2 \alpha}{b \sin \alpha_C} \frac{1}{\cos \alpha} \\ &\quad - C \sin \alpha \frac{d(C \sin \alpha)}{dr} - C \cos \alpha \frac{d(C \cos \alpha)}{dr} \\ &= -C_f \frac{C^2}{b \sin \alpha_C} \frac{1}{\cos \alpha} - \frac{1}{2} \frac{dC^2}{dr} \end{aligned} \quad (6.14)$$

This equation is rearranged into

$$\frac{1}{\rho C^2} \frac{dp}{dr} = \frac{C_f \sec \alpha}{b \sin \alpha_C} - \frac{1}{2C^2} \frac{dC^2}{dr} \quad (6.15)$$

However, the quantity  $\rho C^2$  can be expressed as a function of the Mach number by employing the ideal gas law, equation 2.1, and the definition of the Mach number, equation 6.3. Hence

$$\rho C^2 = \frac{\gamma \rho C^2}{\gamma} = \frac{\gamma p C^2}{\gamma R T} = \gamma p M^2 \quad (6.16)$$

Upon combining equation 6.7, 6.15 and 6.16 the following relation is found

$$\frac{1}{p} \frac{dp}{dr} = -\frac{\gamma M^2}{2} \left( \left( \frac{1}{1 + \frac{\gamma-1}{2} M^2} \right) \frac{1}{M^2} \frac{dM^2}{dr} + \frac{2C_f \sec \alpha}{b \sin \alpha_C} \right) \quad (6.17)$$

when assuming the diffuser is adiabatic, that is  $dT_0/dr = 0$ . From here on the final equations will use non-dimensionalized quantities. The pressure is non-dimensionalized with the compressor inlet stagnation pressure, while the passage width  $b$  and radius  $r$  is normalized with the impeller tip width and radius, respectively. Thus

$$P_D = \frac{p}{p_{00}} \quad (6.18)$$

$$B_D = \frac{b}{b_2} \quad (6.19)$$

$$R_D = \frac{r}{r_2} \quad (6.20)$$

Introducing these variables, equation 6.17 takes the form of

$$\frac{1}{P_D} \frac{dP_D}{dR_D} = -\frac{\gamma M^2}{2} \left( \left( \frac{1}{1 + \frac{\gamma-1}{2} M^2} \right) \frac{1}{M^2} \frac{dM^2}{dR_D} + \frac{2C_f \sec \alpha}{B_D \sin \alpha_C} \frac{r_2}{b_2} \right) \quad (6.21)$$

This is an auxiliary equation needed in subsequent calculations. One of the final ordinary differential equations is the squared Mach number  $M^2$  related to the non dimensional radius  $R_D$ . This is determined from the differentiated continuity equation, but first some of the terms



in this relation need to be determined. Inserting equation 6.16 in the meridional equilibrium equation one obtain

$$\frac{1}{C \cos \alpha} \frac{d(C \cos \alpha)}{dr} = \frac{\tan^2 \alpha}{r} - \frac{\sec^2 \alpha}{\gamma M^2} \frac{1}{p} \frac{dp}{dr} - \frac{C_f \sec \alpha}{b \sin \alpha_C} \quad (6.22)$$

In the same manner, inserting equation 6.7 into the differentiated ideal gas law, equation 6.11, yields

$$\frac{1}{\rho} \frac{d\rho}{dr} = \frac{1}{p} \frac{dp}{dr} + \left( \frac{\frac{\gamma-1}{2} M^2}{1 + \frac{\gamma-1}{2} M^2} \right) \frac{1}{M^2} \frac{dM^2}{dr} \quad (6.23)$$

after, again, assuming the diffuser is adiabatic. Combining equation 6.10, 6.22 and 6.23 while introducing the non-dimensional parameters presented above gives

$$\frac{1}{P_D} \frac{dP_D}{dR_D} = -\frac{\gamma M^2}{\gamma M^2 - \sec^2 \alpha} \left( \left( \frac{\frac{\gamma-1}{2} M^2}{1 + \frac{\gamma-1}{2} M^2} \right) \frac{1}{M^2} \frac{dM^2}{dR_D} - \frac{C_f \sec \alpha}{B_D \sin \alpha_C} \frac{r_2}{b_2} + \frac{1}{B_D} \frac{dB_D}{dR_D} + \frac{\sec^2 \alpha}{R_D} \right) \quad (6.24)$$

Finally, the term  $1/P_D \cdot dP_D/dR_D$  can be eliminated by inserting equation 6.21 into the above expression. The squared Mach number at any radius  $R_D$  is then determined by

$$\frac{1}{M^2} \frac{dM^2}{dR_D} = -\frac{2 \left( 1 + \frac{\gamma-1}{2} M^2 \right)}{M^2 - \sec^2 \alpha} \left( \left( \gamma M^2 - \tan^2 \alpha \right) \frac{C_f \sec \alpha}{B_D \sin \alpha_C} \frac{r_2}{b_2} - \frac{1}{B_D} \frac{dB_D}{dR_D} - \frac{\sec^2 \alpha}{R_D} \right) \quad (6.25)$$

Another of the final ordinary differential equations is the relation determining the flow angle  $\alpha$  at any non-dimensional radius  $R_D$ . As was the case for the squared Mach number, a few algebraic manipulations need to be conducted first. To begin, the relation

$$\tan \alpha = \frac{C_\theta}{C_m} \quad (6.26)$$

is differentiated and divided by itself to yield

$$\frac{1}{\tan \alpha} \frac{d \tan \alpha}{dr} = \frac{1}{C_\theta} \frac{dC_\theta}{dr} - \frac{1}{C_m} \frac{dC_m}{dr} \quad (6.27)$$

By inserting equation 6.13 and 6.22 into the above relation, including the non-dimensional parameters  $P_D$ ,  $B_D$  and  $R_D$ , the result is

$$\frac{1}{\tan \alpha} \frac{d \tan \alpha}{dR_D} = \frac{\sec^2 \alpha}{\gamma M^2} \frac{1}{P_D} \frac{dP_D}{dR_D} - \frac{\sec^2 \alpha}{R_D} \quad (6.28)$$

Finally, the flow angle can be determined by combining the auxiliary equation 6.21, the expression for the squared Mach number, equation 6.25, and equation 6.28. The final expression is given by

$$\frac{1}{\tan \alpha} \frac{d \tan \alpha}{dR_D} = \frac{\sec^2 \alpha}{M^2 - \sec^2 \alpha} \left( \left( 1 + (\gamma - 1) M^2 \right) \frac{C_f \sec \alpha}{B_D \sin \alpha_C} \frac{r_2}{b_2} - \frac{1}{B_D} \frac{dB_D}{dR_D} - \frac{M^2}{R_D} \right) \quad (6.29)$$

Thereby, solving equation 6.25 and 6.29 simultaneous will determine the whole flow field in the vaneless diffuser. It is also of interest to determine the pressure at any non-dimensional radius  $R_D$  from the impeller discharge conditions, and this is a rather straight forward task.

Combining the continuity equation 6.9, the ideal gas law, equation 2.1, and the definition of the Mach number, relation 6.3, one obtain

$$\frac{p_2}{\sqrt{T_2}} M_2 \cos \alpha_2 r_2 b_2 = \frac{p}{\sqrt{T}} M \cos \alpha r b \quad (6.30)$$

and by inserting equation 6.5 together with the non-dimensional parameters  $P_D$ ,  $B_D$  and  $R_D$  into the above relation, the pressure can be found through

$$\frac{P_D}{p_2} = \frac{1}{R_D B_D} \frac{\cos \alpha_2 M_2}{\cos \alpha M} \sqrt{\frac{1 + \frac{\gamma-1}{2} M_2^2}{1 + \frac{\gamma-1}{2} M^2}} \quad (6.31)$$

The last equation to solve is the one describing the trajectory of a fluid particle, and a schematic sketch of the developed mean stream surface is shown in figure 6.3. As can be seen from this

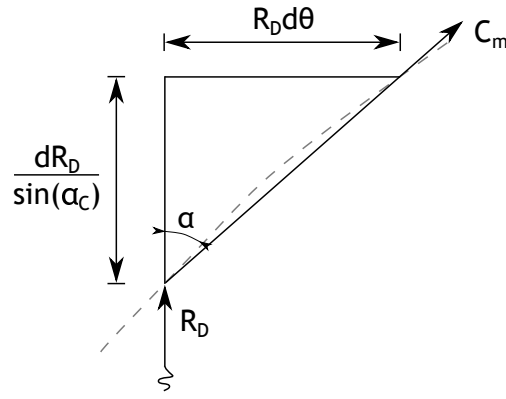


Figure 6.3: A developed view of the mean stream surface, showing the incremental change in position of a fluid particle. Reproduced from Stanitz (1952)

figure, the direction of the fluid particle can be written

$$\tan \alpha = \frac{R_D d\theta}{\frac{dR_D}{\sin \alpha_C}} \quad (6.32)$$

and hence the change in the tangential direction with the radius turns out to be

$$\frac{d\theta}{dR_D} = \frac{\tan \alpha}{R_D \sin \alpha_C} \quad (6.33)$$

Thus, by integrating the above relation over the whole diffuser channel, the position of a fluid element during it's transportation in the annulus space can be determined.

As can be noted, a whole lot of number crunching was necessary to end up with the final expressions. However, this is well worth the effort, since much more accurate results can be obtained than using simple relationships such as equation 6.1.

To use the above relations, some knowledge of the friction factor is required. Here, the form recommended by Japikse (1996) is employed as seen below.

$$C_f = k \left( \frac{1.8 \cdot 10^5}{Re} \right)^{0.2} \quad (6.34)$$

where  $k$  is a constant and  $Re$  the Reynolds number, in turn defined by

$$Re = \frac{\rho C b}{\mu} \quad (6.35)$$

here,  $\mu$  denotes the dynamic viscosity. Japikse (1996) notes that there has been a large range of values applied to  $k$ , and the model is therefore probably not sufficient to explain all flow phenomena in the vaneless diffuser. Nevertheless it is used in this analysis. Also note that the friction factor varies along the flow path, since both the density, velocity and passage width change along the same.

One important conclusion drawn by Braembussche (2013) is that the action of friction forces results in a type of blockage, as compared to an ideal frictionless case. The friction reduces the increase of static pressure, and hence the density at all radii. The decreased static pressure results in lower densities, and consequently higher meridional velocities; the exact same result as with increased blockage. Further, an increased meridional velocity implies a smaller flow angle thus compensating somewhat for the long flow passages generally found in vaneless diffusers.

## 6.2 Geometrical construction

The geometry of a vaneless diffuser is by itself very simple. However, there exist a number of different way the diffuser walls can be designed as shown in figure 6.4. This figure shows a

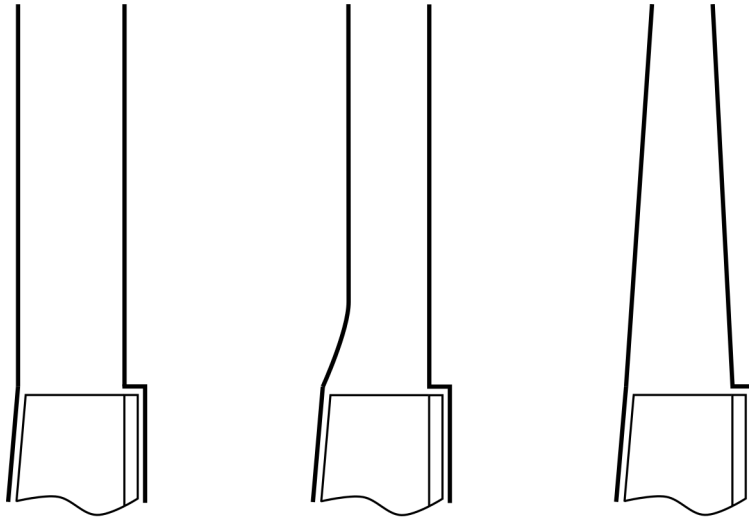


Figure 6.4: Different type of vaneless diffusers. To the left a diffuser with completely parallel walls, in the middle a diffuser with "front pinch" and to the right, a diffuser with both the hub and shroud wall inclined to the radial direction

couple of different diffuser configurations, but is by no means exhaustive. Employing parallel hub and shroud contours yields one of the more simpler diffuser geometries possible. Having non-parallel walled diffusers seem to give some advantages though, mainly by stabilizing the highly unsteady flow. Also, as noted by Cumpsty (2004), the higher meridional velocity associated with a *pinched* diffuser reduces frictional losses by giving a shorter fluid flow path

within the diffuser, other parameters held constant. Further, for reasonable amounts of pinch, no throat of the vaneless diffuser exit. This is why the vaneless diffuser is quite insensitive to different operating conditions and thus has a large operating range.

Here, the geometry recommended by Aungier (2000) is employed. Using these guidelines generally lead to pinched designs similar to the middle diffuser of figure 6.4. The hub contour is given by a polynomial at any tangential angle  $\theta$  in the form of

$$z_h = A + Br + Cr^2 \quad (6.36)$$

where  $A$ ,  $B$  and  $C$  are constants in turn defined by

$$C = \frac{\cot \alpha_{C2h}}{2(r_2 - r_3)} \quad (6.37)$$

$$B = -2r_3C \quad (6.38)$$

$$A = -z_{2h} - Br_2 - Cr_2^2 \quad (6.39)$$

where  $r_3$  is the so-called blend radius, the radius at which the diffuser pinch is turned into straight line segments, see figure 6.5. This geometry ensures that the diffuser's hub contour

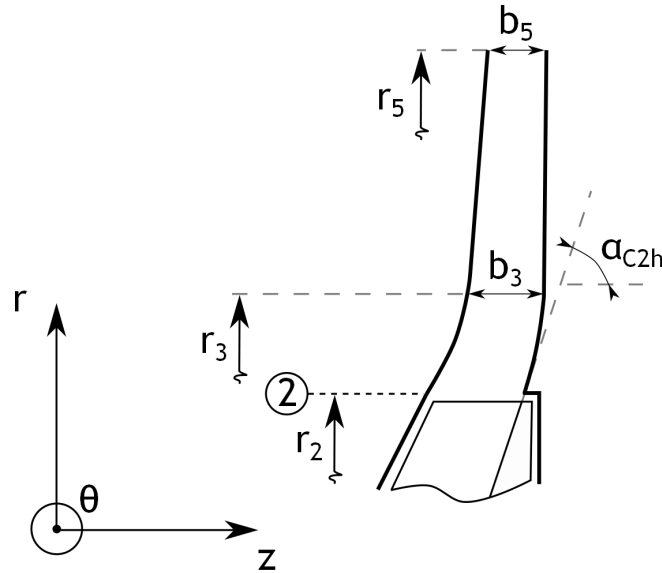


Figure 6.5: The geometric construction of the vaneless diffuser walls. Note that the hub contour slope of the vaneless diffuser at  $r_2$  equals the slope of the impeller's hub contour at the same position

slope is equal to the impeller hub's slope at the radius  $r_2$ . After the blend radius, the vaneless diffuser's hub contour is purely radial, and extends to the exit radius  $r_5$ . Instead, the shroud contour slope at  $r_2$  may differ from the slope of the impeller contour at the same location. Hence, some pinch at the diffuser inlet may appear. Also, the straight line element does not need to be fully radial, and will have a slope defined by

$$z'_{3s} = \frac{b_3 - b_5}{r_5 - r_3} \quad (6.40)$$

The shroud contour is also defined by a similar polynomial as the hub contour, namely

$$z_s = D + Er + Fr^2 \quad (6.41)$$

where once again  $D$ ,  $E$  and  $F$  are constants expressed as

$$F = \frac{z_2 - z_3 + z_3'(r_3 - r_2)}{(r_3 - r_2)^2} \quad (6.42)$$

$$E = z_{3s}' - 2r_3F \quad (6.43)$$

$$D = z_{2s} - r_2E - r_2^2F \quad (6.44)$$

Hence, rather simple expressions for the geometry are given and after constructing a hub contour, the shroud contour easily follows.

### 6.3 Calculation procedure

The calculation procedure is rather straight forward. After generating the geometry from specified design parameters, the main calculation can be started. It mainly consists of solving the above presented ordinary differential equations, after which all results of interest can be determined. A main difference from the impeller analyses can be observed; no iterative solution is necessary as seen in figure 6.6, showing the different calculation steps.

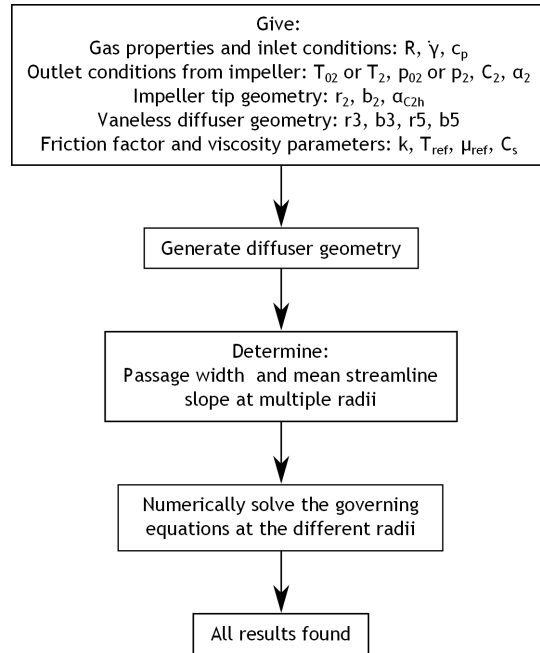


Figure 6.6: The different steps needed to determine all results of interest for the vaneless diffuser, from a set of input parameters

### 6.3.1 Input parameters

As is the case for any fluid dynamics problem, some medium properties need to be specified. Comparing with the previous impeller analyses, the same parameters determining the gas behaviour need to be given. This includes the specific gas constant  $R$ , the ratio of specific heats  $\gamma$  and the specific heat at constant pressure. However, as will be seen below, some additional gas properties must also be specified in this analysis.

Following the medium specification, are the inlet parameters. In this case the inlet condition equals the exit condition of the impeller. The exit absolute velocity  $C_2$  is a typical parameter known at the design phase, and a major influence factor on both the size and performance of any diffuser. Together with the velocity, the flow angle  $\alpha_2$  into the diffuser must also be specified. This parameter is almost of even greater importance than the velocity itself, since not only do the losses and discharge pressure depends heavily on it's magnitude, but also the stability. Choosing a too large angle will yield a very long flow path with large friction losses. Also, too large an angle, yields very low meridional velocities, with potential back flow as a result. Is the angle instead chosen too small the friction losses would be rather small, but instead the discharge kinetic energy quite high. A high meridional discharge velocity implies large exit losses, causing a large efficiency reduction. Japikse (1996) also describes how the amount of pinch can influence the rapid change of flow angle at the diffuser inlet part.

Further, the inlet thermodynamic condition must be specified. Having already given the velocity  $C_2$ , it suffice to specify either the static,  $T_2$  or stagnation temperature  $T_{02}$ , since they are directly related to each other through equation 2.5. To fully determine the thermodynamic condition something must be said about the pressure as well. Again, either the static  $p_2$  or stagnation pressure  $p_{02}$  may be specified, since knowing one of these parameters and both the static and stagnation temperatures, the unknown can be calculated by direct application of equation 2.6.

Turning the attention to the diffuser geometry, the impeller tip radius  $r_2$  and width  $b_2$  must, of course, be given in order to size the diffuser to this boundary condition. As was seen above, the hub contour also demands some information of the impeller tip hub contour slope, another parameter needed to be specified. Further, to control the amount of pinch the blend radius  $r_3$  and passage width  $b_3$  must be in full control of the designer. Already mentioned is how the pinch can influence the flow right at the impeller discharge. How much pinch one should employ must be evaluated at each separate case, and is dependent on both the inlet flow angle and velocity magnitude. Finally, the overall size of the vaneless diffuser is set by the discharge radius  $r_5$ , together with the passage width  $b_5$  at this location. The size can be restricted by its application, for instance by weight or space reasons. Also, the length of the flow passage, as well as the discharge conditions, is directly coupled to both  $r_5$  and  $b_5$ . The length of the diffuser section can be changed in order to allow greater impeller absolute exit flow angles without the risk of return flow in the vaneless diffuser. Shorter diffusers can handle larger  $\alpha_2$  angles, because of it's better stability, see Breambussche (2013). The same author also describes how more narrow diffusers tolerate more distorted flow fields. However, both a shorter and narrower diffuser will lead to higher exit meridional velocities, and hence lower amounts of diffusion. Wide diffusers, being more unstable, are nevertheless less dependent on the diffuser pinch since any flow stability will occur further downstream. Hence these could be a good choice if the diffuser is to be short, and no experience with pinch exist.

Finally, some parameters determining the friction factor need to be specified. As is seen in equation 6.34, the constant  $k$  need a value assigned to it. How this value should be chosen is non-trivial, and Japikse (1996) reports values ranging from 0.0056 to 0.025. Here, some

experience is needed to pick values suitable to the type of radial compressor being designed. The constant  $k$  may also vary along the flow path, enabling more control of the friction factor's variation as a fluid particle is transported within the diffuser. Since the friction factor has a Reynolds number dependence, the viscosity must also be calculated for the fluid at each radius. This is most easily done by specifying a reference viscosity  $\mu_{ref}$  at a reference temperature  $T_{ref}$  and using formula 2.11 to calculate the viscosity from the known static temperature. Also, the constant  $C_s$  in equation 2.11, being only dependent of the fluid to be compressed, must be given.

### 6.3.2 Calculation model

The whole vaneless diffuser analysis begins with generating the geometry of the flow path. By knowing the impeller exit radius  $r_2$ , the hub tip slope  $\alpha_{C2h}$ , the diffuser blend radius  $r_3$  and the diffuser discharge radius  $r_5$  the hub geometry can be generated with aid of equations 6.36 to 6.39. By also knowing the different passage widths  $b_2$ ,  $b_3$  and  $b_4$  the whole shroud geometry is determined as well through equations 6.40 to 6.44. Since the whole geometry now is specified, using the method outlined in appendix C yield not only the passage width distribution, but also the mean streamline coordinates. Both of these results are necessary to enable any subsequent calculation of the flow properties within the diffuser.

The next step is to solve the ordinary differential equations 6.25, 6.29 and 6.33. Here, this is done with a fourth order Runge-Kutta numerical integration whose main logic and underlying mathematics is presented in appendix F. This integration is performed at discrete steps with numerical estimates of the derivatives in the differential equations. In order to obtain an as high accuracy as possible, the steps need to be rather small. However this presents no difficulties, since the calculation itself is rather straight forward. Hence, the calculation starts at the impeller discharge radius, where all properties and conditions are known. From this radius the properties at the next radius step is determined. This procedure is repeated until the last radius step, the discharge radius  $r_5$ , is arrived at. At each step the known passage width is used as geometry input. Also, the mean streamline slope  $\alpha_C$  must be determined, which is most easily done from the mean streamline coordinates. The procedure for doing this is schematically depicted in figure 6.7. A very simple technique is applied, working better for larger amount of radius steps than smaller. Since the numerical Runge-Kutta solution procedure requires a large number of calculation points anyway, the accuracy of the stream line slope can be expected to be rather high. As is seen in this figure, the slope at an arbitrary radius  $r_i$ , not coinciding with the start or end point, can be determined by

$$\alpha_{i,+\Delta r} = \arccos \left( \frac{z_{i+1} - z_{i-1}}{\sqrt{(z_{i+1} - z_{i-1})^2 + (r_{i+1} - r_{i-1})^2}} \right) \quad (6.45)$$

if the change in radius would be negative, it is necessary to compensate for this by

$$\alpha_{i,-\Delta r} = 2\pi - \alpha_{i,+\Delta r} \quad (6.46)$$

Would the point of interest be the first one of the mean streamline, no point prior the current exist, and the solution is to use the current point in determining the slope through

$$\alpha_{1,+\Delta r} = \arccos \left( \frac{z_2 - z_1}{\sqrt{(z_2 - z_1)^2 + (r_2 - r_1)^2}} \right) \quad (6.47)$$

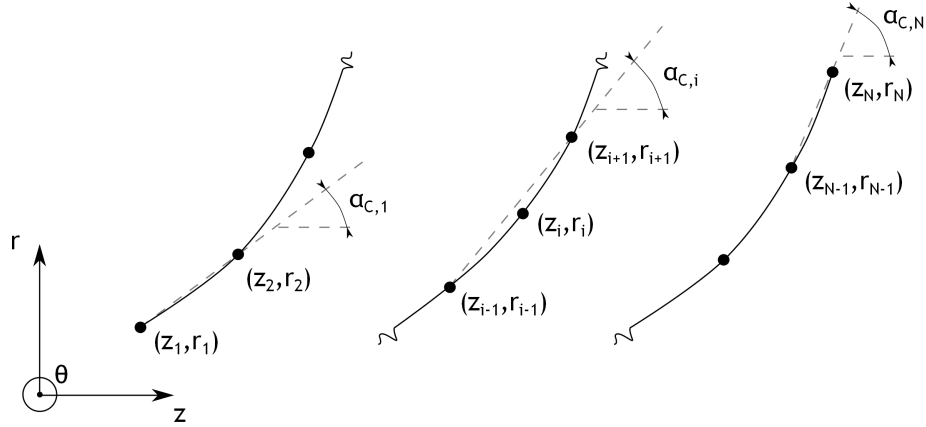


Figure 6.7: The determination of the local streamline slope. Shown to the left and right are the special cases of the first and last point of a streamline respectively. In the middle is the typical case of a point with adjacent points on each side of it

The same procedure is used for the last point  $N$ , and the resulting slope would be

$$\alpha_{n,+\Delta r} = \arccos \left( \frac{z_N - z_{N-1}}{\sqrt{(z_N - z_{N-1})^2 + (r_N - r_{N-1})^2}} \right) \quad (6.48)$$

where a similar compensation as suggested by equation 6.46 is needed for negative radii changes in either of the two cases. Also, at each radius step, the friction factor need to be determined. Because of this, the thermodynamic properties is also needed at every radius since the friction factor depends on the Reynolds number, as seen in equation 6.34. At each calculation step, the static temperature need to be determined through equation 2.5. The pressure is also easy to calculate with the above derived relationship, formula 6.31. Therefore the thermodynamic state is fully known, and therefore also the Reynolds number.

Following this procedure at each and every incremental radius station, the properties are known everywhere in the diffuser. This completes the one-dimensional analysis of this component.



## Chapter 7

# Vaned diffuser design

Many times a vaneless diffuser can not do the job of diffusing the flow efficiently enough, and it is then necessary to use diffusers of other types. By employing vaned diffusers, a given diffusion level can often be supported with a significantly smaller exit radius  $r_5$ , as compared to a vaneless diffuser. One reason is that employing vanes gives an additional degree of freedom in controlling the flow, see figure 7.1. Also, as noted by several authors, for instance Japikse (1996)

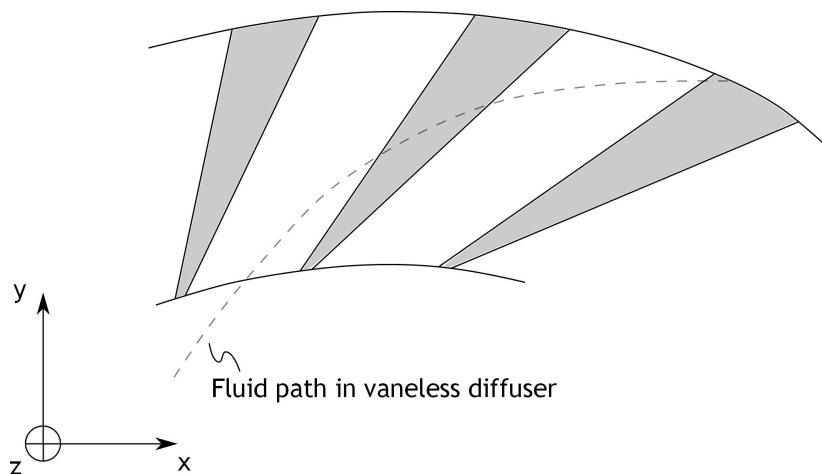


Figure 7.1: Comparison between vaned and vaneless diffusers. The fluid path in vaneless diffusers can be expected to be much longer. The vaned diffuser is of a wedge type

and Cumpsty (2004), the efficiency of a vaned diffuser is usually higher, at least at the design point. The higher efficiency is mainly a result of the shorter fluid passage. Further, employing vanes also gives some control of the fluid exit direction, and if designed properly this can minimize losses in components downstream of the diffuser.

This analysis is restricted to vaned diffusers of the wedge type, having the general appearance seen in figure 7.1. The wedge diffuser is a member of the channel diffuser family, a group of diffusers usually not employing airfoil cascade type of vanes. Another typical type of channel diffusers employ conical passages, drilled around the circumference of the diffuser part. Breambussche notes that channel diffusers are used at higher pressure ratios ( $PR_{stage} > 3$ ) as compared to other types of vaned diffusers.

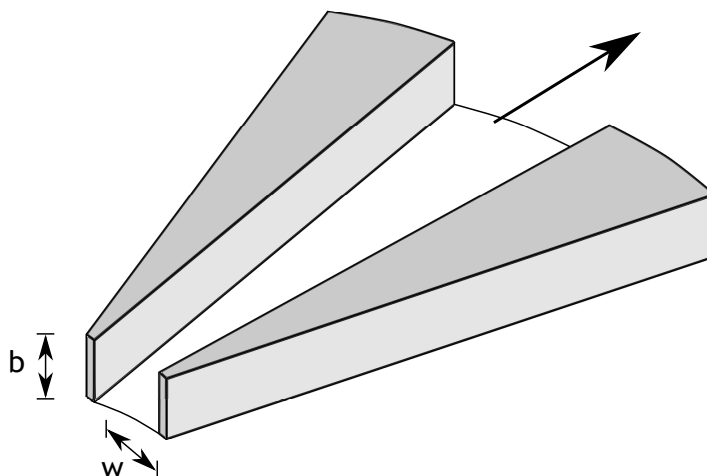


Figure 7.2: A typical wedge diffuser, showing its diverging rectangular channel. Only two of the wedges are shown for reasons of clarity

This chapter starts with presenting the basic relations and fundamental concepts. Following this section is the geometrical relations and design aspects of the wedge diffuser. Finally, the method of calculation is presented, describing how the preceding sections are used to characterize any chosen wedge diffuser design.

## 7.1 Basic relations

Any vaned diffuser design employs a certain amount of vaneless space between the impeller discharge and the diffuser itself. It is needed, not only to even out unsteady fluctuations to some extent, but also to diffuse very high speed flow to more manageable levels. As thoroughly discussed by Japikse (1996), it is a very complicated and non-trivial matter to choose the extent of the vaneless space. From chapter 6, the vaneless space can be fully determined by solving the ordinary differential equations 6.25, 6.29 and 6.33. By doing this, the condition at the vaned diffuser inlet is fully determined. The subsequent analysis assumes full knowledge of the vaned diffuser inlet state.

As was the case for the vaneless diffuser, ordinary differential equations must be solved to get a reasonable accuracy of the diffuser performance prediction. However, the analysis become somewhat simpler, since the flow within the channel diffuser is considered steady and one dimensional. Also, the velocity has only one component along the channel. Under this assumption, "classic" compressible channel flow relations can be used, greatly easing the calculation procedure. The derivation of the governing equations are quite similar to the one found in chapter 6, and are presented in appendix G. In what follows, the main equations are just presented and modified to suite the wedge diffuser geometry. A schematic sketch of a wedge diffuser is shown in figure 7.2. A reasonable assumption, and a major simplification, is an adiabatic diffuser. Since, no rotary parts exists within the vaned diffuser, this implies a constant stagnation temperature. Hence

$$\frac{dT_0}{dx} = 0 \quad (7.1)$$

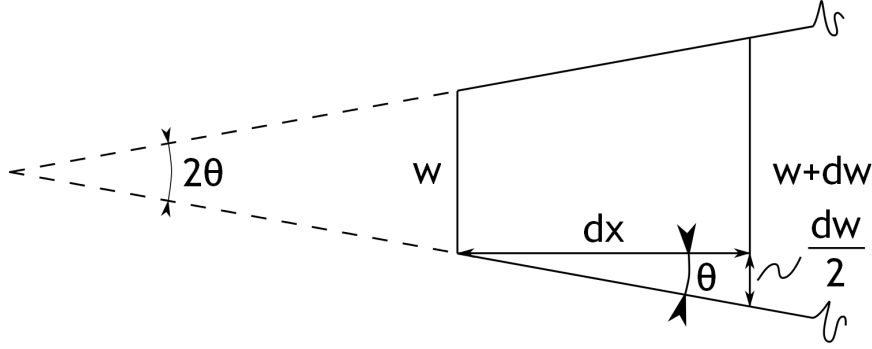


Figure 7.3: The definition of a channel diffuser's divergence angle  $2\theta$ . What is shown is a schematic one-dimensional diffuser, with a change in width  $w$  over the incremental step  $dx$

where the coordinate  $x$  is directed along the channel's length, in line with the analyses conducted in appendix G. As is seen in figure 7.2, the passage area  $A$  can be written

$$A = bw \quad (7.2)$$

An additional constraint on the analysis is now imposed; the hub to shroud passage height  $b$  is set to a constant value. Consequently, the channel area found between two adjacent wedges only diverges in one of the two possible directions. Thus, the change in passage area along the  $x$  coordinate can be written

$$\frac{dA}{dx} = b \frac{dw}{dx} \quad (7.3)$$

Further, by studying figure 7.3 and introducing the diffuser divergence angle  $2\theta$  it is seen that the change in width can be expressed according to

$$\tan \theta = \frac{1}{2} \frac{dw}{dx} \quad (7.4)$$

Inserting these relations into the governing equations G.20 and G.26 found in appendix G, one obtain

$$\frac{1}{M^2} \frac{dM^2}{dx} = 2 \left( \frac{1 + \frac{\gamma-1}{2} M^2}{1 - M^2} \right) \left( \left( \frac{1}{b} + \frac{1}{w} \right) \gamma M^2 C_f - \frac{2}{w} \tan \theta \right) \quad (7.5)$$

and

$$\frac{1}{p_0} \frac{dp_0}{dx} = - \left( \frac{1}{b} + \frac{1}{w} \right) C_f \gamma M^2 \quad (7.6)$$

where the hydraulic diameter  $d_H$  has been substituted in the form of

$$d_H = \frac{4A}{\text{wetted perimeter}} = \frac{4wb}{2w + 2b} = \frac{2wb}{w + b} \quad (7.7)$$

The friction factor  $C_f$  is, within the vaned diffuser channel, assumed to be well approximated by "traditional" pipe friction correlations. Aungier (2000) presents a convenient way to calculate the friction factor depending on the Reynolds number and surface roughness. Here, however, the walls are assumed smooth enough to make the surface roughness negligible. The friction factors are based on the local Reynolds number within the flow channel, where the Reynolds number itself is defined as

$$Re_{VD} = \frac{\rho C d_H}{\mu} \quad (7.8)$$

and is thus based on the hydraulic diameter of the channel. For laminar flow, here defined as  $Re_{VD} < 2000$ , the friction factor  $C_{f,l}$  can be calculated by

$$C_{f,l} = \frac{16}{Re_{VD}} \quad (7.9)$$

If instead the flow is turbulent,  $Re_{VD} > 2000$ , the turbulent friction factor  $C_{f,t}$  is found from

$$\frac{1}{\sqrt{4C_{f,t}}} = -2\log_{10} \left( \frac{2.51}{Re_{VD}\sqrt{4C_{f,t}}} \right) \quad (7.10)$$

## 7.2 Geometrical construction

First, the vaneless space geometry must be determined. In fact, the geometry used is the exact same as in the vaneless diffuser analysis, and here it suffice to note that the vaneless space is used to turn the hub and shroud contour into fully radial. Following the vaneless space is the wedge diffuser itself and some basic geometrical features of a such a construction is seen in figure 7.4. All of the wedges' sides are constructed from straight line elements, somewhat

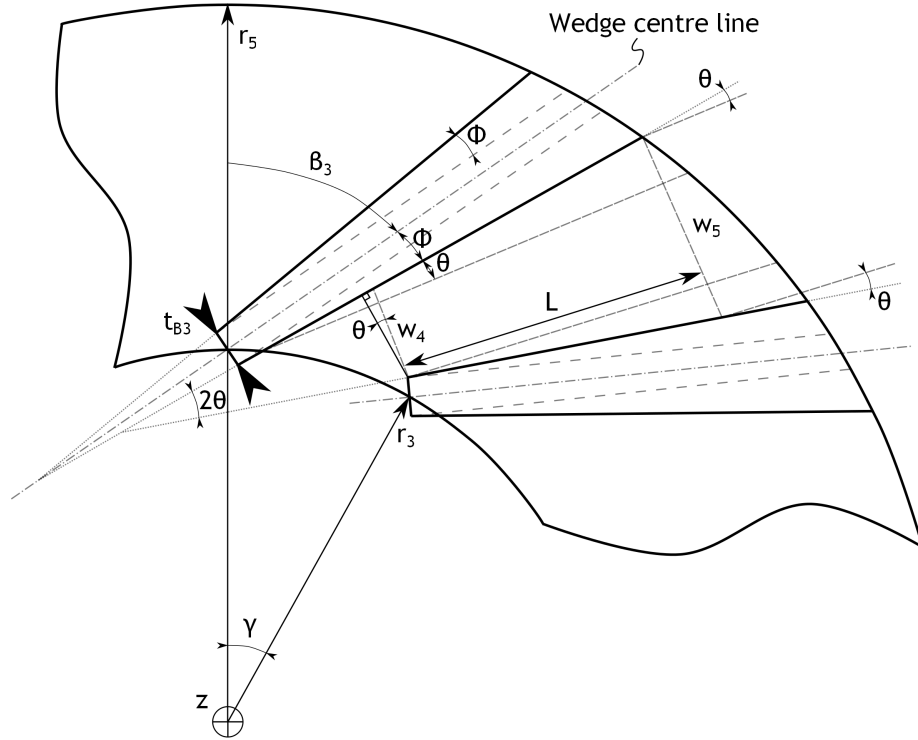


Figure 7.4: The basic geometric parameters for determining a wedge diffuser design. Note the diffuser divergence angle  $2\theta$ . Only two wedges are shown for reasons of clarity

simplifying the analysis. Also, the angle defining the wedges' own (half) divergence angle,  $\Phi$ , is equal on both sides of the wedge centreline. A leading edge thickness of  $t_{B3}$  is included, while the trailing edge thickness is fully determined by the geometry. By employing  $Z_D$  number of wedges, the angle  $\gamma$  between any similar point of two adjacent vanes can be expressed as

$$\gamma = \frac{2\pi}{Z_D} \quad (7.11)$$

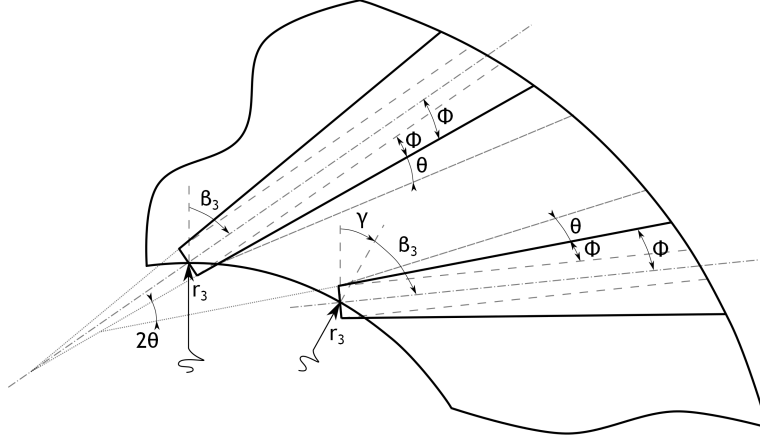


Figure 7.5: Some geometrical features in detail, used to find a relation between the wedge divergence angle  $\Phi$ , the channel divergence angle  $2\theta$  and the tangential angle between adjacent wedges  $\gamma$

Another important geometrical relation can be found by studying the different angles in more detail, see figure 7.5. From the various angles it is clear that

$$\beta_3 + 2(\Phi + \theta) = \gamma + \beta_3 \quad (7.12)$$

which reduces to

$$\Phi = \frac{\gamma}{2} - \theta \quad (7.13)$$

Two other geometric parameters of great importance are the area ratio  $AR$  and length to width ratio  $L/w$ .  $AR$  is the channel's exit to inlet area ratio, and since the passage width between hub and shroud is set constant, it is here directly related to the passage widths at these locations by

$$AR = \frac{A_5}{A_4} = \frac{b_5 w_5}{b_4 w_4} = \frac{w_5}{w_4} \quad (7.14)$$

As the name implies, the  $L/w$  is the ratio of the passage length to width. The width is here defined as the inlet width  $w_4$ , and the length  $L$  defined in figure 7.4. Hence

$$\frac{L}{w} = \frac{L}{w_4} \quad (7.15)$$

however, it is not at all obvious which length to use, since the passage has different lengths on the wedges' suction and pressure side. However, using the definition here, the actual channel length to width ratio will never become too small, a situation that could occur if  $L$  is defined differently.

### 7.3 Calculation procedure

As has already been stressed, the first step is to perform a vaneless space calculation, in order to come up with the conditions at the radius where the vaned diffuser is begun. After doing this, the whole geometry of the vaned diffuser must be determined. It suffices to perform the calculation for two adjacent wedges, the rest of the geometry is just evenly distributed over

the annulus. When having established the geometry, the channel flow calculation can begin. This is done over several steps, where the ordinary differential equations are solved repeatedly. The calculation procedure is outlined in figure 7.6.

### 7.3.1 Input parameters

Similar to all analyses, the gas properties must be known prior any calculation. Again, the needed parameters are the specific gas constant  $R$ , the ratio of specific heats  $\gamma$  and the specific heat at constant pressure  $c_p$ . These three gas specific parameters determine the behaviour of the gas, but as will become apparent, parameters characterizing the viscosity must also be provided.

Further, the inlet condition to the whole diffuser must also be known. This "station" along the compressor coincide with the impeller exit condition, hence the impeller exit state is of great importance. The exit (absolute) velocity  $C_2$  is a component of large significance to the diffuser, and one of the major reasons for employing a vaneless space at all. Usually this velocity is very high, and need some diffusion before actually entering the vaned diffuser. Were it not for this vaneless space, the operating range would be extremely restricted, with a large possibility of choking at comparatively low mass flows. From this velocity, and after specifying either the stagnation  $T_{02}$  or static temperature  $T_2$ , the non-specified temperature can be determined, simply by using equation 2.5. On a similar basis the stagnation  $p_{02}$  or static pressure  $p_2$  can be calculated by specifying one of them, and employing relation 2.6 to find the other. The absolute flow angle  $\alpha_2$  at the impeller exit is another parameter needed as input. This angle is often determined from an impeller analysis, but as has been described in previous chapters, it is usually set to match the downstream diffuser. When choosing this angle for vaned diffusers, one must keep in mind that the selected value is usually only valid at the design conditions. If, for instance, reducing the impeller rotating speed, this angle can be expected to change. Depending on how much the angle changes, the performance of the vaned diffuser will be lowered, finally leading to choking or flow instabilities, see Cumpsty (2004). Further, some geometric data of the impeller exit is needed in order to enable the construction of the vaneless space's hub and shroud contours. As was the case for the vaneless diffuser analysis, the impeller tip width  $b_2$ , tip radius  $r_2$  and tip hub contour slope  $\alpha_{C2h}$  must be specified.

Instead turning the attention to the vaneless space itself, some geometric features must be known. This includes the radius  $r_3$  where the vaneless space ends and the wedge diffuser instead takes over. Specifying this radius together with the corresponding width  $b_3$  enables the whole geometry up to this point to be determined. How to correctly choose these two parameters is extremely hard, and this region is associated with high Mach numbers, unsteady flow and various viscous effects, see Japikse (1996). Hence, some experience is needed to make wise choices. Further, the simple methods of this analysis will not suffice to model the flow even close to the actual situation encountered in reality. However, it serves it's purpose of providing first estimates of the overall performance. Moving on, the friction factor for the vaneless space calculation need a specified value of the constant  $k$ . This parameter is also non-trivial to pick correctly, but any designer with modest experience has some idea of what level to expect. Also, the option to specify a  $k$  value ranging form one value at the impeller discharge to another at the vaneless space exit exist. This is a powerful way to more precisely model the flow, where the friction factor can be made directly dependent (other than the Reynolds number dependence already included) on the actual position along the flow path. Additionally, to enable the viscosity to be determined anywhere, some extra gas properties

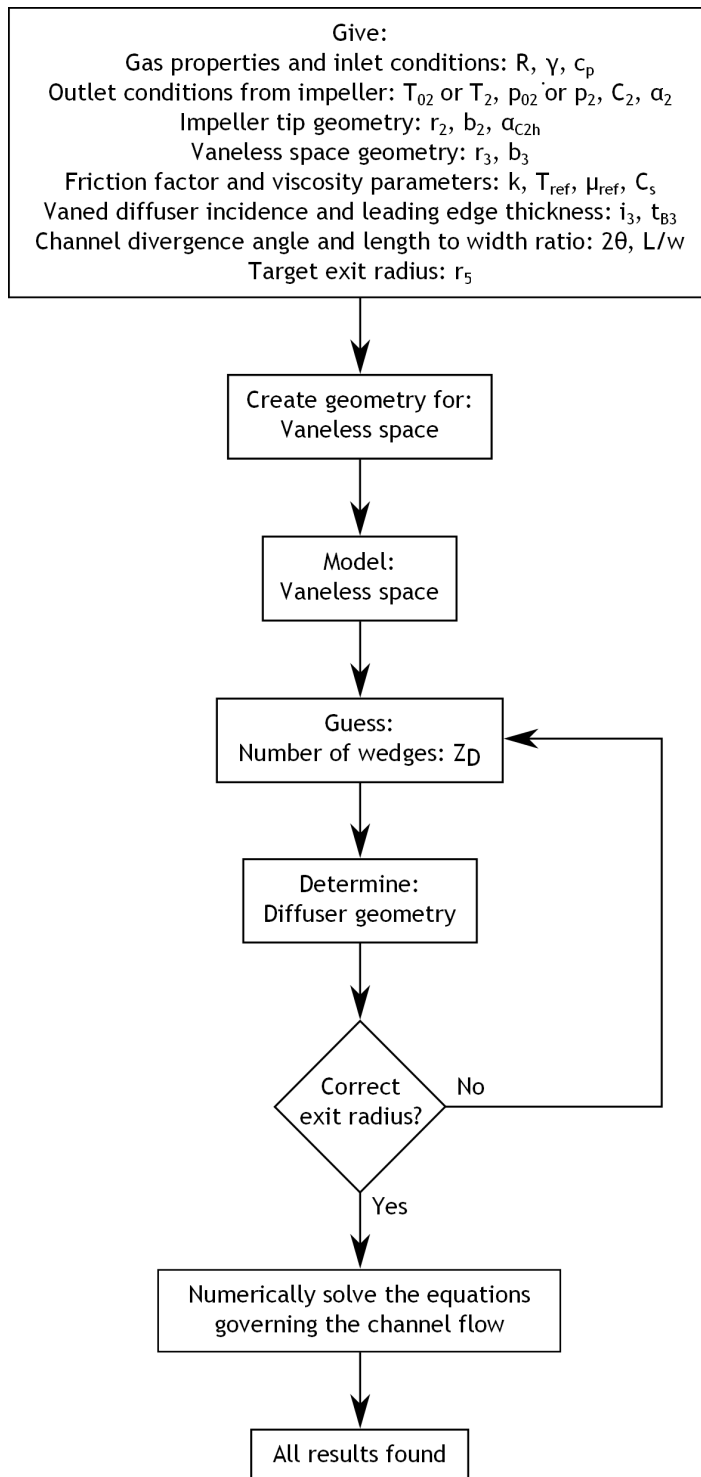


Figure 7.6: The different steps needed to determine the performance of a wedge diffuser. Note the iteration for the correct geometry

must be given. These are the reference viscosity  $\mu_{ref}$  and temperature  $T_{ref}$ , together with the gas dependent parameter  $C_s$  in Sutherland's law, equation 2.11.

Finally, parameters relating to the wedge diffuser itself needs specification. In order to situate the wedges to the flow direction some knowledge about the incidence  $i_3$  is required. The choice of incidence plays a huge part in the resulting performance. However, as described by Japikse (1996), the actual inlet incidence is very hard to determine in practice, making the design incidence decision even harder. Also, the wedge leading edge thickness  $t_{B3}$  must be specified, a parameter influencing the amount of diffuser inlet blockage. A thinner leading edge is from an aerodynamic point of view advantageous, but some consideration to structural integrity must be made. Further, a set of very important parameters determining the wedge diffuser performance are the flow channels' divergence angle  $2\theta$  and length to width ratio  $L/w$ <sup>1</sup>. When analysing any diffusion process in channels, these are the variables to consider. It is now widely known that the divergence angle  $2\theta$  of a channel diffuser must be kept relatively low, around  $10^\circ$ , see Aungier (2000). Increasing the value too much will inevitably lead to flow separation, and hence large losses. If instead picking a too small angle, quite long channels will result for a given pressure rise. Too long a channel will result in large friction losses, again reducing the efficiency of the diffuser. Instead, the length to width ratio gives the designer direct means to control the channel's length, and thereby the amount of friction losses to be expected. Ideally, this ratio should be in the order of 15 to 20, see Japikse (1996). Many times designers are forced to use smaller values, since space reasons usually are of high importance, and an as good compromise as possible must be found. To directly address the issue of space limitations, the diffuser's exit radius  $r_5$  must also be specified. One of the reasons for employing a vaned diffuser at all, is the weight and volumetric advantage it posses over the vaneless diffuser. Hence, it is reasonable to assume that the designer must work with an upper limit of this radius while finding a compressor configuration. The divergence angle, length to width ratio and the exit radius are all of high importance and determine, to a large extent, the diffuser's performance. Many times, choosing parameters very near the stall limit of the channels yield high diffuser efficiencies. However, any experienced designer know that margins are needed in order to have reasonable efficiencies at off-design operation as well. Typically, a decreased channel divergence angle would give the needed margin, see Braembussche (2013). Therefore, a compromise based on engineering experience and judgement is needed.

### 7.3.2 Calculation model

After using the input parameters relating to the vaneless space in the exact same manner as outlined in chapter 6, the design of the wedge diffuser can take place. It should be noted that no in-depth analysis of the so-called semi-vaneless space, the region where one wedge is present for the flow about to enter the diffuser's channels, are performed. However, as a first approximation, the flow in the semi-vaneless space can be assumed isentropic. Cumpsty (2004) notes that a large part of the pressure recovery takes place in this region. It is also here the operating range between surge and choke of the whole stage may be determined, see Braembussche (2013). Because of the importance of this highly complex region, a flow separation here would be considered catastrophic. With isentropic flow, both the stagnation temperature and pressure is preserved, making the calculations rather easy. An one-dimensional continuity equation takes the form of

$$\dot{m} = \rho_3 C_3 \cos \alpha_3 A_3 = \rho_4 C_4 A_4 \quad (7.16)$$

---

<sup>1</sup>The area ratio  $AR$  could also be included, but is dependent on  $2\theta$  and  $L/w$



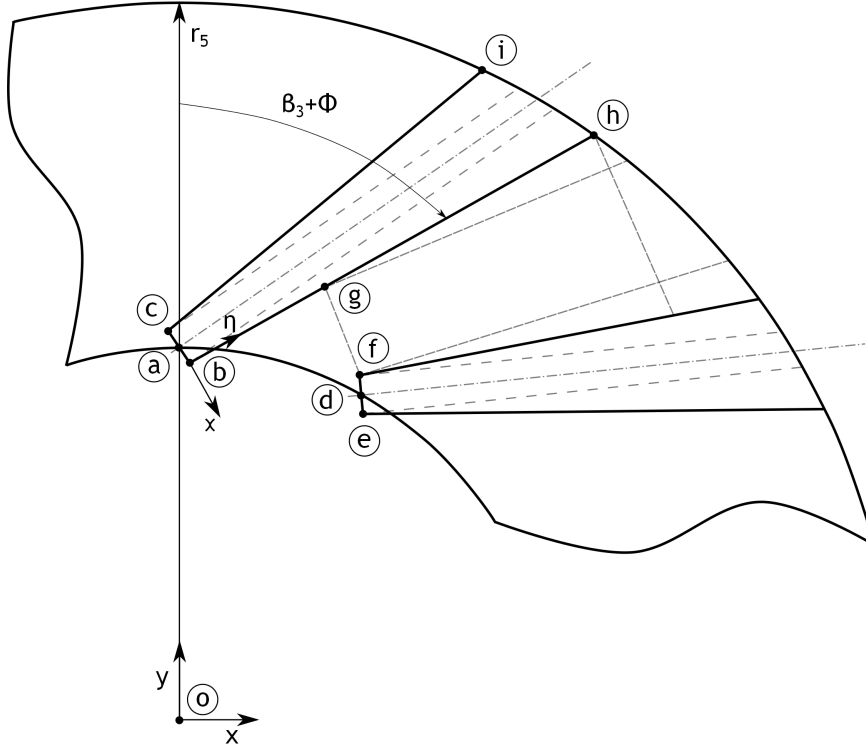


Figure 7.7: The different points used in order to set up the diffuser geometry. Two wedges must be analysed in order to determine the channel inlet width  $w_4$

Using this equation together with relation 2.1, 2.5 and 2.6 enables the throat condition to be fully determined.

When determining the geometric construction of the diffuser, the first step is to determine the exact wedge geometry by considering two adjacent wedges. The first wedge is most easily placed with the leading edge directly above the  $z$  axis as was shown in figure 7.4. Also, to ease the construction of the wedges, points according to figure 7.7 is inserted at locations of interest. A good starting point is to determine the centreline angle of the first wedge. From the known flow angle  $\alpha_3$  it is set from the given incidence

$$\beta_3 = \alpha_3 - i_3 \quad (7.17)$$

Knowing  $\beta_3$ , creating the leading edge from the specified thickness  $t_{B3}$  is a simple matter, see the left sketch of figure 7.8. Point  $a$  is located above the  $z$  axis, at a radius equal to the vaneless space exit radius  $r_3$ . The other two points  $b$  and  $c$  are located at the edges of the leading edge, and their respective coordinates may be found by simple trigonometry. In what follows, an iterative solution is necessary, beginning with a guessed amount of wedges  $Z_D$ . From this guess, the angle between the wedges  $\gamma$  and the wedge divergence angle  $\Phi$  (not to be confused with the channel divergence angle  $\theta$ ) may be calculated using formula 7.11 and 7.13. Knowing these angles, the leading edge of the adjacent blade may be determined, again using figure 7.8 as a guide.

In order to make the following analyses easier, a rotated coordinate system is employed and can be thought of as being placed with it's origin at point  $b$ . This is also depicted in figure 7.7,

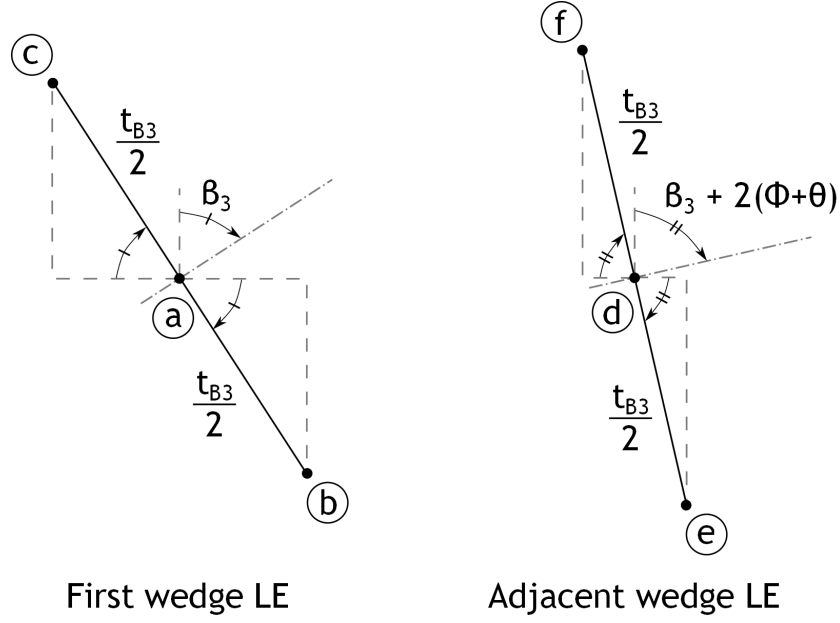


Figure 7.8: The leading edges of the first wedge, and the adjacent wedge. The geometric features are necessary to study when determining the wedge diffuser's channel properties

and the rotated coordinate angle may be written

$$\phi_{coord} = -(\beta_3 + \Phi) \quad (7.18)$$

measured from a Cartesian coordinate system, typically placed in the origin  $o$ . By working in the rotated coordinate system, it can be seen from figure 7.4 that the passage width  $w_4$  can be determined from

$$w_4 = \frac{\overline{bf}_\chi}{\cos \theta} \quad (7.19)$$

where  $\overline{bf}_\chi$  denotes the vectorial length between point  $b$  and  $f$  along the  $\chi$  axis. Knowing  $w_4$  implies knowing the point  $g$  which now also is easily determined from simple trigonometric relations. Further, since  $w_4$  has been determined, the channel length is found directly from the specified length to width ratio and equation 7.15. From the value of the channel length  $L$ , point  $h$  can be found with aid of figure 7.9. Working with the rotated coordinate system, the wedge's wall length of the channel can be calculated by

$$\overline{gh}_\eta = \frac{L}{\cos \theta} \quad (7.20)$$

here,  $\overline{gh}_\eta$  denotes the vectorial length between point  $g$  and  $h$  along the  $\eta$  axis. Now, point  $h$  is fully determined. As a matter of fact, the outer radius  $r_5$  of the whole diffuser is also known, since point  $h$  is located right at this radius. Generally this radius will not equal the target exit radius, and the number of wedges must be changed accordingly. If the newly determined radius is smaller than the desired, the amount of wedges must decrease. This can be explained by the fact that fewer wedges would force the length  $L$  of the channel to increase as a consequence of a wider inlet width  $w_4$ , keeping the length to width ratio unchanged. Hence, the above procedure is repeated until convergence.

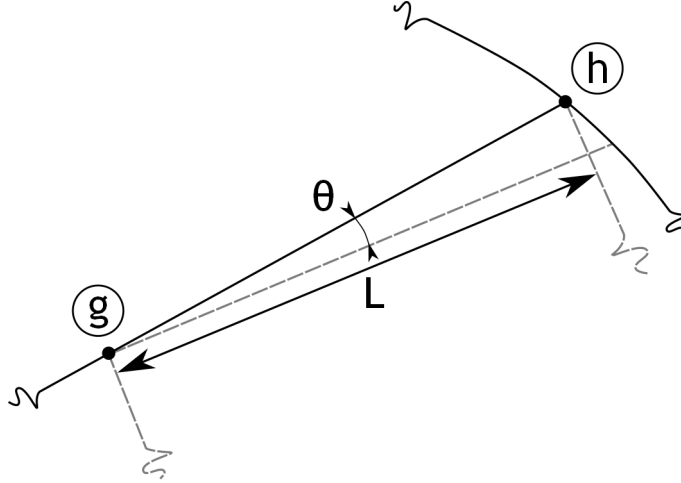


Figure 7.9: The channel length  $L$  and it's relation with the wall length  $\overline{gh}$  and channel divergence angle  $\theta$

After the correct exit radius has been found, the amount of wedges may not be an integer. Therefore, the result from the above iteration must be rounded off. This, however also affects the geometry, and a recalculation of the exact same form as outlined above must be made. Of course, the exit radius will not longer exactly match the desired value.

One more point defining the wedge remains to be determined, namely point  $i$ . Again, a small trigonometric exercise is necessary, using figure 7.10 as a basis. The angle  $\delta$  may be found directly from the known points  $o$  and  $c$ , along with the length of the line  $\overline{oc}$ . From figure 7.4 it is obvious that the slope of the line  $\overline{ci}$  is  $\beta_3 - \Phi$ , as measured from the  $y$  direction. Further, the angle  $\xi$  is determined by

$$\xi = \pi - \beta_3 + \Phi - \delta \quad (7.21)$$

Applying the law of cosines, the length of the line element  $\overline{ci}$  turns out to be

$$|\overline{ci}| = |\overline{oc}| \cos \xi + \sqrt{|\overline{oc}|^2 \cos^2 \xi + r_s^2 - |\overline{oc}|^2} \quad (7.22)$$

where  $|\overline{oc}|$  is the length of the line extending from  $o$  to  $c$ . Now, point  $i$  is fully determined from the length  $|\overline{ci}|$  and the slope of the same line.

Knowing all points defining the wedge, all other wedges may be determined by simply rotating each point by an angle  $\gamma$ . Hence, the geometry of the whole wedge diffuser, including the vaneless space is now determined, and the next step is to solve the flow within a single channel. This is done by solving equations 7.5 and 7.6 with Runge-Kutta integration as presented in appendix F. The method of inserting quasi normals need not be applied here, since the passage area vary in a purely linear (and known) form, as was seen in equation 7.4. Having solved the ordinary differential equations, all parameters of interest are determined, and the wedge diffuser analysis is done.

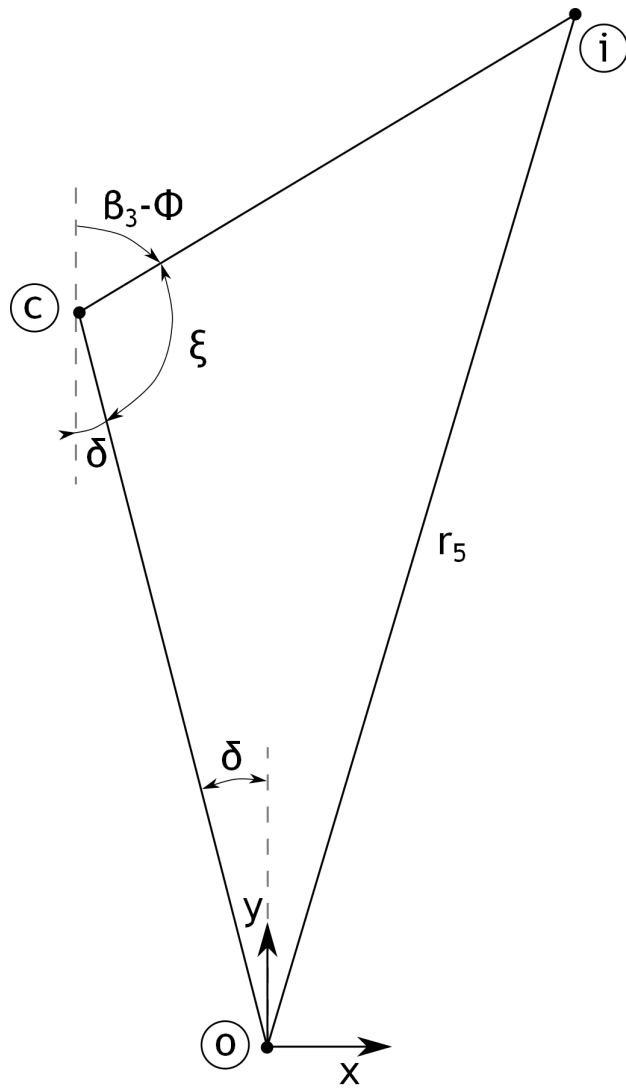


Figure 7.10: The geometrical features needed to find the last point of interest, namely point  $i$

# Chapter 8

## Computer implementation

All analyses presented in chapters 3 to 7 have been implemented into a computer environment. This chapter begins with describing the main features of the result, without going in to any programming details. The chapter continues with introducing each analysis in its implemented form, describing what results the designer can find using the code. The program suite was named LURC, **Lund University Radial Compressor**, in order to distinguish it from similar work from the same university division focusing on other types of compressor turbomachinery, see for instance N. Falck (2008) [21].

### 8.1 Basic program structure

MATLAB<sup>®</sup> was chosen as a programming language, being familiar to many engineers. Also some convenience when implementing the code itself can be found. The MATLAB<sup>®</sup> suit contain tools for creation of GUI:s (graphical user interfaces), making implementation of such features rather straight forward. Also, tools for plotting, vector algebra etc. are available and at hand. The MATLAB<sup>®</sup> version R2012b (8.0.0.783) was used throughout the project.

The computerized analysis consists of several so-called functions, many of them being interconnected. In this context a function means an executable program, in need of input data to work properly. A schematic sketch of the most important interrelations are presented in figure 8.1. Here it is seen that a main GUI is used to enable the user to communicate with the different analysis functions. Two-way arrows indicate that information must be carried both ways; from the GUI to the analysis function and from the analysis function to the GUI. Information towards a function from the GUI is typically input data, such as rotating speed or mass flow. Conversely, information in the opposite direction would be some type of result, after running one of the design tools. The results themselves can in turn be simple variables, such as a discharge static pressure but also vectors containing multiple data points used for graphical representations.

Between different functions some data exchange must also be possible. If, for instance, an impeller has been designed in the impeller preliminary design tool it must be possible to use the discharge data as input in any of the two diffuser analyses. The same applies for the detailed impeller calculation tool. However, one extra link exist from the detailed impeller analysis; the possibility to use the generated three-dimensional geometry in a subsequent internal impeller flow analysis.

In order to keep the GUI function what it is meant to be, a mean to translate user input into computer terminology, it has been aimed to perform as few calculations within the GUI

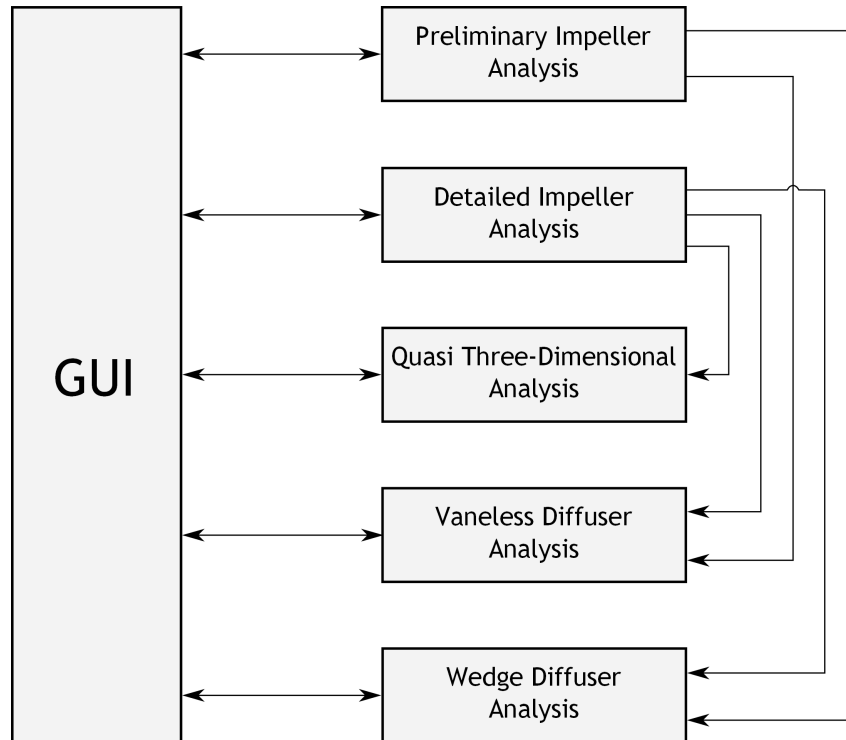


Figure 8.1: The interrelations between the different main functions of the analysis program LURC. Note that many analysis functions must be able to communicate with each other

itself as possible. In some instances, some calculations have been necessary, typically when handling graphical results having no strong relation with the analysis tool in question.

To ease any further work, such as new analysis tools or extension of current design methods all files have been commented in an as large extent as possible and necessary. This ensures that the program can be held up to date and extended when desired.

## 8.2 Common features and components of the analysis tools

While implementing the GUI the aim has been to keep all analysis tools as similar as possible. By doing this, any user will quite quickly get a feel for where and how a certain action may be executed and where to find the results. Further, so called tool-tips have been implemented giving a short explanation of the different variables encountered, when hovering the mouse pointer over the parameter of interest. An example of both a tool-tip and a text box where data should be entered is shown in figure 8.2. A text box where data should be entered is *always* shown with a white background, typical of most modern computer programs. A short description of the parameter to be entered is given before the text box itself. Following the text box is the unit of the parameter in question, ensuring that the user understand what is to be entered. In the example given in figure 8.2 above the axial tip width should be entered. From the tool-tip string one find out that it is the impeller width defined purely in the axial direction. Finally, the width should be entered in units of meter as indicated by the unit text.

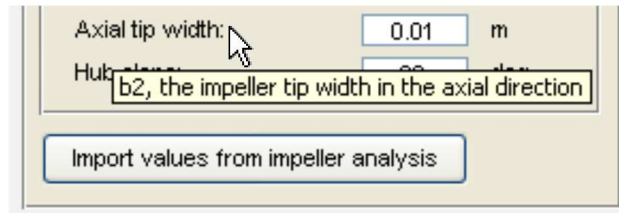


Figure 8.2: A data input box, also showing a tool-tip string when hovering with the mouse pointer over the description of the parameter

Results involving single parameters, such a pressure or temperature are also presented in text boxes, however these are *always* greyed out, as shown in figure 8.3. Of course, a greyed out

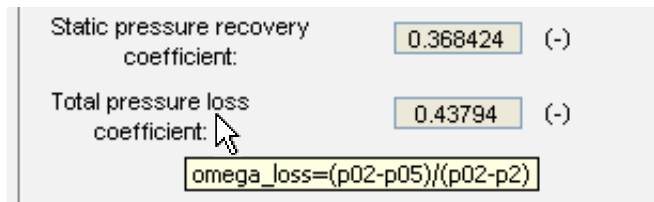


Figure 8.3: A result text box, with its greyed out background. Also note that tool-tips are available for result parameters

result text box cannot be modified by the user. As is also obvious in figure 8.3 is the inclusion of tool-tips for results as well. Further, units are always written out. In the above example, a total (stagnation) pressure loss was found to have the value of 0.43794. It is dimensionless, as indicated by the unit text "(-)". The tool tip string reveals how the pressure loss is defined.

Buttons are used whenever the user want to change the current design tool, for instance from the preliminary impeller analysis to the wedge diffuser tool. Also, they are used when some action need to be taken, such as when starting a calculation or importing results from another analysis. Two examples of such buttons are shown in figure 8.4. In some instances



Figure 8.4: Two examples of different buttons. To the left a button to change the current design tool to another, to the right a button to initiate a calculation

buttons are greyed out. This means that the button is currently inactive, and some other action must be performed before the task of interest can be initiated. Again, tool-tips are used in order to clarify what will happen when the specific button is clicked.

One type of GUI element allows different data to be entered, depending on what the user knows. These elements are so-called radio buttons, where one of multiple options must be

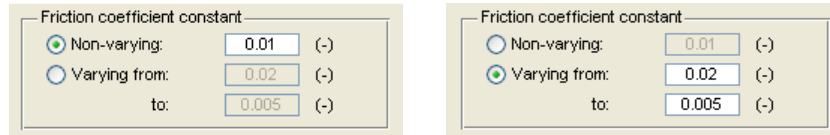


Figure 8.5: One example of a typical use of radio buttons. Here, two different options are available to two the user, where one must be chosen

chosen. One example is shown in figure 8.5. Apparently, two different options are at hand; a non-changing friction factor constant or a varying friction factor constant. By clicking on the corresponding radio button, the different text boxes for data entering changes. Selecting the above option activates the text box where non-changing friction factor data should be entered. The other text boxes are automatically greyed out and made inactive, in order to ensure the users understands what and where to enter data.

Check boxes are instead used for non-mandatory options, such as displaying specific graphical output. A check box for turning the visibility of the mean streamline on and off is presented in figure 8.6. Another difference, besides being non-mandatory to check, compared

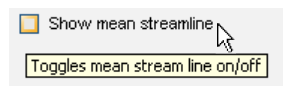


Figure 8.6: A check box for showing and hiding the mean stream line of an impeller design

to the radio buttons is that, if available, multiple check boxes may be checked. They are thus less restrictive than the radio buttons, ideal for presenting results in a way fully determined by the user.

## 8.3 Results of the individual analyses

This section describe the results from each of the analyses presented in chapters 3 to 7, together with the main features of the computer program. The focus lies on how the different results are presented. What input parameters necessary for each analysis has already been described in previous different chapters and will not be repeated here again.

### 8.3.1 Start-up of LURC

Using LURC requires having the MATLAB<sup>®</sup> suit installed on a computer. LURC is simply started by double-clicking on the MATLAB<sup>®</sup> function *LURC.m*. By doing this the program is started, showing the start-up view as seen in figure 8.7. Having started LURC, the different design tools are available by clicking on the corresponding buttons located at the top of the window. The start-up view itself serves no purpose more than introducing the program, giving feedback to the user that it is ready for further actions.



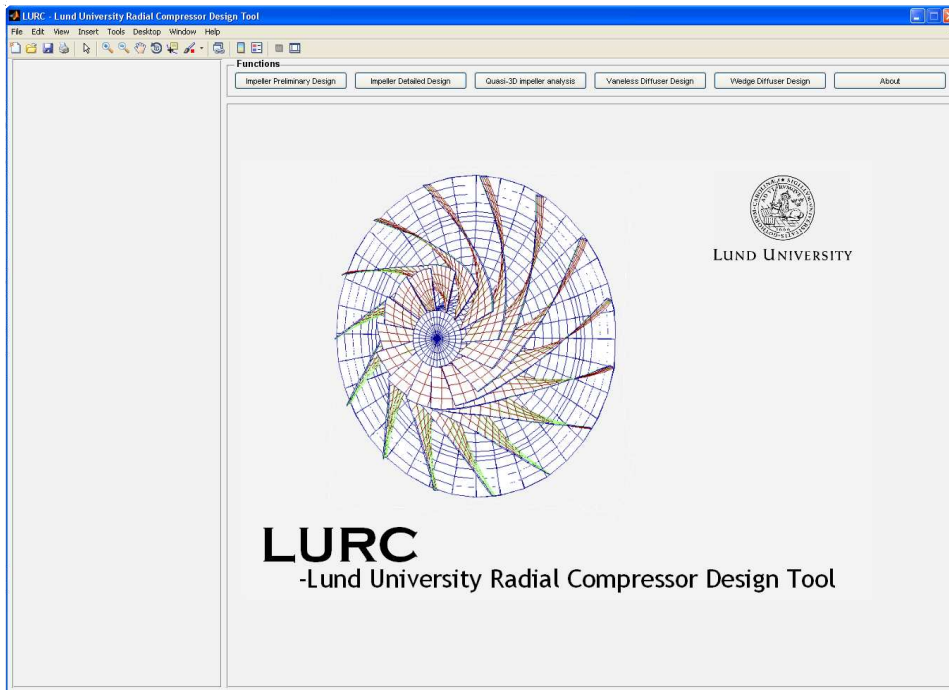


Figure 8.7: The start-up view of LURC. Note the different menu options at the top bar of the window

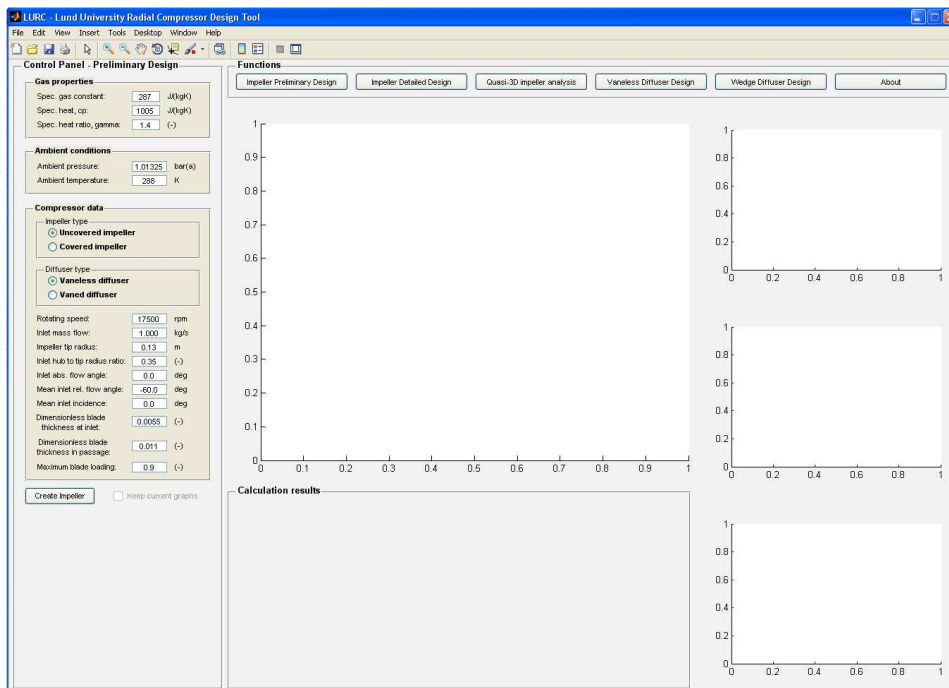


Figure 8.8: The view of the preliminary impeller design, before any user actions have taken place. Note the different axes, intended for presenting results

### 8.3.2 Preliminary impeller design

By starting the preliminary impeller design tool a screen as depicted in figure 8.8 shows up. Here, a control panel is displayed to the left, where the user is required to enter design data. In the middle, bottom, a panel for results are shown while the rest of the window have different axes<sup>1</sup>, prepared to show calculation results.

By filling in design data and pressing the button labelled *Create impeller* the complete analysis is run. All results are calculated immediately, no further actions from the user are required. In the result panel at the bottom, various single-parameter results are presented in greyed-out text boxes. A typical view is seen in figure 8.9. This result panel shows the

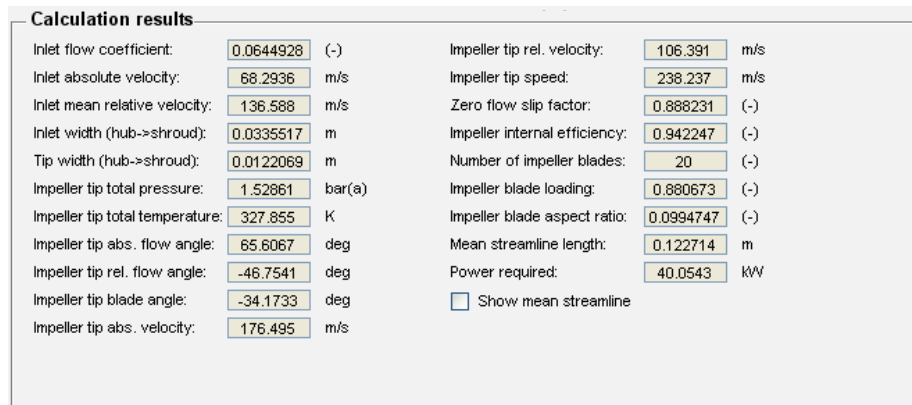


Figure 8.9: A typical view of preliminary impeller calculations, showing the result panel

main results of interest. Included are not only geometrical features such as inlet and discharge hub-to-shroud widths but also, for instance, thermodynamic discharge conditions. A result of huge importance are the flow coefficient, since many of the different parameters described in chapter 3 are highly dependent on this. Most of the presented parameters follows directly from the analysis, while some require a few simple extra calculations. This include, for instance, the required power input which is easily found from equation 2.19. The impeller blade loading is also presented, generally differing somewhat compared to the desired one entered in the control panel. This does of course stem from the fact that the number of impeller blades must be an integer. The analysis makes sure that the design becomes somewhat conservative; blades are added until the blade loading is less or equal to the set value.

The impeller hub and shroud contours found by the preliminary impeller design tool are also presented, and a typical result is seen in figure 8.10. These curves are one of the main results from this analysis, giving the designer a vital piece of information. Such contour plots are typically used for checking whether the found impeller geometry will have reasonable shapes with not too large curvatures. Further, since no generation of these contours are required from the user, this tool is ideal for the non-experienced designer. This group of users will quite quickly get a feel for how impeller geometries are typically chosen. Additionally, in the result panel an option for the impeller contour plots appears after running the analysis. With the aid of a check box, the user can toggle the mean stream line visibility on and off. The mean stream line is of some interest, since many of the parameters in the preliminary impeller design

<sup>1</sup>Axes are areas reserved for plotting in MATLAB<sup>®</sup>. They can be thought of as representing a coordinate system.

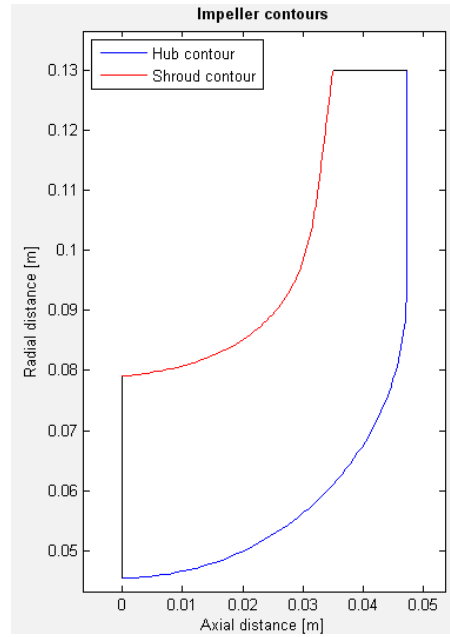


Figure 8.10: Impeller hub and shroud contours found by the preliminary impeller design tool. The hub consists of a circular arc, while the shroud contour is constructed from a three-point cubic spline as explained in chapter 3

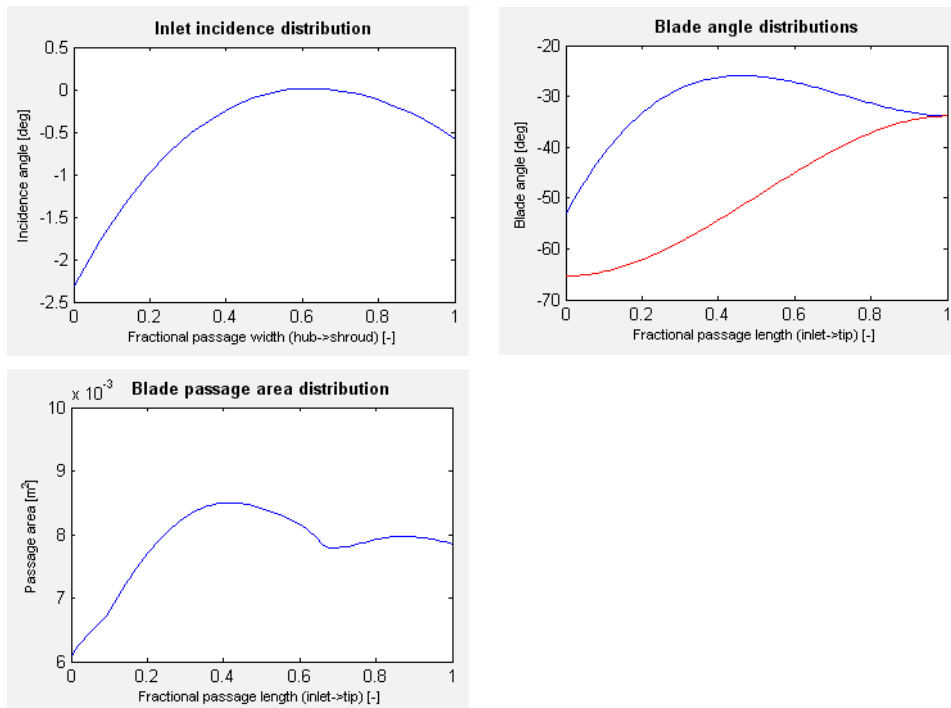


Figure 8.11: The final set of results from the preliminary impeller design tool. This include the inlet incidence distribution, the blade angle distribution at hub and shroud and the passage area distribution of the whole impeller

are set at this location, and it is thus interesting and important to know where this mean position is located.

Another set of results are also presented in the shape of three different axes on the right hand side of the window. These are showed in a collapsed format in figure 8.11. The first axes show the inlet incidence distribution along the (non-dimensionalized) inlet width. At the mean stream line position, the incidence equals the value set in the control panel by the designer. Further, its variation follows the rules described in chapter 3; with the shroud incidence set to 25% of the hub incidence. An indication of too large incidences here, might lead to redefinition of some design parameters.

A second axes shows the blade angle distribution, along both hub (blue line) and shroud (red line) of the impeller. These distributions correspond to the mean camberline angles, and are plotted versus the non-dimensional impeller passage length. Note that meridional passage lengths are different at hub and shroud, something that must be kept in mind while evaluating the result. Usually the hub blade angle distribution appears more "extreme" than the distribution at the shroud; however since the meridional passage length is longer at the hub location, the changes in blade angles are somewhat relaxed.

The third axes presents the passage area distribution, again versus the non-dimensionalized impeller passage length. Ideally the passage area changes should be smooth, and the designer may find that the passage area changes are too extreme. This passage area is somewhat idealized, since it assumes that the flow are perfectly guided by the blades. Nevertheless, it gives an important indication on how the area open to the flow changes along the impeller.

One final feature of the preliminary impeller design deserves attention. Having run the analysis also opens the possibility to keep the current impeller contours in the main axes. By checking this check box, the contours are coloured green and remain left in the axes, even when running a new impeller analysis. This function enable identification of changes in geometry, while varying one or more design parameters. Again, such a feature is well suited for designers with little or no experience exploring the influence of different settings.

### 8.3.3 Detailed impeller analysis

LURC takes the shape of figure 8.12 when starting the detailed impeller analysis tool. The control panel where design data should be entered is located to the left, the result panel at the bottom and various axes in the middle and to the right. As compared to the preliminary impeller design tool more data must be known and given as input to the calculation. This is expected, since more paramters are under direct control of the designer, as described in chapter 4.

Upon filling in appropriate data and clicking on the button *Pre-calculation* the main part of the impeller analysis is run. All features but the three-dimensional geometry generation described in chapter 4 are employed, including the optimized impeller inlet for minimum relative tip Mach number. The calculation result shows up in the result panel, together with some additional functions as seen in figure 8.13. All results relating to the inlet and exit of the impeller follows directly from the analysis itself; few extra calculations are necessary. The results themselves are quite straight forward to interpret, if it is unclear what any parameter means the tool-tips can give some guidance. One of the axes to the right also presents some result of the analysis, the inlet incidence distribution. Such a result is shown in figure 8.14. As was the case for the preliminary impeller design tool, the incidence distribution is shown as a function of the dimensionless passage width, from hub to shroud. The designer should check that all of the result parameters and the incidence levels are reasonable, before going

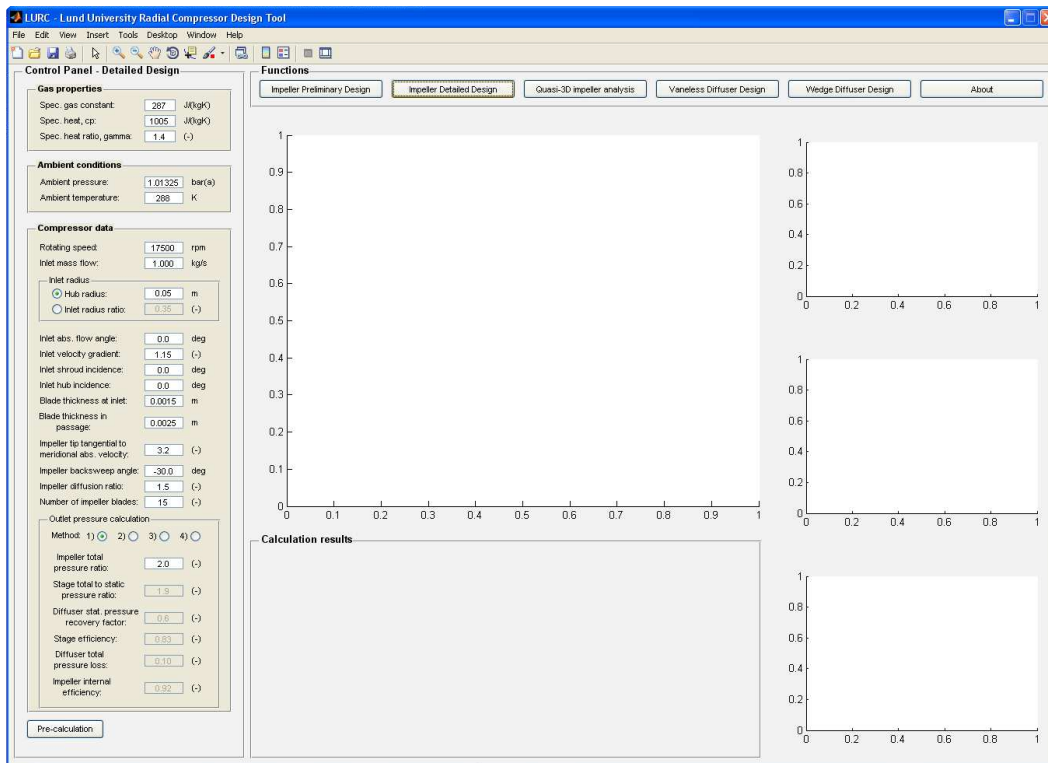


Figure 8.12: The window when starting the detailed impeller design tool. It has the same general outline as the preliminary detailed design tool.

Calculation results	
Inlet flow coefficient:	0.0263228 (-)
Inlet hub abs. velocity:	58.3445 m/s
Inlet shroud abs. velocity:	81.452 m/s
Inlet hub blade angle:	-57.5134 deg
Inlet shroud blade angle:	-61.4674 deg
Inlet shroud rel. velocity:	170.633 m/s
Inlet width (hub->shroud):	0.0318168 m
Tip width (hub->shroud):	0.00823473 m
Impeller tip total pressure:	2.0265 bar(a)
Impeller tip static pressure:	1.4995 bar(a)
Impeller tip total temp.:	362.794 K
Impeller abs. flow angle.:	72.646 deg
Impeller tip abs. velocity:	245.207 m/s
Impeller tip velocity:	321.171 m/s
Zero flow slip factor:	0.860202 (-)
Impeller internal efficiency:	0.857785 (-)
Machine Mach number:	0.944137 (-)
Power required:	75.1685 kW

Geometry specification and final calculation	
Impeller axial width to tip radius ratio:	0.50 (-)
<input type="button" value="Create hub/shroud contours"/> <input type="button" value="Create blade angle distr."/>	
Impeller inlet rake angle:	10 deg
<input type="button" value="Calculate!"/> <input type="button" value="Determine 3D geometry"/>	
Impeller exit rake angle:	deg

Figure 8.13: The result panel after running a detailed impeller pre-calculation. Not only calculation results shows up, but also additional functions

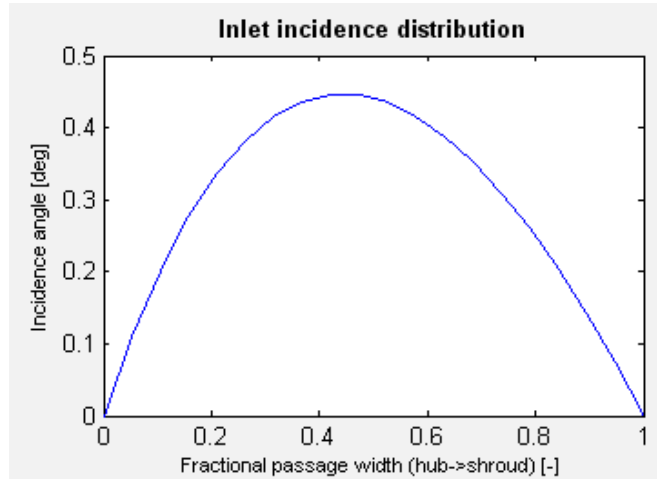


Figure 8.14: The inlet incidence distribution as found by the detailed impeller pre-calculation. Of course, at hub and shroud these equal the design values entered by the user

any further. Since many parameters may influence one and the same result, for instance a discharge static pressure, the designer can take many different paths in order to find satisfying results.

Having run the pre-calculation another set of buttons and text boxes appears in the result box, as was seen in figure 8.13. After filling in the impeller axial width to impeller tip radius ratio and clicking on the button *Create hub/shroud contours*, hub and shroud contours appear in the main axes located at the middle of the window. Together with these contours are also different Bezier curve handles shown as squares, see figure 8.15. By allowing the user to interactively shape the contours of the hub and shroud, the impeller design can be fine tuned to each individual design case. Both the inlet and exit impeller widths are locked, and cannot be modified by other means than a re-run of the pre-calculation with different design settings. Also, the impeller axial width can no longer be changed.

When suitable impeller contours have been found, the blade angle distribution need specification. These can be set by clicking on the button *Create blade angle distr.*, and again the main axes located in the middle of the window shows two Bezier curves with Bezier handles, as depicted in figure 8.16. Using this graphical interactive tool, the blade mean camberline angles can be set at both hub and shroud. The angles are plotted versus the dimensionless passage distance, allowing both curves to be shown simultaneously.

When satisfied with the mean camberline angle distribution the button labelled *Calculate!* may be pressed. By doing so, the passage area distribution with the current geometry is determined. The three axes located to the right presents the chosen impeller contours, mean camberline angle distribution and the passage area distribution, as shown in figure 8.17. The axes showing the contours and camberline angles are of course identical to the plots depicted before, but are presented again in order to have them conveniently accessible when evaluating the result. The passage area distribution are also plotted versus the dimensionless passage distance. Similarly to the preliminary impeller analysis, it is a somewhat idealized area distribution, assuming the flow completely follows the blades.

One final function exist; the possibility to create a three-dimensional representation of the impeller. After clicking on the *Calculate!* button the possibility to enter an inlet rake angle

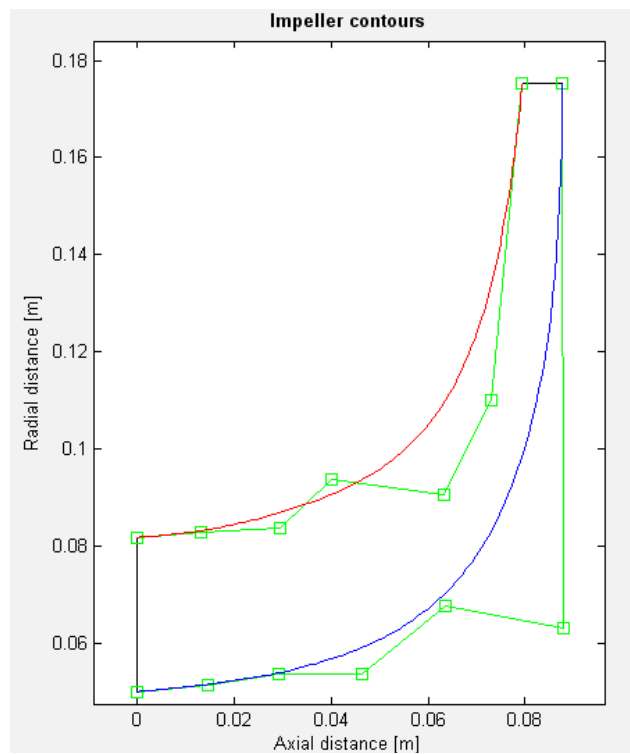


Figure 8.15: Editable Bezier hub and shroud contours, together with handles with which the designer can modify the contour shapes

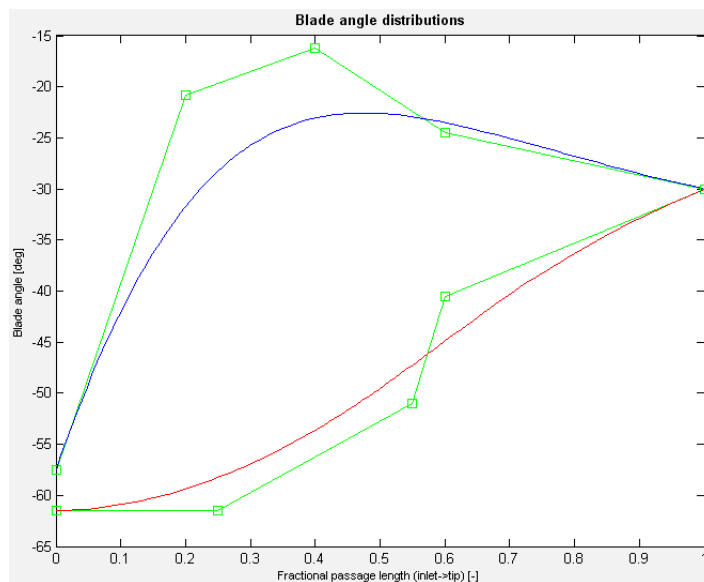


Figure 8.16: Editable Bezier mean camberline angles. Again Bezier handles are included to let the designer freely select any distribution. The mean camberline at hub is drawn with a blue line, while the shroud camberline is coloured red

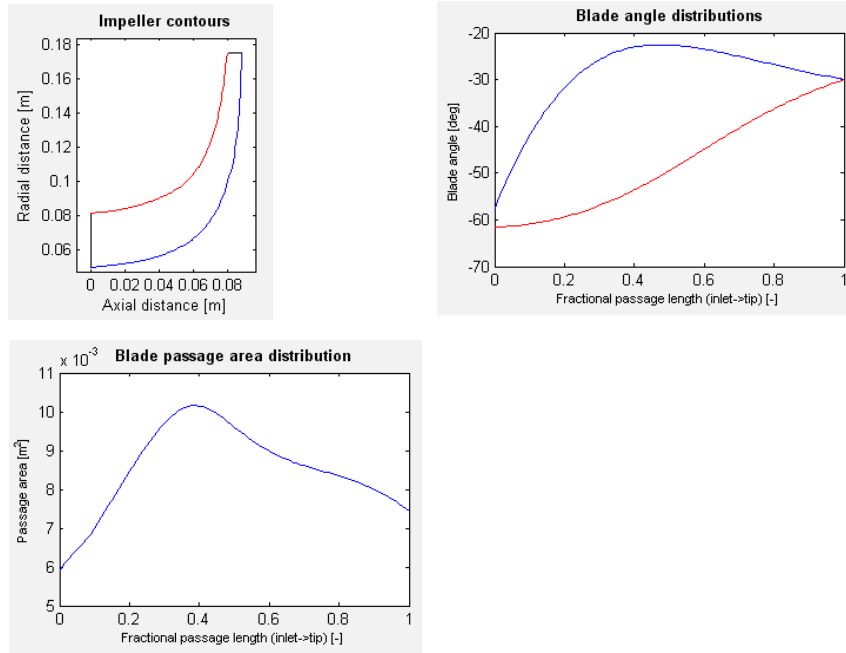


Figure 8.17: The result presented in the right hand axes of the window after clicking the *Calculate!* button. The axes are shown collapsed for convenience

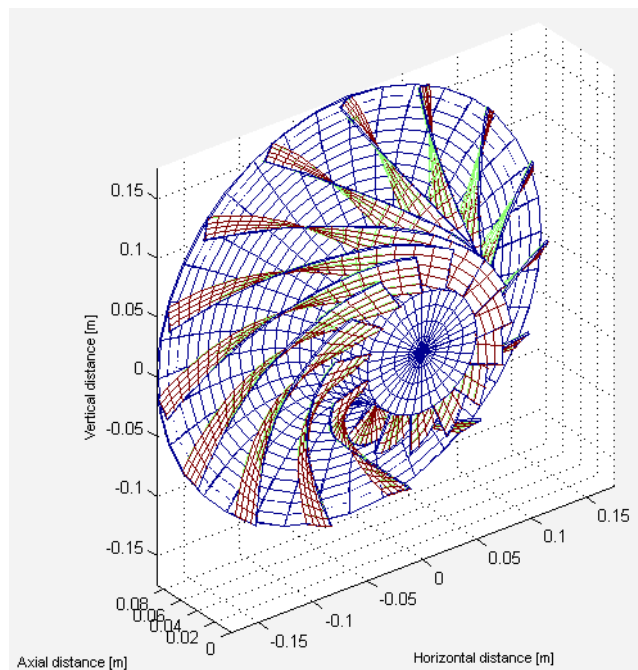


Figure 8.18: A three-dimensional impeller geometry generated in the detailed impeller analysis tool. This particular impeller had an exit rake angle of  $2.7^\circ$  with an inlet rake angle of  $10^\circ$



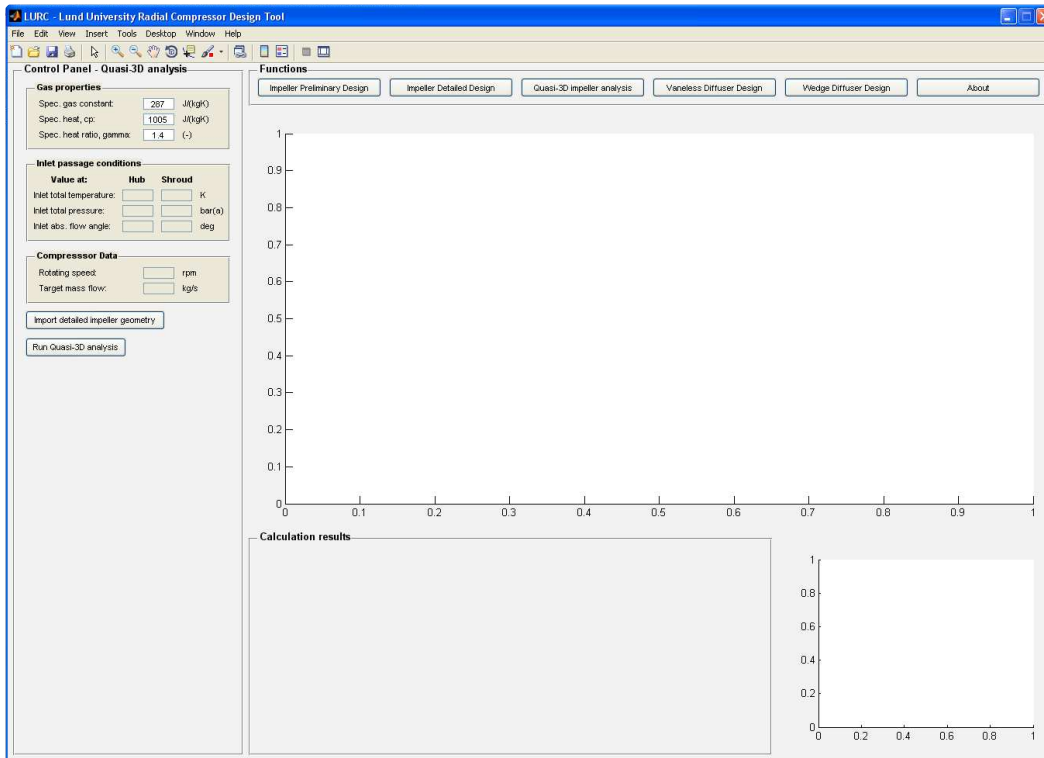


Figure 8.19: The view of the quasi three-dimensional impeller analysis. Note the small amount of input data needed in the control panel to the left

opens up. This angle are typically adjusted to fine tune the exit rake angle, which must be kept within reasonable limits. By entering an inlet rake angle and pressing the button *Determine 3D geometry*, the exit rake angle are presented in a result text box while the three-dimensional geometry are generated. The resulting geometry is displayed in the main axes located at the middle of the window. A typical three-dimensional geometry generated are shown in figure 8.18. Many times it is found that the exit rake angle becomes, in absolute values, very large. It is then necessary to alter either the impeller contours, mean camberline angle distributions or the inlet rake angle. In the worst case a complete redefinition of the design may be necessary. Regardless of what changes must be made, a somewhat iterative approach is needed to find a design working not only aerodynamically and thermodynamically well, but also one that is manufacturable and feasible in practice.

### 8.3.4 Impeller internal flow analysis

The impeller internal flow analysis, or equivalently the quasi three-dimensional analysis, have a start-up window as shown in figure 8.19. A control panel is located on the left hand side, where input data must be entered. At the bottom a panel reserved for presenting results appear, while two axes aid the display of the calculation findings. These axes are located in the middle of the window and at the bottom right.

In order to run the impeller internal flow analysis the geometry of the impeller must already have been generated. This is done by using the impeller detailed design tool, as described in

the previous section. Thus, by clicking on the button *Import detailed impeller geometry*, the results of the detailed impeller analysis tools are imported, together with the inlet properties chosen for this design. Of course, these inlet properties may be altered and changed arbitrary by the designer if desired. Also, the desired mass flow and rotating speed are imported; these may also be changed at any time. The three-dimensional geometry is plotted in the main axes located in the middle of the window, giving the user some feedback that the geometry has been fetched. Such a plot looks exactly like the one shown in figure 8.18 and need no further explanation. It is important to note that no changes to the geometry itself are possible using the quasi three-dimensional design tool. This tool is strictly used for the flow analysis itself. If changes to the geometry are needed one must resort to the detailed impeller design analysis. This presents no problem since easy access to both tools are available with aid of the menu bar at the top of the window.

Having set the correct inlet conditions, the quasi three-dimensional flow analysis may be initiated by pressing the *Run Quasi-3D analysis* button. If the analysis converges without any errors a dialogue box appears as shown to the left in figure 8.20. No results are presented if

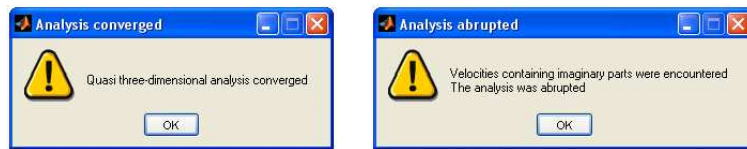


Figure 8.20: Different dialogue boxes appears depending on whether the analysis converges or not. To the left is the dialogue box shown after a converged solution and to the right the dialogue box when the quasi three-dimensional analysis did not converge

the solution did not converge, but the dialogue box to the right of figure 8.20 is generated. Different reasons can exist when convergence problems appear, usually one can track the issue to supersonic velocities on some of the blade surfaces. Since the analysis depends on a stream function solution, it will diverge if velocities higher than the sonic ditto appears. Thus, some parameter(s) must be altered. Sometimes it is sufficient to alter some inlet conditions which can be done directly in the quasi three-dimensional analysis tool. In some cases, a complete redefinition of the whole impeller geometry itself is necessary, which must be carried out with the detailed impeller analysis tool. If instead the solution does converge, results are presented and the axes at the bottom right presents the stream surface pattern as found by the calculation. The result panel typically takes the form of figure 8.21. The results are a direct consequence of the analysis, and gives the designer important information of the discharge conditions, and the final mass flow of the impeller. This mass flow may be reduced during the solution process due to choking conditions in the hub-to-shroud solution. A typical stream surface pattern is shown in figure 8.22.

As was seen in figure 8.21 additional options appeared at the right hand side of the result panel. These are plot tools, allowing the designer to determine what velocity results should be visible on the main axes located in the middle of the window. By checking different radio buttons, one can choose between relative velocities or Mach numbers. Also, the choice between blade-to-blade flow velocities or hub-to-shroud velocities (through-flow velocities) can be made with simple radio buttons. A set of check boxes are also available, from which the user can pick certain stream surfaces to be included in the plot result. More than one stream surface can be presented at the same time by checking multiple check boxes. Typical Mach

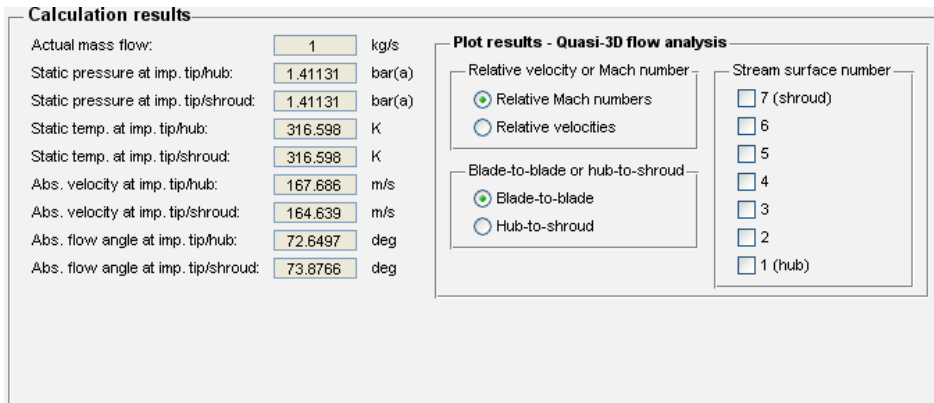


Figure 8.21: The result panel of a quasi three-dimensional flow analysis showing single parameter results to the left. To the right different options for presenting velocity distributions graphically are available

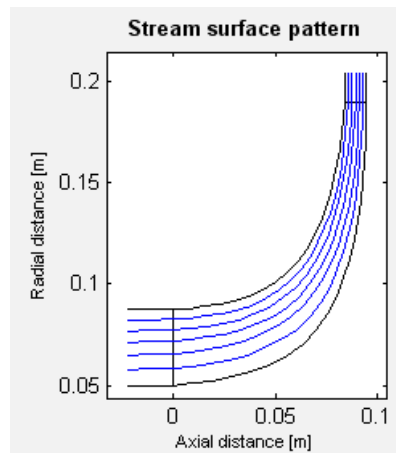


Figure 8.22: An example of stream surface patterns, whose positions are iteratively updated in the quasi three-dimensional analysis

number distributions in the blade-to-blade plane is shown in figure 8.23. The Mach number or velocity distributions are plotted against the dimensionless blade surface distance, enabling all distributions to be shown in the same axes. Blue lines represent pressure side conditions, while red lines indicate suction side conditions. In this figure, it is seen that the Mach number distributions meet each other at the trailing edge, as implied by using the Kutta condition as one of the boundary conditions.

If instead choosing hub-to-shroud relative Mach numbers results similar to those of figure 8.24 can be expected. Here, Mach numbers based on the meridional through-flow velocity are presented as a function of dimensionless meridional distance. These can show quite large differences between hub and shroud surfaces, the difference stemming from the solution of the momentum equation. As has already been stressed, which stream surfaces to plot is in full control of the designer, in the above example only two of the available seven stream surfaces were shown.

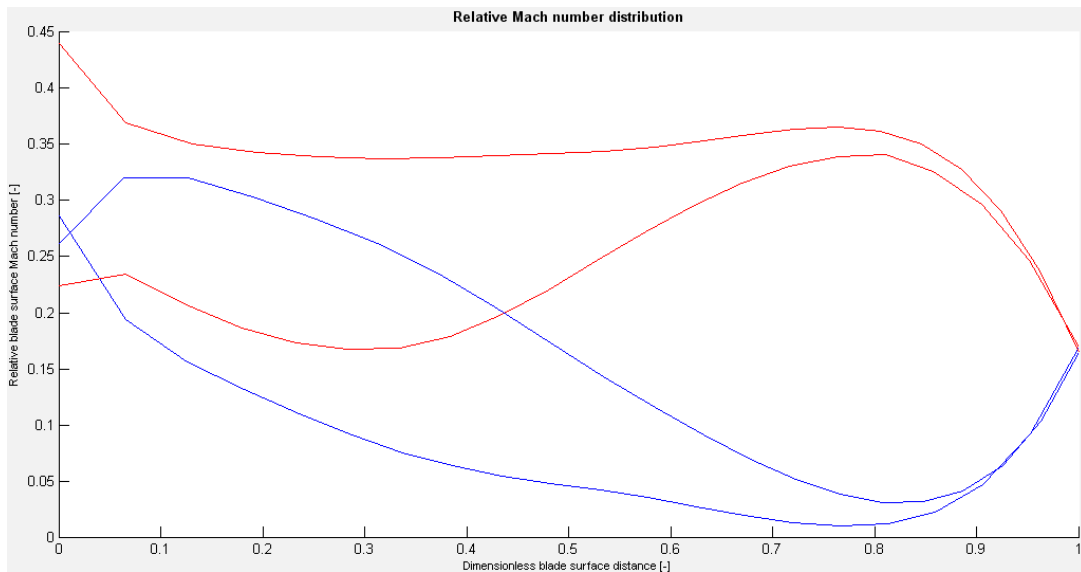


Figure 8.23: Mach number distributions as found by the impeller internal flow analysis. These are blade-to-blade Mach numbers, where red lines indicate the suction side and blue lines the pressure side. The velocity distribution with higher levels of Mach numbers is located at the shroud, while the one with lower levels represents the hub surface

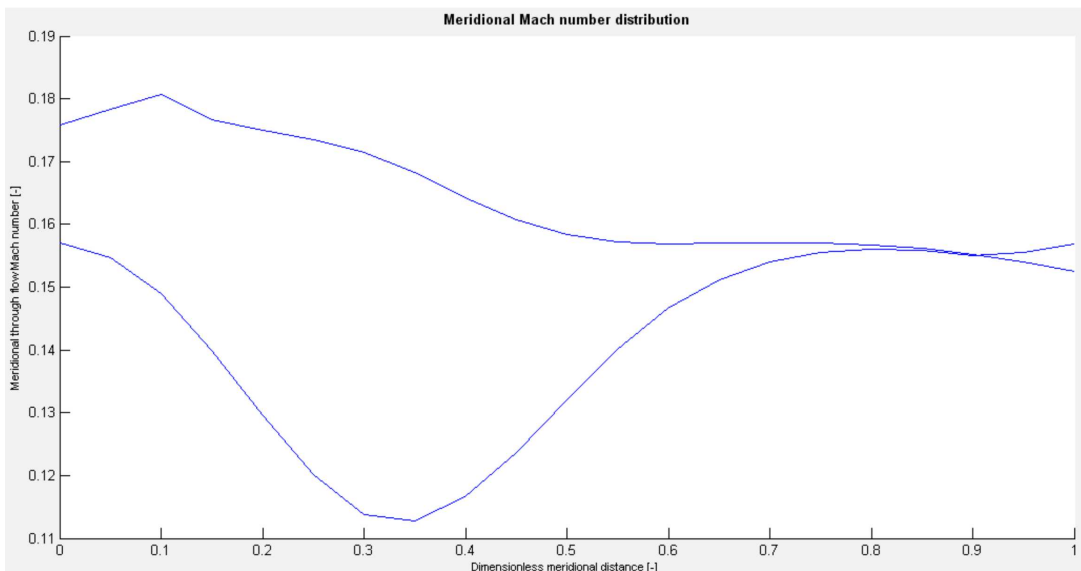


Figure 8.24: Typical meridional Mach number distributions as found by the hub-to-shroud flow analysis. The top curve represents meridional through-flow Mach numbers at the shroud surface, while the lower corresponds to meridional Mach numbers on the hub surface

### 8.3.5 Vaneless diffuser analysis

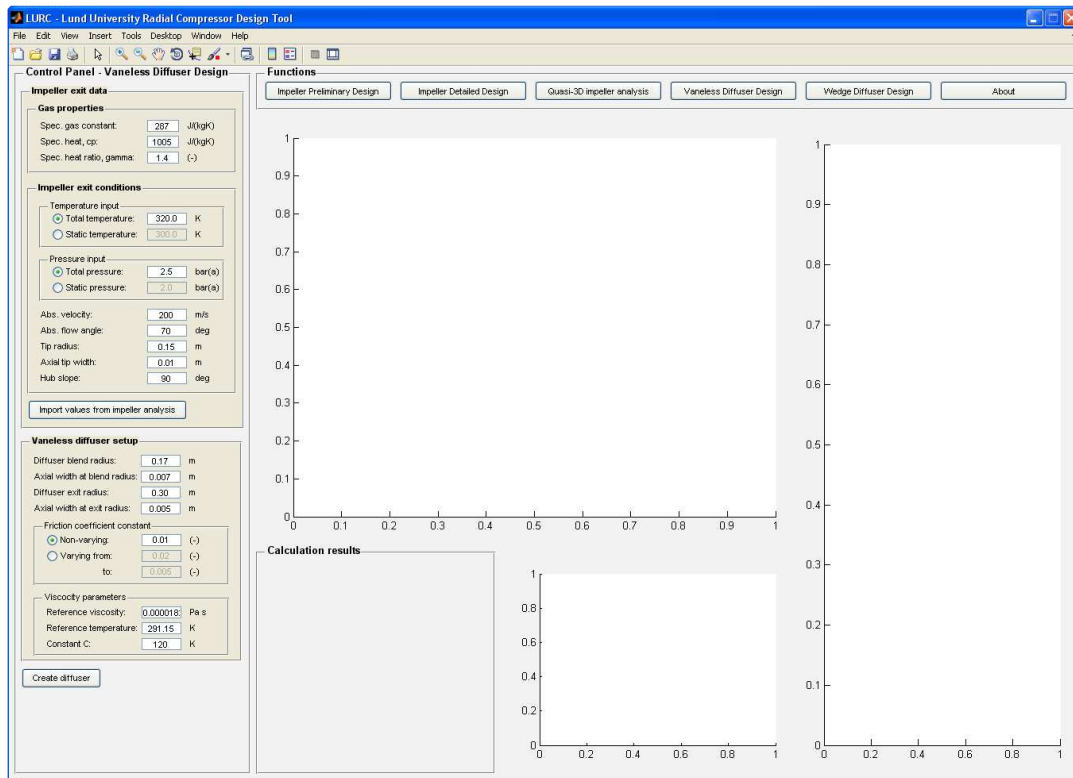


Figure 8.25: The start-up view of the vaneless diffuser design tool. Note the similarity of the layout between this and the impeller analyses

When starting the vaneless diffuser design tool the view of figure 8.25 is found. A control panel where input data is to be entered is located to the left, a result panel at the bottom and three axes; one in the middle, one at the bottom and one at the right hand side. In order to make it as easy as possible for the user, all layout features have been kept as similar as possible to the different impeller design tools.

The analysis allows the user to manually enter diffuser inlet data. This is well suited to use, for instance, when no impeller design is known or the exact impeller discharge conditions are at hand. Another approach is to import impeller discharge data from a previous impeller analysis pressing the button *Import values from impeller analysis*. This does, of course, mean that an impeller must have been designed using either the preliminary or detailed impeller design tool.

When satisfied with the design parameters, the analysis is run by clicking on the *Create diffuser* button. By doing so, the complete analysis is run. In the bottom panel, the key results are presented as shown to the left in figure 8.26. Of huge interest are the velocity distribution within the diffuser, since the main purpose of the component is to lower the velocity. This distribution is plotted in the axes at bottom, right next to the result panel. A typical velocity distribution, as a function of the non-dimensionalized fluid path length, is shown to the right in figure 8.26. A small kink in the velocity distribution may be seen in the inlet portion. This is due to the vaneless diffuser pinch, where the diffuser walls converge quite rapidly. To a certain extent, this contraction counteract the diffusing mechanism of the fluid particle radius increase.

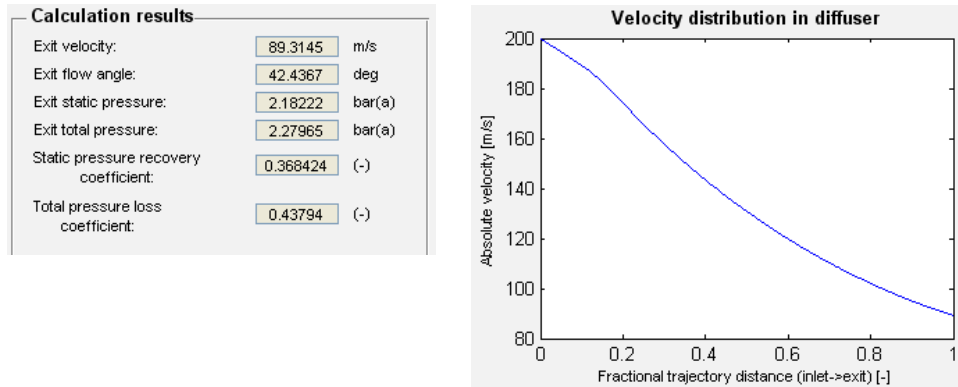


Figure 8.26: To the left a result panel of the vaneless diffuser design tool after running the analysis. Note that most of the parameters relate to the diffuser exit condition. To the right the velocity distribution, as a function of the non-dimensionalized fluid path length, within the diffuser is shown.

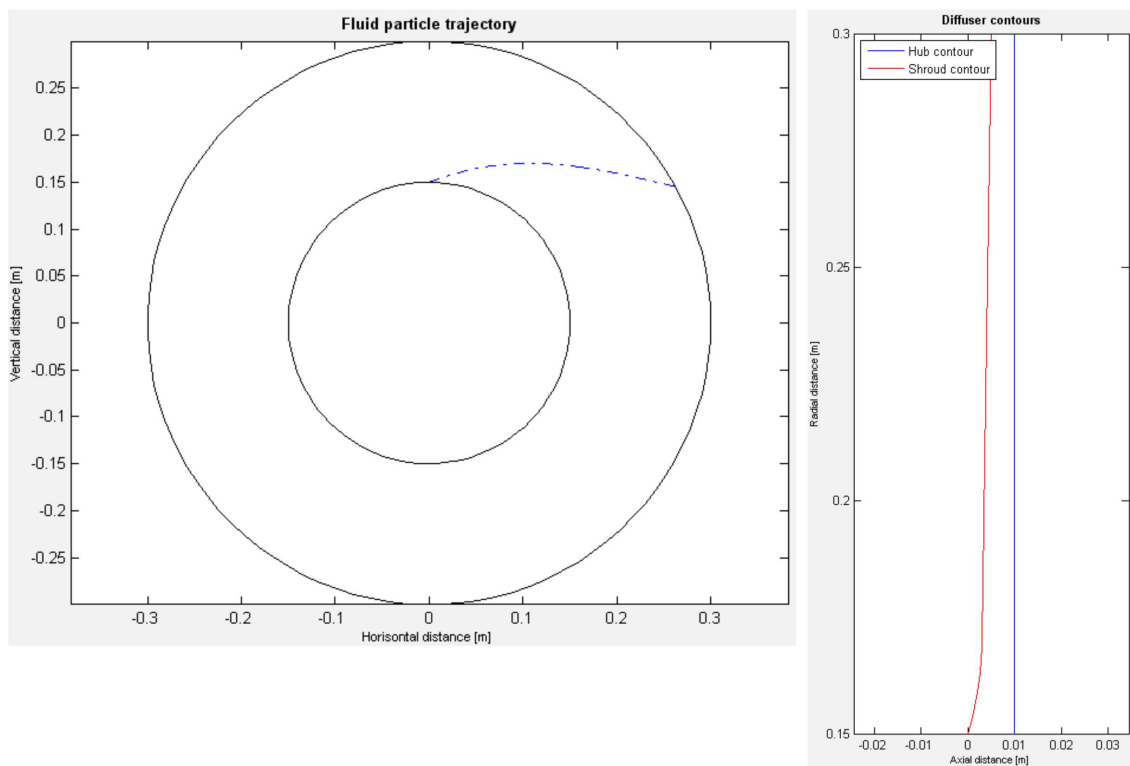


Figure 8.27: The final results of the vaneless diffuser analysis tool. To the left are an axial view of the diffuser shown, together with a fluid particle trajectory. To the right, the diffuser contours as found by the analysis are shown

In order to let the designer get a feel for how long the actual fluid path is, an axial view of the vaneless diffuser is shown in the main axes, in the middle of the window. Together with the diffuser outer and inner radius, an imaginary fluid particle's trajectory is also included. An example of such a plot is shown to the left in figure 8.27.

Since fluid paths tend to be quite long in vaneless diffusers, this graphical result is of very high importance. Also, it makes it easy to study how the fluid trajectories alters when, for instance, changing the friction coefficient. To the right of figure 8.27 are the hub and shroud contours as determined by the analysis. How the contours are shaped is also an important piece of information. One example could be if the diffuser pinch turns out to be too extreme. This is easily spotted in this axes, and corrective measures can be taken by altering the geometry data input.

Two of the results of the vaneless diffuser analysis are the static pressure recovery coefficient and diffuser total (stagnation) pressure loss. These can be used as input data in the detailed impeller analysis tool, as a mean to determine the impeller exit thermodynamic condition. Hence, these are conveniently used in that impeller analysis tool. However, if the impeller and diffuser are intended to work together, the inlet condition to the vaneless diffuser depend on the impeller solution. Hence, an iterative approach is needed to correctly match these components with each other, if one of these parameters is used as impeller input data. This has also been noticed by Japikse (1996).

### 8.3.6 Wedge diffuser analysis

The last analysis tool available in LURC is the wedge diffuser design tool. When initiating this tool the window takes the form of figure 8.28. The same features as in the vaneless diffuser design tool can be recognised; a control panel to the left, a result panel and an axes at the bottom, a main axes in the centre and an axes at the right hand side of the window. As can be seen in the control panel, quite a lot of data must be entered. If an impeller analysis has been run before entering the wedge diffuser analysis tool a similar feature as for the vaneless diffuser design tool can be found; a button labelled *Import values from impeller analysis*. By clicking this button, all inlet parameters of the wedge diffuser are imported.

After entering all necessary design data, the analysis can be started by pressing the *Create diffuser* button. The analysis is then run, solving equations governing both the vaneless space and the channel diffuser flow. When the calculation is finished, the result panel is updated, presenting all vital results. Typical results of this analysis is shown to the left in figure 8.29. Most of the results presented are related to the vaneless space and wedge diffuser exit. Some geometrical features are also included, such as the number of wedges and each channel's area ratio. The axes also presents important results. Next to the result panel, an axes shows the velocity distributions within the vaneless space and diffuser channels, see the right hand side of figure 8.29. Coloured in blue is the vaneless space velocity distribution while the red curve represents the corresponding distribution within the channel diffuser itself. The velocities are plotted versus the non-dimensionalized fluid path, enabling both distributions to be visible in the same axes. A quick look at this axes might lead to the conclusion that the diffusion process within the channels are much more efficient than within the vaneless space since the velocity seem to be lowered much more rapidly here. However, one must bare in mind that the vaneless space is generally much shorter than the channel diffuser part and can thus not be expected to lower the velocity as much as within the whole channel diffuser part. Hence, when interpreting this axes it is important to remember that the velocities are presented versus the *non-dimensionalized* fluid path. Further, it is seen that the velocity distributions

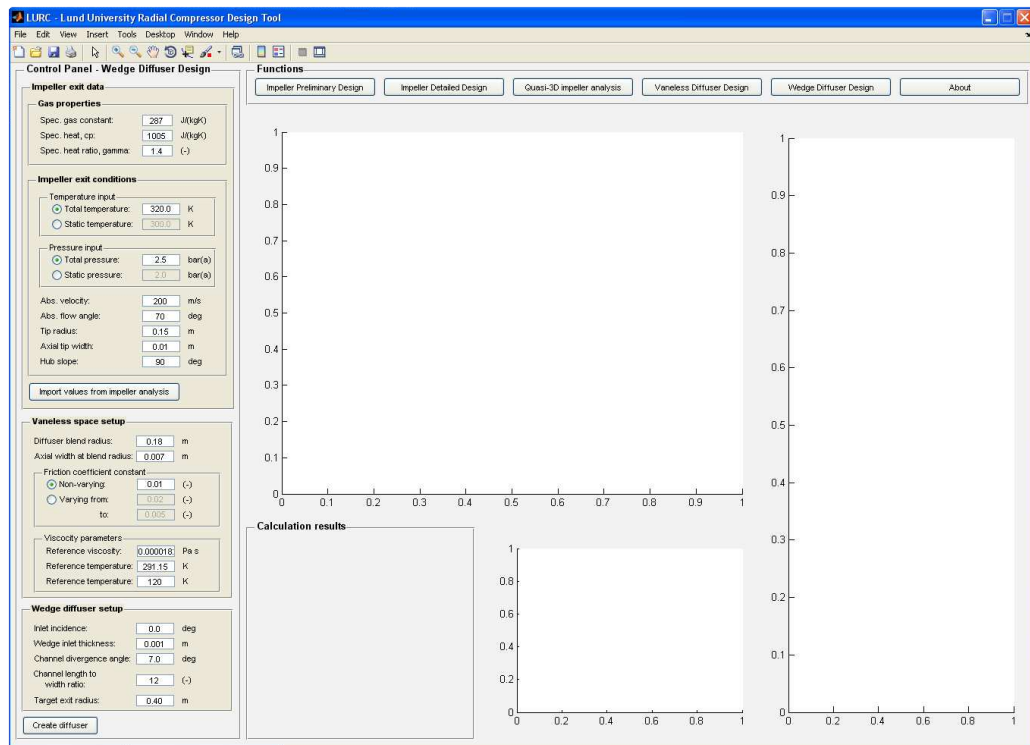


Figure 8.28: The general outline of the wedge diffuser design tool. The main difference from the vaneless diffuser tool is some additional input data

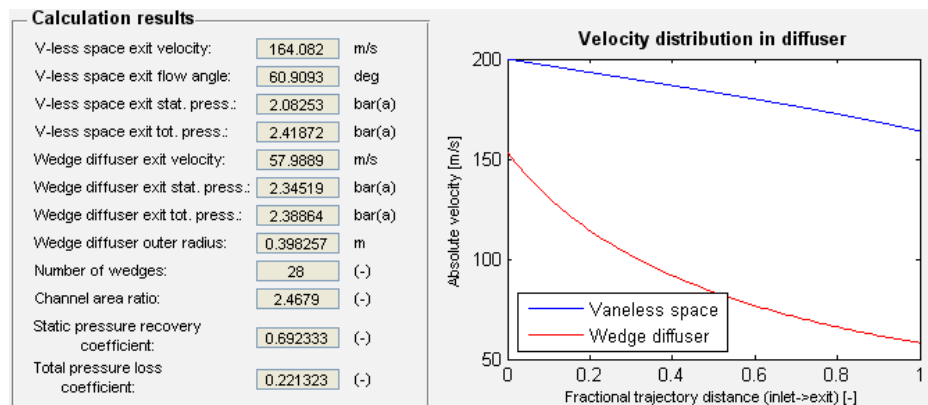


Figure 8.29: The result panel (left) and velocity distribution in both the vaneless space and within the channels (right) shown as a consequence of the wedge diffuser analysis being run



don't have the exact same velocities at the vaneless space - channel diffuser interface. This is because some diffusion (modelled as isentropic) takes place in the inlet region of the wedges, see chapter 7.

The other two axes presents results similar to what they were showing in the vaneless diffuser analysis tool, see figure 8.30. To the left, the vaneless space trajectory can be seen together with the channels created by all wedges. The general layout of the wedge diffuser is quite interesting to observe, and also how the different channel properties (length to width ratio, divergence angle) may change the same. Also, by simply comparing geometries with the vaneless diffuser analysis tool, any designer will quite quickly get a feel for the quite space efficient diffusion realized with a vaned diffuser. To the right of figure 8.30, the diffuser contours are shown. The hub contour is coloured blue and the shroud contour red. Also displayed is a black cross showing where the wedge diffuser is located.

As was the case for the vaneless diffuser analysis tool, within the results panel both the static pressure recovery coefficient and diffuser total (stagnation) pressure loss are presented. If one of these parameters are used in an impeller analysis to find the inlet state to the diffuser, an iterative approach is required, as was described in section 8.3.5.

### 8.3.7 About

One final menu option exists at the top menu bar of LURC. By clicking on the button *About* a very brief introduction to the program and the different design tools appears, see figure 8.31. This serves as a quick start guide to LURC, and is by no means exhaustive.

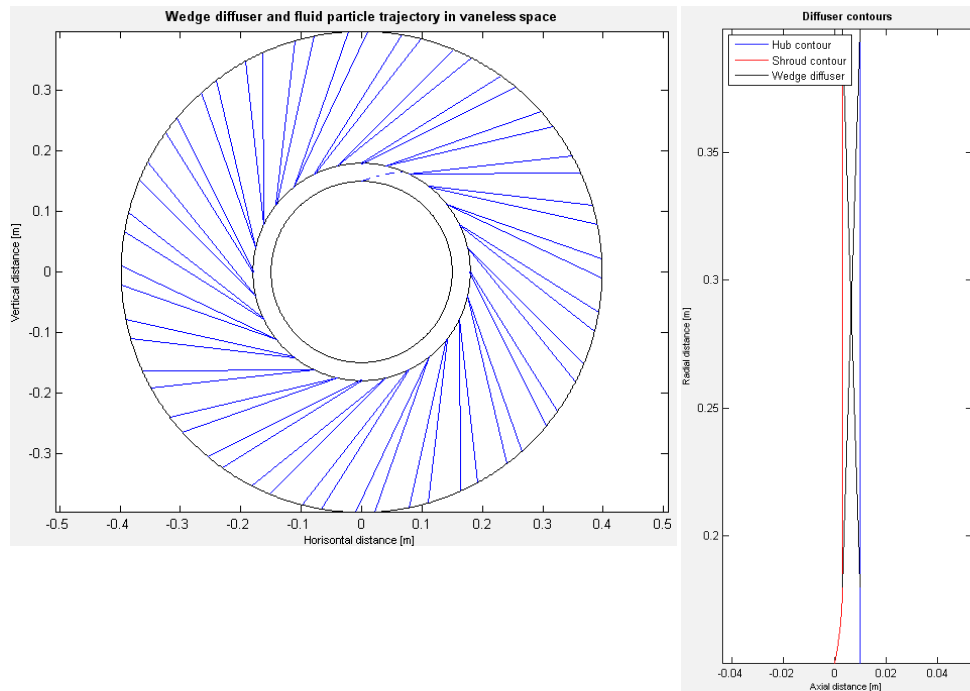


Figure 8.30: The geometry result of the wedge diffuser analysis. To the left are the trajectory within the vaneless space shown, along with all wedges characterizing the diffuser. To the right are the hub and shroud contours of the diffuser shown.

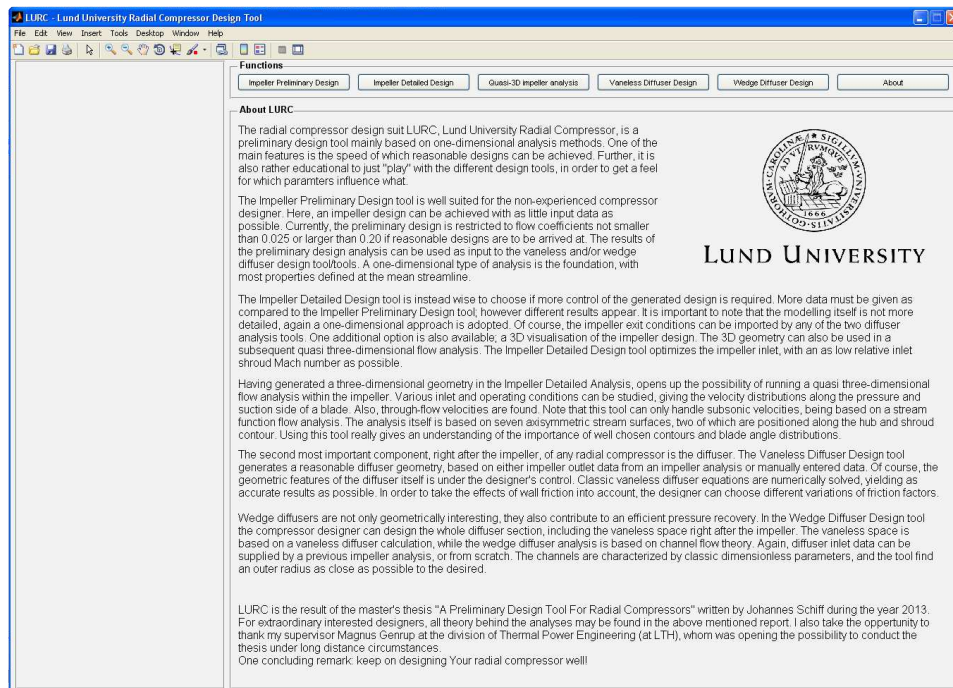


Figure 8.31: The About-view in LURC. This part of the program gives quick background information and some guidance to the different design tools

# Chapter 9

## Conclusions

This final part of the report gives some concluding remarks, mainly referring to the questions given in section 1.3. Also, potential improvement areas of the analyses are brought up.

### 9.1 Questions answered

The first question that was to be answered were how to model the impeller in a quick and efficient manner. This question has been answered in chapter 3 and 4 where two different models were outlined. Although both models are one-dimensional, they have been implemented in two separate ways. The preliminary impeller analysis provide a very fast mean to find an impeller geometry and performance. Since many of the important parameters, such as impeller internal efficiency, are determined completely within the analysis the results can be assumed rather reasonable. The detailed impeller analyses is also a very fast tool, but will require some knowledge of the user when selecting design data. It is not impossible at all to use this tool and find an internal impeller efficiency above 1. Thus, this tool require, to a larger extent, critical evaluation of the results calculated. Also, since the geometry of the impeller may be determined completely by the designer it gives a huge freedom of design choices. However, it again requires wise choices of the designer to get results applicable in practice. Nevertheless, both models can with no doubt be regarded as both quick and efficient giving the first question in section 1.3 two answers.

To answer the second question, if there is a method to study the impeller in a more thorough way, the answer is simply yes. To dig a little deeper, chapter 5 gives the full length answer, describing a type of analysis having found broad application within the turbomachinery field. Streamline curvature methods are widely accepted throughout the industry, see for instance Casey and Robinson (2008). This method must also be regarded very quick and efficient, giving the designer an idea of the velocity distribution in matter of tenths of a second. The quasi three-dimensional flow analyses implemented is based on the detailed impeller design and any changes found necessary in the internal flow analysis is easily changed using the detailed impeller analysis tool.

The third question found in section 1.3 related to the vaneless diffuser; how can an analysis method for these components be found? The answer is given in chapter 6. Here, a model taking not only compressible effects but also the phenomena of wall friction into account has been employed. Using this type of model is an improvement compared to the very simple constant angular momentum theory. Although the use of a friction factor can by no means model all phenomena encountered in a vaneless diffuser, it serves as a convenient and efficient way to

incorporate deviations from constant angular momentum behaviour. Further, the computer implementation allows a varying friction factor along the fluid path, giving the designer an extra degree of freedom when analysing a vaneless diffuser.

Finally, the last question, in what way a vaned diffuser can be modelled, is answered throughout chapter 7. In this work, the analysis was focused towards channel diffusers of the wedge type. Since all vaned diffusers contain some amount of vaneless space, the theory of vaneless diffusers was again applied to this part of the diffuser. Within the channels compressible channel flow theory was applied, again making use of the friction factor concept. Using the one-dimensional methods for modelling diffusers gives rise to fast solutions and reasonable result of the expected performance levels. However, the flow leaving the impeller is everything but one dimensional, something any designer must keep in mind.

Looking at the computer program in general, it is a rather straight forward design suite, enabling the designer to quickly change what design tool to use. Also, many of the different analyses are interconnected, enabling results from one module to be used in another. Using computers of current standard, solving problems in any of the design tools takes no longer than a few seconds. The program thus fulfil the main objective; being a fast and efficient computer program, taking many different aspects of the compressor into account. Also, a lot of effort have been put in to make LURC as easy and intuitive as possible to use. One of the intentions has been to allow any engineer interested in radial turbomachinery to use the program, regardless of what knowledge level he or she has.

## 9.2 Future work - possible improvements

Developing a modelling program such as LURC one quite quickly understand the limitations of one semester's work. There is simply not enough time to include and model all phenomena as one would want. Below is a list with different areas where future work could be focused.

- The inlet section of the compressor has been neglected in this work. Some model for this rather important section could be included, somewhat altering the flow field into the impeller
- At outlet of the impeller, the flow has been assumed one dimensional. Japikse (1996) presents the now well known theory for the jet and wake model yielding more accurate results at this location. This model should be feasible to implement together with the detailed impeller design tool
- The quasi three-dimensional flow analysis could be extended to handle supersonic velocities. This makes it necessary to depart from a stream function solution of the blade-to-blade flow. Inclusion of such a solution would make the analysis very stable, with less tendency to diverge during early iterations
- To take the quasi three-dimensional analysis even further, including effects of "spanwise" mixing in the quasi three-dimensional analysis, meaning fluid exchange between different stream surfaces, would be advantageous. Also, some mean of entropy increase along stream surfaces would be desirable to model
- The semi vaneless space of the wedge diffuser is a zone having an extremely complicated flow field. Modelling this area as isentropic is convenient but also a rather crude assumption. Thus, finding a model for the interface between the vaneless space and channel diffuser part is a potential improvement area

- No model has been incorporated for the volute, following the diffuser. This is a very important component, usually having an impact of the whole compressor characteristic. Breambussche (2013) provide a very thorough analysis of this component. Alternatively, a model for return channels may be implemented
- So called splitter blades have been neglected. These are blades situated at the rear part of the impeller, in between the full blades, spanning part of the impeller flow passage. The geometry generation and quasi three-dimensional flow analysis of the impeller could be extended to include these



# Chapter 10

## Bibliography

- [1] S.L. Dixon, B. Eng, *Thermodynamics of Turbomachinery Fifth Edition, in SI/Metric units*, Elsevier Butterworth-Heinemann 1998.
- [2] R.H. Aungier, *Centrifugal Compressors A Strategy for Aerodynamic Design and Analysis*, ASME 2000.
- [3] D. Japikse, *Centrifugal Compressor Design and Performance*, Concepts ETI, Inc. 1996.
- [4] R.A. Van den Braembussche, *Centrifugal Compressors Analysis & Design, Course Note 192, Revised Edition*, Von Karman Institute 2013.
- [5] C. Rodgers, *Typical Performance Characteristics of Gas Turbine Radial Compressors*, Journal of Engineering for Power, p. 161-175, April 1964.
- [6] Y.A. Çengel, M.A. Boles, *Thermodynamics An Engineering Approach Sixth Edition (SI Units)*, McGraw-Hill 2007.
- [7] N.A. Cumpsty, *Compressor Aerodynamics*, Krieger Publishing Company 2004.
- [8] *CVDI 2045 Acceptance and performance tests on turbo compressors and displacement compressors; test procedure and comparison with guaranteed values*, VDI-verlag GmbH, Düsseldorf, 1993.
- [9] J.D. Stanitz, *One-dimensional Compressible Flow In Vaneless Diffusers Of Radial And Mixed-flow Centrifugal Compressors, Including The Effects Of Friction, Heat Transfer And Area Change*, NACA Washington, January 1952.
- [10] E.M. Greitzer, C.S. Tan, M.B. Graf, *Internal Flow Concepts and Applications*, Cambridge University Press 2006.
- [11] G.F.C. Rogers, H.Cohen, H.I.H. Saravanamuttoo, P.V.Straznicky, *Gas Turbine Theory*, Prentice Hall 2009.
- [12] J.D. Anderson Jr., *Fundamentals Of Aerodynamics SI*, McGraw-Hill 2011.
- [13] R.H. Aungier, *Centrifugal Compressor Stage Preliminary Aerodynamic Design and Component Sizing*, ASME 1995.
- [14] S.A. Korpela, *Principles Of Turbomachinery*, John Wiley & Sons Inc, 2011.

- [15] M. Casey, D. Rusch, *The Design Space Boundaries For High Flow Capacity Centrifugal Compressors*, ASME Turbo Expo 2012, ASME paper no. GT2012-68105.
- [16] M.V. Herbert, *A Method Of Performance Prediction For Centrifugal Compressors*, National Gas Turbine Establishment 1980.
- [17] M. Casey, F. Gersbach, C. Robinson, *An Optimization Technique For Radial Compressor Impellers*, ASME Turbo Expo 2008, ASME paper no. GT2008-50561.
- [18] C-H. Wu, *A General Theory Of Three-Dimensional Flow In Subsonic And Supersonic Turbomachines Of Axial-, Radial-, And Mixed-Flow Types*, NACA Washington, January 1952.
- [19] M. Casey, C. Robinson, *A New Streamline Curvature Throughflow Method For Radial Turbomachinery*, ASME Turbo Expo 2008, ASME paper no. GT2008-50187.
- [20] R.H. Aungier, *Axial-Flow Compressors A Strategy For Aerodynamic Design And Analysis*, ASME 2003.
- [21] N. Falck, *Axial Flow Compressor Mean Line Design*, master's thesis at the Division of Thermal Power Engineering, Department of Energy science, Lund University, February 2008.
- [22] K.F. Riley, M.P. Hobson, S.J. Bence, *Mathematical Methods for Physics and Engineering Third Edition*, Cambridge University Press 2006.



# Appendix A

## Rotated coordinate systems

When constructing different geometrical objects, for instance the impeller contours, it is sometimes advantageous to make use of  $\tan \alpha_C$  for describing the slope. This approach works fine until large slopes in the vicinity of  $90^\circ$  angles are encountered. Here, the slope becomes infinite and any calculation would fail. One way to overcome this drawback is by utilizing rotated coordinate systems as outlined by Aungier (2000). If the coordinate system is rotated, the  $90^\circ$  angle in the original coordinate system is no longer  $90^\circ$  in the rotated one. A typical example is shown in figure A.1. If, for instance, the slope of the point  $(X_2, Y_2)$  is needed in a

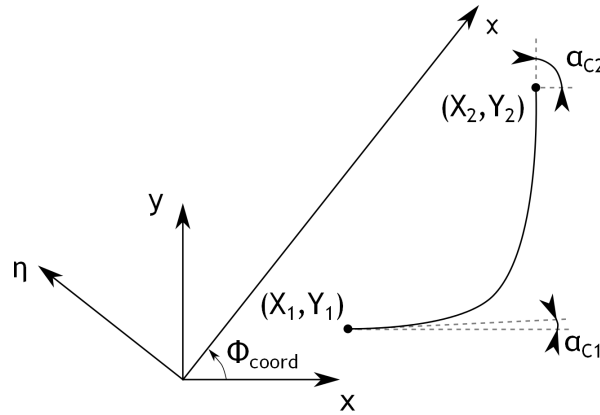


Figure A.1: An example of a typical curve encountered in radial compressors, together with the original  $x - y$  coordinate system and a rotated  $\chi - \eta$  coordinate system

calculation one would end up with an infinite slope in the non-rotated coordinate system. The solution is therefore to rotate the coordinate system by the angle  $\phi_{coord}$ . This angle is chosen so the rotated  $\chi$  coordinate direction coincide with that of a straight line drawn from the start to the end point of the contour. Hence

$$\sin \phi_{coord} = \frac{Y_2 - Y_1}{\sqrt{(X_2 - X_1)^2 + (Y_2 - Y_1)^2}} \quad (\text{A.1})$$

$$\cos \phi_{coord} = \frac{X_2 - X_1}{\sqrt{(X_2 - X_1)^2 + (Y_2 - Y_1)^2}} \quad (\text{A.2})$$

and the rotated coordinates are given by

$$\chi = x \cos \phi_{coord} + y \sin \phi_{coord} \quad (\text{A.3})$$

$$\eta = y \cos \phi_{coord} - x \sin \phi_{coord} \quad (\text{A.4})$$

In the rotated coordinate system the new end point slopes becomes

$$\eta'_1 = \tan(\alpha_{C1} - \phi_{coord}) \quad (\text{A.5})$$

$$\eta'_2 = \tan(\alpha_{C2} - \phi_{coord}) \quad (\text{A.6})$$

The necessary calculations are carried out in the rotated coordinate system. However, the solutions are usually needed in the non-rotated frame of reference, and the results need to be rotated back to the original directions. This can be accomplished with the aid of

$$x = \chi \cos \phi_{coord} - \eta \sin \phi_{coord} \quad (\text{A.7})$$

$$y = \eta \cos \phi_{coord} + \chi \sin \phi_{coord} \quad (\text{A.8})$$

The method is rather straight forward but one must be careful when calculating the angle of coordinate rotation,  $\phi_{coord}$ . The quadrant to which  $\phi_{coord}$  extends to generally depends on which formulas of A.1 and A.2 is chosen. For instance, a negative change in the  $x$ -direction is not recognized by equation A.1. If instead equation A.2 is used a negative change in the  $y$ -direction is not sensed. Therefore any calculation must recognize the change in each coordinate direction and take actions thereafter.

## Appendix B

# Distribution of equally spaced points along a line

Typically when working with quasi normals it is desired to create these between different points along two lines. The points being connected by the quasi normal lines should be positioned at the same dimensionless distance along each line. However, when creating lines it is sometimes hard, not to say impossible, to distribute the points describing the line with equal distance between them. To address this problem the below outlined method is used in all analyses here.

The (two-dimensional) lines being used is described by two vectors. If the line is being created in the  $z - r$  coordinate system the two vectors would contain values for a number of points describing the curve. One vector contains the  $z$ -values and the other the corresponding  $r$ -values of all points. An example of a curve with points distributed unevenly is seen in figure B.1.

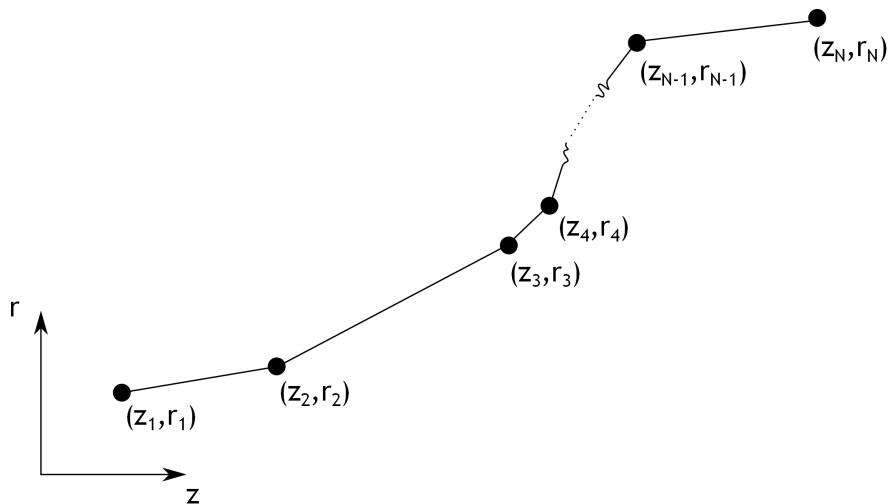


Figure B.1: A typical curve defined by unevenly distributed points. The total number of points is  $N$

The first step is to determine the length  $L$  of the original line. This is a rather straight forward calculation, given by

$$L = \sum_{i=1}^{N-1} \sqrt{(z_{i+1} - z_i)^2 + (r_{i+1} - r_i)^2} \quad (\text{B.1})$$

where  $i$  is an index denoting the current point and  $N$  the total amount of points. After deciding how many points  $N_e$  to be evenly distributed along the line, each line segment's length  $l$  is determined by

$$l = \frac{L}{N_e - 1} \quad (\text{B.2})$$

The line segment  $l$  represents the line length between the evenly distributed points.

When determining the location of all new points, a curvilinear, rotated, coordinate system is employed putting the  $\chi$ -axis along the original curve. Actually, the  $\eta$  coordinate is not needed at all.

The procedure is described with the aid of figure B.2. The first point of the line will of course coincide with the first evenly distributed point. Hence, the curvilinear coordinate system is first placed with it's origin at the first point. The direction of the coordinate system is determined by the current point and next unevenly placed point.

The next step is to determine the distance between the current point and the next unevenly distributed point. In the case of figure B.2a, the distance is obviously longer than the desired spacing  $l$ . Therefore, the next point is obtained simply by moving the distance  $l$  along the  $\chi$  coordinate direction. The curvilinear coordinate system is thus moved to this point, as shown in figure B.2b. This procedure is repeated until a situation as in figure B.2c occurs. Here, the distance  $l$  is longer than the distance between the current point and the next unevenly distributed point. The solution is to calculate this shorter distance  $l'$  and then position the coordinate system the distance  $l - l'$  along the next line, connecting the following unevenly distributed points. This leads to the situation shown in figure B.2d. With these two calculation modes, all approximately evenly spaced points can be distributed along the line.

The method is only approximate, since placing the "new" points along the same line will in general not create the same line. This can be seen in any of the cases in figure B.2. When turning into a new direction along the "old" line, the "new" line would cut any corner upon connecting a line segment between the evenly spaced points. The easiest way to reduce these errors is to use a larger amount of evenly spaced points than unevenly distributed points.

When finished, two new vectors with  $z$  and  $r$  values will have been created, enabling any subsequent calculation being performed with equally spaced points.

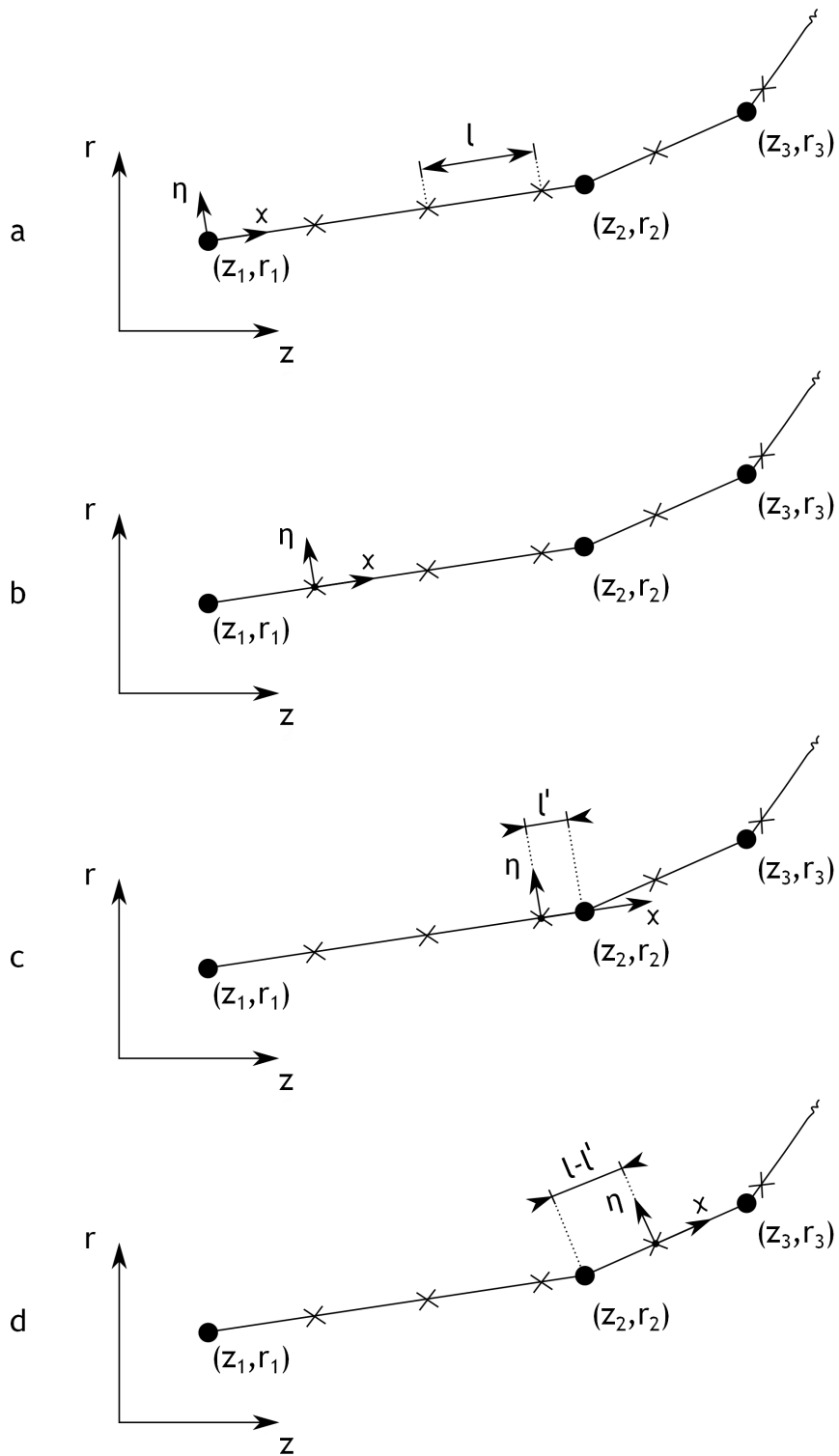


Figure B.2: Four examples of various situations encountered when positioning approximately evenly spaced points. The curvilinear coordinate system  $\chi - \eta$  is moved to each new point (marked with "X") in turn



## Appendix C

# Calculation of passage area and mean streamline

The determination of flow passage areas are vital in all analyses and can conveniently be used in both passages with blades, such as in the impeller, or in passages without any blades, such as in a vaned diffuser. Also, the mean streamline is a vital piece of information in most one-dimensional analyses. As was described in chapter 3, the mean stream surface (and the mean streamline) is here considered to be the surface (or line) containing equal amounts of mass flow above and below it self. As will be noted, this analysis heavily depends on the use of quasi normals in the whole passage to be analysed.

The input needed are the mathematical description of the curves (hub and shroud) defining the axisymmetric flow passage. The quasi normals are created between evenly spaced points along the hub and shroud. Thus the first step is to use the method described in appendix B to distribute the chosen amount of points evenly. If blades exist, the blade angles vary along the hub and shroud. In order to use the blade angle corresponding to the point of interest, the blade angles must be determined with the same resolution as the hub and shroud contour. The result is that each point describing a contour not only is associated with two geometrical coordinates, but also a blade angle. Some features of the method have similarities with the procedure for creating the shroud contour in chapter 3.

A quasi normal is created between the current point on the hub and shroud contour. Along this line, a rotated coordinate system is located, with the  $\chi$ -axis in the direction of the quasi normal. The deviation of the quasi normal from an actual normal is taken into account with the aid of the angle  $\epsilon$  as outlined in chapter 2. As described for the preliminary impeller analysis, chapter 3, a mean value of the shroud and hub deviation is used. In order to determine  $\epsilon$ , the local slope of the contour is needed. Here, a simple central differentiation scheme is employed for determining this slope. In the rotated coordinate system, the values of the points adjacent to the current point is used to calculate the slope. With figure C.1 in mind this would imply, taking the shroud as an example, calculating the slope of the shroud before and after the point of interest. The shroud slope before the point may be found from

$$\alpha_{Cs,i,1,+\Delta\eta} = \arccos \left( \frac{\chi_i - \chi_{i-1}}{\sqrt{(\chi_i - \chi_{i-1})^2 + (\eta_i - \eta_{i-1})^2}} \right) \quad (\text{C.1})$$

under conditions when the change in  $\eta$  is positive. Would the change in  $\eta$  be negative, the slope would be given by

$$\alpha_{Cs,i,1,-\Delta\eta} = 2\pi - \alpha_{Cs,i,1,+\Delta\eta} \quad (\text{C.2})$$

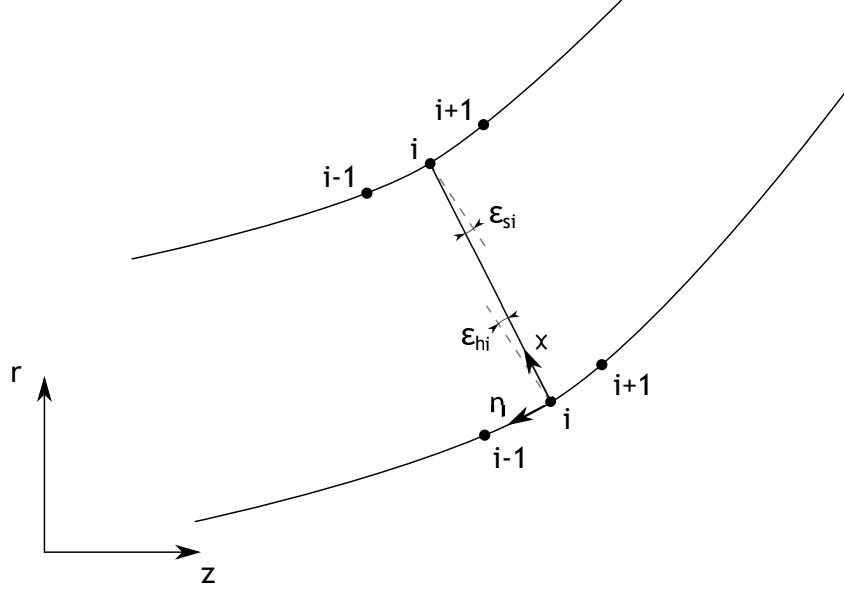


Figure C.1: The main procedure when calculating  $\epsilon$  at both hub and shroud. Adjacent points ( $i + 1$  and  $i - 1$ ) to the current point  $i$  is also shown. A rotated coordinate system  $\chi - \eta$  is employed

in the same manner, the shroud slope after the point is instead calculated from

$$\alpha_{C_{s,i,2,+\Delta\eta}} = \arccos \left( \frac{\chi_{i+1} - \chi_i}{\sqrt{(\chi_{i+1} - \chi_i)^2 + (\eta_{i+1} - \eta_i)^2}} \right) \quad (\text{C.3})$$

which is true when the change in  $\eta$  is positive. Would the change in  $\eta$  be negative, the slope would be given by

$$\alpha_{C_{s,i,2,-\Delta\eta}} = 2\pi - \alpha_{C_{s,i,2,+\Delta\eta}} \quad (\text{C.4})$$

The contour slope at point  $i$  is then determined from the average of the two angles

$$\alpha_{C_{s,i}} = \frac{1}{2} (\alpha_{C_{s,i,1,\pm\Delta\eta}} + \alpha_{C_{s,i,2,\pm\Delta\eta}}) \quad (\text{C.5})$$

Finally, the deviation angle  $\epsilon_{s,i}$  would be given by

$$\epsilon_{s,i} = \frac{3\pi}{2} - \alpha_{C_{s,i}} \quad (\text{C.6})$$

in the rotated frame of reference. The exact same procedure is undertaken for the hub and need no extra explanation. However, special treatment is needed for the first and last point since they don't have points before and after themselves, respectively. The solution is to just take the current and single adjacent point into consideration when determining the slope (this represents a simple forward or backward differentiation scheme).

The next step is to actually determine the passage area, including effects from blade blockage. The calculation must be divided into several discrete steps along the quasi normal, since the blade angles vary (linearly) along the quasi normal. Since the mean streamline also is to be determined, steps with equal amounts of passage areas is suitably used (assuming the



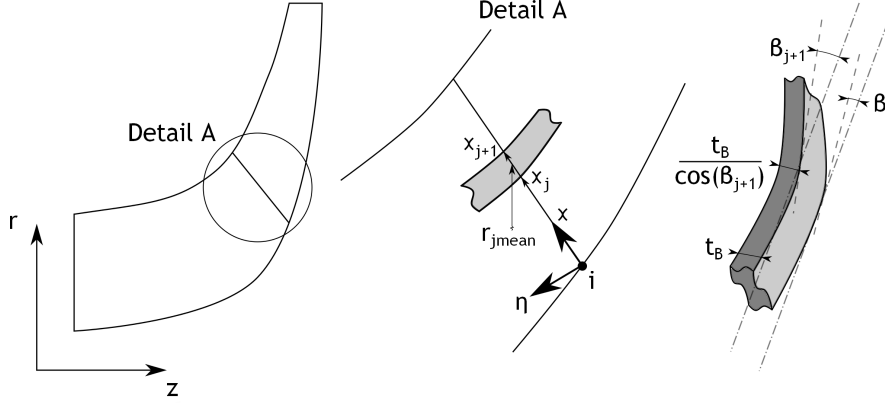


Figure C.2: The main features of the passage area determination. The left figure gives an overview of the problem, showing a typical gas path to be analysed. The middle figure shows the details of the calculation, and the last figure to the right displays the main features of a blade segment

fluid properties are homogeneous in the whole passage). Figure C.2 supports the following reasoning. This is actually the very same figure as shown in chapter 3, emphasising the very similar procedures. An iterative approach is needed as shown in figure C.3. Here the calculation is begun by guessing the size of the  $N$  equal incremental areas of the current quasi normal.

$\chi_j$  is the  $\chi$  coordinate at a blade segment's lower end, as seen in figure C.2. The corresponding blade angle at the position  $\chi_j$  is given by

$$\beta_j = \beta_{h,i} + (\beta_{s,i} - \beta_{h,i}) \frac{\chi_j - \chi_{h,i}}{\chi_{s,i} - \chi_{h,i}} \quad (\text{C.7})$$

where  $\beta_{h,i}$  and  $\beta_{s,i}$  are the blade angles at hub and shroud of the current quasi normal  $i$ , respectively.  $\chi_{h,i}$  denotes the rotated  $\chi$  coordinate at hub, while  $\chi_{s,i}$  denotes the corresponding value at shroud. The incremental annulus area can be approximated by

$$A_{incr,j} = (\chi_{j+1} - \chi_j) \left( 2\pi\bar{r}_j - \frac{Z_I t_B}{\cos \bar{\beta}_j} \right) \cos \epsilon \quad (\text{C.8})$$

here,  $\chi_{j+1}$  is the coordinate of the blade segment's upper end.  $\bar{r}_j$  is the mean radius of the area increment in the non-rotated frame of reference and  $\bar{\beta}_j$  is the mean blade angle of the same element, defined by

$$\bar{\beta}_j = \frac{\beta_j + \beta_{j+1}}{2} \quad (\text{C.9})$$

Further, as is seen in equation C.8, the term  $\cos \epsilon$  has been included. Incorporating this term here will make the determination of the mean streamline coordinate somewhat more accurate, since measures are taken for compensating for the not perfectly normal quasi normal. Geometrically, this can be seen in figure C.2. The passage area determined is the ideal one, assuming the fluid follows the blades without any deviation. Therefore the incremental passage area  $A_{passage,incr,j}$  can be calculated by

$$A_{passage,incr,j} = A_{incr,j} \cos \bar{\beta}_j = (\chi_{j+1} - \chi_j) \left( 2\pi\bar{r}_j \cos \bar{\beta}_j - Z_I t_B \right) \cos \epsilon \quad (\text{C.10})$$

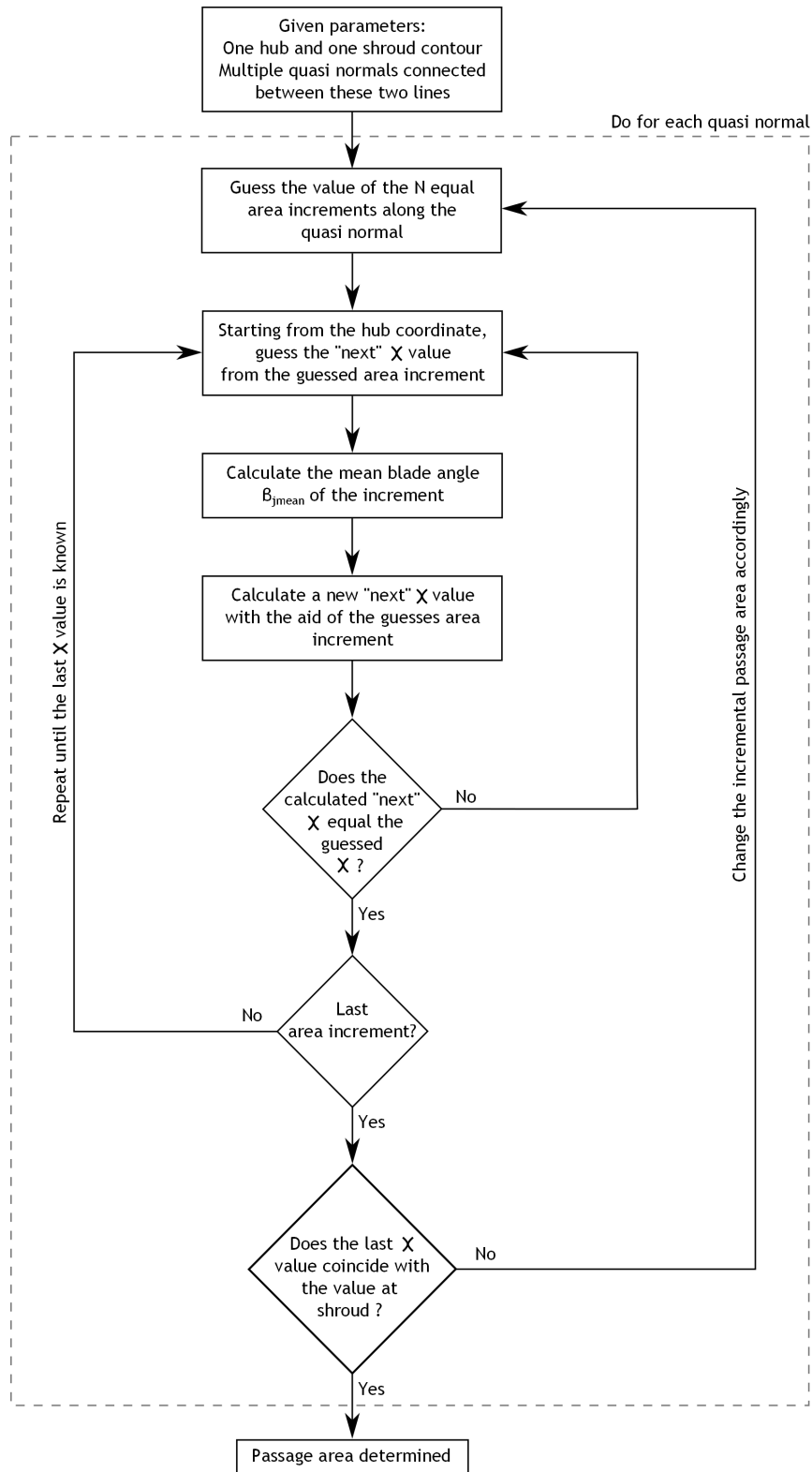


Figure C.3: The iteration loop to determine a passage area along a quasi normal. Note one outer iteration loop for the incremental passage areas, and one internal loop for determining the "next"  $\chi$  value.

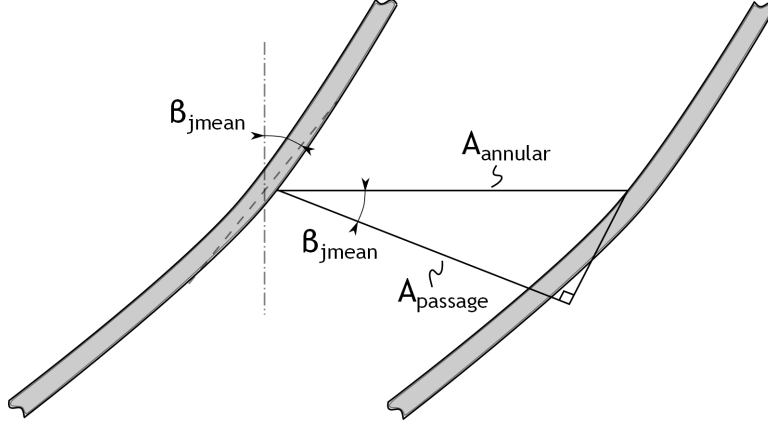


Figure C.4: The calculation from an annular area to a passage area. Only the area between two blades are shown, when performing the calculation outlined here, the area in the whole circumference is determined

as is seen in figure C.4. The first calculation is performed at the hub, since the first  $\chi$  coordinate is known here. From equation C.10 the "next"  $\chi$  value,  $\chi_{j+1}$ , can be determined. Hence, the next calculation is begun at this new  $\chi$  value, and the procedure repeated until the last area increment has been used. At this point the last determined  $\chi$  value,  $\chi_{N+1}$ , should correspond to the value of the shroud along the current quasi normal. Generally this is not the case, and the whole calculation is repeated with altered values of the area increments until convergence.

Having determined the area increments, the passage area  $A_{passage,i}$  at the current quasi normal  $i$  is easily obtained by a simple multiplication according to

$$A_{passage,i} = N A_{passage,incr,j} \quad (C.11)$$

Since equal area increments was chosen and the flow is assumed homogeneous in the whole flow passage, the mean streamline coordinate reduces to the value of the middle  $\chi$  coordinate,  $\chi_{N/2+1}$ . This method also lend itself to easily determine the local passage width. By simply taking the difference of the hub and shroud  $\chi$  values, and compensating for the quasi normal's "non-normalness" through

$$b_i = (\chi_N - \chi_1) \cos \epsilon \quad (C.12)$$

the local passage width  $b_i$  is determined.

Finally, the mean streamline length  $L_S$  can approximately be determined from the now known mean streamline coordinates, see figure C.5. The coordinates are assumed to be rotated back in the non-rotated frame of reference. In this figure the mean streamline coordinates determined by the passage area method above is situated in one and the same (meridional) plane, see the below line. However, the mean streamline will change direction and not stay in this meridional plane. Here, the flow is assumed ideal, in the sense that it follow the blades perfectly. Hence, a simplified mean streamline (or mean camberline) is shown as the top line in figure C.5, constructed of straight line elements. The mean blade angle of a line segment is

$$\bar{\beta}_i = \frac{\beta_i + \beta_{i+1}}{2} \quad (C.13)$$

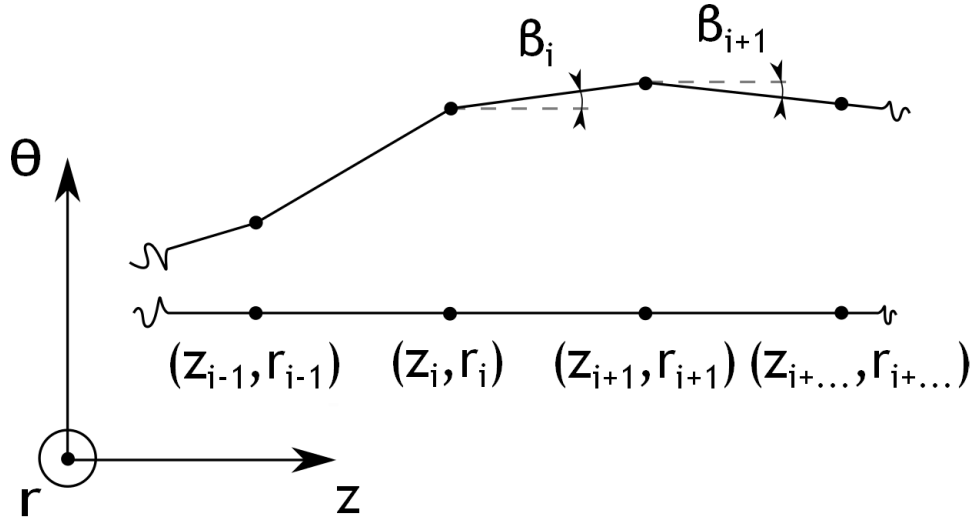


Figure C.5: A schematic representation of the method for determining a mean streamline length. An arbitrarily three-dimensional representation of a streamline is shown above. Below, a schematic two dimensional streamline from the above passage area calculations are shown. This line lies in a meridional plane

and the length of the line segment  $l_{s,i}$  would be

$$l_{s,i} = \frac{\sqrt{(z_{i+1} - z_i)^2 + (r_{i+1} - r_i)^2}}{\cos \bar{\beta}_i} \quad (\text{C.14})$$

The total length of the mean streamline (with  $N$  number of points) are found from

$$L_S = \sum_{i=1}^{N-1} l_{s,i} \quad (\text{C.15})$$

Of course, since the flow was assumed ideal, following the blades perfectly, the mean camberline length  $L_B$  equals the mean streamline length  $L_S$ .

## Appendix D

# Crossing of blade and stream surfaces

When performing a blade-to-blade flow analysis it becomes necessary to find the coordinates in all three dimensions of where stream surfaces connect with blade surfaces. The method of finding these coordinates is based on blade surfaces created of the linear blade segments presented in section 4.2.

In order to find the point of crossing the stream surface must be characterized by a set of points, between which straight lines are drawn. The stream surface's points are only known in  $z$  and  $r$  coordinates. Again, a rotated coordinate system is employed, as shown in figure D.1. Looking at point  $i$ , the angle of the rotated coordinate system to the axial direction is determined by

$$\phi_{coord} = \arccos \left( \frac{z_{C,i+1} - z_{C,i}}{\sqrt{(z_{C,i+1} - z_{C,i})^2 + (r_{C,i+1} - r_{C,i})^2}} \right) \quad (D.1)$$

Having this rotated coordinate system, the stream surface segment between points  $i$  and  $i + 1$  are fully determined by the coordinate  $\chi$ . Of course, the stream surface segment has a constant  $\eta = \eta_C$  coordinate. In order to find the location of the surface crossing, the dimensionless parameter  $\xi$  is introduced denoting the dimensionless distance along a blade segment. Any blade surface element coordinate can then be determined by

$$x_{bs} = x_{h,bs} + \xi (x_{s,bs} - x_{h,bs}) \quad (D.2)$$

$$y_{bs} = y_{h,bs} + \xi (y_{s,bs} - y_{h,bs}) \quad (D.3)$$

$$z_{bs} = z_{h,bs} + \xi (z_{s,bs} - z_{h,bs}) \quad (D.4)$$

where subscript  $bs$  denote blade surface coordinates. Relation D.2, D.3 and D.4 are a useful set of equations since all blade coordinates at hub and shroud are known if, again, using the three-dimensional blade representation described in section 4.2. The radial position of a point along the blade surface can be expressed as

$$\begin{aligned} r_{bs} &= \sqrt{x_{bs}^2 + y_{bs}^2} = \sqrt{(x_{h,bs} + \xi (x_{s,bs} - x_{h,bs}))^2 + (y_{h,bs} + \xi (y_{s,bs} - y_{h,bs}))^2} \\ &= \sqrt{r_{h,bs}^2 + 2\xi (x_{h,bs} (x_{s,bs} - x_{h,bs}) + y_{h,bs} (y_{s,bs} - y_{h,bs})) + \xi^2 \left( (x_{s,bs} - x_{h,bs})^2 + (y_{s,bs} - y_{h,bs})^2 \right)} \end{aligned} \quad (D.5)$$

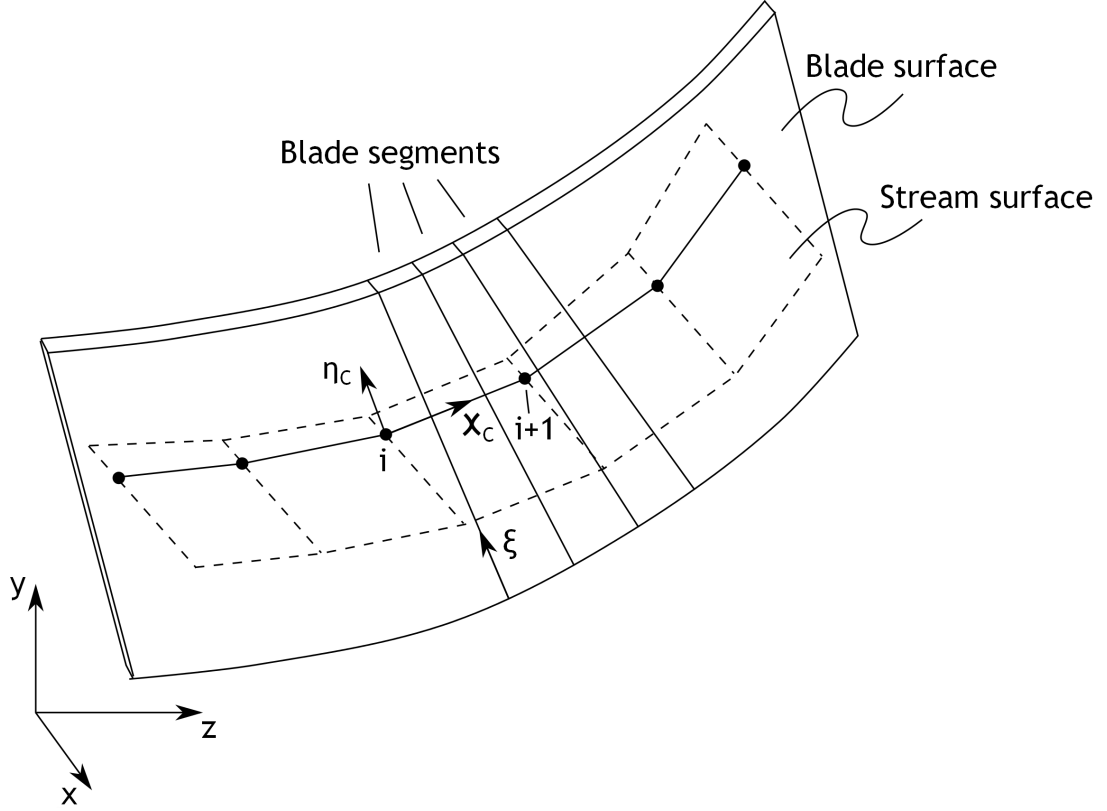


Figure D.1: The basic three-dimensional geometry of a stream surface crossing a blade surface. The stream surface is constructed of linear line segments, while the blade is constructed of linear blade segments.  $\xi$  denotes the non-dimensional distance along a blade segment

Both the radial coordinate  $r_{bs}$  and axial coordinate  $z_{bs}$  are easily expressed in the rotated frame of reference following the procedure outlined in appendix A. The coordinates are consequently given by

$$\chi_{bs} = z_{bs} \cos \phi_{coord} + r_{bs} \sin \phi_{coord} \quad (D.6)$$

$$\eta_{bs} = r_{bs} \cos \phi_{coord} - z_{bs} \sin \phi_{coord} \quad (D.7)$$

An iterative solution is required to find the actual coordinates of the surface crossing;  $\xi$  is altered until the  $\eta_{bs}$  coordinate of the point on the blade surface corresponds to the  $\eta_C$  coordinate of the stream surface segment.

Before any iterative calculation is initiated, a first check to find out whether the stream surface element of interest crosses the "current" blade element is necessary. If this is not the case, the iteration will most likely fail to converge; anyhow implausible coordinates of the crossing would appear if convergence were achieved. The check is rather simple, and incorporates another rotated coordinate system, see figure D.2. This time a coordinate system is placed with its  $\eta$  axis along a straight line extending from the hub to shroud, at the "current" blade element. Note that the check is carried out entirely in a  $z - r$  plane. The exact same procedure to find the angle of the rotated coordinate system as above is used. Also, the next point,  $i + 1$ , of the stream surface must be expressed in the rotated frame of reference. If the  $\chi$  value of this "next" point is larger than the  $\chi$  value of the blade element line, the stream

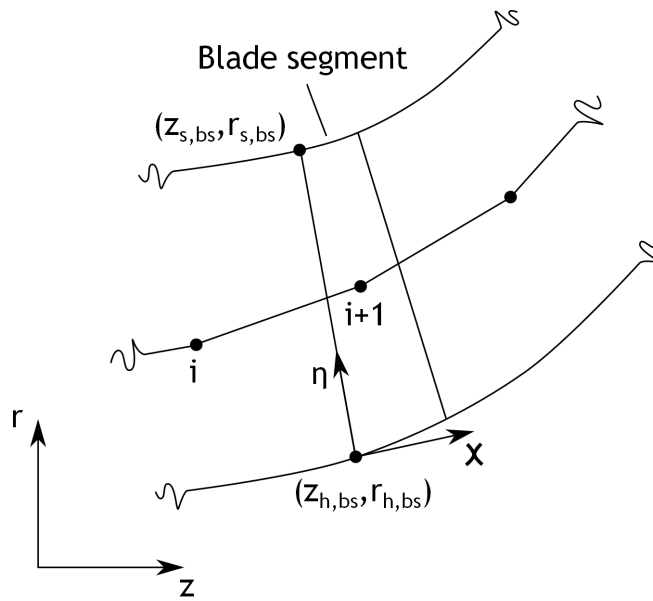


Figure D.2: The procedure for determining whether the stream surface element actually cross the "next" blade element. A rotated coordinate system is placed with it's  $\eta$  direction along the blade element

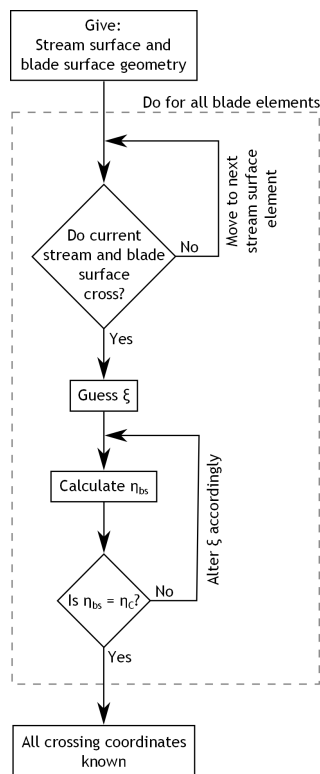


Figure D.3: The iterative calculation to find the coordinates of all blade and stream surface crossings. Note that the procedure must be repeated for all blade elements

surface must cross the blade element. If it is instead found that the line segments do not cross one must consider the next stream surface element, and check whether this element cross the "current" blade element.

The complete iterative method is outlined in figure D.3. After finding all  $\xi$  values of the crossings, the corresponding blade surface coordinates are found through equation D.2, D.3 and D.4.



## Appendix E

# Determination of meridional and tangential equilibrium in vaneless space

When determining the ordinary differential equations to solve the compressible flow in an annulus vaneless space it is needed to consider the meridional and tangential force equilibrium. These two relations are derived here, with the fundamental ideas outlined by Stanitz (1952).

All forces stem from three sources; pressures, wall shear stresses and accelerations. First, turning the attention to the meridional equilibrium equation, figure E.1 shows the pressures and shear stresses of interest. As is seen in this figure, two contributions of pressure forces can be found to have an impact in the meridional direction. One of these are the pressure forces working exactly in the meridional direction at the top and bottom of the fluid element. The differential change of pressure forces over the element (directed in the *negative* meridional direction) can be expressed as

$$\left( pbrd\theta + \frac{d(pbrd\theta)}{dr}dr \right) - pbrd\theta = \frac{d(pbrd\theta)}{dr}dr \quad (\text{E.1})$$

The other pressure forces of interest is the ones working at the sides of the fluid element, somewhat inclined to the positive meridional direction. The resultant differential change in these pressure forces (in the *positive* meridional direction) would be

$$\begin{aligned} & \left( p + \frac{dp}{dr}dr \right) \left( brd\theta + \frac{d(brd\theta)}{dr}dr \right) - pbrd\theta \\ &= pbrd\theta + p\frac{d(brd\theta)}{dr}dr + \frac{dp}{dr}brd\theta dr + \frac{dp}{dr}\frac{d(brd\theta)}{dr}drdr - pbrd\theta \\ &\approx p\frac{d(brd\theta)}{dr}dr \end{aligned} \quad (\text{E.2})$$

where the last relation neglects high order terms. Hence, the resulting pressure forces in the *negative* meridional direction becomes

$$\begin{aligned} \text{Resulting pressure forces} &= \frac{d(pbrd\theta)}{dr}dr - p\frac{d(brd\theta)}{dr}dr \\ &= \frac{dp}{dr}brd\theta dr \end{aligned} \quad (\text{E.3})$$

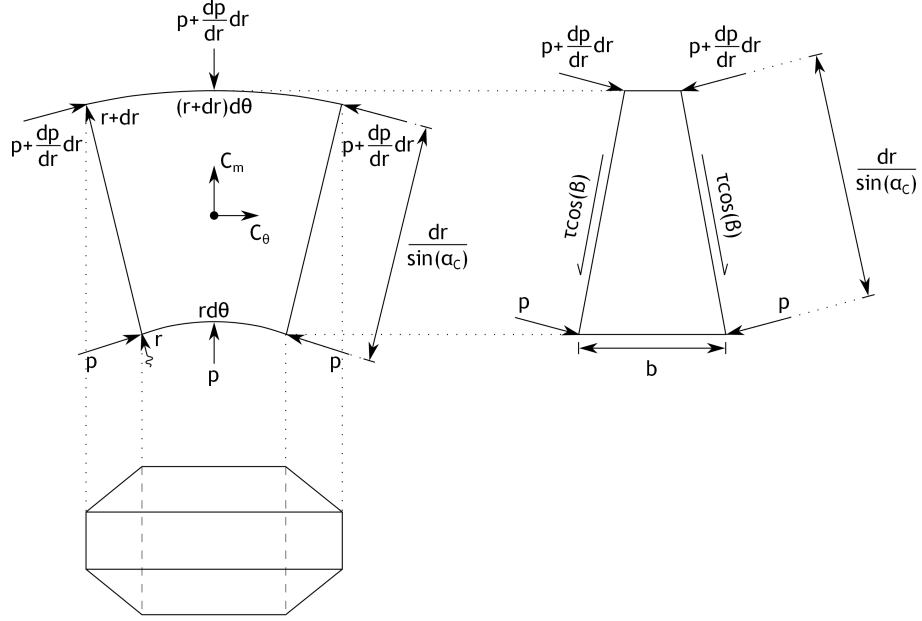


Figure E.1: Sketch of the pressures and wall shear stresses taken into account when determining the meridional equilibrium equation

The friction forces, instead, operates on the two remaining surfaces. Here, an incremental surface area  $dA$  is approximately given by

$$dA = \frac{rd\theta dr}{\sin \alpha_C} \quad (\text{E.4})$$

and the total friction force directed in the *negative* meridional direction from both walls will be

$$\text{Resulting friction force} = 2\tau_w \cos \alpha \frac{rd\theta dr}{\sin \alpha_C} = C_f \rho C^2 \cos \alpha \frac{rd\theta dr}{\sin \alpha_C} \quad (\text{E.5})$$

where equation 6.2 was utilized to eliminate the wall shear stress. Both the pressure and friction forces need to counteract the forces stemming from two different accelerations directed in the *positive* meridional direction. One of the acceleration forces is the centripetal acceleration from the tangential velocity component, expressed as

$$\text{Centripetal acceleration} = \frac{C_\theta^2}{\frac{r}{\sin \alpha_C}} = \frac{C_\theta^2 \sin \alpha_C}{r} \quad (\text{E.6})$$

The other acceleration needed to be taken into account originates from the change in meridional velocity. This acceleration can be written

$$\begin{aligned} \text{Meridional acceleration} &= \frac{dC_m}{dt} = \frac{dC_m}{d\left(\frac{r}{\sin \alpha_C}\right)} \frac{d\left(\frac{r}{\sin \alpha_C}\right)}{dt} \\ &= \frac{dC_m}{d\left(\frac{r}{\sin \alpha_C}\right)} C_m = \frac{dC_m}{dr} C_m \sin \alpha_C \end{aligned} \quad (\text{E.7})$$

In order to determine the forces stemming from the different accelerations, the mass of the fluid element need to be determined. By using equation E.4 this becomes

$$dm = \rho b dA = \rho \frac{br d\theta dr}{\sin \alpha_C} \quad (\text{E.8})$$

Thus, the total differential force in the meridional direction due to different accelerations can be written

$$\begin{aligned} \text{Resulting acceleration force} &= \rho \frac{br d\theta dr}{\sin \alpha_C} \left( \frac{C_\theta^2 \sin \alpha_C}{r} - \frac{dC_m}{dr} C_m \sin \alpha_C \right) \\ &= \rho br d\theta dr \left( \frac{C_\theta^2}{r} - \frac{dC_m}{dr} C_m \right) \end{aligned} \quad (\text{E.9})$$

Equating the sum of equations E.3 and E.5 with equation E.9 yield the meridional equilibrium equation as

$$\frac{1}{\rho} \frac{dp}{dr} + C_f \frac{C^2 \cos \alpha}{b \sin \alpha_C} = \frac{C_\theta^2}{r} - C_m \frac{dC_m}{dr} = \frac{(C \sin \alpha)^2}{r} - C \cos \alpha \frac{d(C \cos \alpha)}{dr} \quad (\text{E.10})$$

The tangential equilibrium equation is derived in a similar way, but contains fewer components. Here, only the friction forces can balance the acceleration of the fluid in the tangential direction. Again, the wall friction operates on a differential area given by equation E.4, and thus the frictional force in this direction becomes

$$\text{Resulting friction force} = 2\tau_w \sin \alpha \frac{rd\theta dr}{\sin \alpha_C} = C_f \rho C^2 \sin \alpha \frac{rd\theta dr}{\sin \alpha_C} \quad (\text{E.11})$$

This force is directed in the *negative* tangential direction. As was the case for the meridional equilibrium, the acceleration consists of two components. The first acceleration appears due to the change in tangential velocity, and is given by

$$\begin{aligned} \text{Tangential acceleration} &= r \frac{d\left(\frac{C_\theta}{r}\right)}{dt} = r \left( \frac{1}{r} \frac{dC_\theta}{dt} - \frac{C_\theta}{r^2} \frac{dr}{dt} \right) \\ &= \frac{dC_\theta}{dr} \frac{dr}{dt} - \frac{C_\theta}{r} \frac{dr}{dt} \\ &= C_m \sin \alpha_C \left( \frac{dC_\theta}{dr} - \frac{C_\theta}{r} \right) \end{aligned} \quad (\text{E.12})$$

The second source of tangential acceleration emerge from the Coriolis acceleration, and becomes

$$\text{Coriolis acceleration} = 2C_m C_\theta \frac{\sin \alpha_C}{r} \quad (\text{E.13})$$

Hence, the total acceleration are the sum of the two contributors, both of which are pointed in the *positive* tangential direction. Equation E.8 determines the mass of the fluid element, therefore the force due to accelerations becomes

$$\begin{aligned} \text{Resulting acceleration force} &= \rho \frac{br d\theta dr}{\sin \alpha_C} C_m \sin \alpha_C \left( \frac{dC_\theta}{dr} + \frac{C_\theta}{r} \right) \\ &= \rho br d\theta dr C_m \left( \frac{dC_\theta}{dr} + \frac{C_\theta}{r} \right) \end{aligned} \quad (\text{E.14})$$

Upon equating equations E.11 and E.14 the tangential equilibrium is determined through

$$-C_f \frac{C^2 \sin \alpha}{b \sin \alpha C} = C_m \frac{dC_\theta}{dr} + C_m \frac{C_\theta}{r} = C \cos \alpha \frac{dC \sin \alpha}{dr} + C \cos \alpha \frac{C \sin \alpha}{r} \quad (\text{E.15})$$

Both the meridional and tangential equilibrium equation are now known. These can be used in the final derivation of the ordinary differential equations for determining the flow properties at any radius  $r$  of an annulus vaneless space.

## Appendix F

# Runge-Kutta numerical integration of ordinary differential equations

The Runge-Kutta integration is a rather straight forward method of integrating ordinary differential equations. The solutions are performed in discrete steps, and the method is sometimes referred to a "stepping solution". When solving a problem with a Runge-Kutta integration, from the starting point, estimations of the function's value in the next point is found by approximating the local derivatives. Here, the method outlined by Riley, Hobson and Bence (2006) [22] is the foundation to derive a second order Runge-Kutta solution. The procedure presented below can be generalized to higher orders of solution, however the qualitative reasoning is exactly the same and suffice for the current discussion.

The parameter  $y$  is a function of  $x$  and the derivative of  $y$  with respect to  $x$  can be written

$$\frac{dy}{dx} = f(x, y) \quad (\text{F.1})$$

where  $f(x, y)$  is used in order to make the following expressions somewhat easier. From here on, subscript  $i$  will denote the current (known) point, while subscript  $i + 1$  is the "next" point, desired to be determined with aid of the Runge-Kutta integration. The change in  $x$  between the two points, the step itself, is denoted  $h$ . Hence

$$h = x_{i+1} - x_i \quad (\text{F.2})$$

One advantage of using the Runge-Kutta integration is that no other than first derivatives need to be determined. To still obtain a high accuracy, these terms are arranged in such a manner to approximate the higher orders of derivatives. The very basis of the Runge-Kutta method is Taylor series expansions. First, a second order expansion around point  $i$  is made according to

$$\begin{aligned} y_{i+1} &= y_i + hf_i + \frac{h^2}{2} \frac{df_i}{dx} + \mathcal{O}(h^3) \\ &= y_i + hf_i + \frac{h^2}{2} \left( \frac{\partial f_i}{\partial x} + f_i \frac{\partial f_i}{\partial y} \right) + \mathcal{O}(h^3) \end{aligned} \quad (\text{F.3})$$

where  $\mathcal{O}(h^3)$  denotes terms of higher orders neglected in what to follow. It is assumed that this relation can be expressed as

$$y_{i+1} = y_i + \alpha_1 hf_i + \alpha_2 hf(x_i + \beta_1 h, y_i + \beta_2 hf_i) \quad (\text{F.4})$$

where the coefficients  $\alpha$  and  $\beta$  are arbitrary constants, but must be chosen so as to make expression F.4 equal equation F.3. As is obvious from the above relations is that the method approximates derivatives away from the point  $i$  by using weighted function arguments  $x$  and  $y$ . Again using a Taylor expansion, the function  $f_i$  with weighted arguments can be expressed as

$$f(x_i + \beta_1 h, y_i + \beta_2 h f_i) = f_i + \beta_1 h \frac{\partial f_i}{\partial x} + \beta_2 h f_i \frac{\partial f_i}{\partial y} + \mathcal{O}(h^2) \quad (\text{F.5})$$

where any terms of higher orders are discarded. Substituting equation F.5 into equation F.4 one obtain

$$y_{i+1} = y_i + (\alpha_1 + \alpha_2) h f_i + \alpha_2 h^2 \left( \beta_1 \frac{\partial f_i}{\partial x} + \beta_2 f_i \frac{\partial f_i}{\partial y} \right) \quad (\text{F.6})$$

Comparing equations F.3 and F.6, it is seen that the constants  $\alpha$  and  $\beta$  must fulfil the following criteria

$$\alpha_2 = 1 - \alpha_1 \quad (\text{F.7})$$

and

$$\beta_1 = \beta_2 = \frac{1}{2(1 - \alpha_1)} \quad (\text{F.8})$$

where the constants  $\beta_1$  and  $\beta_2$  should be equal, as is obvious when inserting them in equation F.4. At this point four unknowns ( $\alpha_1$ ,  $\alpha_2$ ,  $\beta_1$  and  $\beta_2$ ) exist, but only three equations. Hence, some arbitrariness exist in specifying the absolute values of these parameters. A typical choice is  $\alpha_1 = 0.5$ , which would yield the final equation in the form of

$$y_{i+1} = y_i + \frac{1}{2} (a_1 + a_2) \quad (\text{F.9})$$

where  $a_1$  and  $a_2$  is determined by

$$a_1 = h f(x_i, y_i) \quad (\text{F.10})$$

$$a_2 = h f(x_i + h, y_i + a_1) \quad (\text{F.11})$$

In the same manner a fourth order Runge-Kutta solution (many times termed "RK4") can be written

$$y_{i+1} = y_i + \frac{1}{6} (b_1 + 2b_2 + 2b_3 + b_4) \quad (\text{F.12})$$

where  $b_1$ ,  $b_2$ ,  $b_3$  and  $b_4$  is determined by

$$b_1 = h f(x_i, y_i) \quad (\text{F.13})$$

$$b_2 = h f\left(x_i + \frac{1}{2}h, y_i + \frac{1}{2}b_1\right) \quad (\text{F.14})$$

$$b_3 = h f\left(x_i + \frac{1}{2}h, y_i + \frac{1}{2}b_2\right) \quad (\text{F.15})$$

$$b_4 = h f(x_i + h, y_i + b_3) \quad (\text{F.16})$$

## Appendix G

# One-dimensional channel flow

When analysing the vaned diffuser, or more specifically, the vaned channel diffuser of the wedge type, the need for an approach capable of determining one-dimensional compressible flow including effects of friction becomes apparent. Further, any change in passage area must be sensed by the model, since a main feature of the diffuser is a diverging flow passage. Here, the main ideas presented by Greitzer, Tan and Graf (2006) are employed in order to derive the governing equations. As will be noted, some features are similar to the derivation of the differential equations enabling the vaneless diffuser analysis presented in chapter 6. For the sake of completeness, all relations are derived from simple fluid dynamic relations, even though some expressions will take the exact form found in the vaneless diffuser analysis. A schematic sketch of a typical flow channel is shown in figure G.1. This figure depicts a rectangular section, however, the derivation is valid for any channel shape. Also shown are the notations for the passage width  $w$ , and the passage height  $b$ . Generally these vary along the coordinate  $x$ , hence a variable channel passage area  $A$  is implied. The analysis being one-dimensional, all parameters of interest will only (uniformly) vary along the  $x$  direction.

A relation relating the gas properties to thermodynamic dittos is the ideal gas law, equation 2.1. Taking the derivative of this, and noting that the specific gas constant  $R$  is constant along the channel one obtain

$$\frac{1}{p} \frac{dp}{dx} = \frac{1}{\rho} \frac{d\rho}{dx} + \frac{1}{T} \frac{dT}{dx} \quad (\text{G.1})$$

where the derivative was divided by the ideal gas law itself. Noting that the mass flow is constant at any cross section, a one dimensional continuity equation anywhere in the channel takes the form of

$$\dot{m} = \rho C A = \text{const.} \quad (\text{G.2})$$

Taking the derivative with respect to  $x$ , and again dividing the result with the equation itself yields

$$\frac{1}{\rho} \frac{d\rho}{dx} + \frac{1}{C} \frac{dC}{dx} + \frac{1}{A} \frac{dA}{dx} = 0 \quad (\text{G.3})$$

Equation 2.8 instead relates the stagnation and static temperature to the Mach number  $M$ . By taking the derivative of this equation, the result is

$$\frac{dT_0}{dx} = \frac{dT}{dx} \left( 1 + \frac{\gamma - 1}{2} M^2 \right) + T \frac{\gamma - 1}{2} \frac{dM^2}{dx} = 0 \quad (\text{G.4})$$

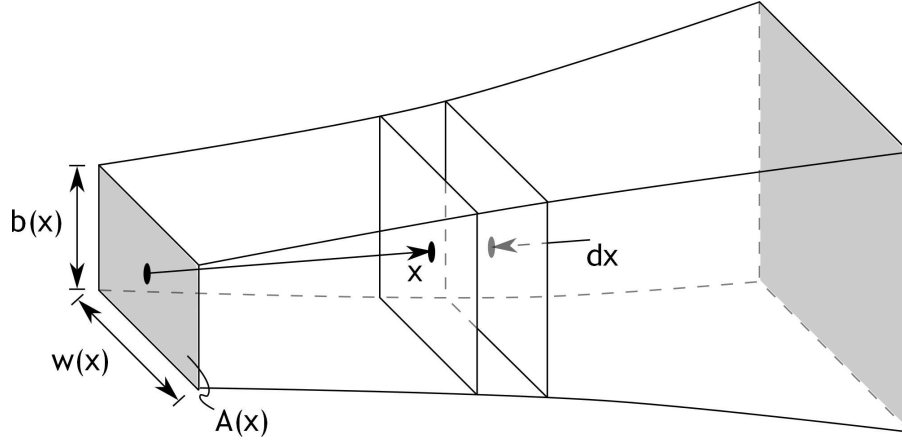


Figure G.1: A schematic fluid channel, showing the main features used in the derivation. The coordinate  $x$  is directed along the channel, where the width  $w$  and height  $b$  characterize the passage area  $A$ . Also shown are an incremental passage element with length  $dx$  along the channel

If this is divided by the governing equation 2.8, the change in stagnation temperature can be written

$$\frac{1}{T_0} \frac{dT_0}{dx} = \frac{1}{T} \frac{dT}{dx} + \frac{\frac{\gamma-1}{2} M^2}{1 + \frac{\gamma-1}{2} M^2} \frac{1}{M^2} \frac{dM^2}{dx} = 0 \quad (\text{G.5})$$

Another useful relationship can be found by taking the derivative of the Mach number itself, equation 6.3. Solving for the velocity  $C$ , one find

$$\frac{1}{C} \frac{dC}{dx} = \frac{1}{2} \left( \frac{1}{M^2} \frac{dM^2}{dx} + \frac{1}{T} \frac{dT}{dx} \right) \quad (\text{G.6})$$

One additional equation must be found in order to relate the difference in pressure in the channel to the acceleration and friction forces encountered. This can be achieved by studying the different forces acting on an incremental fluid element, such as that seen in figure G.2. This figure shows a section of a fluid element, covering the whole passage. In order to yield a steady equilibrium flow, the sum of the forces from upstream and downstream fluid, friction and acceleration must equal zero. Starting with the pressure forces, these stem not only from the pressure difference in the channel's direction, but also from pressure exerted by the walls against the fluid. Since the flow passage area in general changes, these forces have two components where only one is directed into the one dimension considered, the  $x$  direction. In total, these pressure components must act on the change in passage area along the incremental length  $dx$ , that is on the area  $dA/dx \cdot dx$ . It is assumed that the overall magnitude of these wall pressures can be thought of as mean pressures along the walls. Hence, the total pressure forces in the *negative*  $x$  direction become

$$\begin{aligned} \text{pressure forces} &= \left( p + \frac{dp}{dx} dx \right) \left( A + \frac{dA}{dx} dx \right) - pA \\ &\quad - \left( p + \frac{1}{2} \frac{dp}{dx} dx \right) \frac{dA}{dx} dx \approx A \frac{dp}{dx} dx \end{aligned} \quad (\text{G.7})$$



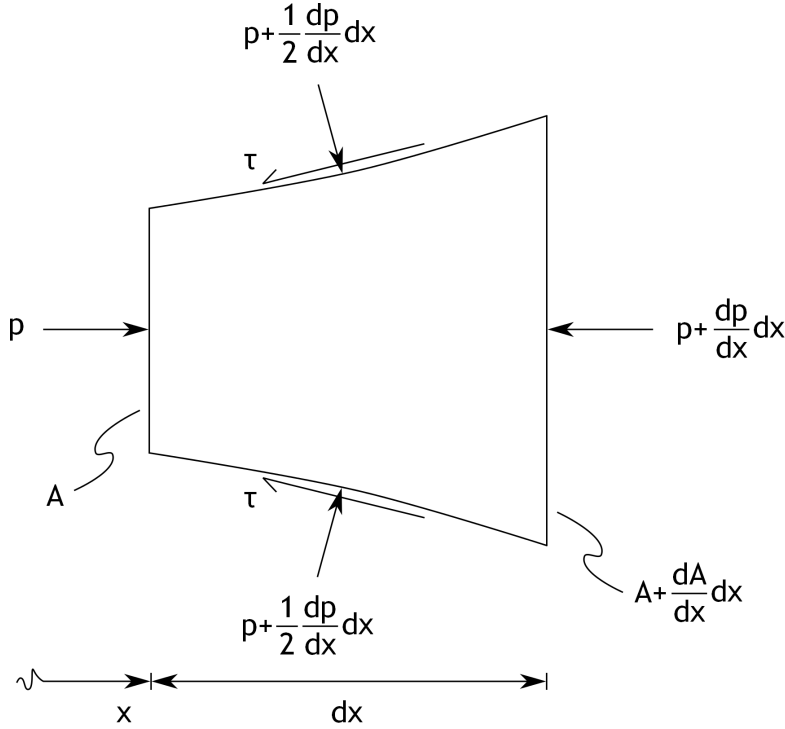


Figure G.2: An incremental fluid element filling the whole channel area. Only a two-dimensional section of the element is shown, hence only two of the surrounding walls. It is understood that wall friction shear stresses act around the whole circumference of the element

where the last equality implies discarding high order terms. In order to cope with the wall friction forces, the hydraulic diameter  $d_H$  concept is useful. A hydraulic diameter is defined by

$$d_H = \frac{4A}{\text{wetted perimeter}} \quad (\text{G.8})$$

Here, the wetted perimeter is the total circumference of the channel. For the rectangular section of interest the wetted perimeter would equal  $2(b + w)$ . The friction forces exerted on the incremental fluid element's wall area  $A_w$  can consequently be written

$$\begin{aligned} \text{friction forces} &= \tau_w dA_w = \tau_w (\text{wetted perimeter}) dx \\ &= \frac{4A}{d_H} \tau_w dx = \frac{4A}{d_H} C_f \frac{1}{2} \rho C^2 dx \end{aligned} \quad (\text{G.9})$$

To eliminate the wall shear stresses, the friction factor  $C_f$  was introduced through equation 6.2. These friction forces are directed into the *negative* flow direction. In order to eliminate the density the following useful trick is employed, making use of both the ideal gas law and the definition of Mach number

$$\rho C^2 = \frac{pC^2}{RT} = \frac{\gamma p C^2}{\gamma RT} = \gamma p M^2 \quad (\text{G.10})$$

Combining the above relations yields

$$\text{friction forces} = \frac{2A}{d_H} C_f \gamma p M^2 dx \quad (\text{G.11})$$

Finally, turning the attention to forces associated with any fluid acceleration, the acceleration itself can be written

$$\frac{dC}{dt} = \frac{dC}{dx} \frac{dx}{dt} = \frac{dC}{dx} C \quad (\text{G.12})$$

The mass of an incremental fluid element filling the whole passage can, for sufficiently small incremental steps  $dx$ , be determined through

$$dm = \rho A dx = \frac{\gamma p M^2}{C^2} A dx \quad (\text{G.13})$$

again using the density trick, equation G.10. Thus, the acceleration forces become

$$\text{acceleration forces} = \frac{dC}{dt} dm = \gamma M^2 p A \frac{1}{C} \frac{dC}{dx} dx \quad (\text{G.14})$$

Summing all forces acting on the fluid elements yields the final equation needed to solve the equation governing the one-dimensional flow. Hence

$$A \frac{dp}{dx} dx + \frac{2A}{d_H} C_f \gamma p M^2 dx + \gamma M^2 p A \frac{1}{C} \frac{dC}{dx} dx = 0 \quad (\text{G.15})$$

or equally

$$\gamma M^2 \frac{1}{C} \frac{dC}{dx} + \frac{1}{p} \frac{dp}{dx} + \frac{2C_f \gamma M^2}{d_H} = 0 \quad (\text{G.16})$$

These equations must now be combined to bring about a solution enabling the flow condition to be calculated at any location  $x$ . The first step is to eliminate the pressure gradient in equation G.16. A suitable expression for this pressure gradient can be found by combining equations G.1 and G.3, yielding

$$\frac{1}{p} \frac{dp}{dx} = \frac{1}{T} \frac{dT}{dx} - \frac{1}{C} \frac{dC}{dx} - \frac{1}{A} \frac{dA}{dx} \quad (\text{G.17})$$

Inserting this expression into equation G.16 and rearranging gives

$$\left(\gamma M^2 - 1\right) \frac{1}{C} \frac{dC}{dx} + \frac{1}{T} \frac{dT}{dx} - \frac{1}{A} \frac{dA}{dx} + \frac{2C_f \gamma M^2}{d_H} = 0 \quad (\text{G.18})$$

Using the found derivative of the Mach number, equation G.6, and some minor algebraic manipulations this expression instead takes the form of

$$\left(\frac{\gamma M^2 - 1}{2}\right) \frac{1}{M^2} \frac{dM^2}{dx} + \left(\frac{1 + \gamma M^2}{2}\right) \frac{1}{T} \frac{dT}{dx} - \frac{1}{A} \frac{dA}{dx} + \frac{2C_f \gamma M^2}{d_H} = 0 \quad (\text{G.19})$$

The final expression is determined by inserting equation G.5 in the above equation, eliminating the static temperature gradient. After some rearranging the following result is generated, describing how the squared Mach number is changed along the flow passage

$$\frac{1}{M^2} \frac{dM^2}{dx} = \frac{1 + \frac{\gamma-1}{2} M^2}{1 - M^2} \left( -\frac{2}{A} \frac{dA}{dx} + \left(1 + \gamma M^2\right) \frac{1}{T_0} \frac{dT_0}{dx} + \frac{4C_f \gamma M^2}{d_H} \right) \quad (\text{G.20})$$

Integrating this formula numerically would yield the Mach number distribution. However, it is also of interest to determine how the thermodynamic properties varies with the passage

length  $x$ . Here, a relation relating the stagnation pressure change along the channel is sought, and the first step is to take the derivative of equation 2.9. This yields

$$\frac{dp_0}{dx} = \frac{dp}{dx} \left(1 + \frac{\gamma-1}{2}M^2\right)^{\frac{\gamma}{\gamma-1}} + p \frac{\gamma}{2} \left(1 + \frac{\gamma-1}{2}M^2\right)^{\frac{1}{\gamma-1}} \frac{dM^2}{dx} \quad (\text{G.21})$$

Dividing this relation with it's governing equation, relation 2.9, gives the following expression

$$\frac{1}{p_0} \frac{dp_0}{dx} = \frac{1}{p} \frac{dp}{dx} + \frac{\gamma M^2}{2} \left( \frac{1}{1 + \frac{\gamma-1}{2}M^2} \right) \frac{1}{M^2} \frac{dM^2}{dx} \quad (\text{G.22})$$

Again, the static pressure gradient must be eliminated. A suitable expression for the pressure gradient can be found by combining equation G.6 and G.17. Doing this, one end up with

$$\frac{1}{p} \frac{dp}{dx} = \frac{1}{2} \frac{1}{T} \frac{dT}{dx} - \frac{1}{2} \frac{1}{M^2} \frac{dM^2}{dx} - \frac{1}{A} \frac{dA}{dx} \quad (\text{G.23})$$

The static temperature gradient can in turn be dealt with by combining the above relation with equation G.5. After a minor mathematical exercise, the static pressure gradient can be written

$$\frac{1}{p} \frac{dp}{dx} = \frac{1}{2} \frac{1}{T_0} \frac{dT_0}{dx} - \frac{1}{A} \frac{dA}{dx} - \left( \frac{\gamma M^2}{2} + \frac{1-M^2}{2} \right) \left( \frac{1}{1 + \frac{\gamma-1}{2}M^2} \right) \frac{1}{M^2} \frac{dM^2}{dx} \quad (\text{G.24})$$

By substituting the above derived relationship into the stagnation pressure variation along the channel, equation G.22, the following relation is found

$$\frac{1}{p_0} \frac{dp_0}{dx} = \frac{1}{2} \frac{1}{T_0} \frac{dT_0}{dx} - \frac{1}{A} \frac{dA}{dx} - \frac{1}{2} \left( \frac{1-M^2}{1 + \frac{\gamma-1}{2}M^2} \right) \frac{1}{M^2} \frac{dM^2}{dx} \quad (\text{G.25})$$

Finally, the expression for the stagnation pressure's variation along the channel can be found by making use of the found Mach number variation. Thus, putting equation G.20 into relation G.25 yields

$$\frac{1}{p_0} \frac{dp_0}{dx} = \left( -\frac{\gamma M^2}{2} \right) \left( \frac{1}{T_0} \frac{dT_0}{dx} + \frac{4C_f}{d_H} \right) \quad (\text{G.26})$$

A remarkably simple relation, considering the amount of algebra needed to derive it. Nevertheless, this equation also need numerical solving, and is most easily solved simultaneous with equation G.20. The Runge-Kutta integration presented in appendix F can be used for this, by performing the calculation along discrete steps of the channel.